REPORT DOCUMENTATION PAGE

Form Approved
OMB No. 0704-0188

The public reporting burden for this collection of information is estimated to average 1 hour per response, including the time for reviewing instructions, searching existing data sources, gathering and maintaining the data needed, and completing and reviewing the collection of information. Send comments regarding this burden estimate or any other aspect of this collection of information, including suggestions for reducing the burden, to Department of Defense, Washington Headquarters Services, Directorate for Information Operations and Reports (0704-0188), 1215 Jefferson Davis Highway, Suite 1204, Arlington, VA 22202-4302. Respondents should be aware that notwithstanding any other provision of law, no person shall be subject to any penalty for failing to comply with a collection of information if it does not display a currently valid OMB control number.

PLEASE DO NOT RETURN YOUR FORM TO THE ABOVE ADDRESS.

1. REPORT DATE *(DD-MM-YYYY)*	2. REPORT TYPE	3. DATES COVERED *(From - To)*
24-08-2010	Final Technical Report	Sep 2007 - Mar 2010

4. TITLE AND SUBTITLE

Final Technical Report
Hawaii Energy and Environmental Technologies (HEET) Initiative

5a. CONTRACT NUMBER

5b. GRANT NUMBER

N00014-07-1-1094

5c. PROGRAM ELEMENT NUMBER

6. AUTHOR(S)

Rocheleau, Richard E.
Bethune, Keith; Davies, Kevin
Virji, Maheboob
Antal, Michael J., Jr.
Cooney, Michael J.
Liaw, Bor Yann
Masutani, Stephen M.

5d. PROJECT NUMBER

09PR08720-00

5e. TASK NUMBER

5f. WORK UNIT NUMBER

7. PERFORMING ORGANIZATION NAME(S) AND ADDRESS(ES)

University of Hawaii
2530 Dole Street, Sakamaki D200
Honolulu, HI 96822

8. PERFORMING ORGANIZATION REPORT NUMBER

9. SPONSORING/MONITORING AGENCY NAME(S) AND ADDRESS(ES)

Office of Naval Research
Regional Office Seattle
1107 NE 45th Street, Suite 350
Seattle WA 98105-4631

10. SPONSOR/MONITOR'S ACRONYM(S)

ONR

11. SPONSOR/MONITOR'S REPORT NUMBER(S)

12. DISTRIBUTION/AVAILABILITY STATEMENT

Approved for public release; distribution is unlimited.

13. SUPPLEMENTARY NOTES

14. ABSTRACT

This report covers efforts by the Hawaii Natural Energy Institute of the University of Hawaii under the ONR-funded HEET Initiative that addresses critical technology needs for exploration/utilization of seabed methane hydrates and development/testing of advanced fuel cells and fuel cell systems. Methane hydrates work included: hydrate thermochemistry and kinetics; environmental impacts of methane release from seafloor hydrates; hydrate engineering applications; and international collaborative R&D. For fuel cells accomplishments included: test stand and infrastructure upgrades to the Hawaii Fuel Cell Test Facility; work on understanding the SO2 contamination mechanism and SO2 contamination recovery; preliminary testing of Protonex H2/air stacks under pure oxygen in support of NUWC; and fuel contamination efforts via a Modelica model which worked with previous experimental results of CO poisoning. Fuel processing and purification work included testing of a reverse-vortex-flow non-thermal plasma reactor to study methane reforming. Further work was also carried out with novel fuel cell concepts including biocarbons and bio-fuel cells.

15. SUBJECT TERMS

Fuel Cells, Fuel Cell Testing, MEA Assembly, Hardware-in-Loop Testing, Fuel Processing and Purification, Fuels Purity, Methane Hydrates, Biocarbons, Bio-Fuel Cells

16. SECURITY CLASSIFICATION OF:			17. LIMITATION OF ABSTRACT	18. NUMBER OF PAGES	19a. NAME OF RESPONSIBLE PERSON
a. REPORT	b. ABSTRACT	c. THIS PAGE			Yaa-Yin Fong, Director of Research Services
U	U	U	UU	133	19b. TELEPHONE NUMBER *(Include area code)* (808) 956-9081

FINAL TECHNICAL REPORT

Hawaii Energy and Environmental Technologies (HEET) Initiative

Office of Naval Research
Grant Award Number N00014-07-1-1094
For the period September 27, 2007 to March 31, 2010

Hawaii Natural Energy Institute

School of Ocean and Earth Science and Technology
University of Hawaii at Mānoa

August 2010

20100901106

Table of Contents

Section No.	Section Title	Page
1	Executive Summary	1
2	Introduction	6
3	Fuel Cell Systems	7
3.1	PEM Fuel Cell Testing and Component Development	7
3.1.1	Test stands/Infrastructure Upgrades	7
3.1.2	Cell and Component Testing	8
3.1.2.1	Air Contaminant Studies: SO_2 Contamination Mechanism.	8
3.1.2.2	Recovery from SO_2 Contamination	15
3.1.2.3	Component Evaluation: Operation of Protonex Stacks Under Oxygen	16
3.1.2.4	Component Evaluation: Segmented Flow-Field Optimization	23
3.1.2.5	Fuel Contaminant Studies: Modelica Model Development	27
	Reference	28
3.1.3	MEA Fabrication Laboratory	28
3.1.4	Papers and Presentations Resulting from 2009 Efforts	29
3.2	Fuel Cell Hardware-in-Loop Capability	30
3.3	Novel Fuel Cell and Component Development	31
3.3.1	Biocarbons for Use in Fuel Cells	31
3.3.1.1	Scope of Work and Approach	31
3.3.1.2	Technical Accomplishments	32
3.3.1.3	Papers and Presentations Resulting from Efforts	33
3.3.2	Enzymatic Bio-Fuel Cells	35
3.3.2.1	Scope of Work and Approach	35
3.3.2.2	Technical Accomplishments	36
3.3.2.3	References	46
3.3.2.4	Papers and Presentations Resulting from Efforts	47
4	Fuel Processing and Purification Studies	51
4.1	Scope of Work and Approach	51
4.2	Laboratory Setup and Operation	51
4.2.1	Front End	52
4.2.2	Reformer Section	53
4.2.3	Back End	56
4.2.4	Start Up	57

4.3 Testing Activities and Rationale 57
4.3.1 Parametric Tests 57
4.3.2 Factorial Design 57
4.3.3 Data Reduction 58
4.4 Technical Accomplishments 59
4.4.1 Parametric Tests 59
4.4.1.1 Gap Distance 59
4.4.1.2 Steam Input 61
4.4.1.3 Methane Input 63
4.4.1.4 Orifice Size 65
4.4.1.5 Power Input 67
4.4.1.6 Post Reaction Chamber Fill 68
4.4.1.7 Volumetric Flow Rate 70
4.4.2 Factorial Tests 72
4.4.2.1 First Full Factorial Test 72
First Factorial Test Results 75
4.4.2.2 Path of Steepest Ascent, Methane Conversion Metric 76
4.4.2.3 Path of Steepest Ascent, Selectivity Metric 77
4.4.2.4 Second Factorial Test 78
Second Factorial Test Results 78
4.5 Papers and Presentations Resulting from Efforts 80

5 Methane Hydrates 81
5.1 Scope of Work and Approach 82
5.1.1 Hydrate Thermochemistry and Kinetics 82
5.1.2 Environmental Impacts of Methane Release from Seafloor Hydrates 82
5.1.3 Hydrate Engineering Applications 83
5.1.4 International Collaborative R&D 83
5.2 Technical Accomplishments 83
5.2.1 Methane Hydrate Destabilization 83
5.2.1.1 Reagent Destabilization of Methane Hydrates 83
5.2.1.1.1 Determination of Reagent Effectiveness from Raman Calorimetry Experiments 84
5.2.1.1.2 Theory 84
5.2.1.1.3 Heat and Mass Considerations During Hydrate Destabilization 85
5.2.1.2 Subsea Power Generation: Heat Capacity of Water at Elevated Pressure 106
Experiments to Determine the Heat Capacity of High Pressure Water 107

5.2.2 Environmental Impacts of Methane Release from Seafloor Hydrates 113
5.2.2.1 Modeling 113
Carbon Isotope Fractionation by Aerobic CH_4-oxidizing Bacteria 113
5.2.2.2 Hydrate Microbiology 120
Preliminary Beaufort Sea Sample Analysis Results 121
5.2.3 Hydrate Engineering Applications 123
THF/H_2 Hydrate Synthesis Experiments 123
5.2.4 International Collaborative R&D 127
5.3 Publications Resulting from Efforts 127
5.4 References 128

Final Technical Report for the
Hawaii Energy and Environmental Technologies (HEET) Initiative
Grant Award Number N00014-07-1-1094
(September 27, 2007 to March 31, 2010)

1. Executive Summary

This report summarizes work conducted under Grant Award Number N00014-07-1-1094, the Hawaii Energy and Environmental Technologies (HEET) Initiative, funded through the Office of Naval Research (ONR) to the Hawaii Natural Energy Institute (HNEI) of the University of Hawaii. The effort under this award focused on critical technology needs associated with the development and testing of advanced fuel cells and fuel cell systems, fuel processing and purification, and the exploration and utilization of seabed methane hydrates. This represents the fifth award of this initiative.

Major accomplishments under the first grant award, Number N00014-01-1-0928, included the planning, design and construction of the Hawaii Fuel Cell Test Facility (HFCTF), which opened in May 2003. In partnership with industry, HNEI established test protocols and initiated a variety of long-term durability studies. The methane hydrates activities under the first agreement initiated studies to characterize hydrate thermochemistry and kinetics, hydrate microbiology and development of international collaborations.

Under the second award (N00014-04-1-0682), HNEI expanded its test capabilities with the addition of three new fuel cell test stands at the HFCTF, including two for fuels purity studies. Tests to characterize the effects of trace amounts of contaminants in the hydrogen fuel were initiated. The third stand was designed for high speed dynamic testing for use in Hardware-in-Loop (HiL) work. Modeling and simulation of a fuel cell energy/power system for use in an unmanned underwater vehicle (UUV) was also completed and reported. Novel fuel cell component research was conducted to explore the use of biocarbons in fuel cell bipolar plates and development of enzymatic bio-fuel cells. A small effort in alternative fuel research was continued, focused on fuel processing and gas conditioning for hydrogen production. HNEI's activities in the area of methane hydrates included studies of hydrate destabilization phenomena, with shakedown testing of HNEI's destabilization facility and design and fabrication of a novel fiberoptic probe to identify sample aspects within the calorimeter sample cell using Raman spectroscopy. HNEI sponsored and manned the organizing committee of the 4th International Workshop on Methane Hydrates that took place in Victoria, British Columbia, Canada on 9-11 May 2005.

Under the third award (N00014-06-1-0086), the capacity of the HFCTF was again expanded, increasing the total number of test stands to eight, with modification of existing test stands for increased performance. The dynamic HiL test stand was modified to enhance response and to improve operating flexibility, safety, and test stand reliability. Simulation tools for evaluation and screening of fuel cell systems for UUV propulsion systems were developed. HNEI continued research on fuel processing and gas conditioning for hydrogen production, focused on sulfur removal from fuel gas using activated-carbon-based sorbents, and reformation of seafloor methane for use in underwater fuel cells. Work continued in the development of novel fuel cells and components, specifically in the areas of biocarbons for fuel cell use and development of

enzymatic bio-fuel cells. HNEI's activities in the area of methane hydrates included an expanded effort in hydrate destabilization with development of a novel instrument that combined spectroscopy and calorimetry to study reagent-induced decomposition of the hydrates. As part of our goal to promote international collaboration, HNEI personnel participated in a multi-national research cruise off New Zealand in June and July 2006.

Under the fourth award (N00014-06-1-1055), more test stands were again added to the HFCTF, bringing the total to eleven. Several existing stands were modified to allow testing of small stacks. Several test stands were used to support Ion Tiger, an ONR-funded unmanned aerial vehicle (UAV) project. Research focused primarily on understanding the performance impact of contaminants present in the anode and cathode feed streams. The HiL test stand was also upgraded for testing of fuel cell stacks up to 1 kW. Simulation tools were modified for evaluation of fuel cell systems for propulsion of a UAV. A plasma reforming effort was initiated with the design, construction, and testing of two different plasma arc reactor designs. The reverse-vortex reactor performed better than the planar plasma, gliding arc design. In support of the DARPA-sponsored Direct Carbon Fuel Cell research project at SRI International (SRI), HNEI prepared biocarbons from various biomass feedstocks to aid in optimizing performance of SRI's carbon fuel cells. Development of enzymatic bio-fuel cells continued, focused on enzyme immobilization utilizing macroporous chitosan polymer composites. The methane hydrates activities included significant progress in understanding hydrate destabilization using thermodynamic inhibitors. The impact of seafloor methane from hydrates on the marine environment was explored via both experiments and modeling. HNEI again supported and helped organize the 6th International Workshop on Methane Hydrate R&D that was held in Bergen, Norway in May 2008. The workshop was attended by scientists, engineers, and other stakeholders from 12 countries and a meeting report is available from the Naval Research Laboratory (NRL).

Under this current award (N00014-07-1-1094), several upgrades to test stands and infrastructure were implemented, focused on ensuring the quality of gases in the facility and additional enhancements for stack testing. Substantial effort was devoted to work on understanding the SO_2 contamination mechanism and SO_2 contamination recovery. Preliminary testing of Protonex hydrogen/air stacks under pure oxygen was conducted in support of the Naval Undersea Warfare Center (NUWC) at Newport, RI. A new segmented-cell flow-field design was developed and validated for use in future contaminant and flow-field design work. In addition, HNEI conducted fuel contamination efforts via a Modelica model which worked with previous experimental results of CO poisoning. While minor upgrades were made to the HiL test system, again to support stack testing, most of the HiL effort during this period was supported by a separate award, Ion Tiger, directed toward testing of stacks for UAV application. Complete test results for this work have been reported under that program.

Fuel processing and purification work included continued efforts to characterize a non-thermal plasma reactor for methane reforming. Parametric tests were conducted using electrode gap distance, post-reaction-chamber fill, axial exit diameter, equivalence ratio, steam input, and power input as independent variables. System performance was characterized using methane conversion, selectivity, efficiency, H_2 yield, and specific energy ratio, as metrics. Over the range of experimental conditions, the parametric test determined that the post reaction chamber fill did

not produce significant improvement in the conversion of methane, and that decreasing the axial exit diameter degraded system performance.

HNEI continued providing biocarbons to SRI in support of its DARPA-sponsored work with direct carbon fuel cells. SRI test results remain confidential, but researchers there feel more fundamental knowledge is needed. HNEI research aimed at acquiring the needed fundamental knowledge is continuing under NSF and HEET support. In addition, HNEI completed a study of carbonization of sewage sludge from a treatment plant on O'ahu. Sewage sludge is a promising feedstock for charcoal production. Cost estimations of HNEI's commercial-scale Flash Carbonization™ reactor were completed, revealing the high cost of providing compressed air for operation of a pressurized catalytic afterburner (CAB) needed to meet emissions regulations. To speed progress and reduce costs, a $1/10^{th}$ scale canister has been designed and fabricated to facilitate the development of a $1/10^{th}$ scale atmospheric-pressure CAB that will not employ an air compressor.

The focus of the enzymatic bio-fuel work continued to be enzyme immobilization utilizing macroporous chitosan polymer composites that support both mediator-based and direct-electron-transfer mechanisms. Improved *in situ* surface and interface characterization protocols with improvement on instrumentation and capability have also been achieved in this work. This approach uses spectroscopic imaging ellipsometry and additional complementary tools such as quartz crystal microbalance and electrochemical techniques to study biocatalytic electrodes and their behavior. A model system that includes polymerized methylene green on electrodes as the electron transfer mediator was studied to elucidate the mediator-based electron-transfer mechanisms.

The methane hydrates activities comprised four subtasks: Hydrate Thermochemistry and Kinetics, Environmental Impacts of Methane Release from Seafloor Hydrates, Hydrate Engineering Applications, and International Collaborative R&D. Subtasks included: laboratory and analytical investigations of hydrate destabilization by chemical reagents; measurements of the heat capacity of water at elevated pressures; characterization of the microbial community in marine hydrate beds that modulate methane levels in the seafloor sediments and leakage into the water column; development of models to predict the fate of methane released from the seafloor into the water column; exploratory laboratory studies of H_2 storage; and the promotion of international R&D partnerships.

The kinetic behavior of methane hydrate samples as they dissociate in the presence of thermodynamic inhibitors has been investigated experimentally in previous phases of the HEET initiative. During the present reporting period, data from these studies were compared with predictions of models we developed of this phenomenon. A novel approach based on the non-ergodic theory of mobile order thermodynamics (MOT) was proposed to estimate the activity of water in binary mixtures with ethylene glycol and several common alcohols. Calculations were found to be in good agreement with those obtained with the widely used UNIQAC equation, thereby establishing the soundness of the alternative MOT framework for hydrogen-bonded liquids. Consistent with the behavior observed in the dissociation experiments we conducted using the Raman calorimeter, results of this analysis suggest that alcohol molecules with a smaller alkyl group or a greater number of hydroxyl groups lower the activity of water (and, hence, inhibit hydrate formation). Primary alcohol isomers (e.g., 1-propanol) seem to affect the activity of water slightly less than secondary alcohol isomers (e.g., 2-propanol).

Larger-scale dissociation experiments conducted in our hydrate synthesis facility also were modeled. A one-dimensional time-domain representation of the thermal processes was developed. The dissociating hydrate surface either was assumed to be at equilibrium, or its temperature was determined by including an existing intrinsic dissociation kinetic model. Results suggested that the simpler equilibrium assumption was better able to represent experimental data. The apparent difficulty with the intrinsic dissociation formalism may indicate a more general lack of its applicability to situations when hydrates are not decomposed by depressurization, since the definition of a driving fugacity difference then becomes ambiguous. Our experiments and the corresponding analysis tend to indicate that, in most practical situations, hydrate dissociation is controlled by heat and mass transfer at the interface. Although existing models of intrinsic dissociation kinetics could be refined to quantify more precisely the state of disequilibrium of the interface, it is not clear that overall predictive capabilities would improve as a result.

Continuing our investigation of subsea power generation utilizing seafloor methane or hydrates, questions emerged during the assessment of candidate devices regarding the accuracy of the standard IAPWS 1995 model for thermal properties of water and aqueous solutions at the elevated pressures which prevail in the deep ocean. The ability to accurately predict these properties is important to determine the performance of aqueous alkaline fuel cells and other devices that have been proposed for the subsea power system. Experiments were therefore conducted with the Differential Scanning Calorimeter to measure the heat capacity of water at high pressure. Significant differences were found to exist between the 1995 IAPWS model predictions and our data. This study is ongoing and a manuscript has been prepared for publication.

The impact of seafloor methane from hydrates on the marine environment was explored via both experiments and modeling. Biological processes (mostly microbial) in the sediment and the water column are believed to play a major role in determining methane levels throughout the marine environment. The underlying metabolic pathways and the factors that affect these processes are not well understood and have been a focus area of the HNEI methane hydrate task. During the present phase of the HEET initiative, we participated in an oceanographic research cruise in the Beaufort Sea off the North Slope of Alaska, during which additional sediment and pore water samples were collected from shallow and cold water environments in methane-rich areas. These samples are being analyzed to assay the microbial community and determine rates of methane oxidation by methanotrophic bacteria. Related modeling efforts focused on assessing carbon isotope fractionation by aerobic CH_4-oxidizing bacteria under different environmental conditions.

As part of our goal to explore the use of gas hydrates for non-energy related engineering applications, we initiated a study of hydrate H_2 storage. Recently, advances have been reported, in synthesizing H_2 hydrate, that suggest that it may be feasible to store and transport this molecule as a hydrate guest at moderate temperatures and pressures. The key to this appears to be to employ a gas species that readily forms hydrate to initially establish the crystal, and then to substitute H_2 into the interstices of the lattice. Experiments were performed in the Raman calorimeter in which powdered THF (tetrahydrofuran) hydrate was incubated under a high pressure hydrogen gas atmosphere. Although we were unable to detect the Raman signature of the THF/H_2 hydrate, depressurization (and subsequent dissociation) of the solid appeared to

release trapped gas. The H_2 hydrate formation protocol, as well as alternative hydrate promoters, are being explored.

Finally, as part of our goal to foster international collaborative R&D on methane hydrates, HNEI supported and helped to organize the 6th International Workshop on Methane Hydrate R&D that was held in Bergen, Norway in May 2008. A report on that workshop can be downloaded from the Defense Technical Information Center website. During the present reporting period, planning also commenced for the 7th workshop that will be held in Wellington, New Zealand in May 2010. GNS Science, a research organization owned by the Government of New Zealand, is taking the lead for this workshop and HNEI will once again serve on the organizing committee and provide sponsorship.

2. Introduction

The Hawaii Energy and Environmental Technologies (HEET) Initiative, funded to the Hawaii Natural Energy Institute (HNEI) of the University of Hawaii through the Office of Naval Research (ONR), was initiated in the summer of 2001 under Grant Award Number N00014-01-1-0928 to address critical technology needs associated with the exploration and utilization of seabed methane hydrates and the development and testing of advanced fuel cells and fuel cell systems. These efforts and a smaller effort in fuels purification were continued under two subsequent agreements (Award No. N00014-04-1-0682: June 15, 2005 to June 30, 2006; and Award No. N00014-06-1-0086: October 17, 2005 to September 30, 2007. Under these programs, the focal point of our activity was development of the Hawaii Fuel Cell Test Facility (HFCTF) which houses dual facilities for fuel cell testing and for the synthesis and characterization of methane hydrates. Research in these areas was described in these reports. Under the fourth HEET program (Award No. N00014-06-1-1055), for the period September 14, 2006 to December 31, 2008, work was continued in the areas of fuel cell systems and methane hydrates.

Our fifth (the current) HEET program (Award No. N00014-07-1-1094), was for the period September 27, 2007 to March 31, 2010, and this award has included continuation of our efforts in the areas of fuel cell systems and methane hydrates and greater emphasis on the production and purification of alternative fuels. The remaining sections of this report focus on each of the major areas covered within the HEET initiative. Section 3 is on fuel cell systems, with subsections for each of the associated subtasks for these systems. Section 4 reports results for alternative fuels. Section 5 covers methane hydrates, including subsections for the subtasks of this area.

3. Fuel Cell Systems

This task area is organized into three subtasks: polymer electrolyte membrane (PEM) fuel cell testing and component development, Hardware-in-Loop (HiL) and system simulation, , and novel fuel cells. Under this grant , HNEI performed minor upgrades to the Hawaii Fuel Cell Test Facility (HFCTF), conducted comprehensive air and fuel contamination studies, and conducted preliminary testing of hydrogen (H_2)/air fuel cell stacks in hydrogen and pure oxygen to evaluate their potential for unmanned undersea vehicle (UUV) applications. This grant supported minor modification to HNEI's HiL test system. During this grant period, the HiL test system was used primarily in support of the separately-funded Ion Tiger project (Cooperative Agreement NOO 173-08-2-C008) which involved conducting testing for development of an unmanned aerial vehicle (UAV). Work also continued in the area of novel fuel cells. Details for the activities conducted under each of these subtasks are given below.

3.1 PEM Fuel Cell Testing and Component Development

Primary activities in this area encompassed continued development of testing infrastructure and capabilities, and research focused on fuel cell contaminants. The latter studies involving SO_2 (airside) contamination, use of Modelica to characterize fuel contaminant effects, , component evaluation of H_2/air stacks operated under pure oxygen.

3.1.1 Test Stands/Infrastructure Upgrades

Minor upgrades were performed on the existing Hawai'i Fuel Cell Facility (facility) test stations and the facility supply equipment. The facility nitrogen gas supply system was upgraded with the installation of a passive catalytic/absorbent nitrogen purification system. Although sourced from liquid dewers, which inherently results in high purity nitrogen, sub-ppm quantities of carbon monoxide were found to influence certain experiments involving longer-duration nitrogen purging. Based on specifications of the new absorber, nitrogen entering the facility distribution system is now 99.99999% pure, eliminating supply nitrogen contamination as an issue in our testing programs.

HNEI has also been evaluating the benefits of installing additional hydrogen purification at the facility. Use of a proposed palladium membrane purifier unit would remove essentially all potential contaminants from our generated and vendor-supplied hydrogen, yielding 99.999999% pure hydrogen at the distribution header. The proposed system will eliminate source gas hydrogen purity as a concern in our testing programs and provide the facility with an enhanced capability in conducting impurity testing research as well as supporting Navy fuel cell development efforts.

Laboratory safety training was conducted at the facility in March 2009 by the University's Environmental Safety and Health Office (UH-ESHO). Nine persons at the facility received annual certification. The annual fire protection certification of the sprinkler system and fire extinguishers was also performed. UH-ESHO also conducted annual environmental and occupational safety inspection in November 2009. No deficiencies were identified and the report stated that general housekeeping at the facility was very good. Through the first seven years of operation, HNEI has consistently received high marks with regards to safety for operation of the facility.

Under a prior award we demonstrated the usefulness of HNEI's segmented cell system for investigation of PEMFC performance distribution using both cyclic voltammetry (CV) and linear sweep voltammetry (LSV). In those experiments the flow field was a 6-channel serpentine-flow field with wide and deep channels (Figure 3.1.1a). This flow-field, designed to demonstrate the application of the segmented cell, was not optimized and did not yield cell operation at current densities which should have been achievable for the Membrane Electrode Assemblies (MEAs) used in the study, i.e., > 1 A cm^{-2} at 0.65 V. In addition, the quality of the electrochemical impedance spectroscopy (EIS) spectra for the outlet segments was characterized by excessive noise, attributed to poor water management and mass transfer limitations. Thus, a new flow field using a 10-channel serpentine-flow field was designed and implemented,. This design more closely matched the flow channel specifications of HNEI's existing 50 cm^2 single cell with narrow and shallow channels (Figure 3.1.1b). Results obtained using the new flow field are presented in subsequent sections.

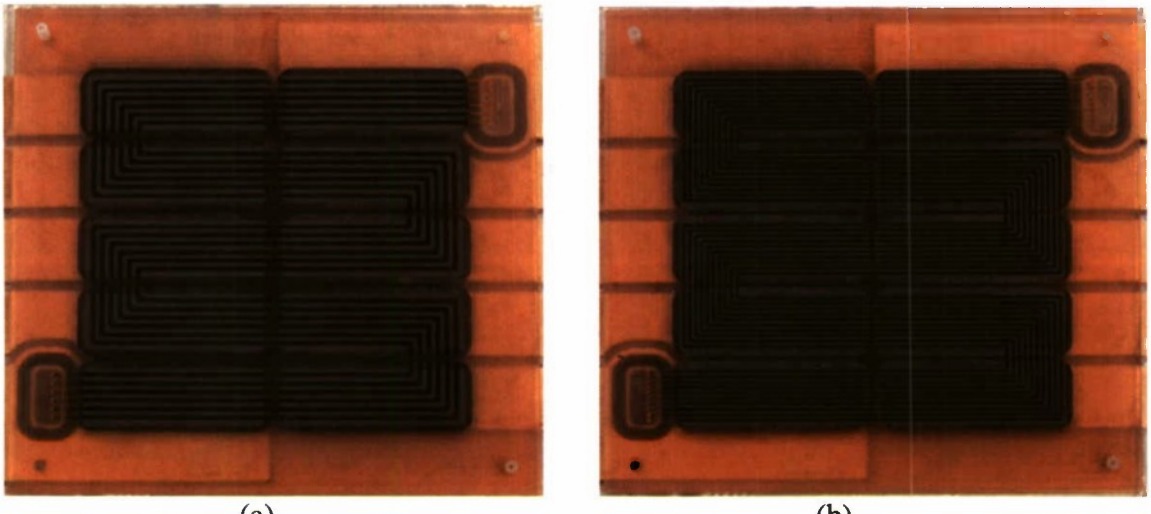

(a) (b)

Figure 3.1.1. Images of segmented flow fields: (a) – 6-channel serpentine [old], (b) – 10-channel serpentine [new].

3.1.2 Cell and Component Testing

Work under this activity includes detailed characterization of the effects of airborne SO_2 and its recovery, evaluation of Protonex stacks using oxygen, testing of the new segmented cell hardware, and development of Modelica-based models to understand the impact of fuel contaminants.

3.1.2.1 Air Contaminant Studies: SO_2 Contamination Mechanism

The main foci during this award period were to (1) study the effect of air contaminants on cell performance and durability, (2) examine contamination mechanisms, and (3) develop mitigation strategies. Under prior work it was shown that SO_2 contamination in the cathode of a PEMFC resulted in a two-stage degradation of cell performance, indicated by an inflection of the voltage degradation rate at a cell voltage of approximately0.65 V. In the present award period additional experiments were conducted to increase understanding of the poisoning processes with particular attention to the behavior around the inflection point. Figure 3.1.2 shows the results of an experiment intended to study the cathode potential impact on the poisoning processes. The

figure shows the cell voltage response vs. time of four MEAs subjected to a 2-ppm SO_2 injection at standard operating conditions (SOC), i.e., 0.6 A/cm^2, 80 °C, 2/2 stoich, 7/7 psi$_g$, and 100/50% RH for different periods of time (corresponding to different dosages) As shown in Figure 3.1.2, SO_2 exposure was interrupted when the cell voltage decreased to 0.675, 0.650, 0.550, and 0.450 V, (for a-d, respectively). When the specified cell voltage was reached, a recovery cycle was initiated whereby the cell was operated in neat H_2/air for approximately 20 hours. The overlap of the degradation curves in Figure 3.1.2 during the first poisoning indicates good reproducibility of the MEA performance and its degradation. For experiments (a) and (b), negligible recovery was observed after returning to neat air. These experiments were terminated after one and two recovery cycles, respectively, as the cell voltage remained below the specified cutoff voltages of 0.675 V and 0.650 V, respectively. This indicated the cell voltage degradation due to SO_2 was mainly irreversible above 0.650 V. This trend began to change with experiment (c) where the cell voltage was allowed to degrade lower to 0.550 V. The cell in experiment (c) showed approximately 35 mV of self-induced recovery after the first recovery cycle. The amount of self recovery slowly decreased with ongoing poisoning/recovery cycles, indicating the presence of an irreversible poisoning process. For experiment (d) where the cell voltage was allowed to decrease to 0.45 V, recovery after the second cycle was the same, indicating that the cell performance degradation of the last four poisoning/recovery cycles, where SO_2 injection and poisoning occurred below 0.53 V, was reversible.

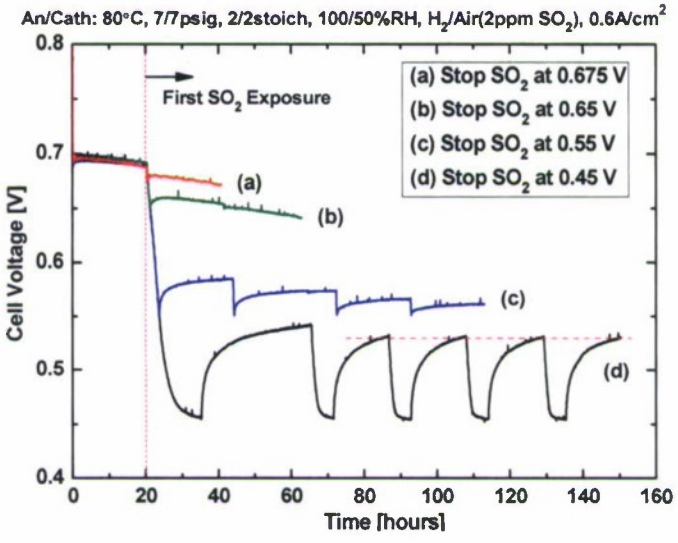

Figure 3.1.2. Cell voltage response to 2 ppm SO_2 vs. time at SOC inducing H_2/air recovery at cell voltages of: (a) 0.675; (b) 0.65; (c) 0.55 and (d) 0.45 V Recovery cycle time was approximately 20 hours. A maximum of five cycles was applied.

These results confirmed that the SO_2 poisoning process consisted of at least two processes, an irreversible and a reversible poisoning process. When the cell voltage was above 0.65 V, the irreversible contamination process dominated. Between 0.65 – 0.53 V, associated reaction rates of the reversible contamination process began to increase. The reversible and the irreversible process reactions then competed with each other, and over time the resulting reversible part of the cell voltage degradation was replaced by an accumulating irreversible part. Below 0.53 V,

cell poisoning was dominated by the reversible process, as all poisoning occurring below 0.53 V was reversible and no cumulative irreversible poisoning contributions were apparent.

The effects of operating conditions on SO_2 contamination were also investigated. Figure 3.1.3 shows the cell voltage response as a function of the SO_2 dosage for various operating conditions including the standard operating conditions. The plots on the left side of the figure show the cell voltage response vs. SO_2 dosage, while the corresponding recovery in neat air is shown on the right side. All experiments used a total exposure of 160 umol SO_2. Except for the test operated at high current density (1 A cm^{-2}), cell voltage degradation curves all showed the inflection point observed in previous experiments. This further confirmed the finding that the cell degradation consisted of at least two processes: a sulfur-coverage-dependent irreversible process and a potential-dependent reversible process. The main trends observed during this parametric study of operating conditions were:

(i) Although higher SO_2 concentrations resulted in lower cell voltages at steady state, nearly identical cell voltages were reached after self-induced recovery following exposure to different SO_2 concentrations.

(ii) Lower temperatures resulted in a slower poisoning process vs. dosage through most of the experiment although the steady-state voltages after 160 umol of SO_2 exposure were nearly identical.

(iii) The self-induced neat air recovery, as indicated by the magnitude of the voltage increase after SO_2 exposure was stopped, was more effective at higher temperatures and higher current density.

(iv) Oxygen stoichiometry and cathode relative humidity showed no significant effects on the poisoning process or the self-induced recovery.

(v) As the self-induced recovery originates from the reversible part of the poisoning process, according to the data in Figure 3.1.3, the magnitude of voltage loss due to the reversible poisoning process is also dependent on the temperature, and not only the cathode potential, as shown in Figure 3.1.2.

Electrochemical impedance spectroscopy (EIS) was also employed to gain additional insights into the changes in the single-cell system during SO_2 contamination experiments. EIS experiments and subsequent analyses utilized equivalent electrical circuit models (ECM) to simulate the various processes of electrochemical systems. By 'fitting' the model to the experimental data one can analyze the impedance responses and extract the individual model parameters. Figure 3.1.4 shows the measured impedance spectra (symbols) in Nyquist plots and the ECM-fitting results (solid lines) at various stages of the experiment for SO_2 poisoning under standard operating conditions. The ECM used for analysis of this data is also shown in Figure 3.1.4. It includes serial resistance inductance terms, an anode model, and a cathode model. R and L represent the serial resistance of the proton and the electron transport in the bulk system and the serial inductance of the cell and system components, respectively. The anode model includes the charge transfer resistance of the hydrogen oxidation reaction, R_a, and the capacitance of the anode catalyst layer, C_a. The cathode model includes the charge transfer resistance of the oxygen reduction reaction, R_c, a constant phase element, CPE, and a Warburg diffusion element, W_d. The impedance response of the CPE is associated with the double-layer capacitance of the real cathode with a rough catalyst layer and a non-uniform catalyst distribution. The impedance response of W_d is a function of the reactant transfer properties diffusion resistance, R_d, in both the gas diffusion layer and electrode.

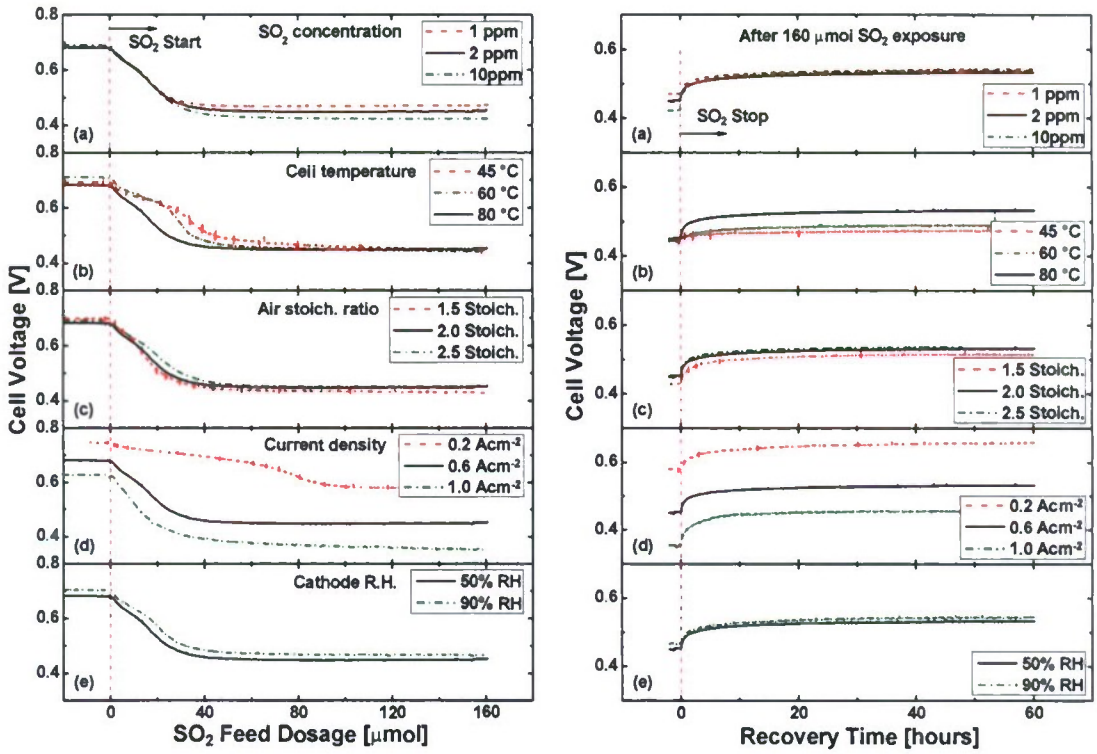

Figure 3.1.3. Cell voltage response vs. SO_2 dosage (left) & cell voltage response vs. recovery time under neat air following 160 umol SO_2 exposure (right) at different operating conditions: (a) SO_2 concentration, (b) cell temperature, (c) air stoichiometry, (d) current density, and (e) cathode R.H.

Electrochemical impedance spectroscopy (EIS) was also employed to gain additional insights into the changes in the single-cell system during SO_2 contamination experiments. EIS experiments and subsequent analyses utilized equivalent electrical circuit models (ECM) to simulate the various processes of electrochemical systems. By 'fitting' the model to the experimental data one can analyze the impedance responses and extract the individual model parameters. Figure 3.1.4 shows the measured impedance spectra (symbols) in Nyquist plots and the ECM-fitting results (solid lines) at various stages of the experiment for SO_2 poisoning under standard operating conditions. The ECM used for analysis of this data is also shown in Figure 3.1.4. It includes serial resistance inductance terms, an anode model, and a cathode model. R and L represent the serial resistance of the proton and the electron transport in the bulk system and the serial inductance of the cell and system components, respectively. The anode model includes the charge transfer resistance of the hydrogen oxidation reaction, R_a, and the capacitance of the anode catalyst layer, C_a. The cathode model includes the charge transfer resistance of the oxygen reduction reaction, R_c, a constant phase element, CPE, and a Warburg diffusion element, W_d. The impedance response of the CPE is associated with the double-layer capacitance of the real cathode with a rough catalyst layer and a non-uniform catalyst distribution. The impedance response of W_d is a function of the reactant transfer properties diffusion resistance, R_d, in both the gas diffusion layer and electrode.

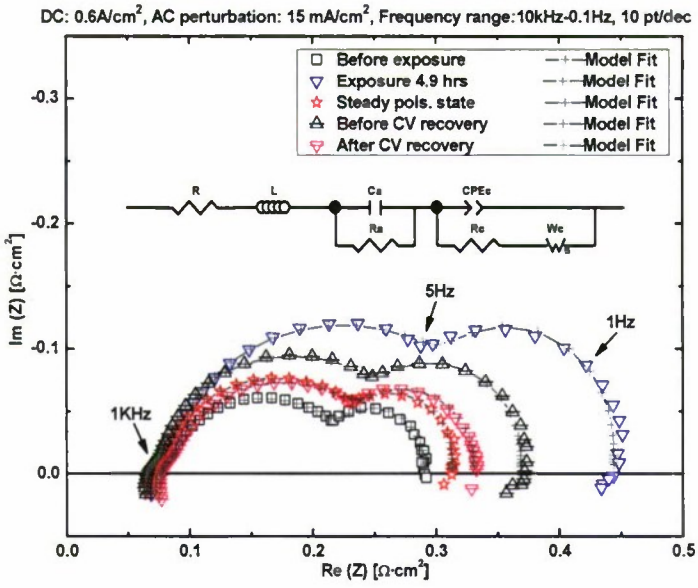

Figure 3.1.4. Measured impedance spectra and ECM fitting results during the SO_2 contamination experiment at standard operating conditions.

The ECM parameters, R_c, R_d, R, and R_a, were extracted from the software simulation package to analyze how variations in these terms throughout the poisoning process and recovery impacted the overall cell performance. Figure 3.1.5 shows the cell voltage and degradation rate, $\partial V/\partial t$ (top graphs), as well as the parameters variations (bottom graphs) during the SO_2 poisoning (a) and recovery (b). Relating these terms to physical processes helped enhance the understanding of the two-stage poisoning process. For example, during SO_2 exposure, two peaks were apparent in the degradation rate curve, which correspond to the two-stage degradation process. Negligible changes in R_a and R were observed and this indicated the exposure of the cathode to 2 ppm SO_2 does not affect the charge transfer resistance of the hydrogen oxidation reaction or the bulk resistance of the bulk system. R_c and R_d were observed to increase rapidly until the maximum degradation rate in the second peak was reached at about 3.7 hrs of exposure, and then decreased to a steady poisoning state after about 14 hrs of exposure. The variations of R_c can be divided into three parts with respect to the two-stage degradation and the steady state in the cell performance. During the irreversible poisoning stage, within about first 1.3 hrs, the increase in R_c is attributed to the irreversible adsorption of SO_2 on cathode Pt, which blocked the active sites of Pt from the oxygen reduction reaction. During the reversible poisoning stage, from 1.3 to 14 hrs, the increase and subsequent decrease in R_d is complicated and the increase may be attributed to the reversible adsorption of SO_2 on cathode Pt, which also reduced the active sites of Pt. During the recovery region, as shown in Figure 3.1.5b, as soon as the SO_2 injection was stopped, R_c increased and then reached a relatively constant value after about 20 hrs; and R_d decreased slightly and then began to increase slowly during the first 20 hrs of the self recovery. The initial decrease in R_d may be attributed to the removal of the SO_4^{2-} around the Pt/C particles, and the subsequent increases in R_c and R_d may be due to a combination of the desorption of the sulfur adsorbate and the shifting back of the oxygen-reduction reaction (ORR) pathway. Interpretation of EIS spectra involves a complex balance between using an appropriate equivalent circuit model that can be validated mathematically, and also relating this model to actual reaction pathways. As shown above, the use of EIS is a valuable tool in impurity studies, allowing for empirical

parameter extraction which assists in the understanding of the electrochemical reaction pathways occurring during poisoning and recovery processes. Future studies at HNEI, will begin to utilize EIS as a standard diagnostic tool. Previously, only the bulk resistance was being measured during standard impurity experiments.

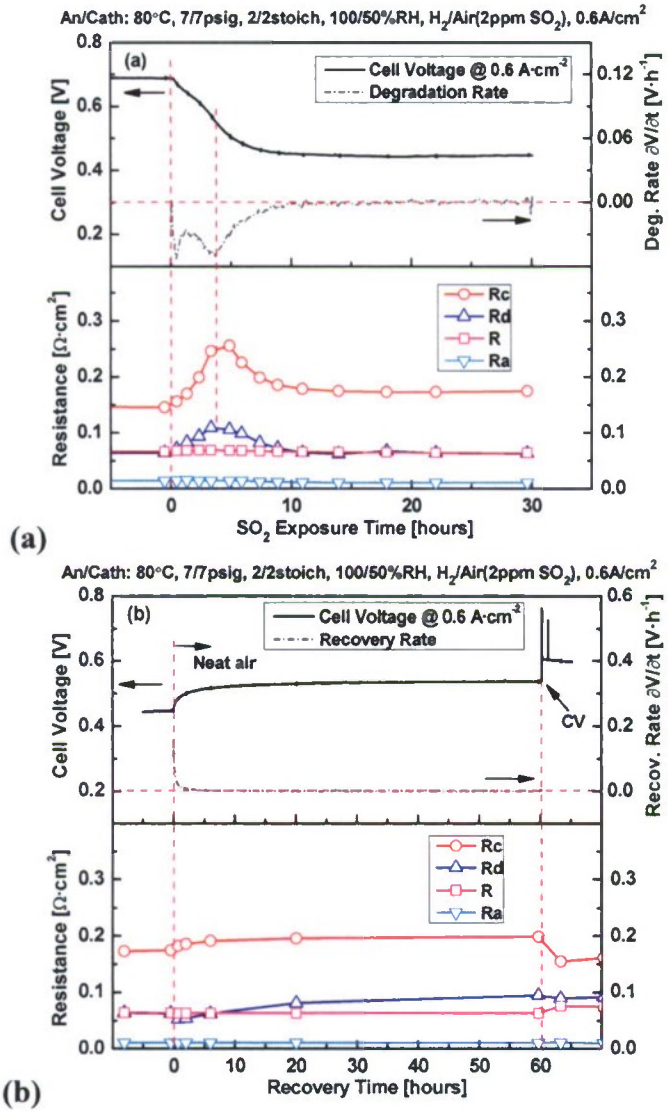

Figure 3.1.5. Cell voltage response and degradation rate $\partial V/\partial t$ (top graphs), and the ECM parameter variations (bottom graphs) during SO_2 poisoning (a) and recovery (b) at standard operating conditions.

In collaboration with NRL, HNEI performed an SO_2 poisoning experiment aimed at analyzing the 'sulfur balance,' i.e., quantifying the inlet and outlet species and correlating these values with the performance degradation observed. The sulfur balance was investigated using an *in-situ* gas chromatograph (GC) and effluent water collection system designed at HNEI. The water samples were sent to NRL for *ex-situ* ion chromatography (IC) analysis. Figure 3.1.6 shows the SO_2 molar flow rate in the inlet and outlet gases of the single cell and the sulfate anion (SO_4^{2-}) in the

effluent water during the SO_2 exposure and recovery stages. Based on GC measurement, the calculated SO_2 concentration in the inlet was close to our designed value of 2 ppm. The SO_2 flow rate in the outlet gas increased almost immediately following the introduction of SO_2, reaching a steady value at approximately the same time as the cell reached steady-state voltage . Approximately 40% of the SO_2 remained unreacted (left in the effluent gas)at steady state. The presence of SO_2 in the effluent gas during recovery is evidence of its release during the self recovery. The IC results show that the SO_4^{2-} flow rate increased rapidly with the initiation of SO_2 exposure, continued to increase but more slowly when the cell performance reached steady state, and decreased gradually during the self recovery. These results indicate that a portion of the SO_2 was oxidized to SO_4^{2-} during the exposure, the SO_2 oxidation reached equilibrium at steady state; and SO_2 was adsorbed/absorbed in the MEA. The SO_4^{2-} concentration in the water effluent continued to increase slowly during the steady poisoning state, but did not cause further cell performance degradation. Combining the flow rate of SO_2 in the inlet and outlet gases and SO_4^{2-} in the effluent water, the sulfur amount of the inlet was close to that of the outlet at the end of the SO_2 exposure, assuming the sulfur release from Nafion degradation was negligible.

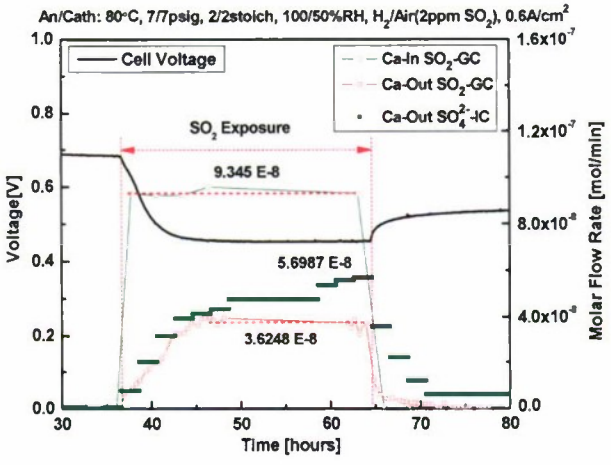

Figure 3.1.6. Cell voltage, SO_2 molar flow rate in inlet and outlet gases, and the sulfate anion in the effluent water analyzed by GC and IC vs. time during 2 ppm SO_2 poisoning experiment.

Although not described in this report, previous EIS analyses in this laboratory led to a theory that the balance between the reversible and irreversible poisoning processes shifted the electron pathway of the oxygen reduction reaction. The fluorine emission rate in a PEMFC is an important parameter for monitoring the Nafion degradation. Generally, the Nafion electrolyte degradation is attributed to the attraction from H_2O_2, which may be an intermediate product of the "series two electron pathway" ORR. In order to confirm the shifting of the ORR pathway, the fluorine emission rates in the cell exhaust water were also measured by the IC analysis. The fluorine emission rates are shown in Figure 3.1.7. Before the SO_2 exposure, the fluorine emission rate in both cathode and anode was very low. Following the SO_2 injection, the emission did not change on either the cathode or anode side during the first two hours, but then increased rapidly following the inflection point in the voltage degradation. When the cell reached its steady-state poisoned value, the fluorine emission rates reached a constant value, and

decreased abruptly when the SO_2 injection was stopped. These results indicate that the presence of SO_2 increased electrolyte degradation at all potentials but was 7-8 times worse at voltages below the inflection point in comparison with values at the higher potentials during the pre-poisoning and irreversible stages. The degradation product also permeated through the membrane to the anode side. These results provided additional evidence of changes in the oxygen-reduction reaction pathway during the reversible poisoning process. This work also demonstrated the effectiveness of effluent water analyses for gas-phase impurity studies.

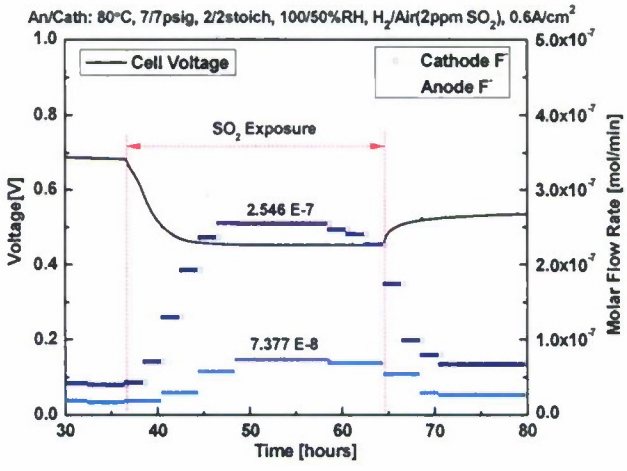

Figure 3.1.7. Cell voltage response and fluorine emission rates in the effluent water vs. time during the 2 ppm SO_2 poisoning experiment.

3.1.2.2 Recovery from SO_2 Contamination

A collaboration was again formed with NRL's fuel cell group under the direction of Dr. Lyons to evaluate potential recovery/mitigation methods for removal of adsorbed sulfur species from operational fuel cell cathodes. Previous investigations of recovery methods that included applying open-circuit voltage, current-voltage sweeps, purging with neat air and cyclic voltammetry proved to be either slow and incomplete or fast and corrosive. Based on initial work performed at NRL, HNEI and NRL worked together to develop an automated system to evaluate various recovery. This system and subsequent testing were implemented at HNEI.

Five new recovery methods were compared, each following a 3-hour exposure to 1 ppm SO_2 in air at 60 °C. The recovery concepts included variations of cathode potential and gas environment (N_2 or air). In addition, they were broken into "driven" and "non-driven" cell methods. The driven methods used a power supply (potentiostat) to access potential ranges outside of the fuel cell's operating range and to drive electrons in and out of the cathode. The non-driven methods were limited to the fuel cell's potential range (0.0-0.95 V vs. anode). In the optimum method, the fuel cells were switched from operation with air on the cathode to operation in air-starvation mode, to a point at which only N_2 remains (*in-situ* N_2). During the air-starvation mode a reductive environment was created where the adsorbed sulfur species were being reduced to S^0. A voltammetry recovery scan was then performed while keeping the cell at temperature and pressure. During this recovery step the reduced sulfur species was oxidized to sulfate (SO_4^{2-}), which can be removed as a water soluble anion from the catalyst surface.

The results of this study indicated that driven-cell recovery methods during fuel cell operation can rapidly recover a fuel cell's air polarization performance after exposure to 1 ppm SO_2 at 60 °C. As shown in Figure 3.1.8, the optimal upper scan limit for the recovery scan was determined to be 1.1 V at 60 °C, where sufficient sulfur species oxidation occurred with the least amount of platinum loss. The complete recovery of the air polarization performance was independent of the fuel cell atmosphere (air or *in-situ* N_2) on the cathode during recovery. Complete recovery was only possible with the driven method and the application of potential cycling. Potential holds and load cycling did not fully recover the fuel cell air polarization performance. The driven recovery using potential cycling with *in-situ* N_2 was the only operational recovery method capable of developing the potentials needed for oxidation of adsorbed sulfur species to S^0 and the desorption of S^0. The recovery time for this method was under 3 minutes.

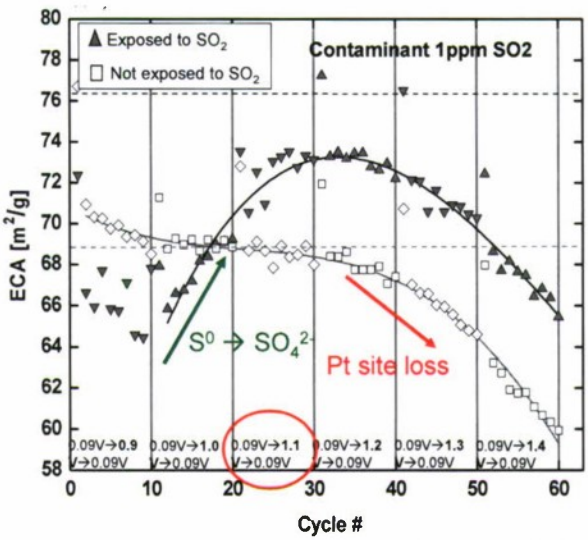

Figure 3.1.8. Optimization of the potential range for cyclic potential scan recovery, run with *in-situ* N_2 during air-starvation step; scans were conducted with 20 mV/s scan rates; plotted are the electrochemically active surface area (ECA) values calculated for cathode electrodes not exposed to SO_2 and exposed to 1 ppm SO_2; each data point represents 1 ECA cycle.

3.1.2.3 Component Evaluation: Operation of Protonex Stacks Under Oxygen

This activity supported the Naval Undersea Warfare Center at Newport (NUWC) efforts to characterize available fuel cell stacks for use in unmanned underwater vehicles (UUV), specifically, to measure stack performance under pure oxygen operation. NUWC requested this data to generate first-order models to evaluate whether gas-supplied PEMFC systems were a more optimal technical path than the direct oxidation/reduction of borohydride and hydrogen peroxide PEMFC systems. This supported the NUWC effort to evaluate systems using humidified gaseous hydrogen from the decomposition of borohydride, and humidified gaseous oxygen derived from the decomposition of hydrogen peroxide in NUWC-designed reactors. As HNEI was already working with Protonex through the Ion Tiger unmanned aerial vehicle (UAV) program, older-generation Protonex M250 H2/Air stacks were readily available for H2/O2 testing. The short time frame requested to provide baseline data precluded evaluation of other

stacks. HNEI also purchased additional M250 stacks from Protonex with a higher rated pressure capacity, i.e., 30 psig. The M250 stack size is 36 cells with an active area of 18.8 cm^2 per cell.

As a first step, HNEI and NUWC developed a limited-scope performance evaluation test plan for the Protonex M250 platform under H2/O2 operation. The first test matrix involved short-duration polarization curves, oxidant utilization sweeps, and relative humidity sweeps while working within the limits of the UUV group recommendations, M250 specifications (e.g., 30 psig pressure limit), and existing test facility hardware, to provide data in a timely manner. An overview of the test conditions utilized in the first matrix is provided in Table 3.1.1. In an actual PEMFC UUV system, reactant supply operation would most likely be a closed loop system, utilizing recycle loops on both the anode and the cathode, but in these preliminary tests only dead-ended and flow-through reactant supplies were tested. Two anode gas supply configurations were tested. The first used the same system for H2/Air operation, i.e., dry hydrogen directly fed into the anode through a pressure regulator, with periodic purging to remove water and/or nitrogen building up in the anode. The second utilized humidified hydrogen in a back-pressure controlled, flow through mode at relatively low flows.

Table 3.1.1. Baseline test matrix conditions for H2/O2 operation of the Protonex M250 stack.

Coolant Inlet Temp	T1	50	deg. C
	T2	70	deg. C
	T3	80	deg. C
	T4	85	deg. C
Relative Humidity	RH1	75	%
	RH2	100	%
	RHSW	100 to 50	Relative Humidity Sweep from 100 to 50%
Cathode Stoich	CS1	1.5	Stoichiometry
	CS2	1.3	Stoichiometry
	CSSW	1.5 to 1.1	Stoichiometry Sweep from 1.5 to 1.1
Pressure	P1	9	psig
	P2	30	psig

The step time for polarization curves was three minutes per step at the low current densities, and five minutes per step at the higher current densities. While sufficiently long for electronic stability, neither time was long enough to assess potential voltage instability due to flooding. Thus, following the initial polarization matrix screening, longer duration testing was conducted to validate the robustness of the Protonex stacks. The protocol agreed upon involved testing at two pressures, i.e., 9 and 30 psig, utilizing a multi-step current profile operating at three different current densities, i.e., 300, 900, and 1500 mA/cm^2, holding for eight hours at each step. HNEI and NUWC also developed plans to send the hydrogen peroxide decomposition reactor from NUWC to HNEI to validate operation of the fuel cell stack using oxygen produced from the decomposition system. The proposed testing was intended to evaluate whether the stabilizers in the liquid hydrogen peroxide would have a detrimental effect on the fuel cell operation. Due to changes in NUWC's UUV PEM program milestone timing, this task was never performed.

Figures 3.1.9 and 3.1.10 present the results of the polarization curves performed on Stack 242846 and Stack 242844. Testing on Stack 242846 included four temperatures and two pressures, with the anode operating in dead-ended mode with periodic purging, and the cathode in flow-through, back-pressure-controlled mode at a stoichiometry of 1.5. Stack 242844 was tested at one

temperature and three pressures with the anode in flow-controlled, back-pressure-controlled mode at a stoichiometry of 1.3. The cathode was operated in the same manner as Stack 242846. Interestingly, the performance of the two stacks, operated under the different test conditions showed minimal change in performance, especially when comparing the power curves. Pressure seemed to be the only parameter that caused any "significant" performance change and led to a tightening of the data sets. Temperature may have shown a more significant effect if the polarization curves had been run at higher current densities. The data do show a slight decrease in performance at higher temperatures, particularly at 80 and 85 °C, with the difference being more pronounced at 9 psig. The 30-psig data showed almost no temperature effect within the operating range tested. This may be related in part to the saturation pressure of water increasing rapidly through the 75 to 85 °C temperature range, causing a decrease in the oxygen partial pressure within the stack which would then be more pronounced at lower pressures. Under the limits of testing implemented, the highest power achieved was on the order of 1 kW at 0.7 V and 2.1 A/cm^2. Under H2/Air, this same stack design only achieved approximately 400 W under similar conditions. Stack 242846 was used in the multi-step current density profile to obtain longevity data.

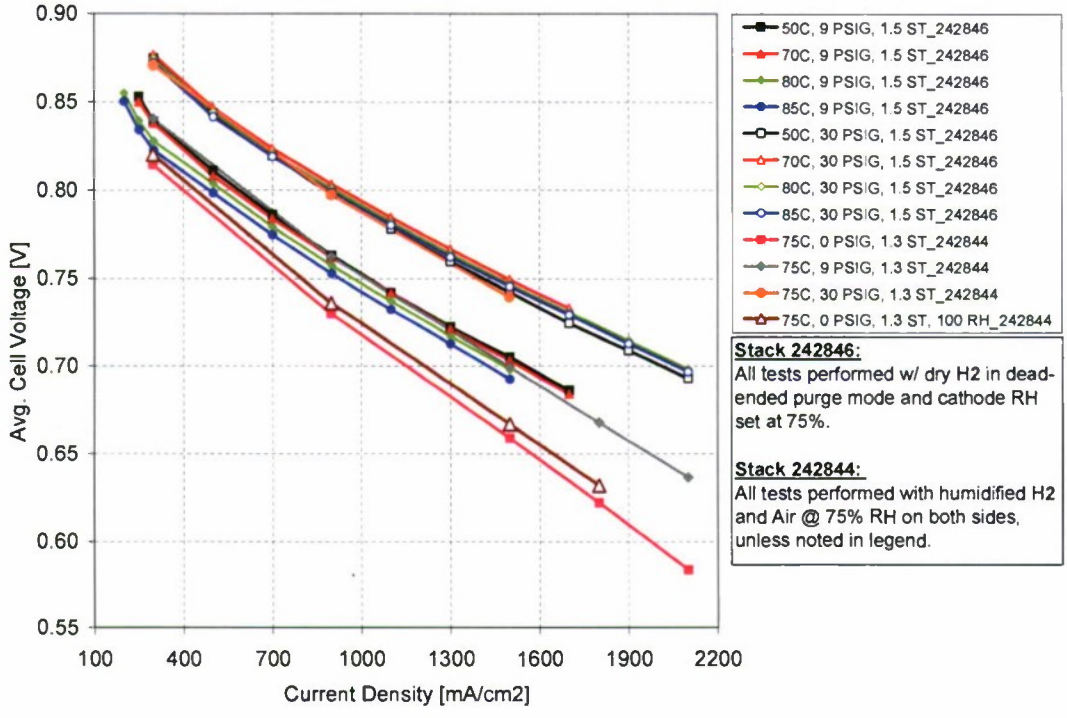

Figure 3.1.9. H2/O2 polarization curve results: average cell voltage vs. current density.

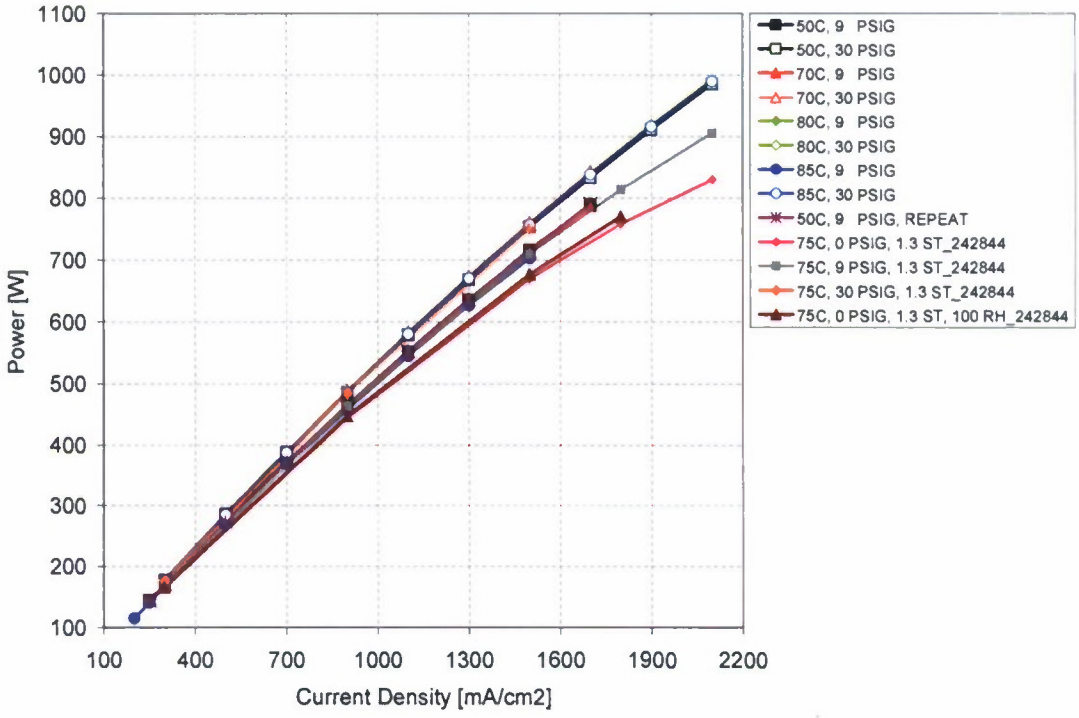

Figure 3.1.10. H2/O2 polarization curve results: stack power vs. current density.

Figures 3.1.11 and 3.1.12 show the individual cell voltages vs. time for the 9-psig multi-step current density experiment and the 30-psig experiment, respectively. The current density during each 8-hr step is provided in the figures. As shown in Figure 3.1.11, the cell voltages were relatively stable during each step, regardless of current at 9 psig. On the macro-scale, a slight decrease in voltage was observed throughout testing, and the loss was higher at the lower current densities. This was attributed to the formation of platinum oxides on the electrode surface, decreasing the availability of platinum sites for oxygen reduction. Platinum oxide formation is known to be more pronounced in the operating range of 0.7 V and higher; however, the observed voltage decay was reversible. After completing 72 hrs at 9 psig, the cell pressure was increased to 30 psig and the multi-step profile was continued. As shown in Figure 3.1.12, operation at higher pressures eventually led to multiple cells exhibiting excessive voltage drops, with cell to cell variations greater than 100 mV. Three snapshots of the cell voltage vs. individual cell numbers are shown in Figure 3.1.13. Snapshot 1 shows that initially only one cell appeared to decrease, with the adjacent cell's performance improving. As time progressed throughout testing, however, the situation became progressively worse, as shown in snapshots 2 and 3. Operation at higher pressures and low gas flows can lead to poor water removal and flooding. There are several scenarios that could explain the cell voltage drops observed. In snapshot 1, where the adjacent cell performance actually improved, plugging of the flow channel at the manifold inlet or along the flow path of individual channels in the cell could lead to a decrease in oxygen and subsequent voltage drop and force more gas into the adjacent channels, improving the performance of those cells. Another possible scenario is insufficient liquid water removal from the pore structure of the electrodes. Localized saturation of the pore structure of the gas diffusion layer or catalyst layer would limit O_2 diffusion, resulting in locally higher current

densities in the unaffected regions of each cell. In addition, local heat generation would then more highly affect adjacent cells. Several alternatives, such as flow surges and dry purges, were attempted once the 30 psig test was halted; however, a pinhole eventually developed in one of the cells, and stack testing was halted. Although stable operation was not achieved under the test conditions, this wasn't unexpected as the operating conditions selected were rather arbitrary and aimed at looking at low flow operation. Further optimization of the test conditions and/or stack design would be required to operate at higher pressures and lower flow rates.

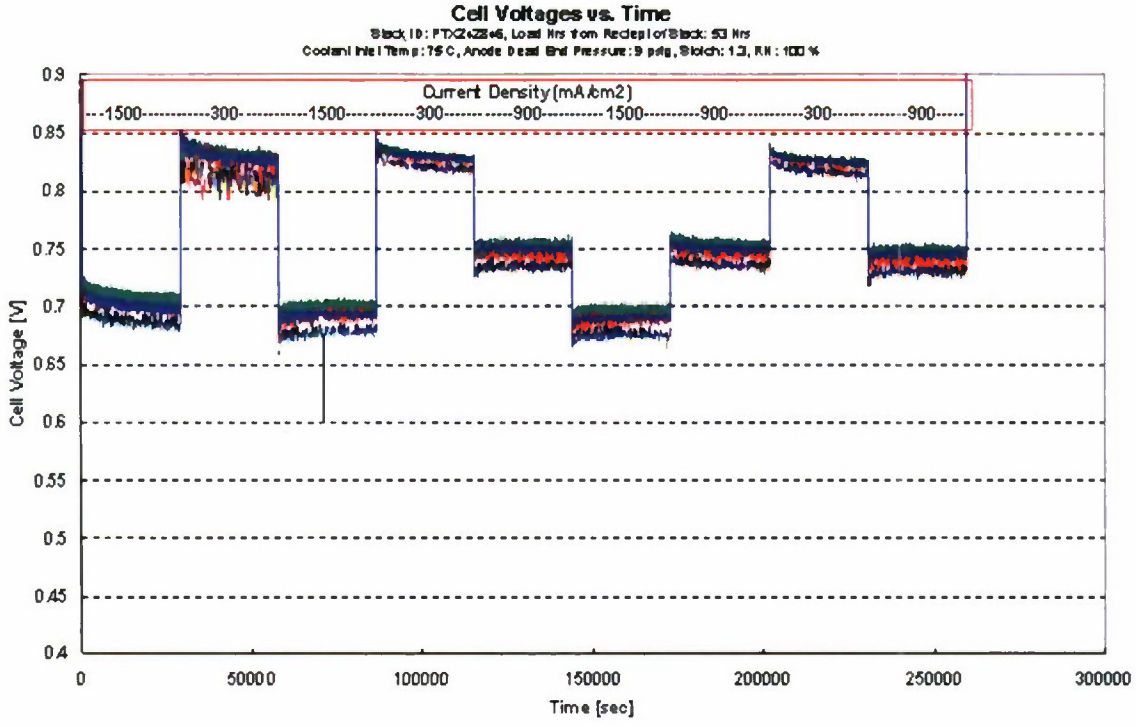

Figure 3.1.11. Stack 242846 cell voltages vs. time during the 9-psig, multi-step current profile experiment utilizing an 8-hour hold at each current density, i.e., 300, 900, and 1500 mA/cm^2.

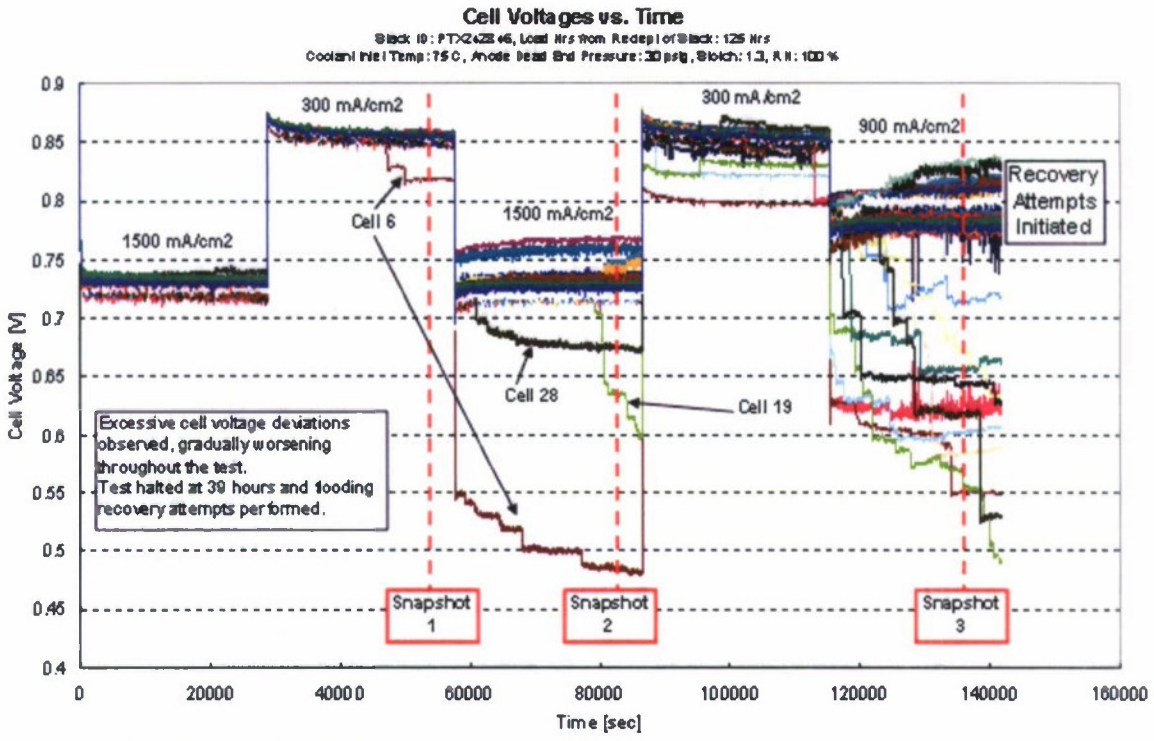

Figure 3.1.12. Stack 242846 cell voltages vs. time during the 30-psig, multi-step current profile experiment utilizing an 8-hour hold at each current density, i.e., 300, 900, and 1500 mA/cm^2.

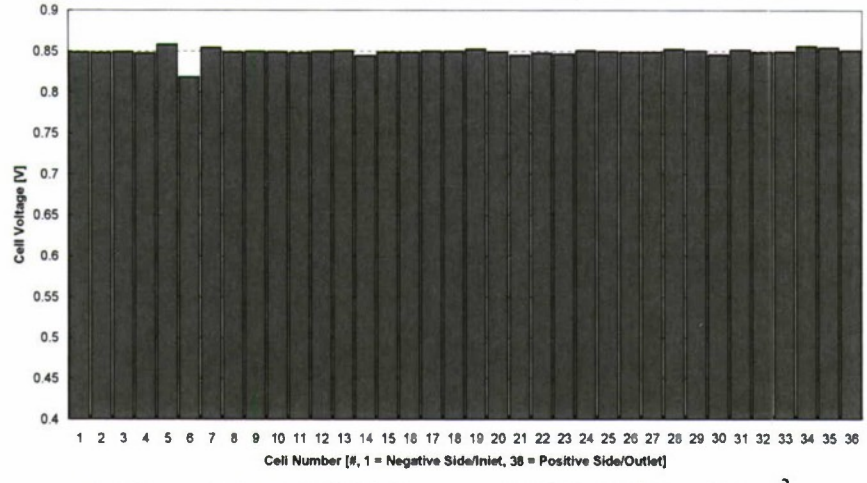

(a) Snapshot 1: Cell Voltage vs. Cell # @ 300 mA/cm^2

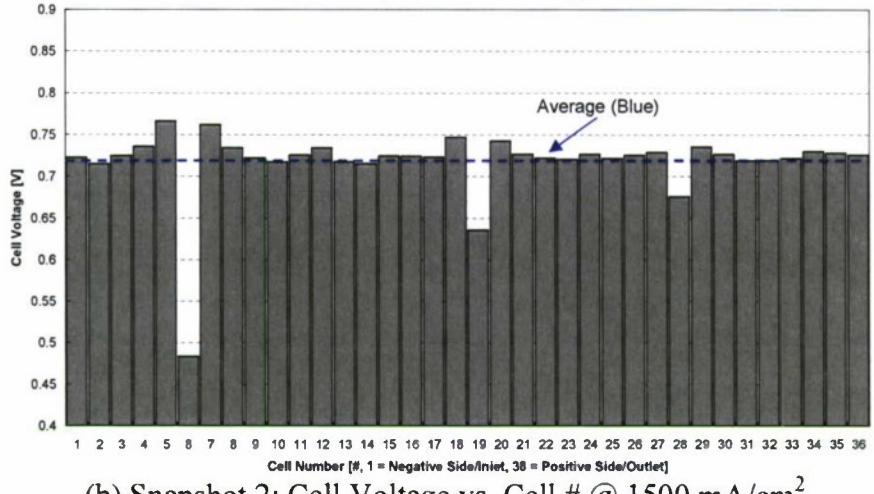

(b) Snapshot 2: Cell Voltage vs. Cell # @ 1500 mA/cm^2

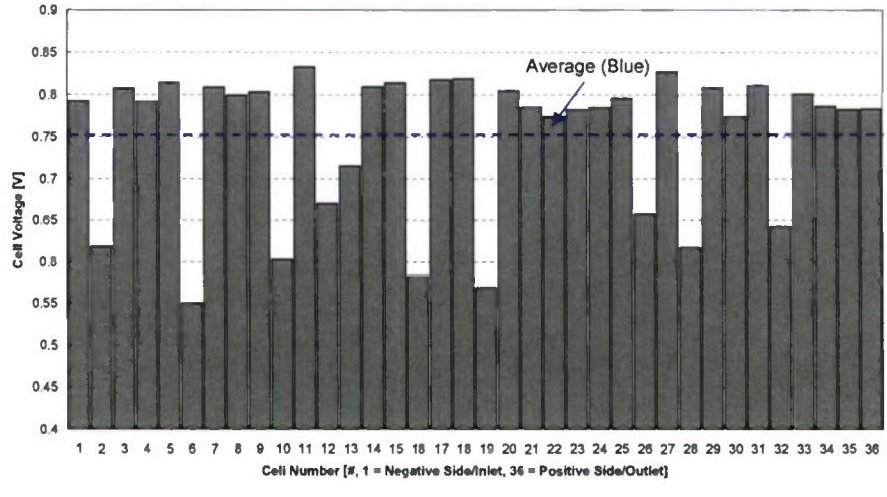

(c) Snapshot 3: Cell Voltage vs. Cell # @ 900 mA/cm^2

Figure 3.1.13. Individual cell voltage snapshots showing the progressive flooding effect observed during the 30-psig, 8-hour multi-step current profile experiment.

3.1.2.4 Component Evaluation: Segmented Flow-Field Optimization

A series of tests were performed to evaluate the improvements made to the segmented-cell flow-field design. These included polarization effects (VI curves) with EIS determination, cyclic voltammetry for electrochemically active surface area determination, and linear sweep voltammetry experiments to determine an equivalent hydrogen crossover current. VI curves were recorded in H_2/air, H_2/He+O_2 with 21% oxygen concentration, and H_2/O_2 configurations at a cell operating temperature of 60 °C. The anode/cathode standard operating conditions were: 2/2 stoichiometry flow rate, 48.3/48.3 kPa_g backpressure, and 100/50% relative humidity. For the H_2/He+O_2 and H_2/O_2 operation, the same flow rates were used as the H_2/air configuration in order to maintain similar water management at any given total cell current density. Consequently, the stoichiometry for H_2/He+O_2 remained at 2/2, while the stoichiometry for H_2/O_2 increased to 2/9.5. Comparison of cell performance at these three gas compositions allowed us to determine the main voltage losses: activation, ohmic, concentration, and mass transfer. The analysis was made based on the following assumptions: negligible anode polarization, insignificant hydrogen crossover, and no internal short circuit in the cell. The activation overpotential (η_{act}) was obtained by subtracting the iR-corrected H_2/O_2 polarization curve from the theoretical open circuit voltage. The ohmic overpotential (η_{Ohm}) was obtained by subtracting the H_2/O_2 values from the respective iR-corrected values. Subtraction of the H_2/He+O_2 data from the H_2/O_2 data yielded the concentration overpotential (η_{conc}), whereas the mass transfer overpotential (η_{MT}) was obtained by subtracting the H_2/air values from the H_2/He+O_2 values. At all three gas configurations, the cell and segment performances were measured by conducting spatial VI experiments under galvanostatic control of the total cell current. The VI experiments were combined with the spatial EIS to determine the cell's and segment's high-frequency resistance (HFR), as well as the electrochemical impedance spectra at each current. CV experiments were conducted for electrochemically-active surface area (ECA) determination using a Parstat 2273 potentiostat/galvanostat from EG&G Instruments Corp. CVs were performed at a cell temperature of 35 °C with a scan rate of 20 mV/sec, while 100% humidified hydrogen and nitrogen was supplied to the reference/counter and working electrodes, respectively, at a flow rate of 750 sccm. For each measurement, three cycles were applied over a potential range from -0.015 to 1.1 V vs. hydrogen reference electrode (HRE). The H desorption peak area of the third cycle was used to determine the ECA. Hydrogen crossover experiments were performed at the same temperature and flow conditions as the ECA experiments using a single potential sweep from 0.1 to 0.4 V vs. HRE at a scan rate of 0.1 mV/sec.

Measurements of a segment's ECA did not reveal any dependence on the flow-field design. Linear sweep voltammetry (LSV) showed that hydrogen crossover had nearly the same distributions for 6- and 10-channel flow fields. This was as expected because the same MEA was used in both experiments, and the change in flow channel design should not have a significant impact on the measured MEA properties. Figure 3.1.14 shows performance distributions of the segments in terms of the cell voltage vs. segment number for five current densities (0.1, 0.2, 0.4, 0.6, 0.8 A cm^{-2}), recorded for the two different flow channel configurations. The new flow fields resulted in slight performance decreases (up to 20 mV) at current densities below 0.2 A cm^{-2}). However, at higher current density (> 0.6 A cm^{-2}) significant improvement was observed; with an increase of the cell voltage in the range of 50-200 mV at 0.6 A cm^{-2}.

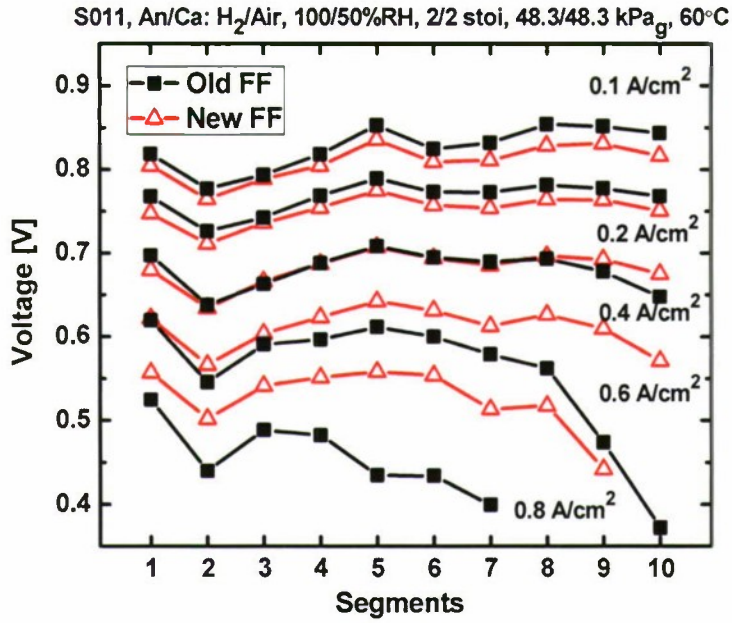

Figure 3.1.14. Voltage distributions using 6-channel (old flow field) and 10-channel (new flow field) flow-field designs.

In order to understand this behavior, additional analysis was conducted to determine the distributions of activation, ohmic, concentration and mass transfer overpotentials. The data indicated that the main contributors to the performance increase were the activation, the concentration, and the mass-transfer overpotentials, whereas the ohmic overpotential did not change. Figure 3.1.15a shows the difference of the activation overpotential distribution for old and new flow fields for current densities ranging from 0.1 to 1.0 A/cm^2. There was a slight increase of this overpotential with 10-channel serpentine flow fields (5-20 mV). Figures 3.1.15b and 3.1.15c show similar data for the concentration and mass transfer overpotentials, respectively. The data shown indicates that the concentration and the mass transfer overpotentials significantly decreased with application of the new flow field and became especially noticeable for the outlet segments Seg07-Seg10. The three overpotentials together accounted for 95-100% of the performance improvement observed in the data shown in Figure 3.1.14.

As shown in the SO_2 impurity work earlier, EIS is one diagnostic tool that can deliver insights into the reaction processes of a fuel cell. Figure 3.1.16 shows the spatial EIS by means of Nyquist plots for Seg01, 04, 07, and 10 recorded at 0.1 and 0.6 A cm^{-2}. The EIS spectra of these four segments represent the trends observed in the whole cell. The typical spectrum for PEMFC operated at H_2/air gas configuration and low current density has two arcs: a high frequency anode arc, representing the hydrogen oxidation reaction (might be negligible) and a high frequency cathode arc, attributed to the effective charge transfer resistance and double-layer capacitance of oxygen reduction reaction, which is known to be rate-determining for a hydrogen fuel cell. In addition, the membrane itself has a resistance which, together with electronic contact resistance, determines the high-frequency resistance (HFR) of an MEA. An increase in the current density shifts the oxygen reduction reaction from kinetic to diffusion control when diffusion of reagents toward or products away from the electrode surface governs the reaction rate. In this case, a low-frequency cathode arc is usually observed, reflecting mass transfer

limitations in the cathode gas phase within the gas diffusion layer (GDL) and the catalyst layer. As shown in Figure 3.1.16a, at low current density EIS spectra are identical for the 6- and 10-channel flow fields. Operation at a higher current density, as shown in Figure 3.1.16b, led to a decrease of the cathode arc size, indicating an increasing driving force for the oxygen reduction and the appearance of a low-frequency arc even for the inlet segments (Seg01-04). On the contrary, for the outlet segments (Seg06-10), there was a significant increase of the cathode and the low-frequency semicircles, and the latter came to dominate the impedance spectrum. The application of 10-channel flow fields significantly reduced the sizes of the cathode and low-frequency arcs for all segments in comparison with 6-channel flow fields, indicating improved diffusion rates and also providing higher quality EIS curves. Thus the 10-channel serpentine flow field improved the cell performance by decreasing the diffusion limitations observed in the 6-channel flow field, and the EIS data fully confirmed the VI results.

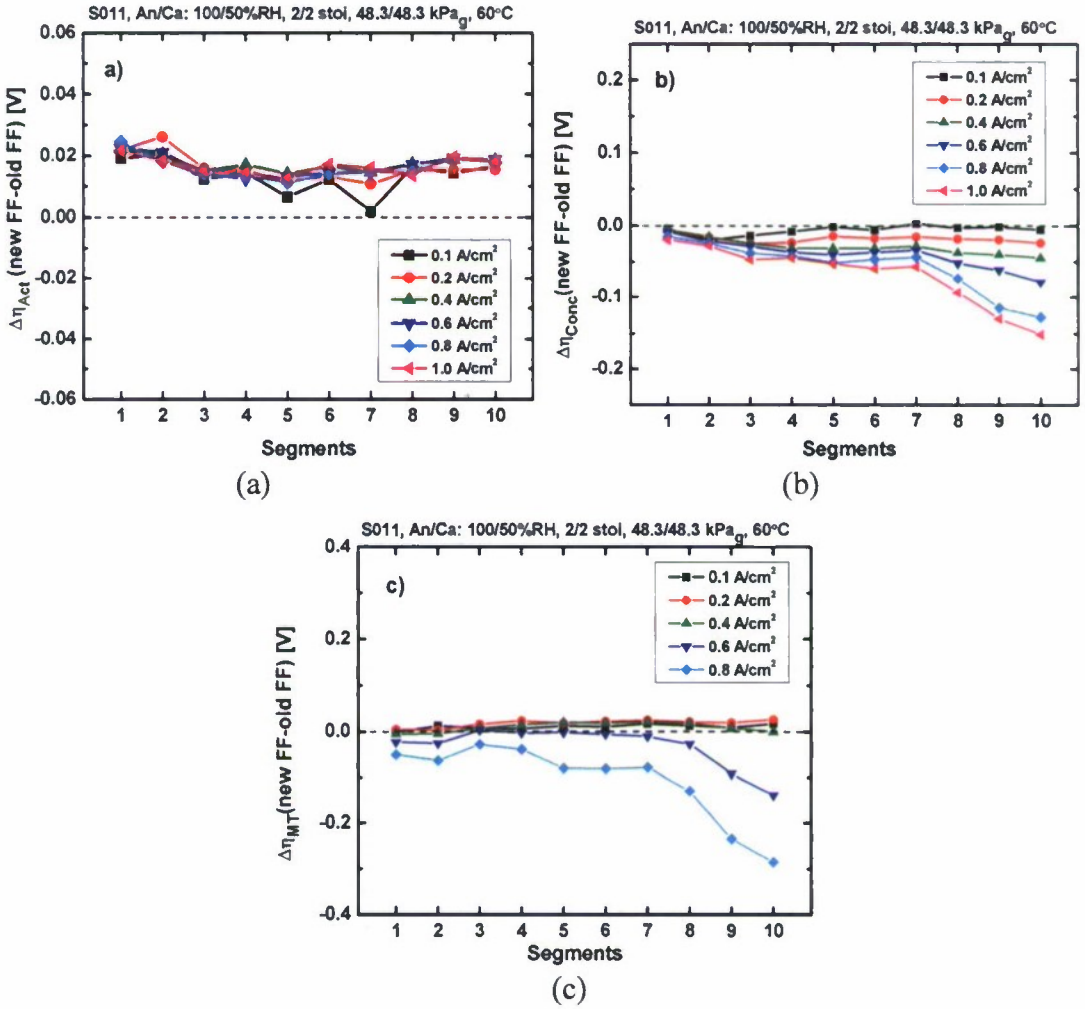

Figure 3.1.15. Distributions of differences in activation (a), concentration (b), and mass transfer (c) overpotentials between new and old flow fields.

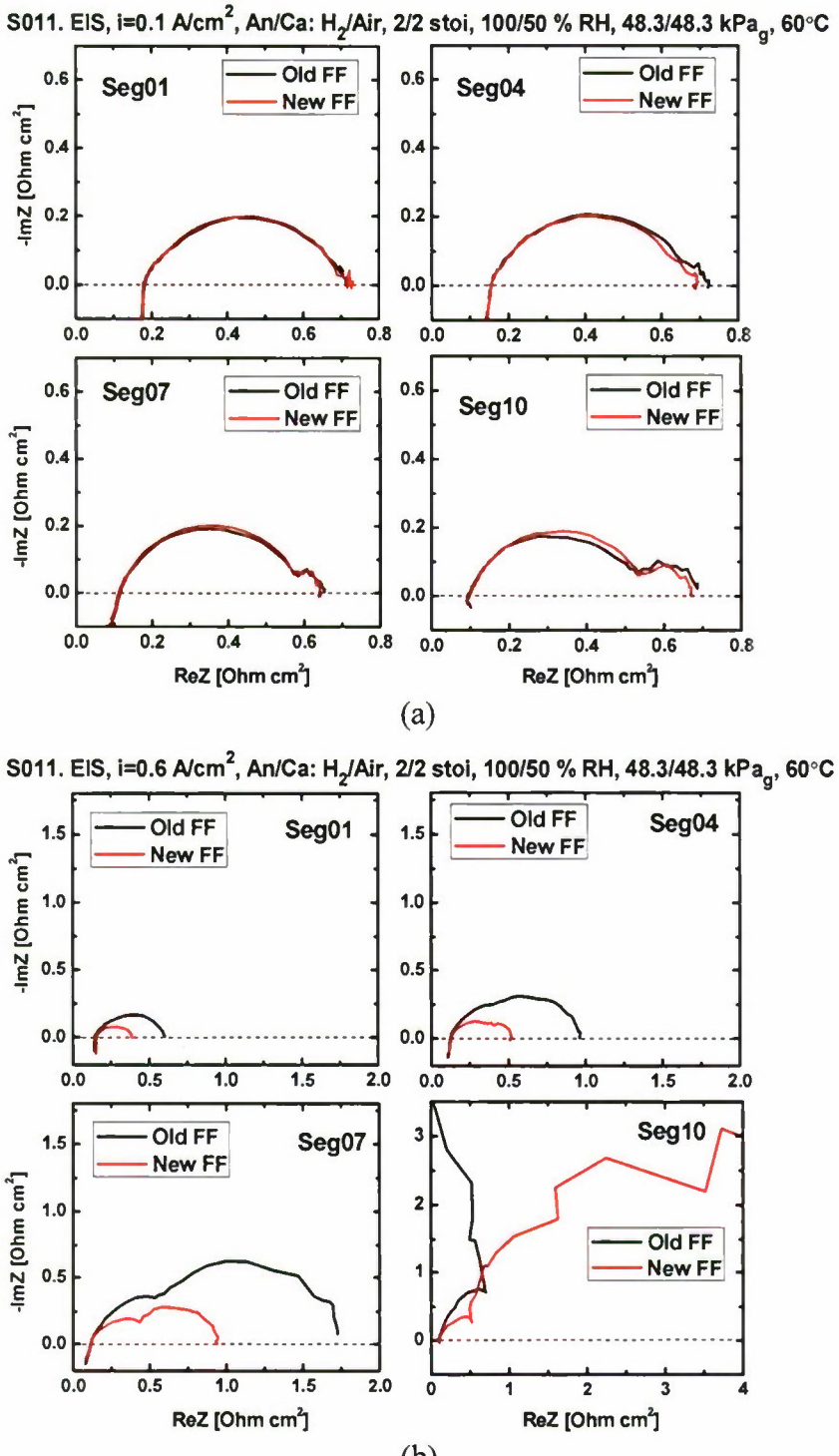

Figure 3.1.16. EIS spectra for Seg01, 04, 07, and 10, recorded at I = 0.1 A cm^{-2} (a) and 0.6 cm^{-2} (b).

3.1.2.5 Fuel Contaminant Studies: Modelica Model Development

The objective of this activity was to develop a modeling tool to assist in understanding the changes in performance of a proton exchange membrane fuel cell (PEMFC) operating with a fuel (anode) stream containing trace amounts of carbon monoxide (CO). CO is known to degrade PEMFC performance and can be present in many hydrogen sources, particularly those produced by hydrocarbon reformation. A model that is able to describe the degradation and recovery processes is needed in order to understand and possibly mitigate the effects of catalyst CO poisoning.

Under other funding, HNEI showed experimentally that the anode overpotential exhibits hysteresis during cycles of CO poisoning; specifically, the overpotential loss attributed to CO adsorption was very different during loading and unloading at the same total CO adsorption level. A PEMFC model based on [1] was used to show that the hysteresis could result from dissimilar CO coverage profiles during the poisoning and recovery processes. The anode reaction rate equation of the model was modified by reducing the rate by a function of the fraction of catalyst covered by CO. The PEMFC model was discretized into multiple segments along the length of the flow channel. The CO coverage was prescribed by a transient profile which loaded and unloaded the segments near the anode inlet before those near the outlet. Figure 3.1.17 shows that the model captured the experimentally observed hysteresis in the anode overpotential during poisoning/recovery cycles.

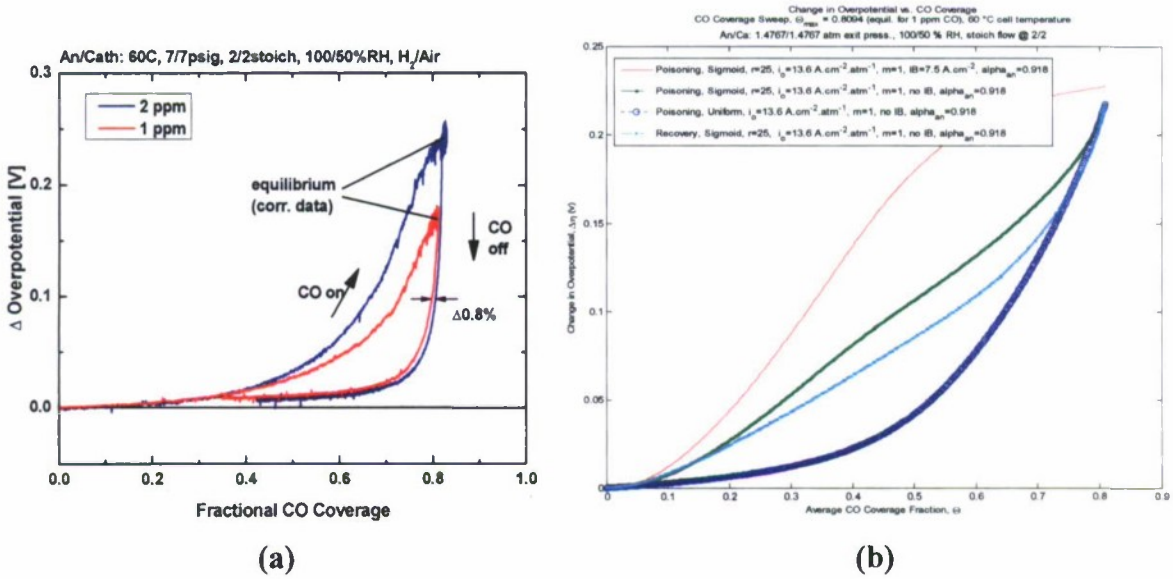

Figure 3.1.17. Change in overpotential vs. total fractional CO coverage during poisoning and recovery from (a) experiment, and (b) simulation, with and without limiting current density (IB) included.

The previous work did not capture the actual processes of loading and unloading, but rather, it applied a prescribed contamination profile. The research during this period sought to calibrate the PEMFC model's free parameters, validate the model, and describe the adsorption and desorption processes that might lead to different CO coverage profiles during loading and unloading. In order to calibrate and validate the model, experiments were performed on a 100

cm^2 cell operating without CO under varying conditions (reactant pressure, cell temperature, anode and cathode flow rates, anode and cathode humidification, and a cathode stream of air or oxygen).

In order to describe the adsorption and desorption processes, the model was enhanced. First, the reactant media model was split into its individual species so that CO could be easily introduced and species flow paths could be connected between the storage volumes and the appropriate reaction or transport processes. Second, the anode catalyst model was reconfigured such that CO adsorption/desorption could be included along with the hydrogen oxidation reaction (HOR; $H_2 \rightarrow 2H^+ + 2e^-$). Figure 3.1.18 shows a schematic of the reconfigured anode catalyst model before the inclusion of CO. In the schematic, there are models of the chemical storage volumes and the HOR, with connections for each chemical species.

Future work includes model calibration and validation along with the addition of the CO adsorption and desorption processes. In the meantime, details and results have been published of the latest working version of the PEMFC model without CO.

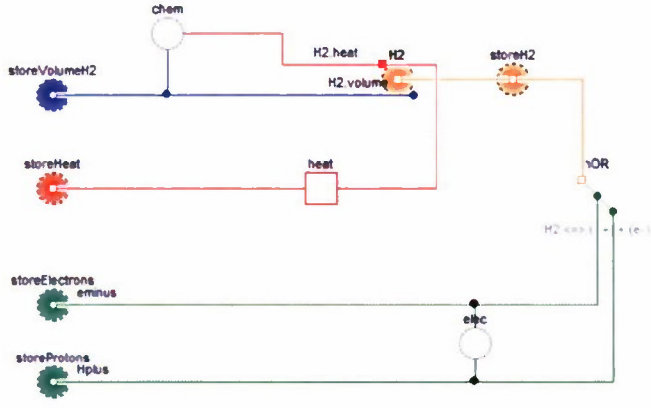

Figure 3.1.18. Diagram of the anode catalyst model.

Reference

[1] K. L. Davies and R. M. Moore. *Object-Oriented Fuel Cell Model Library*, Electrochemical Society Transactions 11: 797-808, 2007.

3.1.3 MEA Fabrication Laboratory

The Graphtec cutter was brought online during the 2009 award period. The cutter is being used to cut gas diffusion media and gaskets to custom sizes used in the segmented-cell hardware and other non-standard hardware. Other than bringing the cutter online, no changes in the MEA fabrication lab occurred.

3.1.4 Papers and Presentations Resulting from 2009 Efforts

PAPERS

Y. Zhai, G. Bender, S. Dorn, R. Rocheleau, "The Multi-Process Degradation of PEM Fuel Cell Performance Due to Sulfur Dioxide Contamination and Its Recovery", Journal of the Electrochemical Society, Vol 157, 2010.

G. Bender, M. Angelo, K. Bethune, S. Dorn, T. Thampan, R. Rocheleau, "Method Using Gas Chromatography to Determine the Molar Flow Balance for Proton Exchange Membrane Fuel Cells Exposed to Impurities," Journal of Power Sources, Vol 193, pp 713-722, 2009.

B. D. Gould, G. Bender, K. Bethune, S. Dorn, O. A. Baturina, R. Rocheleau, K. E. Swider-Lyons, "Operational performance recovery of SO2-contaminated proton exchange membrane fuel cells," Submitted to the Journal of the Electrochemical Society, May 2010.

PRESENTATIONS/CONFERENCE PROCEEDINGS

T. Reshetenko, K. Bethune, R. Rocheleau "Study of Spatial PEMFC Performance under CO Poisoning Using Segmented Cell Approach," 217 Electrochemical Society Meeting, April 25-30, 2010, Vancouver, Canada.

Y. Zhai, K. Bethune, S. Dorn, G. Bender, R. Rocheleau, "Electrochemical Impedance Stereoscopy study on SO_2 contamination in PEMFC," 217 Electrochemical Society Meeting, April 25-30, 2010, Vancouver, Canada.

B. D. Gould, O. A. Baturina, Y. Garsany, G. Bender, K. Bethune, S. Dorn, K. Swider Lyons, "Recovery Methods for Sulfur Deactivated Fuel Cell Cathodes," 238th Meeting of the American Chemical Society, August 16-20, 2009, Washington DC, USA.
K. Swider Lyons, Y. Garsany, B. Gould, O. Baturina, D. Ramaker, G. Bender, K. Bethune, S. Dorn, "Performance Degradation and Recovery of Sulfur-Contaminated PEFC Cathodes," Gordon Research Conference on Fuel Cells, July 26 – 30, 2009, Smithfield, Rhode Island, USA.

K. L. Davies, R. M. Moore, G. Bender, "Model Library of Polymer Electrolyte Membrane Fuel Cells for System Hardware and Control Design," In: Casella, F. (ed.), Proceedings of the 7th International Modelica Conference, Linköping University Electronic Press, 2009.

K. L. Davies, C. L. Haynes, C. J. Paredis, "Modeling Reaction and Diffusion Processes of Fuel Cells within Modelica," In: Casella, F. (ed.), Proceedings of the 7th International Modelica Conference, Linköping University Electronic Press, 2009.

POSTERS

T. Reshetenko, G. Bender, R. Rocheleau, "The effect of local variations in the gas diffusion layer properties on spatial PEMFC performance," Fuel Cell Seminar 2009, November 16-20, 2009, Palm Springs, USA.

Y. Zhai, G. Bender, S. Dorn and R. Rocheleau, Multi-Process Degradation in PEMFC Performance due to Sulfur Dioxide Contamination, Fuel Cell Seminar 2009, November 16-20, 2009, Palm Springs, USA.

3.2 Fuel Cell Hardware-in-Loop Capability

During this grant period, a number of modification to the HiL test system were implemented, all designed to enhance capability for testing of small stacks (previous work was all single cells) and to allow the integration of balance-of-plant components (i.e., blower and humidifier). These modification, funded under HEET, were implemented to allow HiL testing in support of Ion Tiger. Essentially all HiL testing during this period supported Ion Tiger. Complete test results for this work have been reported under that program

3.3 Novel Fuel Cell and Component Development

The effort to develop novel fuel cell components included two major activities: 1) biocarbons for use in fuel cells, and 2) enzymatic bio-fuel cells. Each of these topics is addressed in the following paragraphs.

3.3.1 Biocarbons for Use in Fuel Cells

During 2008, the primary objective of this work was the preparation of biocarbons with widely varied properties for testing by SRI International in their DARPA-sponsored, direct carbon fuel cell research project. A secondary objective was to determine the suitability of sewage sludge for carbonization. Sewage sludge biocarbons were also supplied to SRI for evaluation.

3.3.1.1 Scope of Work and Approach

Because the USA has the largest reserves of coal in the world, and because biomass can be converted into biocarbons quickly and efficiently, there is growing interest in the efficient use of solid carbon fuels. Also, sewage sludge and battlefield refuse can be quickly and efficiently converted into carbon.

A recent Electric Power Research Institute (EPRI) study indicates that "direct" carbon fuel cells have the potential to convert coal or charcoal into electrical power at a system-level efficiency of about 60%, which is over 20% higher than the efficiencies realized by current state-of-the-art integrated gasification combined cycle (IGCC) or advanced pulverized coal power generation systems.

The following companies are engaged in the commercial development of direct carbon fuel cells: SRI International, SARA, Contained Energy Corp. (representing the Lawrence Livermore National Laboratory -- LLNL), Direct Carbon Technologies LLC (representing Stanford University), and CellTech Power. The most promising direct carbon fuel cell results (published by LLNL) were obtained using a biocarbon (charcoal) fuel. The SRI research also emphasizes biocarbon (charcoal) fuel. Much of this work has been supported by DARPA or the U.S. Department of Defense (DoD).

HNEI has developed and patented a quick and efficient ("Flash Carbonization™") process for the conversion of biomass and wastes into biocarbons. The patents have been licensed to the Kingsford Products Co., Carbon Diversion Inc., and Pacific Carbon and Graphite LLC (Duferco Steel). In addition to the production of biocarbons, with ONR support, HNEI has been a leader in characterizing the properties of biocarbons (see section 3.3.1.3 below). Because of this activity, during 2007 EPRI requested HNEI to supply corn cob biocarbons to two direct carbon fuel cell research projects (SRI International and CellTech Power) for testing. Also, HNEI supplied biocarbons to Contained Energy Corp. (representing the LLNL) for testing. The SRI research is supported by DARPA, and the Contained Energy Corp. research is supported by DoD. During the past year HNEI continued to supply biocarbons to SRI International for testing. These biocarbons were sourced from a variety of feedstocks, including corncobs, macadamia nutshells, oak and mahogany woods, jatropha, and sewage sludge. HNEI also evaluated the suitability of sewage sludge for carbonization.

3.3.1.2 Technical Accomplishments

The DARPA-funded SRI International direct carbon fuel cell project drew to a close during the spring of 2009. Corroborating the previous findings of LLNL, the SRI research showed that the properties of the carbon fuel influence the performance of its direct carbon fuel cells. To help SRI identify the desirable properties, HNEI prepared biocarbons with various well-specified properties from a wide variety of biomass feedstocks (e.g., corncobs, macadamia nutshells, oak and mahogany woods, jatropha, and sewage sludge). Biocarbons with low vs. high fixed-carbon contents, low vs. high ash contents, and low vs. high porosities were shipped to SRI for testing and evaluation. The outcome of the tests remains confidential to SRI. As a result of their work the SRI researchers now believe that more fundamental knowledge is needed before a practical carbon fuel cell can be operated. Fundamental work of this nature is underway in HNEI with support from NSF and HEET.

Our HEET funding enabled us to complete a study of the carbonization of sewage sludge taken from the Ewa treatment plant on Oahu, and publish a paper in the archival journal *Energy & Fuels* published by the American Chemical Society. Perhaps our most important results are measurements of the depletion ratios of various heavy metals in the sludge during carbonization. Heavy metals with high depletion ratios leave the carbonization reactor and should be captured to prevent their release into the environment. The heavy metals Hg, As, Se, and Cd all have depletion ratios above 80%; whereas Pb, Zn, Sr, and U have low depletion ratios (typically <20%). In addition to being a concern related to the valorization of sewage sludge, the release of heavy metals (e.g., Hg, As, Se, Cd) into the environment is also a concern for the valorization/disposal of rubber tires, battlefield waste, and even biomass. The abstract of our paper follows:

> *Sewage sludge is a renewable, negative-cost organic material that is well suited for the production of biocarbons. Due to increasing interest in the use of biocarbons for soil beneficiation and carbon sequestration (i.e., "Terra Preta" applications), the aim of this paper is an assessment of the production of sewage sludge charcoal for land application. By use of the Flash Carbonization™ process we measured sewage sludge charcoal yields near 30 wt% and fixed-carbon yields near 18 wt% from sludges with moisture contents near 7 wt%. Increasing the moisture content of the sludge reduced the charcoal and fixed-carbon yields; nevertheless, sewage sludge with 30 wt% moisture was successfully carbonized. The presence of heavy metals in sewage sludge is an important concern. We found that heavy metals with low boiling points (e.g., As, Cd, Hg, Se) were prone to elution from the carbonization reactor. Because the heavy metal content of the sludge used in this work was not high, the charcoal was found to be acceptable for land application according to U.S. EPA regulation 40 CFR Part 503.*

Concurrent with the work described above, we developed a spreadsheet that makes detailed predictions of the capital and operating costs associated with a commercial-scale carbonizer. Prior to the development of this spreadsheet we assumed that compressed air would be virtually free. From the spreadsheet we learned that fuel consumption associated with compressing air to 100 psig is relatively expensive (i.e., its costs are similar to the cost of delivered feedstock). This had a major impact on our plans for the design of the catalytic afterburner (CAB) needed to meet

emissions regulations, because the CAB that we built (nearly ten years ago) requires compressed air.

Recognizing the need to employ a CAB involving fans instead of an air compressor, we sought a quotation from a commercial manufacturer of such afterburners. No commercial manufacturers had significant experience with the effluent of an efficient biomass carbonizer. One manufacturer estimated a cost of $300,000 to fabricate an afterburner whose size alone would exceed the area we have available on campus for our work.

In summary: the commercial scale Flash-Carbonization™ reactor that we have on campus is capable of a large throughput: consequently its testing requires a large quantity of feedstock (e.g., 1000 lb for a single run), a large rented air compressor, a rented power generator, and a very large afterburner. Each test requires months of preparation and the cost of modifying commercial-scale equipment is high. To speed our progress we have designed and fabricated a $1/10^{th}$ scale canister that will fit within the existing pressure vessel and mimic the behavior of a full-size canister. The $1/10^{th}$ scale canister is 12 in D x 9 ft tall and will accommodate about 100 lb of corn cobs. This canister will behave like a "core" of a full-size 3 ft D canister. An air compressor and a power generator that are already available on our site will be sufficient to execute test runs using this canister. Consequently there will be no need to rent costly air-compressors and power generators for each test.

Beginning on 1 June 2010 an experienced and talented Post-Doc from the U. Zaragoza (Spain) and a MSE candidate in ME at UH will join our team. The MSE student will focus his thesis research on the development of a lab-scale CAB that will be operate in conjunction with our lab-scale Flash Carbonization™ reactor. He will also assist the Post-Doc. Using results from the lab-scale CAB, the Post-Doc will be responsible for the design, fabrication and testing of a pilot-scale CAB that will be operated with the $1/10^{th}$ scale canister. The pilot-scale CAB will obtain needed secondary air via fans. Our goal is to meet emissions regulations by the summer of 2011.

3.3.1.3 Papers and Presentations Resulting from Efforts

PAPERS by Michael J. Antal, Jr.

Yoshida, T., Antal, M.J. "Sewage Sludge Carbonization for Terra Preta Applications" *Energy Fuels*, Vol. 23, 5454-5459.

Antal, Jr., M.J., Nihous, G.C. "Thermodynamics of an aqueous-alkaline/carbonate carbon fuel cell" *Ind. Eng. Chem. Res*, Vol. 47, 2008, 2442-2448.

Nunoura, T., Dowaki, K., Fushimi, C., Allen, S., Meszaros, E., and M.J. Antal, Jr. "Performance of a First-Generation, Aqueous-Alkaline Biocarbon Fuel Cell. *Ind. Eng. Chem. Res.* Vol. 46, 2007, pp. 734-744.

Antal, Jr., M.J., Bourke, J., Manley-Harris, M., Fushimi, C., Dowaki, K., and Nunoura, T. "A Model of the Chemical Structure of Carbonized Charcoal" *Ind. Eng. Chem. Res.*, Vol. 46, 2007, pp. 5954-5967.

Antal, Jr., M.J., Meszaros, E., Varhegyi, G., Jakab, E.; Bourke, J., Manley-Harris, M.; and Nunoura, T. "Do all carbonized charcoals have the same chemical structure? Implications of TG-MS measurements." *Ind. Eng. Chem. Res.*, Vol. 46, 2007, pp. 5943-5953.

Antal, Jr., M.J., Varhegyi, G., Meszaros, E., Bourke, J., and Jakab, E. "Combustion Kinetics of Corncob Charcoal and Partially Demineralized Corncob Charcoal in the Kinetic Regime." *Ind. Eng. Chem. Res.,* Vol. 45, 2006, pp. 4962-4970.

Antal, Jr., M.J., Wade, S.R., and Nunoura, T. "Studies of the Flash Carbonization™ Process. 2. Violent Ignition Behavior of Pressurized Packed Beds of Biomass: A Factorial Study." *Ind. Eng. Chem. Res.,* Vol. 45, 2006, pp. 3512-3519.

PRESENTATIONS by Michael J. Antal, Jr.

Organized and chaired a topical session concerning chemical engineering for biofuels production during the *AIChE Annual Meeting* in Nashville from 8 – 13 November, 2009.

Organized and chaired two topical sessions concerning chemical engineering for biofuels production and novel fuel cell applications during the *AIChE Annual Meeting* in Philadelphia from 16 – 21 November, 2008.

Organized and chaired two topical sessions concerning chemical engineering for novel fuel cell applications and biofuels production during the *AIChE Annual Meeting* in Salt Lake City from 4 – 9 November, 2007.

Presented invited seminars on the carbon fuel cell at Eindhoven University (7 February 2006), the University of Missouri at Columbia (10 November 2006), the University of Massachusetts at Boston (16 February 2007), the University of Hawaii at Manoa (25 September 2007), and the Hungarian Academy of Sciences (25 October, 2007).

Organized and chaired three topical sessions concerning chemical engineering for novel fuel cell applications and biofuels production during the *AIChE Annual Meeting* in San Francisco from 13 – 17 November, 2006.

On 28, 29 August 2006, attended a "by-invitation-only" meeting at EPRI Headquarters in Palo Alto and delivered a lecture entitled: "Performance of a First-Generation Aqueous-Alkaline Biocarbon Fuel Cell."

3.3.2 Enzymatic Bio-Fuel Cells

As stated in our previous reports, enzymatic bio-fuel cells (EBFCs) are fuel cells that use enzymatic biocatalysts to convert chemical energy directly to electricity as power sources. They are promising alternatives to complement conventional fuel cell technologies that rely on transitional metal oxides or noble metals as catalysts for conversion of chemical energy, typically stored in hydrogen or other biofuels, to useful electrical energy. An EBFC exhibits some promising technical merits as follows:

- Selectivity – Enzyme catalysts are fuel specific and capable of handling complex fuels in the liquid phase, which can simplify fuel logistics and cell design;
- Abundance in supply – Unlike conventional Pt-based catalysts, enzymatic catalysts can be produced via biological or chemical methods, thus promising a potentially low-cost mass production and unlimited supply;
- Wider range of operation – Due to their selectivity, enzymes are generally more adaptive to extreme conditions and tolerant to contaminants;
- Reformulation – If the gene coding for the enzyme is obtained, a suite of directed evolution techniques exists to create mutants that are more effective in catalysis; and
- Self-assembly – Unique in biological systems, to simplify fabrication processes for micro-devices *in situ.*

The continuation of support shall enable us to focus on fundamental studies to elucidate charge transfer limitations in enzyme-catalytic electrodes, so we can transfer this knowledge into improved engineering designs of practical *bio-fuel cells.* The following long-term objectives have been pursued under this program:

- Establish an array of quantitative *in situ* characterization techniques, test cells, and modeling capabilities to determine limitations to bioelectrocatalysis [1-4], and to construct a test bed that will allow us to refine such techniques in microbial- or enzyme-based bioelectrocatalysis operation [5]; and
- To develop a technology base with know-how to improve performance (e.g., catalyst lifetime, current density) with respect to important process variables such as choice of catalyst, choice of mediators, immobilization matrix, and mode of immobilization (e.g., covalent attachment versus physical entrapment of enzyme).

3.3.2.1 Scope of Work and Approach

Over the course of this project, three major tasks in the EBFC work have emerged:

1) Develop platform fabrication technology to control the resulting multidirectional pore structure of three-dimensional electrodes;
2) Develop qualitative and quantitative fluorescence as a characterization technique for enzyme fuel cells; and
3) Develop *in situ* interface characterization techniques utilizing imaging ellipsometry with quartz crystal microbalance and electrochemical techniques to facilitate fabrication and testing of full bio-fuel cells and to understand the interfacial charge transfer mechanism for future optimization of the charge transfer efficiency.

For this specific funding period, we were funded to pursue the following:

1) Develop and characterize chitosan co-block polymers that immobilize multiple enzymes that can more fully oxidize complex energy fuels, and

2) Continue to apply *in situ* characterization techniques based on spectroscopic imaging ellipsometry with microgravimetric and electrochemical techniques to study the enzyme-electrode interaction on the electrode surface and the associated dynamic behavior, aiming to understanding the charge transfer process with more direct measurements and correlation.

3.3.2.2 Technical Accomplishments

Summary of work from previous project periods. In past reports, we have presented several prototype cells constructed to deliver gas (e.g., hydrogen) fuels. A final working hydrogenase enzymatic bio-fuel cell was constructed and tested (Figure 3.3.1). The design considerations and test applications were described in the June 2005 Final Technical Report. Complete details on this work have been published [1]. From this work we determined, and reported previously, that the use of gaseous fuels is limited by the solubility of the gaseous fuel in the aqueous buffer that is required to maintain enzyme activity.

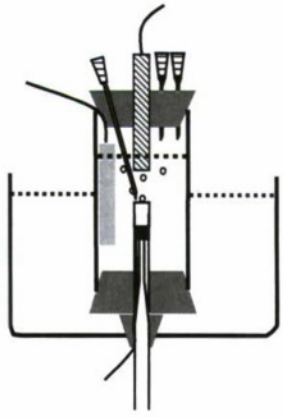

Figure 3.3.1. Hydrogenase enzyme fuel cell.

In past reports we have also commented on the development of a suite of characterization techniques, including potentiostatic DC polarization, dynamic potentiometry, and electrochemical impedance spectroscopy (EIS) combined with spectrophotometric detection of enzyme activity, in order to characterize electrode performance, and to differentiate between the relative contributions towards charge transfer efficiency. Among the results of our efforts, in particular, we believe we were one of the first groups to report charge transfer efficiency for bound enzyme [1] and to report a mass transport modeling effort that can be combined with DC-polarization data to yield information valuable for future electrode development [2]. A detailed description of the technique application, data and results can be found in the literature. A summary can also be found in a book chapter that was published in 2007 [6].

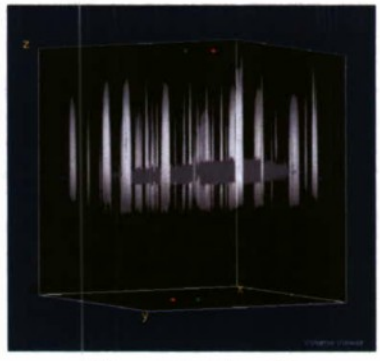

Figure 3.3.2. 3D distribution of tagged enzyme within polymer.

To characterize the distribution of enzymes within the polymer films used to immobilize the enzymes, we have applied the technique of fluorescence. Electrode fabrication methodologies using the immobilization process with polymer films inherently assume that the immobilized enzymes are homogeneously distributed. Our work, which has tagged ethanol-oxidizing enzymes with various fluorescent probes, has used laser-scanning confocal microscopy to image the spatial distribution of the enzyme within the film. Our results, which have been published [3] (see Figure 3.3.2), have clearly demonstrated that this is not necessarily the case, and that the tagged enzymes may not be homogenously distributed within polymer films. To investigate how the charge-charge interaction between the enzyme and the polymer affect the immobilization process, we have also studied the steady-state and dynamic

polarization of fluorescent probes when placed in solution with charged polymers. This work has shown that the enzymes are retained in the micelles of the hydrophobically-modified polymer as it dries, but are not entrapped within those polymers while mixed in free solution [4].

The charge transfer efficiency in a bio-fuel cell is strongly dependent on the interfacial property of the surface, where the charge transfer occurs. The interfacial properties need to be characterized in situ in the environment where the electrocatalytic reaction occurs. To study such property and behavior of the interface, we have developed a unique capability of using spectroscopic imaging ellipsometry with additional supplemental characterization tools to assist us understand the nature of such charge transfer reaction on the electrode surface. Mediator films that were immobilized on electrode surface have been suggested to be an effective medium to promote charge transfer. We have been investigating such mediator immobilization in our laboratory to understand the stability and property of such films. To evaluate film thickness during electrochemical deposition of electrode immobilization matrix or mediator film on electrode surface, we have combined the technique of imaging ellipsometry with the cyclic voltammetric deposition technique to track the thickness of the deposited film with cycle number. Such valuable technique has contributed new information regarding the fundamental reaction kinetics and mechanisms underlying the electrochemical deposition of conductive films onto electrode surfaces (see Figure 3.3.3). The initial work has been published [5]. More, a unique imaging ellipsometric technique in combination with quartz crystal microbalance (QCM) and electrochemical cyclic voltammetric techniques for surface film deposition and characterization has been developed through this effort. Imaging ellipsometry is capable of measuring surface morphology and film thickness in nanometer scale, providing us a powerful surface characterization technique that is *in situ* and non-invasive. We were able to control the polymer film formation with accurate thickness and morphology control during deposition. This technique also helped us understand the stepwise underlying mechanism in the deposition and provided unprecedented details in the film formation process involving redox reactions. We are currently using this technique to study the redox kinetics involved in the NADH oxidation.

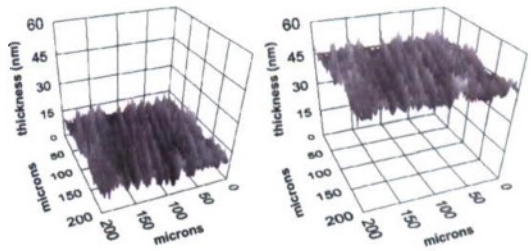

Figure 3.5-3. Film thickness of poly(methylene green films.

During this period, these outcomes were also used to leverage two extramurally funded projects. The first one is a grant from the Intelligence Community Postdoctoral Fellow Research Program to support development of bio-fuel cells for micro-power source applications (B.Y. Liaw, PI). The second is a sub-award from the AFOSR Multi-disciplinary University Research Initiative (MURI) program (M.J. Cooney, PI), awarded to the lead institution, the University of New Mexico (P. Atanassov, PI). Both awards have lent national recognition of this EBFC program.

In collaboration with these partner programs, we have explored chitosan and chitosan-composite scaffolds as a material for the fabrication of macroporous electrodes that can support both mediator-based and direct electron transfer. Work accomplished has included the development of protocols for the fabrication of hydrophobically-modified chitosan scaffolds immobilizing NADH-dependent glucose oxidase, and chitosan/CNT composites for attachment of PQQ-

enzymes. With respect to the fabrication of hydrophobically-modified chitosan scaffolds, we have demonstrated proof-of-principle data that shows that the power density can be significantly increased for mediator-based systems (Figure 3.3.4). This work has been published in the Journal of Materials Chemistry [6]. We have also fabricated three-dimensional chitosan/CNT scaffolds that provide a basis for enzymes that are capable of direct electron transport. The chitosan essentially acts as a binder of the carbon nanotubes and one is left with scaffold structures similar to that presented in Figure 3.3.4, but with carbon nanotubes lining the surface. These scaffolds are highly conductive and represent a new methodology to create multidirectional and multidimensional 3D structures of electrochemically-active carbon nanotube surfaces [7].

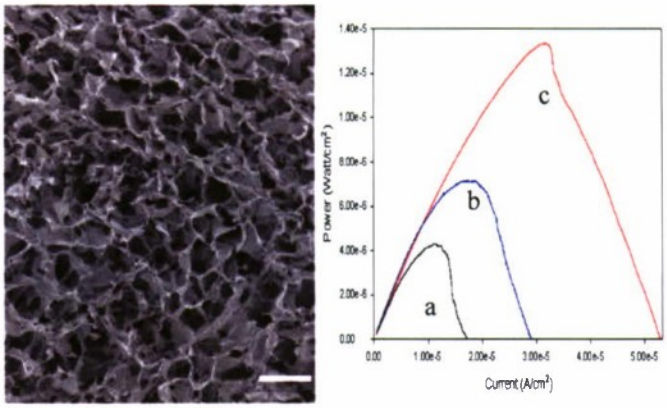

Figure 3.3.4. SEM image of chitosan scaffold (Left) and power curves from chitosan film (a) and scaffolds (b, c).

We have also developed a liquid-phase prototype Bio-fuel Test Cell (Figure 3.3.5). This prototype, which we term the modular stack cell, was designed as a characterization tool. For example, we sent duplicate models of the modular stack cell to three cooperating laboratories in the U.S. that also specialize in enzyme fuel cell development. Each laboratory (Dr. Shelley Minteer at St. Louis University, Dr. Plamen Atanassov at the University of New Mexico, and Dr. Scott Barton at Michigan State University) was given the same protocol to execute (i.e., to develop a poly[methylene green] electrode film that oxidizes NADH), and the electrochemical data from all laboratories were consolidated and statistically analyzed for reproducibility. The results demonstrated that the modular stack cell provides a framework for comparative analysis of systems. The results have been published in the Journal of Electroanalysis [8]. With this confidence, we have fabricated a full ethanol-based bio-fuel cell based on this design (Figure 3.3.6). Although we have achieved full operation (see power curves in Figure 3.3.6) with an air-breathing cathode, this work is still in development [9].

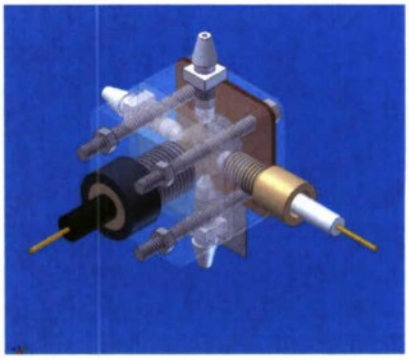

Figure 3.3.5. The modular stack cell.

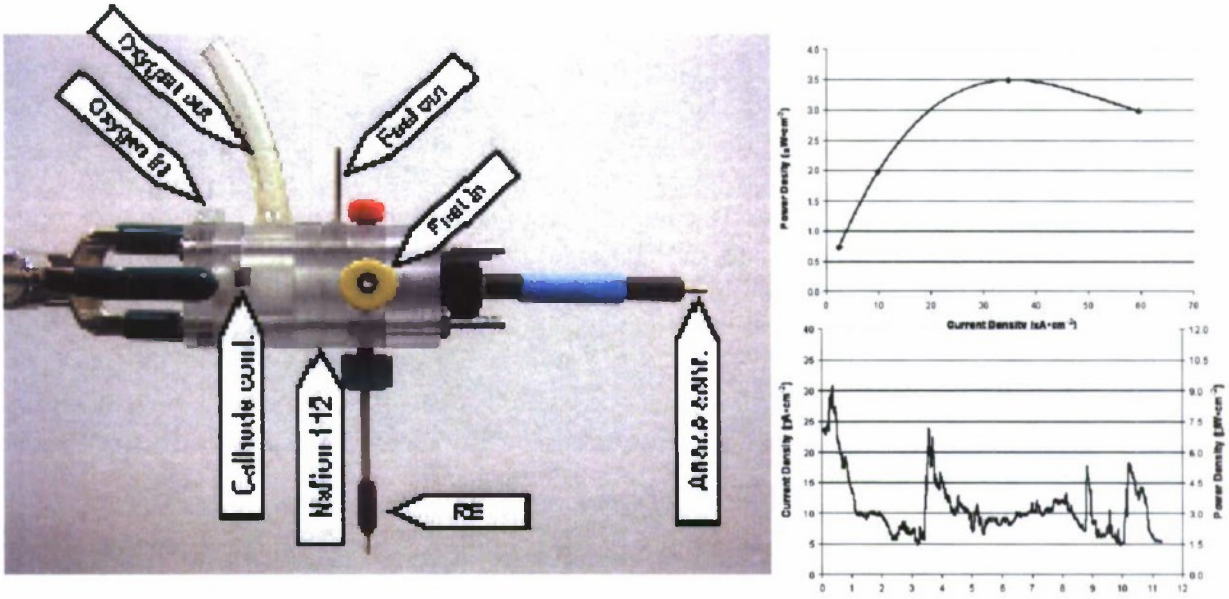

Figure 3.3-6. Operational biofuel cell, based on modular stack cell design.

In addition to these accomplishments, we have also initiated an enzyme immobilization effort to establish a common platform for apo-enzyme reconstitution. The prosthetic group pyrroloquinoline quinine (PQQ) and PQQ-dependent glucose dehydrogenase (PQQ-GDH) has been chemically bound to CHIT-CNT films in the presence of EDC (acronym for 1-ethyl-3-[3-dimethylaminopropyl] carbodiimide hydrochloride), respectively. The immobilized PQQ-GDH in our system displays a quasi-reversible electron transfer with a formal potential $E^{\circ\prime}$ of –0.110 V, which was found to be independent of the scan rate. The bioactivity of the immobilized PQQ-GDH was retained. Additionally, the enzyme-free bound PQQ exhibits a more facile electron transfer with a glassy carbon electrode (GCE) compared to the immobilized PQQ-GDH, suggesting that PQQ-bound CHIT-CNT films hold promise as a platform for the reconstitution of PQQ-dependent apo-enzymes, with potential application in biosensors and bio-fuel cells. Evidence of electron transfer between bound PQQ-GDH and the GCE has been observed when the PQQ-GDH has been coupled with EDC to a CNT-functionalized CHIT film. The experimental results suggest that the presence of CNT in the CHIT film promotes the electron transfer of bound PQQ-GDH to the GC electrode. A quasi-reversible electrochemical reaction, as revealed by a pair of well-defined redox peaks, was also observed by cyclic voltammetry, and additional experimental results suggest that the bioactivity of PQQ-GDH was retained in PQQ-GDH-bound CHIT-CNT/GCE, which permits its use as a platform catalyst combination for a mediated bio-fuel cell anode or amperometric biosensor electrode for glucose detection. It should be noted that PQQ bound to CHIT-CNT film also exhibited an effective charge transfer with GCE, suggesting that it can be used as a promising platform for reconstitution of various PQQ-dependent apo-enzymes. A summary of this work has been published [10].

Of special interest for an enzymatic power generation from ethanol as biofuel are NAD-dependent dehydrogenases, like alcohol dehydrogenase (ADH) or malate dehydrogenase (MDH), which lie within the Krebs cycle. This fundamental metabolic pathway involves eight enzymes for energy production through aerobic respiration. In order to exploit the entire cycle

on a bioanode, and within the context of increased power generation, a polymer system that can immobilize and stabilize all eight enzymes in a three-dimensional matrix is needed. In support of developing macroporous chitosan and chitosan-derivate scaffolds as advanced materials for fabrication of biofuel cell electrodes, as specified in 1), we have immobilized MDH within modified chitosan-polymer scaffolds placed upon a poly(methylene green) modified glassy carbon electrode. The current and power density for this MDH bioanode have been tested in half cell mode (Figure 3.3.7) and are currently being tested in a full biofuel cell. The half cell mode results represent a significant advance in the development of flow-through electrodes and confirms the application of an enzyme immobilized in a modified chitosan polymer. We have also used fluorescence to track the spatial distribution of enzyme immobilized in the hydrophobically-modified polymer (Figure 3.3.8). This work, which has been published [11], clearly demonstrated that the distribution of a fluorescently-tagged enzyme (the pink in Figure 3.3.8) distributes quite differently in various forms of the hydrophobically-modified chitosan polymer (i.e., native, butyl-modified, and ALA-modified).

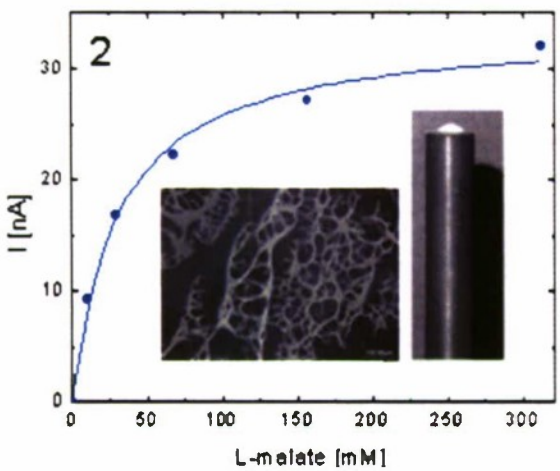

Figure 3.3.7. Electrical results for MDH bioanode.

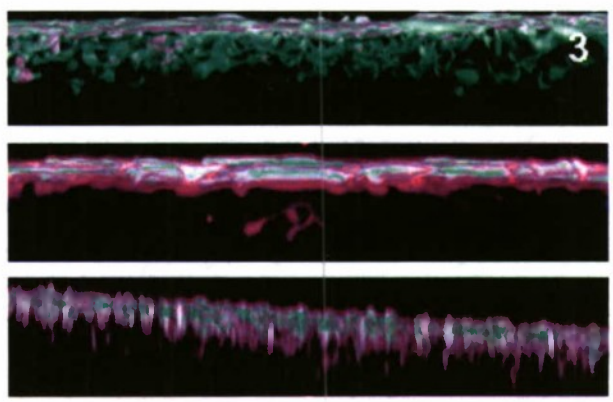

Figure 3.3.8. Enzyme spacial distribution.

Additional work has been executed wherein polarity sensitive fluorescent probes have been attached to enzyme and immobilized within native and modified chitosan polymer (Martin, G. L., Minteer, S. D., and M. J. Cooney. Fluorescence characterization of chemical microenvironments in immobilization matrices: Polarity. The Analyst. **In Press.**). This work has been designed to quantitatively characterize the chemical microenvironment immediately surrounding the enzyme when in the immobilized state. Specifically, polar sensitive probes were used to correlate the relative hydrophobicity of the chemical microenvironment. The results are shown in Figure 3.3.9 wherein acrylodan labeled cMDH was suspended in the presence of aqueous native and modified chitosan (A), immobilized in native and modified chitosan scaffolds (B), immobilized in native and modified chitosan dehydrated scaffolds (B), and immobilized in native and modified chitosan rehydrated scaffolds (C). Figure 3.3.9 compares emission profiles of acrylodan-tagged enzymes in aqueous solution against those immobilized within the polymers. In Figure 3.3.9 (A), the emission peaks of acrylodan-cMDH suspended in

aqueous solutions of native and modified chitosan polymer did not vary relative to each other, suggesting that the various polymers (as 0.5 (w/w)% solutions) provided identical chemical microenvironments (in terms of polarity – i.e., neither were relatively more or less hydrophobic). This assumes that the chemical environment surrounding the tagged enzyme is dominated by water and not the chitosan polymer. In contrast, when the tagged enzymes were immobilized within the same polymers, the emission maxima not only occurred at lower wavelengths, but they also varied significantly across the three polymers (Figure 3.3.9 (B)). This result suggests that when in the immobilized state the various modified polymers provided altered chemical microenvironments, thus corroborating two separate theories: (1) that modified chitosan polymers can provide altered chemical microenvironment, and (2) that the altered chemical microenvironments are most pronounced after the polymer has been precipitated (e.g., through freezing or drying processes) into its final structure. The latter result supports our previous suggestion that the enzymes are not interacting with or being affected by the amphiphilic regions of the polymer, until the freezing or precipitating process. The overall blue shift observed in the dried polymer can be partially attributed to their dehydration during the freeze-drying process. The removal of water molecules surrounding the immobilized enzyme will obviously lead to a reduction in polarity. By contrast, re-hydration should reintroduce water molecules into the chemical environment and thereby increase the relative polarity. To verify this, the scaffold films were rehydrated in identical buffer solution. Although the rehydrated films showed a trend for relatively more polar chemical microenvironments, the same trends in blue shift was observed across all forms of the polymer (Figure 3.3.9 (C)). This confirms that the chitosan polymer does impact the chemical microenvironment of the enzyme when in the immobilized state.

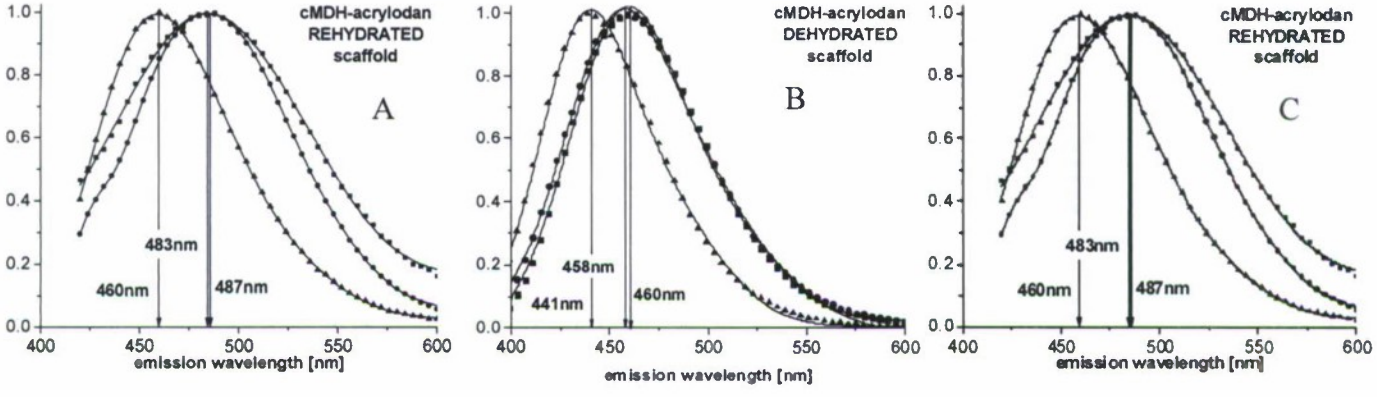

Figure 3.3.9. In all three (A, B and C) the polymers are represented by the following (■ – CHIT ● – ALA-CHIT ▲ – C4-CHIT). All samples were excited with □(ex) = 360 nm.

For the purposes of correlation, malate dehydrogenase was immobilized within the three target polymers: native chitosan, butyl-modified and alpha linoleic acid a poly(methylene green) coated glassy carbon electrode. The electrocatalytic activity of each polymer was then measured in half cell mode using amperometry. The amperometric current of NADH oxidation on poly(methylene green) was measured at an applied potential of +300 mV. The catalytic oxidation of NADH occurs in the chosen potential range (selected to be higher than the half-

wave potential to maximize electrocatalytic reaction). Electrochemical currents, measured at the same potentials, can be used as apparent catalytic activity. The results, normalized to 1.0, are shown in Figure 3.3.10. Normalizing the activity to the highest output, the butyl-modified chitosan gave a 10-fold increase in current density and the ALA-modified a 4-fold increase when compared against the unmodified native chitosan. This suggests that the activity of the immobilized enzyme follows the measurement of the chemical microenvironment in terms of polarity.

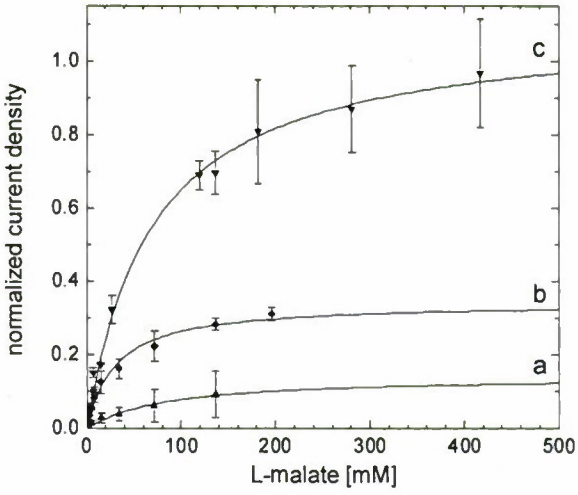

Figure 3.3.10. Electrochemical activity as normalized current density of immobilized MDH in different chitosan polymers. (c): C4-Chitosan film; (b): Chitosan film; (a): ALA-Chitosan film.

The poly(methylene green) mediator has been considered one of the best mediators for a NAD^+-dependent biocatalytic process and thus of great interest to the enzymatic bio-fuel cell operation. However, the interfacial property of this mediator polymer film on biocatalytic electrodes is not well understood to date. We have used electrochemical microgravimetric imaging ellipsometry (EmIE) to study the interfacial property of this mediator compound on Pt or glassy carbon electrode surfaces. The EmIE technique allows us to correlate changes of mass, charge, and ellipsometric measurements in a synchronized manner to derive information on chemical and electrochemical behavior of this polymer mediator film (Figure 3.3.11). This technique can be applied to both steady state and transient dynamic regimes.

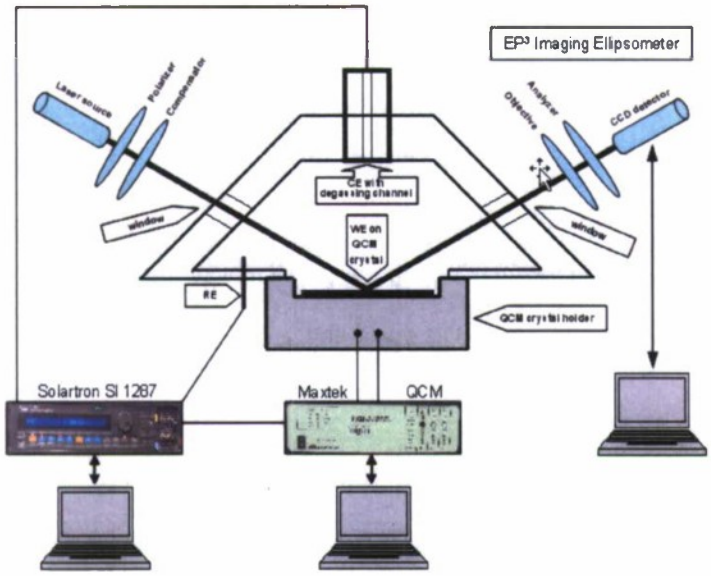

Figure 3.3.11. EmIE measurement set-up.

As a result of such studies, we have produced some interesting results based on the EmIE approach in the study of poly(methylene green) mediator (Svoboda, Cooney, Rippolz, and Liaw 2006; Svoboda and Liaw 2008). Highlights are as follows:

Figure 3.3.12 shows that the transient change of mass and current do not coincide in the synchronized measurements. However, the ellipsometric measurements show that the ellipsometric angle Δ is in sync with transient mass changes at all times, indicating that the mass change is actually detectable and the corresponding change in such a surface film thickness is also measurable by the ellipsometric method. The electrochemical redox reaction, on the other hand, occurs at a different time scale and the corresponding current change is also in sync with the ellipsometric angle change in Ψ, which has a split peak: one corresponds to the mass (thus film thickness) change and the other to the chemical change in the redox process. It is therefore interesting to observe this transient behavior of the film development, where the mass change is related to adsorption, while the redox reaction does not have a direct correlation with mass measured (Svoboda and Liaw 2008).

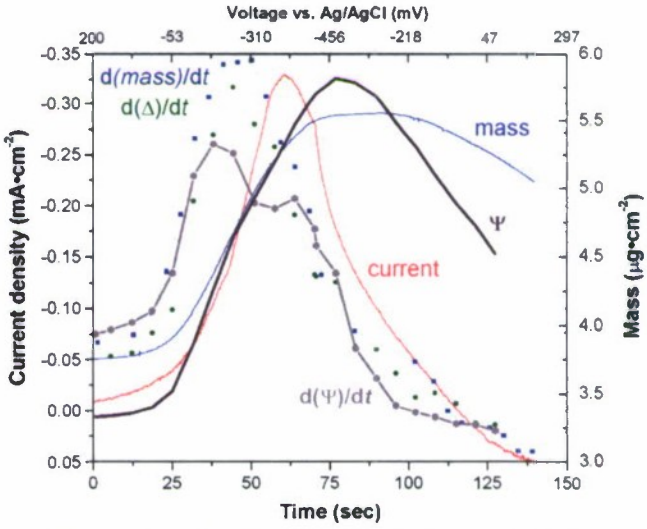

Figure 3.3.12. Current and mass variations.

We also showed that with proper estimates of the parameters in the optical model, we can simulate the film thickness changes with deposition conditions (Figure 3.3.13). This is a powerful tool to allow real-time *in situ* observation with quantitative characterization (Liaw 2010, in press).

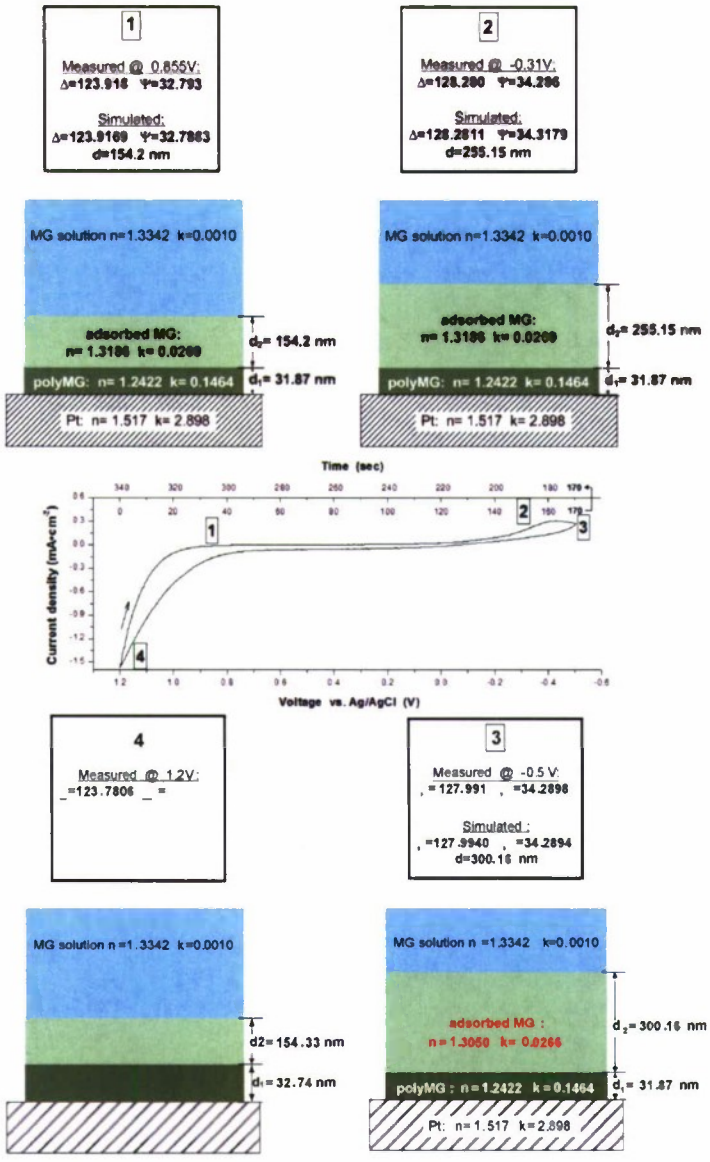

Figure 3.5-13. Simulation of film thickness changes with deposition conditions.

In the effort to continue to develop PQQ-dependent enzymatic systems for bio-anode application[1]; we found the reconstitution of the PQQ-dependent enzymes such as glucose dehydrogenase (GDH) on glassy carbon electrodes with chitosan-carbon nanotube matrix have not been effective in making electronic conduction to promote the enzymatic electrocatalytic kinetics (Sun and Liaw, unpublished). The turnover rate for the reconstituted GDH electrodes has been low. We are searching for other mediators that can provide better relay units for charge transfer.

[1] These enzymes can be bound to either chitosan-CNT or conductive polymers, such as polypyrrole, as novel immobilization approaches that can realize direct electron transfer.

In the effort to develop *in situ* interfacial characterization techniques to assess the practicality of using self-assembled monolayers (SAMs) for enzyme immobilization, we have found that the surface conditions of the glassy carbon or gold electrode are very sensitive to contamination and thus the SAM formation is not reproducible and difficult to control (Svoboda and Liaw, unpublished results). In short, both the mediator-cofactor reconstitution and SAM-based immobilization approaches have produced limited success in improving enzymatic electrocatalysis processes. We consider these techniques to possess limited potential for significant improvement of bio-fuel cell performance at the present time.

Summary of additional work accomplished during this period. Work towards the development and characterization of chitosan co-block polymers that immobilize multiple enzymes that can more fully oxidize complex energy fuels begins with the development of a technique to lay down and characterize micron thin films. This work is in its initial stages and now under the direction of a graduate student. To date, a thin-film fabrication technique has been developed. Specifically, the thin-film scaffolds were prepared using a modified technique based on the procedure outlined elsewhere (Martin, G., Minteer, S. D., and M. J. Cooney (2009). *Spatial distribution of malate dehydrogenase in chitosan scaffolds*. Applied Materials & Interfaces. 1(2):367–372). 50 μL of chitosan solution is deposited using a micropipette onto a glass slide. To ensure that the surface of the glass slides are hydrophilic, they are cleaned and pretreated by submersion in piranha solution (30% H_2O_2:96-98% H_2SO_4 mixed in 1:3 ratio) followed by rinsing with DI water and then air dried with filtered compressed air. The solution is then spread coated using an automated syringe pump (Cole-Parmer Single-Syringe Infusion Pump, 74900) to drag a second glass slide over the meniscus at a rate of 1 μm/s for ~30 min. To prevent air drying during the coating, the entire process is conducted in a closed chamber kept at 20 °C and greater than 95% humidity. Once the coatings are set, the slides are then frozen at -20 °C for 1hr. Thereafter, the slides are vacuum freeze dried for 12 hrs. Analysis of the thin-film size has shown that the surface morphology of all films is not smooth on the level of the microscope's measurements (1 to 10 μm), with fluctuations in height across the films greatest at the lower deposition rate. That said, film height does correlate to deposition rate.

In the effort of continuing to apply *in situ* characterization techniques based on spectroscopic imaging ellipsometry with microgravimetric and electrochemical techniques to study the enzyme-electrode interaction on the electrode surface and the associated dynamic behavior, aiming to understanding the charge transfer process with direct measurements and correlations, We have improved the capability for such characterization. We have upgraded our imaging ellipsometry to a spectroscopic model with a high intensity Xenon arc lamp as white light source, which can provide a wavelength range from 360 nm to 1,000 nm with a monochromator that consists of 46 interference filters to provide ± 6 nm of bandwidth resolution. The spectroscopic model will provide us additional control on the wavelength control for the incident light besides incident angle for more information gathering on the surface and film properties. We are currently using this capability to study the poly(methylene green) mediator properties (Chiu and Liaw). We anticipate receiving more quantitative results on the film characterization.

In addition to these efforts outlined above, through the IC Postdoctoral Fellow Research Program, we have investigated other alternative approaches to harnessing chemical energy in bio-fuels for fuel cell operation [12]. One such investigation has led us to achieve a sustainable

current generation with ammonia oxidation, with assistance from conductive polymers such as polypyrrole (Scott, Cooney, and Liaw 2008). Figure 3.3.14 shows the current production as a function of ammonia concentration in the presence of polypyrrole and hydrogen peroxide at different concentrations in the solution. Without ammonia, the current production was not obvious, even with the presence of peroxide. Therefore, it is a clear indication that the current was produced by the oxidation of ammonia, which was promoted by peroxide in the interaction with polypyrrole.

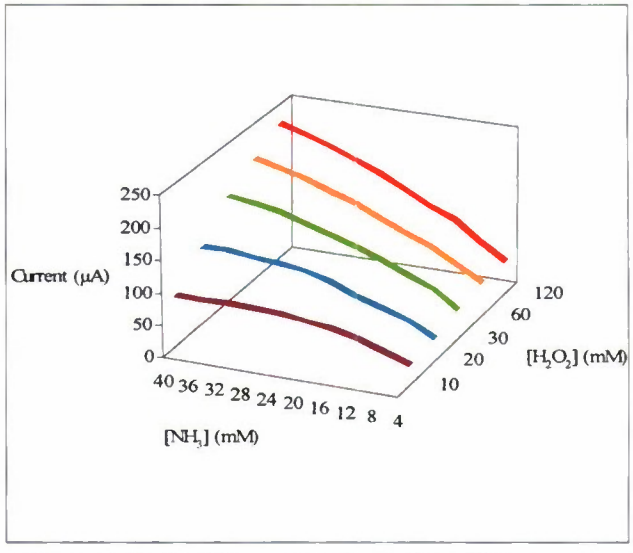

Figure 3.3.14. The current produced from different concentrations of ammonia based on different concentrations of H_2O_2.

In a separate study of glucose oxidation, we also discovered a unique pathway to promote charge transfer of partial oxidation of glucose to produce current with the help of mediators such as methyl viologen (Scott and Liaw 2009). In this study, high current density and power density were observed with glucose oxidation in alkaline solutions with the presence of a mediator.

3.3.2.3 References

1. Johnston, W., Cooney, M.J., Liaw, B.Y., Sapra, R., and Adams, M.W.W., *Design and characterization of redox enzyme electrodes: new perspectives on established techniques with application to an extremophilic hydrogenase.* Enzyme and Microbial Technology, **2005. 36**: p. 540-549.
2. Johnston, W., Maynard, N., Liaw, B., and Cooney, M.J., *In situ measurement of activity and mass transfer effects in enzyme immobilized electrodes.* Enzyme and Microbial Technology, **2006. 39**: p. 131-140.
3. Konash, S., Cooney, M.J., Liaw, B.Y., and Jameson, D., *Characterization of Polymer-Enzyme Interactions using Fluorescence.* Journal of Materials Chemistry, **2006. 42**, p. 4107-4109.
4. Martin, G. L., Ross, J. A., Minteer, S. D., Jameson✉, D. M., and M. J. Cooney✉. *Fluorescence characterization of polymer chemical microenvironments.* Carbohydrate Polymers. doi:10.1016/j.carbpol.2009.02.021.
5. Svoboda, V., Cooney, M.J., Rippolz, C., and Liaw✉, B.Y., *In-Situ Characterization of Electrochemically Polymerized Methylene Green Films on Platinum and Glassy Carbon Electrodes.* Journal of the Electrochemical Society, **2006. 154**(3): p. D113-116.
6. Cooney✉, M. J., Windmesier, M, Lau, C., Liaw, B. Y., Klotzbach, T. and S. Minteer✉. *Design of Chitosan Gel Pore Structure: Towards Enzyme Catalyzed Flow-Through Electrodes.* Journal of Materials Chemistry, **2008. 18**, 667-674.

7. Lau, C., Cooney✉, M. J., and P. Atanassov. *Conductive macroporous composite chitosan-carbon nanotube scaffolds*. Langmuir. **2008**. *24*, 7004-7010.

8. Svoboda, V., Cooney✉, M. J., Liaw, B. Y., Minteer, S., Piles, E., , Lehnert, D. Barton, S. C., Dmitri Ivnitski, D., and P. Atanassov. *Standardization of a common platform for bioelectrocatalysis characterizations*. Electroanalysis, **2008**. 20(10):1099 – 1109.

9. Sun, D., Cooney, M. J., and B. Y. Liaw✉. *PQQ-glucose dehydrogenase immobilized in chitosan / carbon nanotubes composite films*. Electrochemical Solid State Letters. **2008.** 11(6) B101-B104.

10. Martin, G., Minteer, S. D., and M. J. Cooney✉. *Spatial distribution of malate dehydrogenase in chitosan scaffolds*. Applied Materials & Interfaces, **2009**. 1(2):367–372.

11. V. Svoboda and B.Y. Liaw✉, "In-situ transient study of polymer nano-film growth via simultaneous correlation of charge, mass, and ellipsometric measurements." *Pure Applied Chem.*, **2008**. 80:2439–2449.

12. Scott, D., M.J. Cooney, and B.Y. Liaw✉. Sustainable current generation from the ammonia - polypyrrole interaction. *J. Mat. Chem.*, **2008**. 18:3216–3222.

13. Scott D. and B.Y. Liaw✉. Harnessing electric power from monosaccharides — A carbohydrate-air alkaline fuel cell mediated by redox dyes. *Energy Environ. Sci.*, **2009**. 2:965–969.

14. Liaw, B.Y. In situ characterizations of porous media for applications in biofuel cells: Issues and challenges, in *Porous Media: Applications in Biological Systems and Biotechnology*, Z. Vafai, ed., CRC Press, Taylor and Francis Co., Boca Raton, FL, **2010**. Chapter 13, in press.

3.3.2.4 Papers and Presentations Resulting from Efforts

PAPERS

2009 Scott D. and B.Y. Liaw✉. Harnessing electric power from monosaccharides — A carbohydrate-air alkaline fuel cell mediated by redox dyes. *Energy Environ. Sci.* 2:965–969.

2009 Martin, G. L., Ross, J. A., Minteer, S. D., Jameson✉, D. M., and M. J. Cooney✉. *Fluorescence characterization of polymer chemical microenvironments*. Carbohydrate Polymers. doi:10.1016/j.carbpol.2009.02.021.

2009 Martin, G., Minteer, S. D., and M. J. Cooney✉. *Spatial distribution of malate dehydrogenase in chitosan scaffolds*. Applied Materials & Interfaces. 1(2):367–372

2009 Cooney✉, M. J., Petermann, J., Lau, C., and S. D. Minteer✉. *Fabrication and Characterization of Hydrophobically Modified Chitosan Scaffolds*. Carbohydrate Polymers, 75(3):428-435.

2009 V. Svoboda and B.Y. Liaw✉, "In-situ transient study of polymer nano-film growth via simultaneous correlation of charge, mass, and ellipsometric measurements" *Pure Applied Chem.*, 80 (2008) 2439–2449

2008 Cooney, M. J., Lau, C., Martin, G., Svoboda, V., and. S. D. Minteer✉, *Biofuel Cells*. Energy and Environmental Science. Energy & Environmental Science, 1:320 - 337.

2008 Lau, C., Cooney✉, M. J., and P. Atanassov. *Conductive macroporous composite chitosan-carbon nanotube scaffolds*. Langmuir. *24,* 7004-7010.

2008 Scott, D., Cooney, M. J., Liaw✉, B. Y. *Sustainable current generation from the ammonia-polypyrrole interaction.* Journal of Materials Chemistry. (27),3216-3222.

2008 Sun, D., Cooney, M. J., and B. Y. Liaw✉. *PQQ-glucose dehydrogenase immobilized in chitosan / carbon nanotubes composite films*. Electrochemical Solid State Letters. 11(6) B101-B104.

2008 Svoboda, V., Cooney✉, M. J., Liaw, B. Y., Minteer, S., Piles, E., , Lehnert, D. Barton, S. C., Dmitri Ivnitski, D., and P. Atanassov. *Standardization of a common platform for bioelectrocatalysis characterizations.* Electroanalysis, 20(10):1099 – 1109.

2008 Cooney✉, M. J., Windmesier, M, Lau, C., Liaw, B. Y., Klotzbach, T. and S. Minteer✉. *Design of Chitosan Gel Pore Structure: Towards Enzyme Catalyzed Flow-Through Electrodes*. Journal of Materials Chemistry. **18**, 667 – 674.

2008 Cooney✉, M.J., and B. Y. Liaw✉. *In situ characterization techniques for design and evaluation of micro and nano enzyme-catalyzed power sources.* In (P.S Wang and J. B. Kim Editors) Biomolecular Catalysis: Nanoscale Science and Technology. ACS Symposium Series 986, Oxford University Press.

2007 Atanassov, P., Apblett, C., Banta, S., Brozik, S., Barton, S. C., Cooney, M. J., Liaw, B. Y., Mukerjee, S. and S. Minteer. *Enzymatic Biofuel Cells*. The Electrochemical Society *Interface.*

2007 Svoboda, V., Rippolz, C., Cooney✉, M. J., and Bor Yann Liaw✉ *Characterization of electrochemically polymerized methylene green films on platinum and vitreous carbon supports*. The Journal of Electrochemical Society. 154(3): D113 – D116.

2006 Konash, A., Cooney✉, M. J., Liaw✉, B. Y., Bor Yann Liaw, and D. M. Jameson. Characterization of enzyme-polymer interactions using fluorescence. Journal of Materials Chemistry, (42), 4107-4109.

2006 Johnston, W. J, Cooney✉, M. J., and B. Y. Liaw✉. *In situ measurement of effective diffusion coefficients in enzyme immobilized electrodes.* Enzyme and Microbial Technology. 39:131 – 140.

2005 Johnston, W. J., Liaw, B. Y., Sapra, R., Adams, M. W. W., and M. J. Cooney✉. *Design and characterization of redox enzyme electrodes: new perspectives on established techniques with application to an extremeophilic hydrogenase.* Journal of Enzyme and Microbial Technology. 36(4): 540 – 549.

PRESENTATIONS

2008 Lau, C., Minteer, S. D., and M. J Cooney. *Three dimensional chitosan scaffolds for biofuel cell application.* 214th ECS Meeting, October 12-17, Honolulu HI.

2008 Martin, G. L., Ross, J. A., Jameson, D. M., and M. J. Cooney. Fluorescence characterization of chitosan-fluorophore/enzyme interactions. 7th International Weber Symposium, June 6-12, Kauai, Hawaii.

2008 Lau, C., Cooney, M.J., Atannassov, P. *Three dimensional chitosan carbon nanotube composite material for biofuel cell application.* 213th ECS meeting, May 18-23, Phoenix Arizona.

2008 Cooney, M. J. *Microporous chitosan scaffolds as a material for fabrication of enzyme catalyzed flow through electrodes.* 213th ECS meeting, May 18-23, Phoenix Arizona.

2008 Svoboda, V., Liaw, B. Y., Cooney, M.J., Minteer, S., Atannassov, P. *Structure and Morphology of Electrochemically Grown Poly-Methylene Green Films.* 213th ECS meeting, May 18-23, Phoenix Arizona.

Minteer, S. D., Klotzbach, T, Cooney, M. J., and Liaw, B.Y. *Nanopore Engineering of Chitosan Polymer for Enzyme Immobilization and Stabilization.* November 4 -9, 2007. Salt Lake City, Utah.

Cooney, M. J., Liaw, B.Y., Lau, C., and S. D. Minteer. *Application of Mesopore Engineered Chitosan Polymer for Fabrication of Multi-Dimensional and Multi-Directional Enzyme Catalyzed Electrodes.* November 4 -9, 2007. Salt Lake City, Utah.

Scott, D. Liaw, B.Y., and Cooney, M.J. Improved Current Sustainability from the Ammonia, PPy Interaction with H_2O_2 - One Step Closer to a Urine Fuel Cell. The 212th ECS Meeting, October 7-12, 2007.

Liaw, B.Y., Cooney, M.J., Svoboda, V., Konash, A., Jameson, D.M. *In situ characterization of polymer matrices for bio-electrode applications.* 17th International Symposium on Fine Chemistry and Functional Polymers (FCFP-XVII) & 3rd IUPAC International Symposium on Novel materials and their Synthesis (NMS-III), Shanghai, China, October 18th-20th, 2007.

Svoboda, V., Liaw, B.Y., and Cooney, M.J. *In-situ transient characterization of electrochemical polymerization of methylene green with analysis of stepwise reaction mechanism.* 211th ECS Meeting, Chicago Illinois. May 6-11th, 2007.

Liaw, B. Y, Svoboda, V., Cooney, M. J., and Minteer, S. *Fabrication of an effective biocatalytic electrode with in situ characterization of electrode and its materials.* 211th ECS Meeting, Chicago Illinois. May 6-11th, 2007.

Cooney, M. J., Windmeisser, M., Liaw, B.Y., and Minteer, S. *Design of chitosan gel pore structure: towards enzyme catalyzed electrodes.* 211th ECS Meeting, Chicago Illinois. May 6-11th, 2007.

Konash, A., Cooney, M.J., Liaw, B.Y, and Jameson, D. *Enzyme-polymer interaction study using fluorescence probes.* Symposium on Nano-scale Science and Technology in Biomolecular Catalysis. 232nd ACS National Meeting, San Francisco CA, Sept 10 – 14, 2006.

Svoboda, V., Cooney, M.J., Rippolz, C., and Liaw, B.Y. *Development of an Enzymatic Ethanol Bio-Fuel Cell for Micro-Power Generation.* Fuel Cell Seminar, Honolulu HI, November 13 – 17, 2006.

Cooney, M.J., Svoboda, V., Rippolz, C., and Liaw, B.Y. *Design considerations and characterization of enzymatic ethanol fuel cells.* 209th ECS Meeting, May 7-12, 2006, Denver, CO.

Svoboda, V., Cooney, M.J., Rippolz, C. and Liaw, B.Y. *Design Consideration and In-situ Characterization of Bio-Anode for Enzymatic Ethanol Fuel Cell Application.* IBA –HBC 2006, Waikoloa, Hawaii, 9-12 January 2006.

Cooney, M.J., Svoboda, V., Rippolz, C., and Liaw, B.Y. *Design considerations and characterization of enzymatic ethanol fuel cells.* 209th ECS Meeting, May 7-12, 2006, Denver, CO.

Liaw, B.Y., Quinlan, F., Cooney, M.J. *Polypyrrole Deposition in Aqueous Solutions: Film Characteristic Dependence on Deposition Conditions.* 208th Meeting of the Electrochemical Society. Los Angeles, California. Oct. 16-21, 2005.

Liaw, B.Y., Svoboda, V., Cooney, M.J. *Morphological Study of Conducting Polymer via Electrochemical Deposition Using Imaging Ellipsometry and RQCM Technique.* 208th Meeting of the Electrochemical Society. Los Angeles, California. Oct. 16-21, 2005.

Cooney, M.J., Johnston, W. and Liaw, B.Y. *Modeling the relative contribution of mass transfer limitation on performance in enzyme fuel cells.* 207th Meeting of the Electrochemical Society, Quebec City, Canada. May 15 - May 20, 2005.

Quinlan, F., Cooney, M.J. and Liaw, B.Y. *Investigation of polypyrrole morphology with different deposition conditions.* 207th Meeting of the Electrochemical Society, Quebec City, Canada. May 15 - May 20.

Liaw, B.Y., Cooney, M.J., Quinlan, F., Svoboda, V. and Maynard, N. Engineering Effective Bioelectrocatalysis Electrodes for Power Generation. Second International Conference on Polymer Batteries and Fuel Cells (Fuel Cells). Las Vegas, Nevada from June 12 - June 17, 2005.

Johnston, W.A., Cooney, M.J., and Liaw, B.Y. *Evaluating adsorption and charge transfer of redox enzymes bound to carbon support.* The 204th Meeting of the Electrochemical Society, Inc. July, 2003, Orlando, Florida.

4. Fuel Processing and Purification Studies

The objective of this research is to design and fabricate a lab-scale plasma arc unit for reforming logistic fuels. Following fabrication, preliminary tests of the lab-scale unit will be conducted using gaseous fuels, and applications for logistic fuels will be explored.

4.1 Scope of Work and Approach

The scope of work for the proposed research included:

1. Design, construct, and operate a reverse-vortex-flow reformer that utilizes a non-thermal, gliding-arc plasma to reform methane into hydrogen-rich synthesis gas.
2. Conduct parametric tests to determine the effects of the following independent variables on system performance. Performance is characterized by system indicators such as methane conversion, efficiency, hydrogen yield and selectivity, and specific energy requirements. Items to be included are:
    a. The effects of electrode gap distance within the reverse-vortex flow;
    b. The effects of post reaction chamber fill;
    c. The effects of the reactor exit size on system performance;
    d. The effects of the equivalence ratio of fuel to air input;
    e. The effects of steam input on the system; and
    f. The effects of power input to the system.
3. Design and implement a full factorial experiment to find optimal operating conditions for the reverse-vortex reformer.
4. Determine the parametric effects of volumetric flow through the reformer based on the best conditions identified by the full factorial experiment.

The following sections describe in detail the materials, methodologies, and experimental design utilized in this research. It identifies independent and dependent variables of the reverse-flow-vortex plasma reformer system and how they were expected to affect system performance. It also outlines the parametric test procedure utilized to determine the effects of independent variables on system performance. Finally, a description of the factorial experiment design utilized to find optimal system operating conditions is presented.

4.2 Laboratory Setup and Operation

Figure 4.1 on the following page shows a schematic of the laboratory-scale plasma reformer test bed. The test bed includes three main component groups with different functions. The front end of the system meters reactants and prepares them for input into the reverse-vortex reformer. The reformer section includes the reverse-vortex reformer and power supply, and the back end of the system conditions and analyzes the reformed gas mixture.

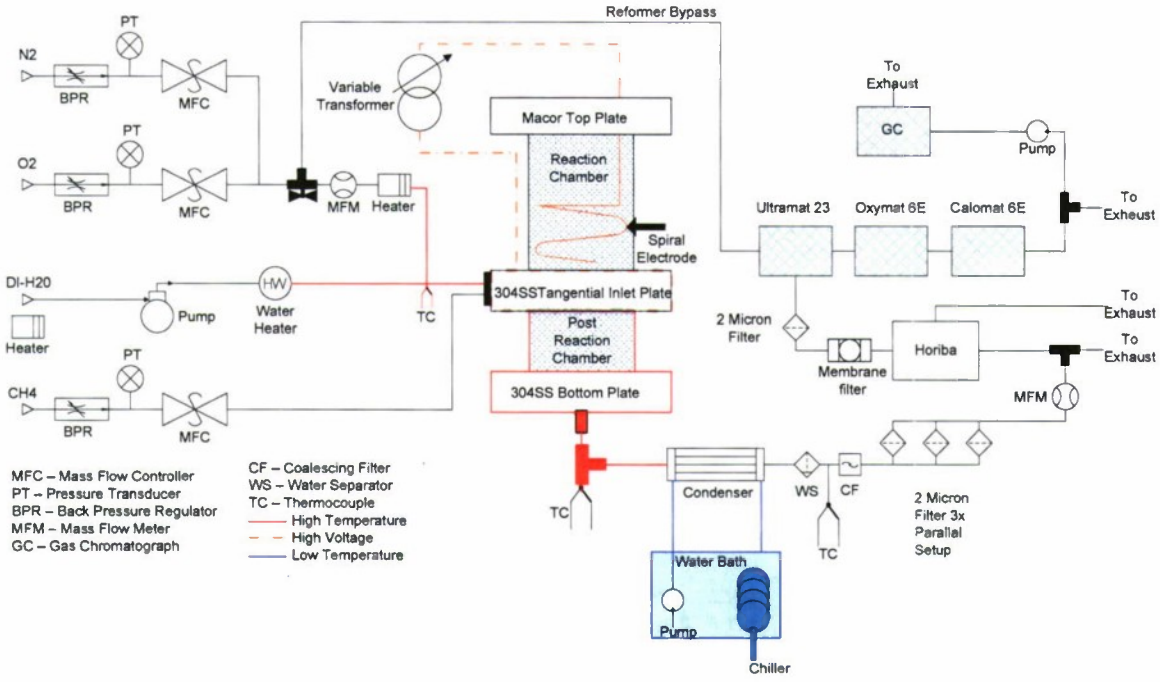

Figure 4.1. Reverse-vortex reformer test bed diagram.

4.2.1 Front End

The front end of the system served to meter reactants into the reverse-vortex reformer. A data acquisition board and LabView software (National Instruments, Austin, TX) running on a laptop computer provided system control and also monitored and recorded data.

A Brooks 5850E mass flow controller metered bottled oxygen and nitrogen to the reformer. The proportions of the two were set to produce a composition very close to air. The air mixture passed through a fabricated resistance heater and mixed with the steam input stream. Heating the air prevented condensation at the point of mixing.

An Eldex 38M 1/8" piston-metering pump capable of delivering 0.01 to 20 ml min^{-1} pushed de-ionized water through a fabricated water heater. A hot plate maintained the de-ionized water reservoir at 50 °C in order to minimize water heater fluctuations downstream. A thermocouple placed at the steam and gas mixing point provided feedback to the data acquisition/control system in order to maintain the mixture at 120 °C. This mixture entered the reverse-vortex-flow reformer via one of two tangential gas inlets. Type 316 stainless steel tubing was used in the front end section of the test bed. A 50 mm length of polytetrafluoroethylene (PTFE) tube was placed between the air/steam delivery components and the 303 stainless steel tangential inlet plate that acted as the reformer's lower electrode. The PTFE tube provided electrical isolation between the two component groups.

A Brooks 5850EM mass flow controller metered bottled grade-4 methane to a second tangential gas inlet in the reformer flange. PTFE tubing provided electric isolation between the methane delivery system and the charged reformer inlet plate.

4.2.2 Reformer Section

The reformer (Figure 4.2) consisted of a top plate, a reaction chamber, an inlet plate, a post reaction chamber, a bottom plate, and upper and lower electrodes. The top plate shown in Figure 4.3 was made from a 101.6 mm x 101.6 mm x 19.1 mm machinable ceramic plate(Macor® Corning Inc., Corning, NY), formed the top of the reaction chamber, and held the upper electrode in place. Macor® is rated for a continuous temperature of 800 °C and a peak temperature of 1,000 °C. It has a low coefficient of thermal expansion, has zero porosity, and will not deform. Initially, all plates were fabricated from Macor®; however, expansion of the quartz tube inserted into the plates caused them to crack. Cracks were also produced by stainless steel NPT fittings threaded into the Macor® at the reactant gas inlets. Thus, as a precaution, aluminum brackets secured by stainless steel threaded rod keep the top plate in constant compression. Stainless steel fabrication of the inlet and bottom plate allowed for stainless steel connections to the rest of the system. A silicon o-ring, set into a groove, provided the seal between the quartz reaction chamber and the Macor® top plate. The reaction chamber was a quartz tube with a length of 100 mm, an outer diameter of 45 mm, and an inner diameter of 42 mm.

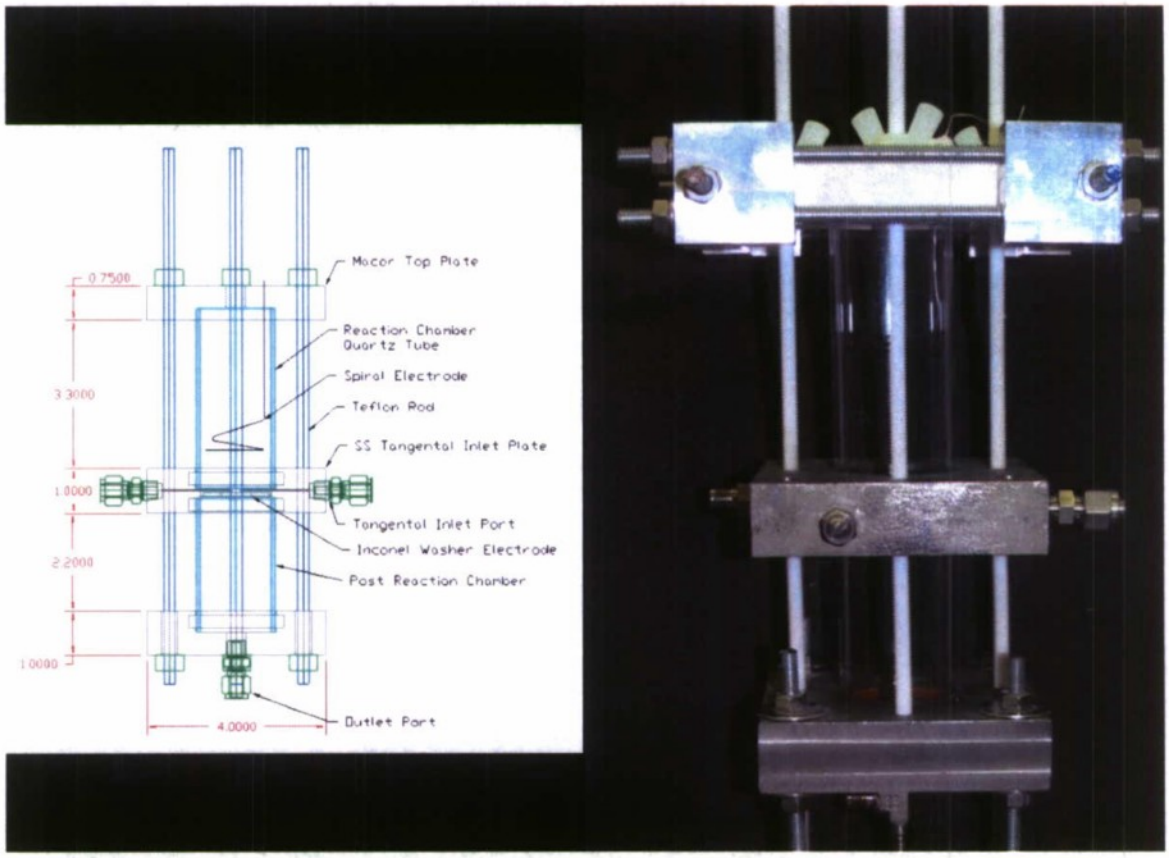

Figure 4.2. Full reformer schematic (dimensions in inches).

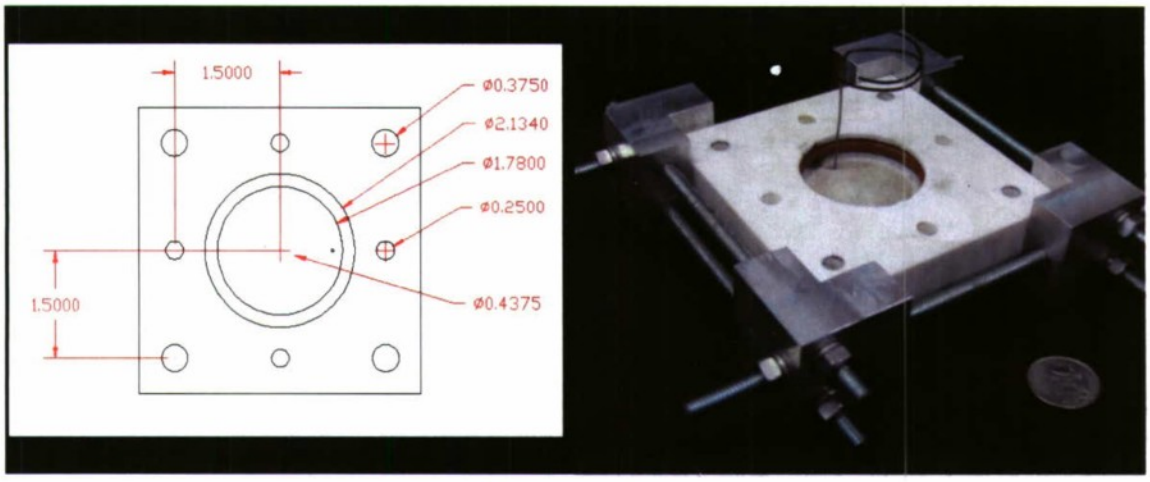

Figure 4.3. Macor® top plate (dimensions in inches).

The 101.6 mm x 101.6 mm x 25.4 mm inlet plate (Figure 4.4), fabricated from 303 stainless steel, served many purposes. Two tangential reactant gas inlets created a reverse-vortex flow path in the reaction chamber. Gas delivery tubing was connected to the plate by 1/8" (3 mm) NPT Swagelok connections. The diameters of the inlets reduced to1.066 mm at the inlet to the reaction chamber. A total reactant gas flow of 2.6 lpm entered the reaction chamber at a velocity of 48 m s^{-1}, but expanded its flow path and slowed upon entry. The resulting flow field caused the arc formed between the Inconel, ring/spiral-type, top electrode and the Inconel bottom electrode to revolve in the reaction chamber. The top electrode had an outer diameter of 38 mm and was made from 1.07 mm diameter Inconel wire. The entire middle inlet plate conducted electricity from the transformer line to the washer electrode. The Inconel washer had an outer diameter of 38 mm, and its inner diameter ranged from 3.4 to 17.4 mm. The washer could be changed in order to change the axial exit diameter and the flow field within the chamber. Inconel was chosen as the material for the electrodes due to its ability to withstand high temperatures and oxidation. Silicone o-rings sealed the interfaces between the inlet plate and quartz tubes of the reaction and post reaction chambers.

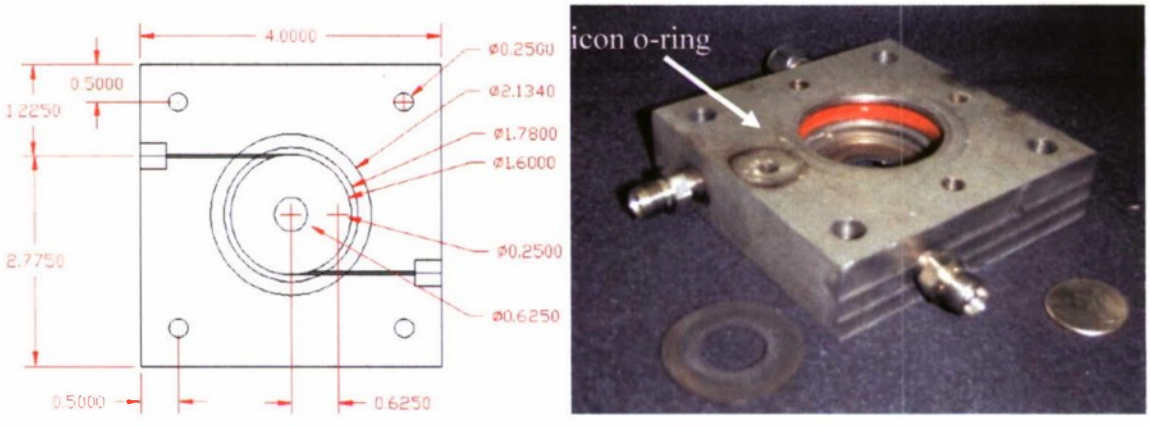

Figure 4.4. 303 Stainless steel inlet plate (dimensions in inches).

The 101.6 mm x 101.6 mm x 25.4 mm, 303 stainless steel bottom plate (Figure 4.5) connected to the quartz tube of the post reaction chamber with the same type of o-ring seal used elsewhere in the system. The bottom plate served as the connection point for the back end of the system. The quartz tube, post reaction chamber served as a mixing zone for the treated gases and electrically isolated the middle plate from the bottom plate and the back end of the system. The tube was 77 mm long with an outer diameter of 45 mm and an inner diameter of 42 mm. The post reaction chamber had thermal insulation (not pictured) around it. Non-conducting PTFE threaded rods held the entire assembly together.

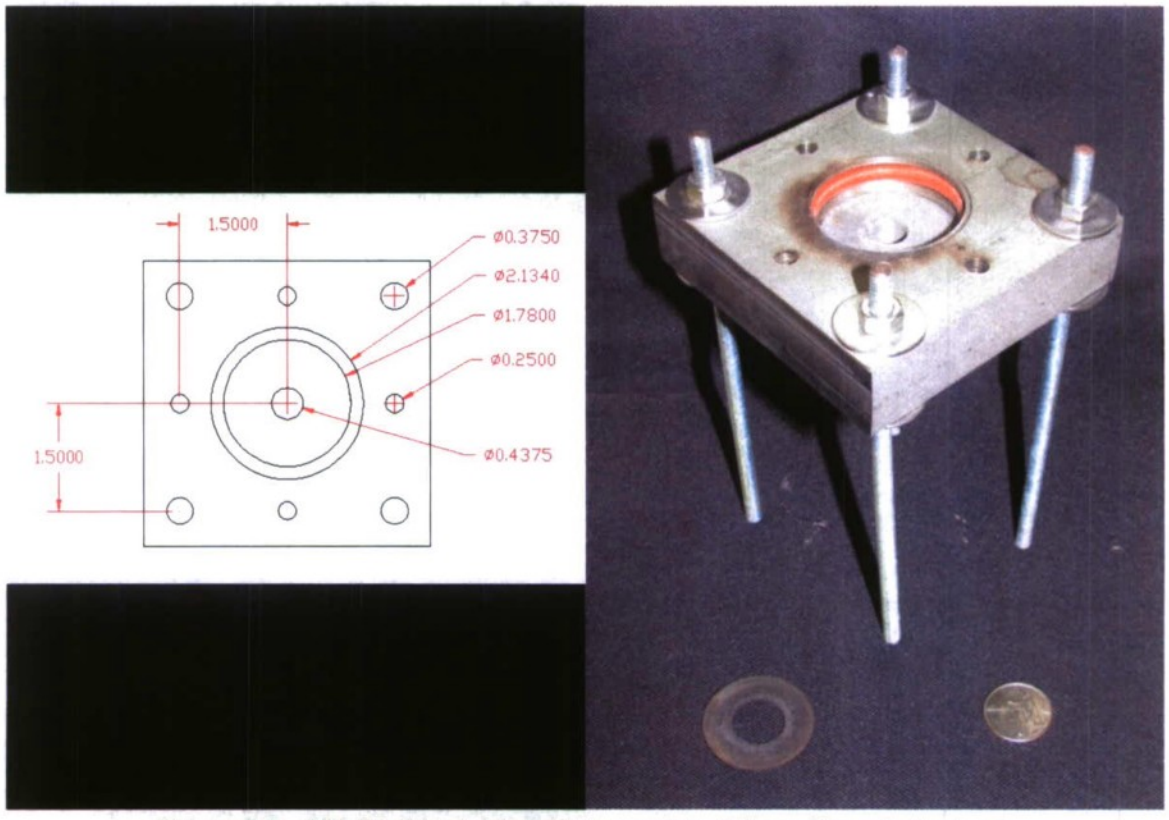

Figure 4.5. 303 Stainless steel bottom plate (dimensions in inches).

The system's power supply used two major components; a neon sign transformer (Lecip Sentry, model 4B15N6-CB, Allanson International, Toronto) and a variable autotransformer (Staco, model 3PN1410B, ISE Inc., Cleveland). The neon sign transformer stepped up the incoming AC voltage 125 times and could provide 250 W at 15 kV when operating at maximum output. The variable autotransformer controlled the incoming voltage to the Sentry transformer and could vary a line voltage of 120 V, 60 Hz over a range of 0 to 140 V. The autotransformer did not have a digital control input; thus, the operator manually adjusted the voltage output. As the arc was a fixed length between the upper and lower electrodes, the power consumed by the arc remained constant over time. A meter (Kill A Watt™, Model p4460) placed inline measured the power from the variable autotransformer to the Sentry transformer. Insulated, high-voltage wires carried the charge from the transformer to the middle plate and upper electrode.

4.2.3 Back End

The back end of the system conditioned the product stream to permit determination of flow rate and composition. Reformate exited the reformer at temperatures on the order of 250 °C and the saturated, hot gases could easily destroy mass flow meters. The reformate left the reactor and passed through a water condenser (Fisher, Pyrex Graham 300 mm) with a water jacket cooled by an external immersion chiller (VWR Scientific, Model 1109). The reformate then passed through a water separator to capture liquid water, further reduce the temperature, and condense any remaining vapor. After this point the reformate temperature was on the order of 26 °C. The reformate flow then proceeded through a coalescing filter (Balston, Model 31G) to remove any remaining water. Finally the gas passed through a parallel array of three 2 μm pore size filters (Swagelok SS-4F-2). A calibrated mass flow meter (Omega, Model FMA1820S) determined the volumetric flow of the reformate prior to analysis.

A sampling unit (Horiba, model PS-200) pulled 2.6 lpm of reformate from the gas stream and removed any remaining vapor. The treated flow then passed through a membrane filter (United Filtration Systems, model SM105.221) and an additional 2 μm pore size filter (Swagelok, model SS-4F-2). Sample flow passed through three on-line gas analyzers in series: (1) a non-dispersive, infrared analyzer (Siemens, model Ultramat 23) measured the volume percentage of methane, carbon monoxide, and carbon dioxide, (2) a zircon dioxide based sensor in the second analyzer (Siemens, model Oxymat 6E) measured the oxygen content, and (3) a thermal conductivity based measurement was made in the final analyzer (Siemens, model Calomat 6E) for hydrogen content. All of the analyzers were networked via an ELAN interface in order to calibrate each and account for interfering gas species.

A pump (Air Dimensions 1/6 hp) pulled a 2 lpm stream from the flow exiting the online analyzers and directed it to the gas chromatograph (GC) equipped with a 6-port injector valve . The pump started 2 min after the GC sampled and ran for 6.5 min, allowing 1.5 min of the 10 min cycle to permit the gas pressure in the sample valve to equilibrate with atmospheric pressure. This ensured that the GC would receive samples of repeatable volume and pressure.

Composition of the reformate was analyzed with a Shimadzu 14A gas chromatograph (Shimadzu, Columbia, MD) equipped with a 1.52 m x 3 mm Carboxen™ 1000 column (SUPELCO, Bellefonte, PA) and a thermal conductivity detector. The GC oven initial temperature of 80 °C was ramped to 150 °C at 30 °C min^{-1} and then to 210 °C at 20 °C min^{-1}. On reaching 210 °C it returned to 80 °C in preparation for the next analysis. Tests were run according to American Society for Testing and Materials (ASTM) Standard D1946-90 – Standard Practice for Analysis of Reformed Gas by Gas Chromatography. Analyses with an initial oven temperature of 80 °C produced the same results as those conducted with the ASTM recommended 45 °C. The higher initial temperature resulted in an analysis time on the order of 10 minutes per sample. The GC was calibrated with a gas standard containing 32.65% H_2, 23.81% CO_2, 12.87% CO, 5.45% CH_4, 1.98% C_2H_4, 1.48% C_2H_6, 1.48% C_2H_2, and a balance of nitrogen. The GC produced a chromatogram and integration of the area under the curve for each of the detected gas components was proportional to the percentage of the corresponding species in the reformate.

4.2.4 Start Up

Before every test the GC and the gas analyzers were turned on and allowed to warm up. Carrier gas was flowed to the GC before the unit was turned on and then the heated zones and thermal conductivity detector were energized. The oven temperature was set to 120 °C and allowed to warm up for at least an hour after which it was reduced to 80 °C and allowed to come to equilibrium. Three blank runs were then performed. At this point, calibration gas was directed through the analyzers at 2.4 lpm and sampled twice by the GC. Calibration of the GC and the analyzers was performed and the percent compositions of the gasses were recorded.

Nitrogen was supplied to the Oxymat 6E analyzer at 350 kPa and was directed to the two remaining analyzers at 1 lpm, atmospheric pressure. At initial power up, the Ultramat 23 analyzer self calibrated with the flowing nitrogen.

The condenser's water pump and chiller were turned on at least an hour before the reformer began to operate, allowing the temperature of the cold water bath to reach steady state.

4.3 Testing Activities and Rationale

4.3.1 Parametric Tests

A parametric test was conducted for each independent variable – one variable was systematically changed while holding all other variables constant at their base case values. Independent variables and their base case values for parametric tests are shown in Table 4.1. Parametric tests helped determine how a single variable affected system performance. They did not show second order effects, nor were they employed to find optimal operating conditions. Parametric tests revealed aspects of system geometry that played vital roles in reformer performance.

Table 4.1. Independent variables, base case values, & value ranges for parametric tests.

Variable	Base case	Range of values for parametric test
Reactor Chamber	0.095 L	fixed
Electrode Gap Distance	25 mm	10 mm to maximum achievable arc length
Post Reaction Chamber	empty	Empty, non-reactive fill, catalytic fill
Axial Exit Size	12.5 mm	6.35 mm, 9.5 mm, 12.7 mm
Oxygen Input	0.56 slpm	fixed
Nitrogen Input	2 slpm	fixed
Methane Input	1 slpm	0.4 - 1.24 slpm
Power Input	200 W	150 – 350 W
Steam Input (as liquid)	1.6 g min^{-1}	0.4 – 2.4 g min^{-1}

4.3.2 Factorial Design

A full factorial experiment explored the effects of four independent variables – methane input, steam input, power input, and gap distance. Due to the strong correlation observed between the gap distance and power input during preliminary testing, the gap distance was included in this design. Each independent variable was assigned a high and low level based around a center point leading to 16 total points per factorial test. During the experiments, a stable condition was maintained at each operating point until a minimum of four gas samples were analyzed via gas

chromatography (GC). This provided sufficient data to calculate a mean and standard deviation at each point. The four-factor factorial design allowed for the determination of optimum values of the four independent variables, estimated the effects of each variable, and identified interactions or higher order effects between variables.

The center point and corresponding step sizes for the first factorial test, shown in Table 4.2, were based on data from the literature and from results of the parametric tests. Test results from the factorial design allowed for the calculation of a path of steepest ascent in the factor space.

Table 4.2. Base case for first factorial design with corresponding step sizes.

Variables	center point	step size	units
Gap Distance	30	2.5	mm
Steam Input	0.8	0.2	ml / min
Methane Input	0.8	0.1	lpm
Power Input	200	10	W

4.3.3 Data Reduction

Calculation of performance indicators from data collected is defined below.

Hydrogen yield is defined by the number of hydrogen atoms in the reformate hydrogen gas divided by the total amount of feed gas hydrogen atoms, as shown in equation (1).

$$Hydrogen\ Yield = \frac{Hydrogen\ Atoms\ in\ H_2\ in\ reformate}{Hydrogen\ Atoms\ in\ Feed\ Gas} * 100 \qquad (\%) \qquad (1)$$

Selectivity (equation (2)) is based on the number of hydrogen atoms in the hydrogen gas of the reformate divided by the total number of hydrogen atoms in the reformate gas. An alternative description of hydrogen selectivity is the hydrogen yield divided by the methane conversion as shown in equation (3). This provides an index of the system's ability to reform methane into hydrogen, with the assumption that any unconverted methane could be recovered or utilized by other processes. For the purposes of this work, the definition of selectivity in equation (3) will be utilized. Hydrogen atoms in steam are not included in calculations of hydrogen yield or selectivity.

$$Selectivity\ of\ Hydrogen = \frac{Number\ of\ H\ atoms\ in\ H_2\ in\ reformate}{Number\ of\ H\ atoms\ in\ reformate} * 100 \qquad (\%) \quad (2)$$

$$Selectivity = \frac{moles\ of\ H_2\ produced}{2(moles\ of\ CH_4\ converted)} * 100 \qquad (\%) \qquad (3)$$

Equation (4) describes the efficiency of the system as the amount of energy in the hydrogen in the reformate divided by the total system energy input from both the plasma and the feed fuel. The lower heating value (LHV) is the heat of combustion measured in MJ kg^{-1}, with the resulting water products in the vapor phase. The LHV is multiplied by the mass flow rate of the given species in order to find the power associated with the gas flow. The efficiency definition

assumes that any CO present in the reformate can be converted to H_2 by the water gas shift reaction.

$$Efficiency\ \eta = \frac{LHV_{H_{2gas}} * (\dot{m}_{H_2} + \dot{m}_{CO})_{reformate}}{Plasma\ Power + LHV_{CH_4\ input} * \dot{m}_{CH_4\ input}} * 100 \qquad (\%) \qquad (4)$$

The specific energy requirement (SER) is defined as the amount of plasma energy used to produce one mole of hydrogen, as seen in Equation (5). Here the input power is measured in kW, and $\dot{n}$ is the molar flow rate. Again the assumption is made that carbon monoxide can later be shifted to produce more hydrogen.

$$SER = \frac{Input\ Power}{(\dot{n}_{CO} + \dot{n}_{H_2})_{produced}} \qquad (kJ\ mol^{-1}\ H_2\ produced) \qquad (5)$$

Lastly, methane conversion is the amount of hydrogen converted divided by the total methane input to the system, as seen in equation (6).

$$Methane\ Conversion = \frac{\dot{m}_{CH_4\ in\ fuel} - \dot{m}_{CH_4\ in\ reformate}}{\dot{m}_{CH_4\ in\ fuel}} * 100 \qquad (\%) \qquad (6)$$

4.4 Technical Accomplishments

This section presents results of the parametric and factorial testing of the reverse-vortex-flow reformer.

4.4.1 Parametric Tests

Parametric tests show the system response to the alteration of one independent variable while holding the others constant. Parametric tests are not designed to find optimal operating conditions or second order effects; rather, they determine the effects of an independent variable on the system and help establish a base case to begin factorial tests. The first set of parametric experiments explored the effects of power input, methane input, steam input, orifice diameter, the presence of catalyst in the post reaction chamber, and electrode gap distance.

4.4.1.1 Gap Distance

As stated in literature, increasing the gap distance increases both the non-thermal properties of the arc and the residence time of the gas within the arc. If the gap distance is too small the arc exists in a thermal regime leading to poor performance. If the gap is too large the arc cannot sustain itself in a non-thermal regime. The maximum arc length also depends on the power supply rating. The gap distance parametric tests were conducted at two different power levels, 160 W and 200 W, to identify stable arc conditions. Other independent variables held constant are shown in Table 4.3.

Table 4.3. Values for independent variables held constant during gap distance parametric tests.

Constant Variable	Input
Methane (slpm):	1
Oxygen (slpm):	0.56
Nitrogen (slpm):	2
Steam (ml/min):	1.6
Power (W):	160 & 200
Orifice Diameter (mm):	17.4
Post Reaction Chamber Fill:	none

Initially the power level was set to 160 W and the gap distance was increased in 5 mm increments from 10 to 30 mm, the latter identifying the point at which the arc could no longer be sustained. Temperature measured at the reformer exit was allowed to reach equilibrium and then five GC measurements of the reformate composition were recorded over the next 50 minutes for each data point. Additionally, the power was set to 200 W and the tests repeated, increasing the gap distance incrementally by 5 mm. Due to the dielectric strength of the medium, the arc could not consume 200 W of power at a gap distance of 10 mm, reaching a maximum of ~185 W. The first point with 200 W input was recorded at 15 mm. This process was continued through a gap of 40 mm at which point the arc could no longer be sustained.

As shown in Figure 4.6, increasing the gap distance resulted in an improvement of all indicators of system performance except for selectivity. This could be due to a more non-thermal plasma, additional residence time of the gases within the arc, or a combination of the two. The increased gap distance seems to have had the strongest effect on methane conversion. Methane conversion increased linearly from 50.1 to 71.4% over a range of gap distances from 15 to 40 mm with arc power of 200 W. At 160 W this linear trend was not as evident as methane conversion increased from 29.0 to 52.6% as the gap distance increased from 10 to 20 mm and then increased at a rate similar to the 200 W case up to a gap distance of 30 mm. The efficiency increased linearly and the 160 W and 200 W cases paralleled each other with the latter higher by nearly 3%. At 200 W, the efficiency increased from 22.7 to 30.5% over the 15 to 40 mm gap distance span. Hydrogen yield increased with increasing gap distance for both the 160 and 200 W tests, with the 200 W case higher than the 160 W case by 6% over the range of gap distances. With 200 W input, the hydrogen yield increased from 35.5 to 47.2% over the range of gaps explored. Specific energy requirements also paralleled each other between the two power input cases with the 160 W tests having a lower SER. At 200 W, the SER decreased rapidly from 271 to 228 kJ mol^{-1} H_2 over the range of gap distances from 15 to 25 mm. At greater gap distance, SER decreased less rapidly, reaching a value of 198 kJ mol^{-1} H_2 at 40 mm.

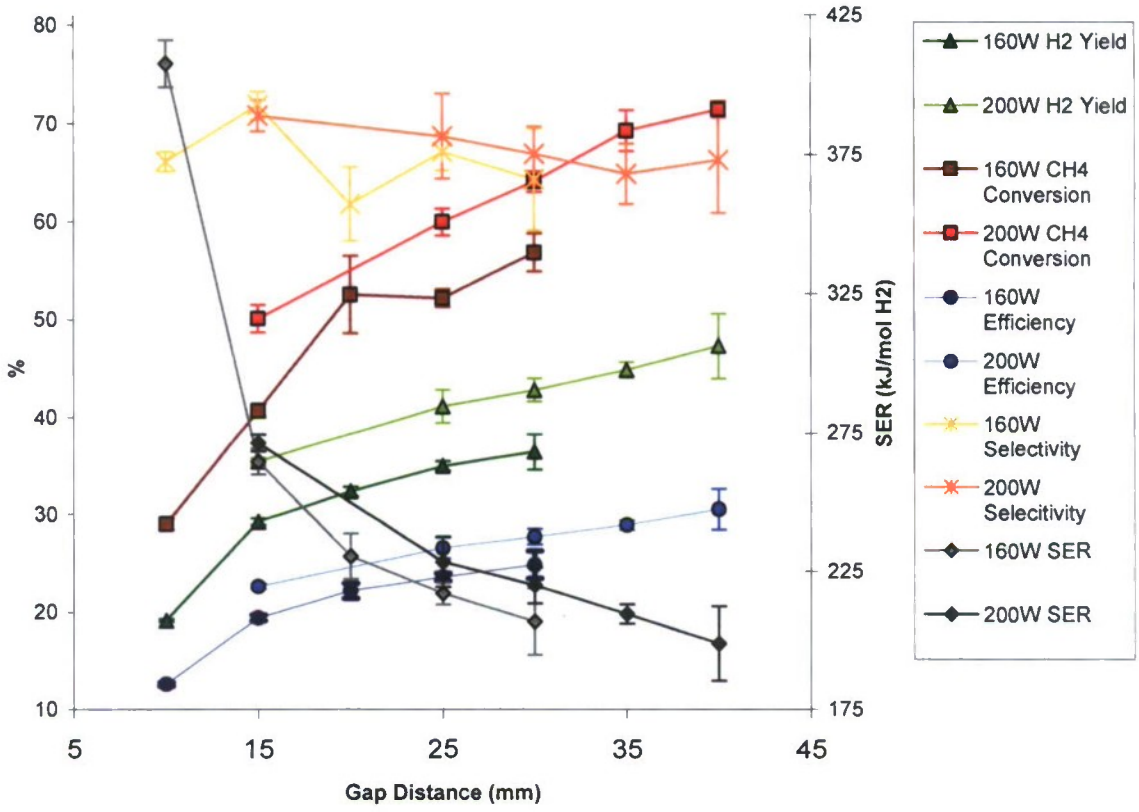

Figure 4.6. Effects of gap distance on reactor performance parameters; H_2 yield, CH_4 conversion, efficiency, and specific energy requirement. Error bars indicate one standard deviation.

As stated earlier, increasing the gap distance generally increased the performance of the reformer; however, at some point, the arc became unstable. With a gap of 40 mm and power input of 200 W the arc was very unstable and extinguished after about 20 minutes. Efforts to reestablish the arc at 40 mm were unsuccessful. At a gap distance of 35 mm and a power input of 200 W the arc was stable for nearly an hour before extinguishing. Efforts to reestablish the arc at 35 mm were also unsuccessful.

A total gap distance of at least 5 mm was required between adjacent points in order to be able to produce significant differences in the performance indices. A step size of 2.5 mm was utilized for the factorial design yielding a difference of 5 mm between high and low levels. A gap of 25 mm was utilized for the base case in the first factorial design. This allowed for the full factor space around the base case to be explored and a path of steepest ascent to be determined without operating at any potentially unstable points. As the gap distance increased in subsequent tests, a point was reached where the arc was no longer stable; however, this was much larger than the parametric tests predicted as the power increasing in tandem, allowed for larger gaps.

4.4.1.2 Steam Input

Steam was added as a reactant gas to prevent the system from developing coking problems. However, the steam absorbed energy for ionization reducing the energy available for the

methane conversion reaction. Table 4.4 lists the independent variables held constant during the steam input parametric tests. As seen in Figure 4.7, the steam had a significant negative impact on the performance of the system.

Table 4.4. Values for independent variables held constant during steam input parametric tests.

Constant Variable	Input
Methane (slpm):	1
Oxygen (slpm):	0.56
Nitrogen (slpm):	2
Gap Distance (mm):	30
Power (W):	200
Orifice Diameter (mm):	17.4
Post Reaction Chamber Fill:	none

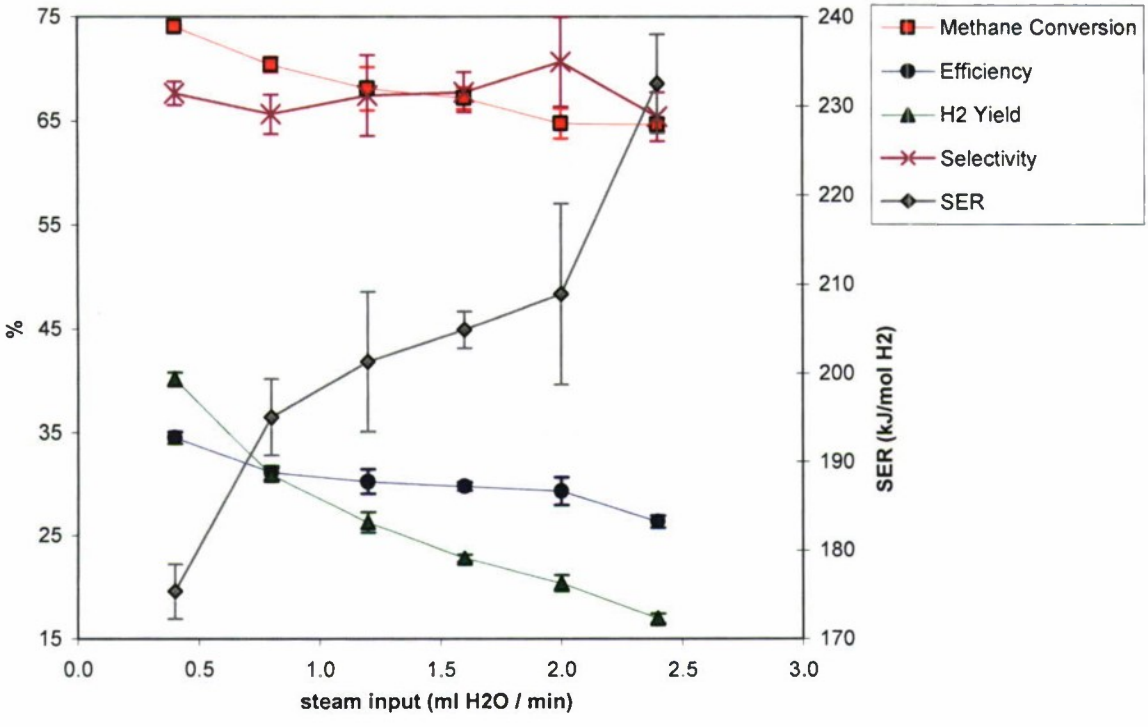

Figure 4.7. Effects of steam input on reactor performance parameters; H_2 yield, CH_4 conversion, efficiency, and specific energy requirements. Error bars indicate one standard deviation.

As steam was added to the system it began to have negative effects on all system performance indicators. From 0.4 to 0.8 ml min^{-1} of input, the negative impact of the steam input was clearly evident. SER increased from 175 to 195 kJ mol^{-1} H_2, efficiency dropped from 34.5 to 30.1%, and hydrogen yield dropped from 40.1 to 30.9%. At greater steam input, the hydrogen yield decreased fairly linearly from 30.9 to 17.0% at 2.4 ml min^{-1} input. Specific energy requirements trended upwards; however, a large error associated with the points made the differences between adjacent points uncertain. Regardless, between 2.0 and 2.4 ml min^{-1} of input the SER increased from 208 to 232 kJ mol^{-1} H_2. From 0.8 to 2.0 ml min^{-1} the efficiency trended downwards slowly with adjacent points having overlapping error bars, and then dropped significantly from 2.0 to

2.4 ml min^{-1} from 29.3 to 26.4%. The methane conversion decreased at a linear rate from 71.4 to 64.8% as steam input increased from 0.4 to 2.0 ml min^{-1} and then leveled off at 64.7% conversion at 2.4 ml min^{-1}. Selectivity varied between 65.6% and 70.6% across the range of steam input with no obvious trends.

The ideal set of system operating conditions included just enough steam in order to thwart any coking problems, while affecting the performance of the system as little as possible. A steam flow rate of 0.8 ml min^{-1} was selected for the base case of the first factorial tests. At this condition there was adequate steam for the elimination of coke formation and limited performance degradation in efficiency, SER, and methane conversion. A step size of 0.2 ml min^{-1} was selected because it provided clear differences in performance indices.

4.4.1.3 Methane Input

In order to change the oxygen to fuel ratio and maintain the correct air composition, the methane input was varied from 0.4 to 1.2 lpm (equivalence ratios of 0.23 to 0.7) while holding the oxygen flow rate constant. Table 4.5 shows the values for the other independent variables and Figure 4.8 shows the results of the methane input parametric tests.

Table 4.5. Values for independent variables held constant during methane input parametric tests.

Constant Variable	Input
Gap Distance (mm):	30
Nitrogen (slpm):	2
Orifice Diameter (mm):	17.4
Oxygen (slpm):	0.56
Post Reaction Chamber Fill:	none
Power (W):	200
Steam Input (ml/min)	1.6

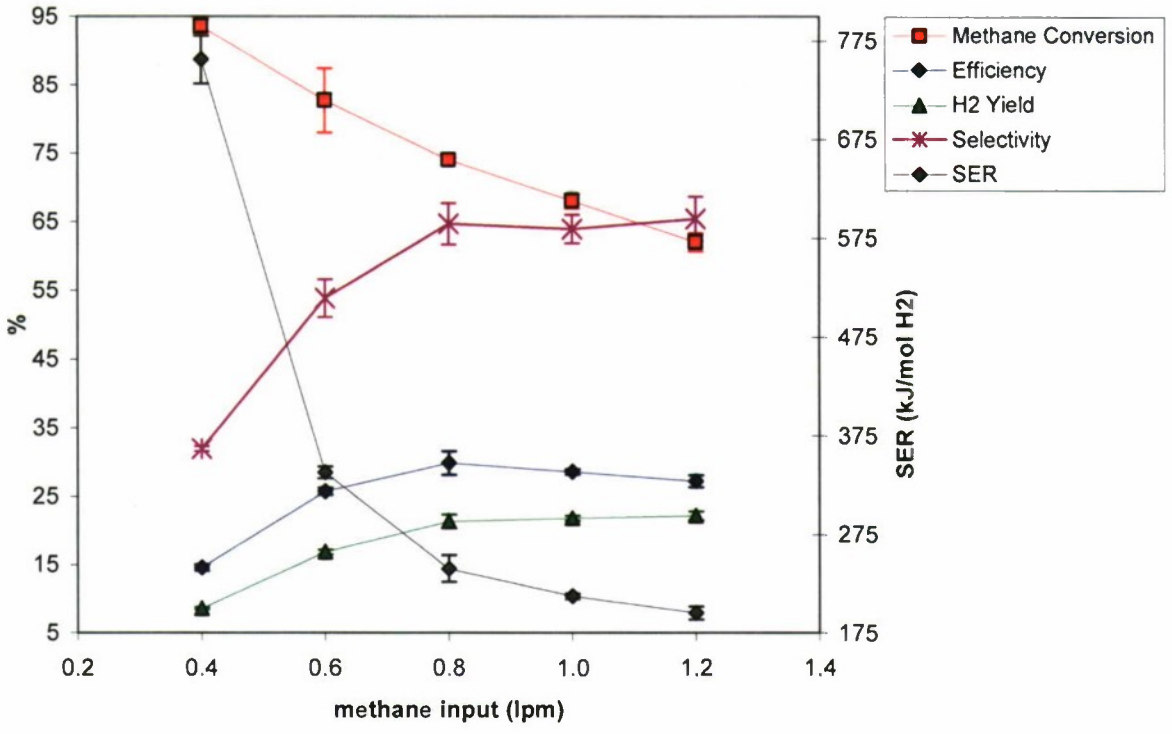

Figure 4.8. Effects of methane input on reactor performance parameters; H_2 yield, CH_4 conversion, efficiency, and specific energy requirements. Error bars indicate one standard deviation.

Methane conversion was most drastically affected by methane input to the system. At a methane input of 0.4 lpm, 95% methane conversion was achieved. This dropped at a fairly linear rate to 62% conversion at 1.20 lpm. Specific energy requirements improved significantly from 760 to 340 kJ mol^{-1} H_2 as the methane flow rate decreased from 0.4 to 0.6 lpm. This was the largest change, but the decreasing SER trend continued over the range of methane flow rates, reaching a low point of 194 kJ mol^{-1} H_2. The improvement in SER was largely due to the hydrogen yield, which increased with little curvature from 8.1 to 21.4% between 0.4 and 0.8 lpm of methane flow. As methane input increased from 0.8 to 1.2 lpm, hydrogen yield increased to 22.2%, suggesting that there was no definite change in performance after 0.8 lpm.

Efficiency also increased from 14.6% to a maximum of 29.9% between inputs of 0.4 and 0.8 lpm. From there it decreased to 27.2% at a flow rate of 1.2 lpm. The selectivity also increased rapidly from 32 to 64.7% as the methane flow rate increased from 0.4 to 0.8 lpm. Selectivity remained constant at ~65% at higher methane flow rates of the test range.

Therefore, a methane flow rate of 0.8 lpm with a step size of 0.2 lpm was chosen as the center point for the factorial design. This allowed for an acceptable methane conversion of around 74%, while maintaining a high efficiency for the system.

4.4.1.4 Orifice Size

The axial exit of the reforming chamber must be significantly smaller than the diameter of the chamber in order to produce the reverse-vortex flow. The arc forms between the upper spiral electrode and the inner edge of the axial exit and can remain there indefinitely. It was assumed that by decreasing the orifice size of the axial exit, the plasma would rotate in a tighter circle at the outlet and effectively fill a larger volume; however, there have been no published results showing the effects of the orifice size. As such, five different orifice sizes ranging from 3.2 to 17.4 mm were used for the parametric tests. These orifices had an orifice diameter to reaction chamber diameter ratio of 7.62 to 41.42%. Table 4.6 shows the values for the independent variables that were held constant, and Figure 4.9 shows the effects of the orifice diameter on the performance of the system.

Table 4.6. Values for independent variables held constant during orifice diameter parametric tests.

Constant Variable	Input
Gap Distance (mm):	30
Methane (SLPM:)	1
Nitrogen (SLPM):	2
Oxygen (SLPM):	0.56
Post Reaction Chamber Fill:	none
Power (W):	200
Steam Input(ml/min)	1.6

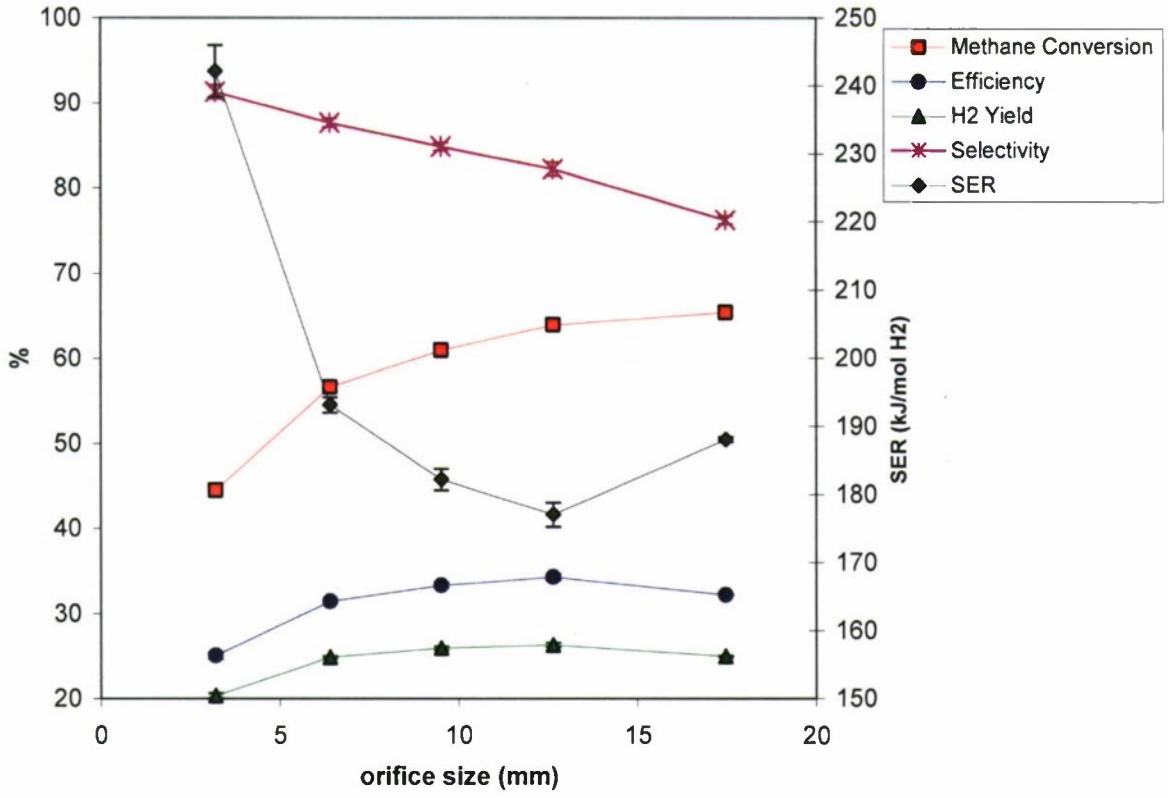

Figure 4.9. Effects of orifice size on reactor performance parameters; H_2 yield, CH_4 conversion, efficiency, and specific energy requirements. Error bars indicate one standard deviation.

Orifice size had significant effects on methane conversion, efficiency, H_2 yield, selectivity and specific energy requirements. The smallest orifice size had the poorest performance for all performance parameters except selectivity. Methane conversion was the most sensitive metric to orifice size. Methane conversion continually increased (44.5 to 65.4%) over the range of orifice sizes (3.2 to 17.4 mm), albeit with diminishing returns.

SER decreased 20% from 242 to 193 kJ mol^{-1} H_2 when the orifice size was increased from of 3.2 to 6.4 mm. SER decreased more slowly as the orifice size increased from 6.4 to 12.65 mm and reached a minimum value of 177 kJ mol^{-1} H_2 at the latter value. SER increased to 188 kJ mol^{-1} H_2 at 17.4 mm.

Efficiency and H_2 yield followed similar trends – both increased with diminishing returns for orifice sizes from 3.2 to 12.65 mm, attaining a maximum value with the 12.65 mm orifice, and then dropping off with an orifice of 17.4 mm. Efficiency increased from 25% at an orifice size of 3.2 mm to 34% at 12.65 mm. Likewise H_2 yield increased from a minimum of 20.4% at 3.2 mm to a maximum of 26.3% at 12.65 mm.

The selectivity dropped fairly linearly from 91.3 to 76.2% over an orifice size range from 3.2 to 17.4 mm. This is because the increases in methane conversion realized with increasing orifice diameter did not produce proportional increases in hydrogen yield. The best efficiency,

hydrogen yield, and SER were observed at an orifice diameter of 12.65 mm and this size was used throughout the factorial design.

Figure 4.10 shows the arc in a nitrogen flow field, connecting to the electrode. The pictures show a 10 s. exposure for each frame.

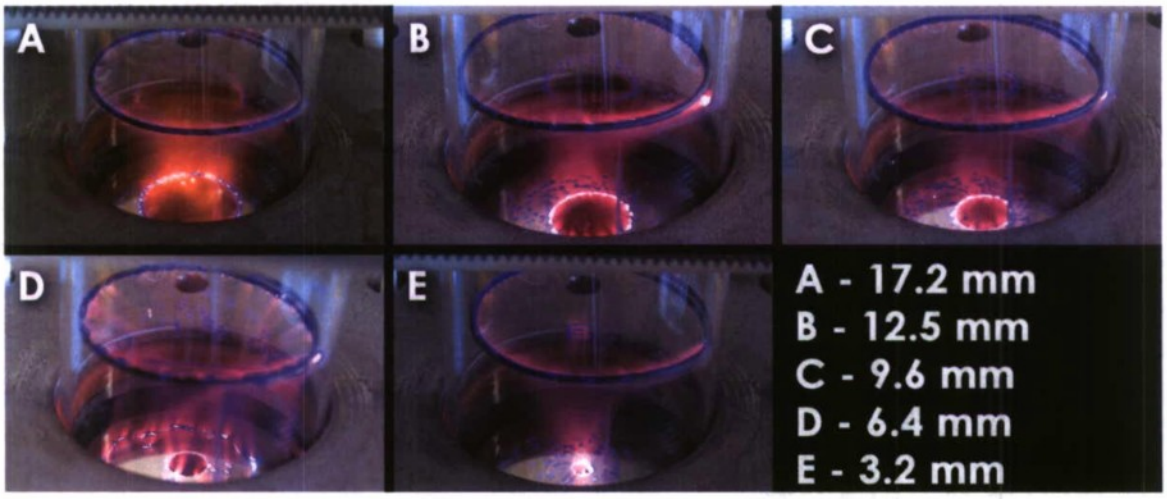

Figure 4.10. Orifice size effects on arc connection in nitrogen at 200 W.

4.4.1.5 Power Input

Initial tests showed that power input to the system drastically affected the reforming of methane. Power input to the system was dependent on both the maximum power output of the power supply as well as the composition of the gas in the reformer. For example, at standard operating conditions for the parametric tests shown in Table 4.7, with the variable autotransformer providing maximum power, and only nitrogen flowing, the system would draw 200 W of power. When the oxygen, steam, and methane were added, 250 W of power was required to overcome the increased dielectric breakdown of the working medium. Parametric tests explored the effects of varying the power input to the system from 175 to 250 W in 25 W increments as shown in Figure 4.11.

Table 4.7. Values for independent variables held constant during power input parametric tests.

Constant Variable	Input
Gap Distance (mm):	30
Methane (slpm):	1
Nitrogen (slpm):	2
Orifice Size Diameter (mm)	17.4
Oxygen (slpm):	0.56
Post Reaction Chamber Fill:	none
Steam Input(ml/min)	1.6

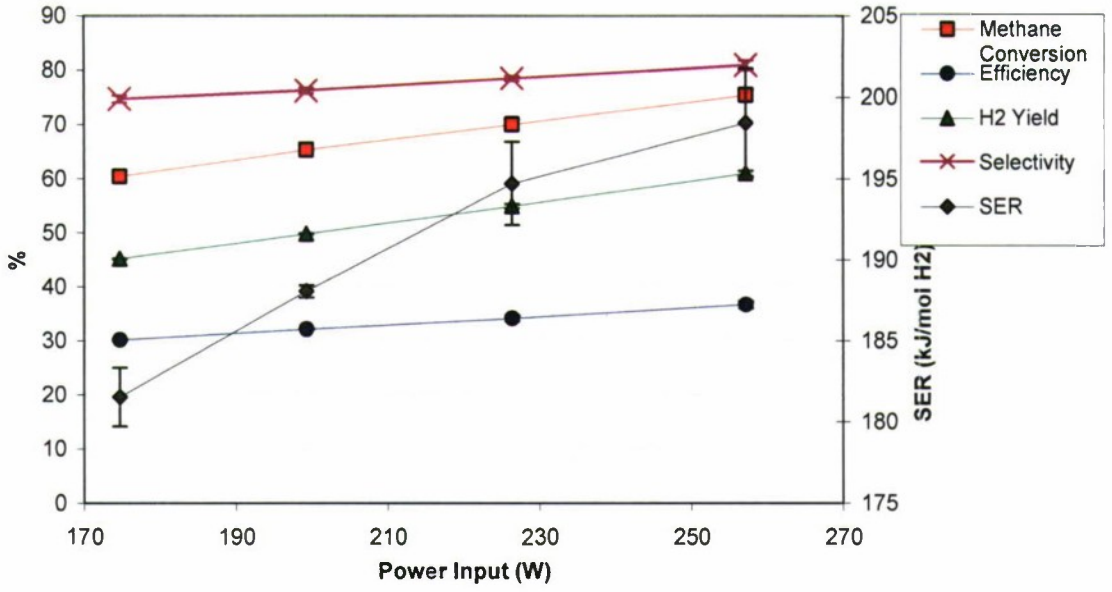

Figure 4.11. Effects of power input on reactor performance parameters; H_2 yield, CH_4 conversion, efficiency, and specific energy requirements. Error bars indicate one standard deviation.

Increasing power from 175 to 257 W increased the methane conversion linearly from 60.5 to 75.4%. Likewise, efficiency increased linearly from 30.2 to 36.7% over the same range. Hydrogen yield also increased linearly from 45 to 61% as power increased from 175 to 257 W. Selectivity showed the same trend increasing linearly from 74.7 to 80.7%. These performance increases came at the cost of specific energy requirements. The SER increased linearly from 177.5 to 194.7 kJ mol^{-1} H_2 over a power range from 175 to 225 W. A further increase to 198.4 kJ mol^{-1} H_2 was observed with a power input of 257 W; however, the errors associated with the SER values at the two higher power set points do not indicate that the increase was significant.

Based on the parametric results, the factorial tests utilized a center point of 200 W with a step size of 10 W. This range of power input allowed for a gap distance of 25 mm to be used and produced significant differences in the response variables.

4.4.1.6 Post Reaction Chamber Fill

The post reaction chamber was filled with different substrates to potentially enhance methane conversion reactions. For these tests, the post reaction chamber was filled to 1/3 of its volume with either 4 mm glass beads (Fisher Scientific, 11-312B) or a nickel based catalyst on a non-reactive alumina support (BASF, Ni 0309-S). Table 4.8 shows the independent variables' values, and Figure 4.12 shows the effects of the post reaction chamber material had on the performance variables.

Table 4.8. Values for independent variables held constant during post reaction chamber fill parametric tests.

Constant Variable	Input
Gap Distance (mm):	30
Methane (SLPM:)	1
Nitrogen (SLPM):	2
Oxygen (SLPM):	0.56
Power Input (W):	200
Steam Input(ml/min):	1.6

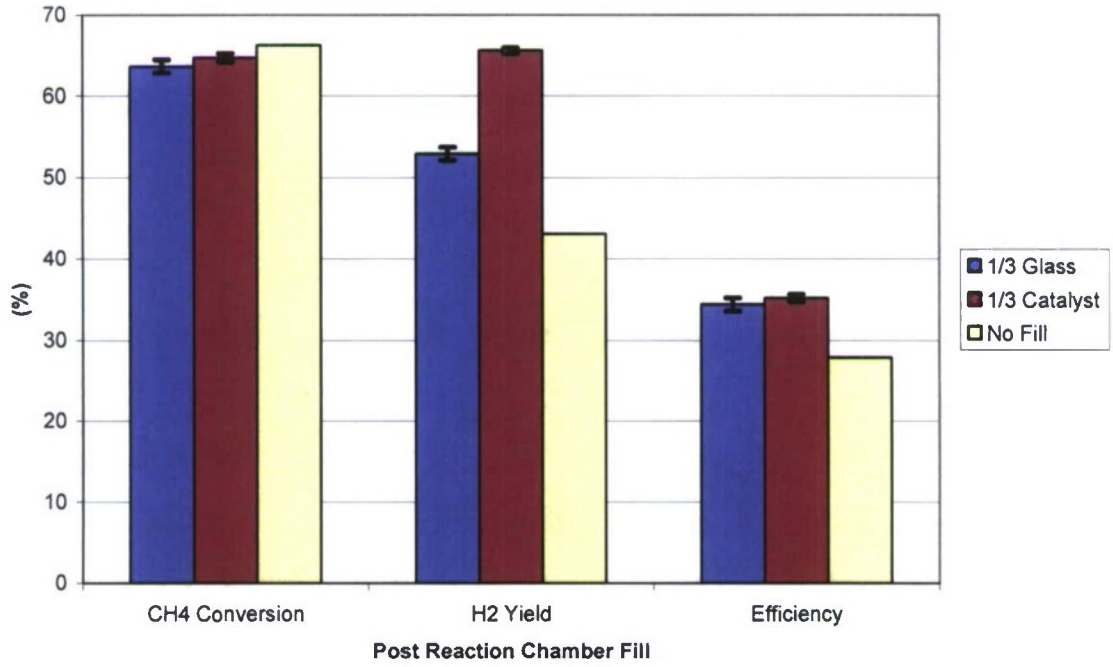

Figure 4.12. Effects of materials in the post-reaction chamber. Error bars indicate one standard deviation.

Figure 4.12 confirms that the post reaction chamber fill did not increase the conversion of methane. The increased hydrogen yield with the catalyst can be attributed to the water gas shift reaction converting CO into H_2 and CO_2. The efficiencies, 31.4, 33.4 and 34.9% for no fill, glass beads, and the catalyst, respectively; however, the efficiency increase was not enough to justify the use of a catalyst. The parametric tests showed a lack of methane reforming improvement, decayed catalysts , and fused glass beads over the course of the experiments. A corrosive gas that proved detrimental to downstream system components was also generated at times. For these reasons, no materials were used in the post reaction chamber during the factorial tests.

4.4.1.7 Volumetric Flow Rate

Literature reports indicate that the volumetric flow rate affected the residence time of the gas in the arc, the arc velocity and the cooling of the arc. To explore this, a parametric test investigating the effect of volumetric flow through the reformer was performed using the best operating conditions identified by the second factorial test (described later in section 3.4.4.2.4). This condition was defined by flow rates of 2 slpm N_2, 0.56 slpm O_2, 1.25 slpm CH_4, steam input of 0.6 ml min^{-1}, a gap distance of 34.5 mm, and a power input of 260 W. As the volumetric flow rate increased, the gas residence time within the plasma decreased and the convective cooling of the arc increased. The latter created a more non-thermal plasma. Table 4.9 shows the design of the parametric test, with a dry inlet flow (total of CH_4, O_2, and N_2) increasing from 1.9 to 5.73 slpm and a total inlet flow (total of CH_4, O_2, N_2, and H_2O vapor at 25 °C and 1 atm pressure) increasing from 2.24 to 6.74 slpm. Corresponding outlet flow rates of 2.63 to 6.37 slpm (dry) were measured. Figure 4.13 shows the effects of the parametric increase in volumetric flow rate on methane conversion, hydrogen yield, selectivity, efficiency, and specific energy requirements.

Table 4.9. Input values and reformate flow rates for volumetric flow parametric tests at 260 W and 34.5 mm gap distance.

Inputs (slpm)			H2O	Dry Gas	Saturated Gas	Reformate
CH4	N2	O2	(g / min)	Flow (slpm)	Flow (slpm)	Flow (slpm)
0.63	1.00	0.28	0.25	1.91	2.24	2.63
0.75	1.20	0.34	0.30	2.29	2.69	3.04
0.88	1.40	0.39	0.35	2.67	3.14	3.47
1.00	1.60	0.45	0.40	3.05	3.59	3.89
1.13	1.80	0.51	0.45	3.43	4.04	4.38
1.25	2.00	0.56	0.50	3.81	4.48	4.78
1.63	2.62	0.73	0.65	4.97	5.85	5.70
1.75	2.82	0.78	0.70	5.35	6.30	6.11
1.88	3.01	0.84	0.75	5.73	6.74	6.37

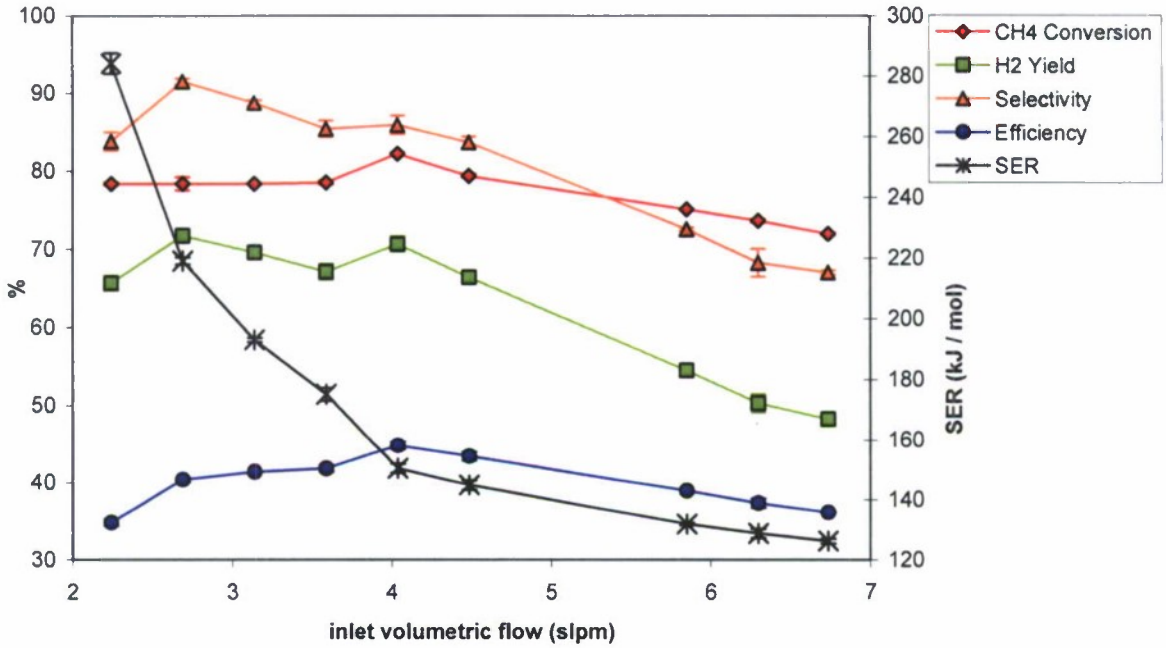

Figure 4.13. Effects of reactant volumetric flow on methane conversion, hydrogen yield, selectivity, efficiency, and specific energy requirements. Error bars indicate one standard deviation.

The volumetric flow had varying effects on the different performance metrics. Methane conversion remained relatively unchanged between 2.24 and 4.48 slpm input to the system, after which it decreased linearly from 79.4 to 72.0% conversion over the range of higher flow rates. Hydrogen yield followed a similar trend, with values of 68 to 72% over the input flow range between 2.24 and 4.48 slpm, and then decreased linearly to a low of 48% at the highest flow rate of 5.7 slpm. Efficiency increased linearly from 34.8 to 44.8% over the flow range of 2.24 to 4.48 slpm and then linearly decreased to 36.1% at an inlet flow of 6.74 slpm. The specific energy requirements benefited the most from the increase in flow rate. As the flow increased the specific energy requirements logarithmically decayed, reaching a minimum of 126 kJ mol^{-1}. This is due to the increase in hydrogen and carbon monoxide production while keeping the arc's power consumption constant. Increasing volumetric flow resulted in higher reactor outlet temperatures as shown in Figure 4.14. This is consistent with increased convective cooling of the arc.

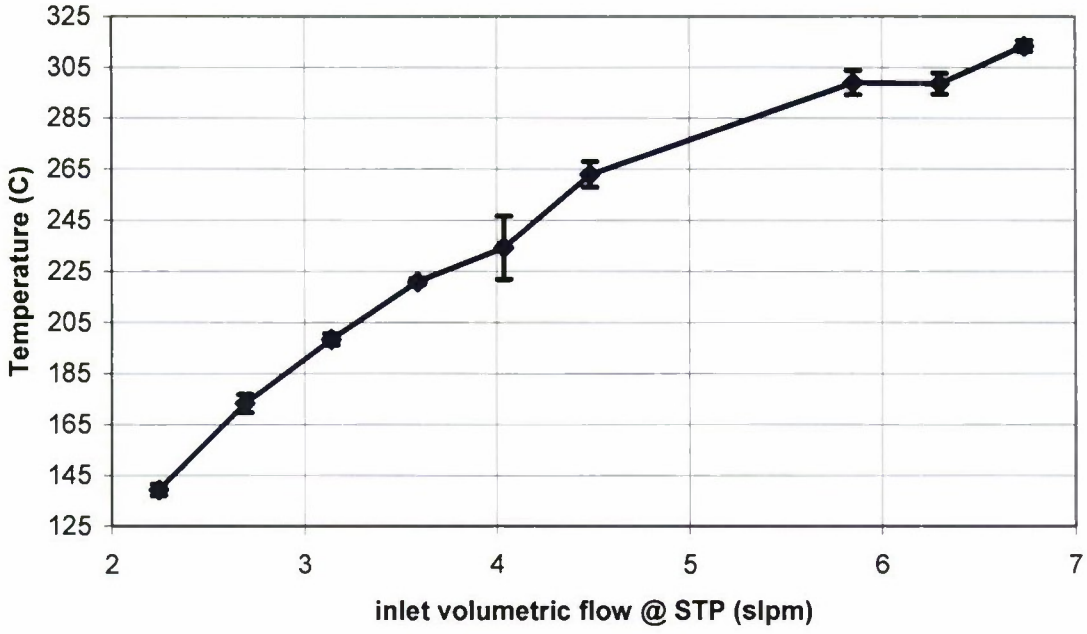

Figure 4.14. Affect of increasing volumetric flow through the reactor on outlet temperature. Error bars show one standard deviation.

4.4.2 Factorial Tests

Factorial tests can be used to identify major trends in a narrow range of factor space. For each of the different independent variables (factors), a main effect can be determined. Interaction effects between a pair of factors and higher order effects can also be measured. Understanding the main effects calculated from an initial factorial experiment allows values of an independent variable to be selected to move the response variables along a 'path of steepest ascent' toward optimal operating conditions. Additional factorial tests can then be performed in a new factor space area, leading to improved system performance and an updated path of steepest ascent. This approach can be repeated until optimal conditions are found.

4.4.2.1 First Full Factorial Test

Center points and step sizes for the independent variable values of the first factorial test were selected from the parametric tests as described in Table 4.10. A full, 2^4 factorial experiment was designed for the independent variables power input, methane input, steam input, and gap distance using two levels for each variable. This design consisted of 16 points per data set as seen in Table 4.11. The +1 and -1 designation used in Table 4.11 refer to the center point value plus or minus the step size identified in Table 4.10. For example, +1 and -1 values for gap distance would be 32.5 (30+2.5) and 27.5 (30-2.5) mm, respectively.

Randomization of the order helped alleviate any test-to-test error. A minimum of four data readings were collected at each of the test conditions to confirm steady-state conditions and provide sufficient data to calculate a standard deviation. Data from the analyzers was recorded for the last 5 minutes of each 10-minute run and averaged. This allowed for the system to come

to equilibrium after system input parameters were changed. The gas chromatograph was sampled at the end of each 10-minute run, again to allow for the system to come to equilibrium after input parameters were changed. The repetition of points for both the parametric tests and the factorial tests allowed for the system drift over time to be measured. Table 4.12 shows the average and standard deviation for similar tests run on three different days during the parametric testing. Likewise, Table 4.13 shows the average and standard deviation for similar tests run on three different days during the factorial testing. As can be seen, the standard deviation is very small from day to day, showing the analysis system remains very constant and tests are repeatable.

Table 4.10. Summary of base case factors and step sizes for first factorial test.

Variables	center point	step size	units
Gap Distance	30	2.5	mm
Steam Input	0.8	0.2	ml / min
Methane Input	0.8	0.1	lpm
Power Input	200	10	W

Table 4.12. Average and standard deviation of gas composition at the same system operating condition on three different days during parametric tests.

Parmetric Tests					
Inputs					
CH4 (slpm)	N2 (slpm)	O2 (slpm)	H2O (ml/min)	Power (W)	Gap (mm)
1.00	2.00	0.56	1.6	200.0	30.0
GC Response					
	H2 (% vol)	N2 (% vol)	CO (% vol)	CH4 (% vol)	CO2 (% vol)
average	21.92	51.19	11.31	9.36	3.23
StDev	0.36	0.28	0.43	0.28	0.16

Table 4.13. Average and standard deviation of gas composition at the same system operating condition on three different days during factorial tests.

Factorial Tests					
Inputs					
CH4 (slpm)	N2 (slpm)	O2 (slpm)	H2O (ml/min)	Power (W)	Gap (mm)
1.00	2.00	0.56	1.6	200.0	30.0
GC Response					
	H2 (% vol)	N2 (% vol)	CO (% vol)	CH4 (% vol)	CO2 (% vol)
average	23.67	55.26	13.15	4.27	3.66
StDev	0.56	0.51	0.39	0.43	0.25

Table 4.11. Design for first factorial tests and results for performance metrics.

Run	Order	Power	Methane	Steam	Gap	Methane Conversion %	H2 Yield %	Efficiency %	SER kJ/ Mol H2	Selectivity %
Center	0	0	0	0	0	80.6	55.2	36.4	195.5	72.7
1	4	-1	-1	-1	-1	82.2	51.5	34.4	219.5	62.7
2	5	1	-1	-1	-1	83.9	55.0	34.8	233.5	65.6
3	16	-1	1	-1	-1	73.5	50.4	35.9	175.5	68.6
4	11	1	1	-1	-1	74.5	53.8	36.2	187.9	72.2
5	13	-1	-1	1	-1	78.4	47.9	31.6	238.9	61.1
6	3	1	-1	1	-1	79.6	50.8	31.8	254.9	63.8
7	9	-1	1	1	-1	69.1	48.6	33.5	188.9	70.4
8	10	1	1	1	-1	69.0	40.0	29.8	247.6	58.0
9	1	-1	-1	-1	1	83.8	52.6	35.1	215.9	62.8
10	12	1	-1	-1	1	88.3	58.0	37.0	218.6	65.8
11	6	-1	1	-1	1	77.2	55.1	38.5	163.7	71.5
12	8	1	1	-1	1	78.3	57.8	39.4	173.7	73.9
13	7	-1	-1	1	1	81.1	52.5	34.2	220.2	64.6
14	14	1	-1	1	1	84.2	53.5	33.9	237.6	63.5
15	2	-1	1	1	1	71.3	50.4	34.4	184.3	70.8
16	15	1	1	1	1	76.0	55.4	36.8	185.3	73.0
							indicates best result for given metric			

First Factorial Test Results

Methane conversion, hydrogen yield, hydrogen selectivity, efficiency, and specific energy requirements have been used as indicators of system performance in the literature. As seen in Table 4.11, the system performance varied depending on the chosen metric. One metric had to be chosen to characterize the performance of the system. Methane conversion was initially chosen to gauge system performance. However, when the path of steepest ascent was followed, as seen in section 3.4.4.2.2, the ultimate purpose of the system to reform methane was no longer realized. Thus, the definition of selectivity shown in equation (3) was adopted as the chosen metric.

All of the operating conditions within the first factorial test produced valid data, i.e., none of the conditions produced inordinate amounts of soot or caused unstable conditions for the plasma arc. This allowed for the complete analysis of the factor space around the center point. Table 4.14 presents the main and interaction effects of the four independent variables. Assuming that the fourth order effects do not exist and are only results of error within the system, any effect measuring less than or equal to 105% of the fourth order effect was deemed insignificant. Within Table 4.14 the effects are the systems response to a given step. Using methane conversion as an example, the effect of one step of power input, or increasing the power by 10 W, increased the methane conversion by 2.41%. Each of the performance metrics could be used to calculate a path of steepest ascent based on the effects system variables have on the given metrics. Methane conversion was the only metric with a second order effect. Power input and gap distance produced a second order effect that was 50% higher than the error estimated by the fourth order effect for methane conversion. No other metrics had significant second or third order effects.

Table 4.14. Summary of results of the first factorial design showing main and higher order effects.

	Methane Conversion %	Hydrogen Yield %	SER kJ / mol	Efficiency %	Selectivity %
A (power)	2.4	1.9	16.5	0.3	0.4
B (methane	-8.6	-1.3	-41.5	1.5	6.0
C (steam)	-3.3	-4.4	21.2	-3.2	-2.2
D (gap)	3.2	4.7	-18.4	2.6	2.9
AB	-0.2	-1.3	4.0	-0.3	-1.5
AC	0.0	-1.8	6.8	-0.6	-2.6
AD	1.0	1.6	-8.8	1.0	1.2
BC	0.0	-1.3	5.1	-0.7	-1.3
BD	0.3	1.8	-4.8	0.7	2.0
CD	0.3	1.4	-7.3	0.5	1.7
ABC	0.0	-0.6	2.6	0.0	-1.5
ABD	0.0	1.6	-6.3	0.7	2.2
ACD	0.3	1.3	-5.3	0.4	1.5
BCD	0.6	0.7	-2.9	0.1	1.0
ABCD	0.7	2.3	-8.5	0.9	2.5
	indicates significant effect				

4.4.2.2 Path of Steepest Ascent, Methane Conversion Metric

Methane conversion was initially chosen as the primary metric to measure system performance. The main effects for methane conversion from the first factorial test were utilized to find the path of steepest ascent. The main effect was multiplied by the original step size (e.g., 10 W x 2.41 for power) to find the change in variables between steps. However, because steam would only have been able to make one step (0.2 ml min^{-1} x (-3.27) = (-0.65 ml min^{-1} $step^{-1}$)) from the initial center value of 0.8 ml min^{-1}, a factor was applied to make the steam step size -0.1 ml min^{-1} $step^{-1}$ and the other three independent variables were adjusted accordingly. This yielded a gap distance step size of 1.2 mm, which was rounded up to 2 mm, and a power input step size of 4 W, which was rounded to 10 W, in order to distinguish effects from noise during the test. As shown in Table 4.15, a path of steepest ascent was calculated that ultimately led to the highest methane conversion percentage. Progressing along the path called for lower methane flow rates, resulting in significantly decreased hydrogen yields, lower efficiency, and higher specific energy ratio as shown in Figure 4.15. The reduction in methane flow rate while holding O_2 input constant resulted in air-fuel mixtures that neared stoichiometric ratios and methane combustion rather than reforming. The low hydrogen generation and the near stoichiometric air-fuel ratio led to a decision to choose a second path of steepest ascent based on selectivity.

Table 4.15. First path of steepest ascent design based on methane conversion metric.

Step #	Steam (ml / min)	CH4 Input (LPM)	Gap (mm)	Power (W)
1 (base)	0.8	0.8	30	200
2	0.7	0.7	32	210
3	0.6	0.6	34	220
4	0.5	0.5	36	230
5	0.4	0.4	38	240
6	0.3	0.3	40	250

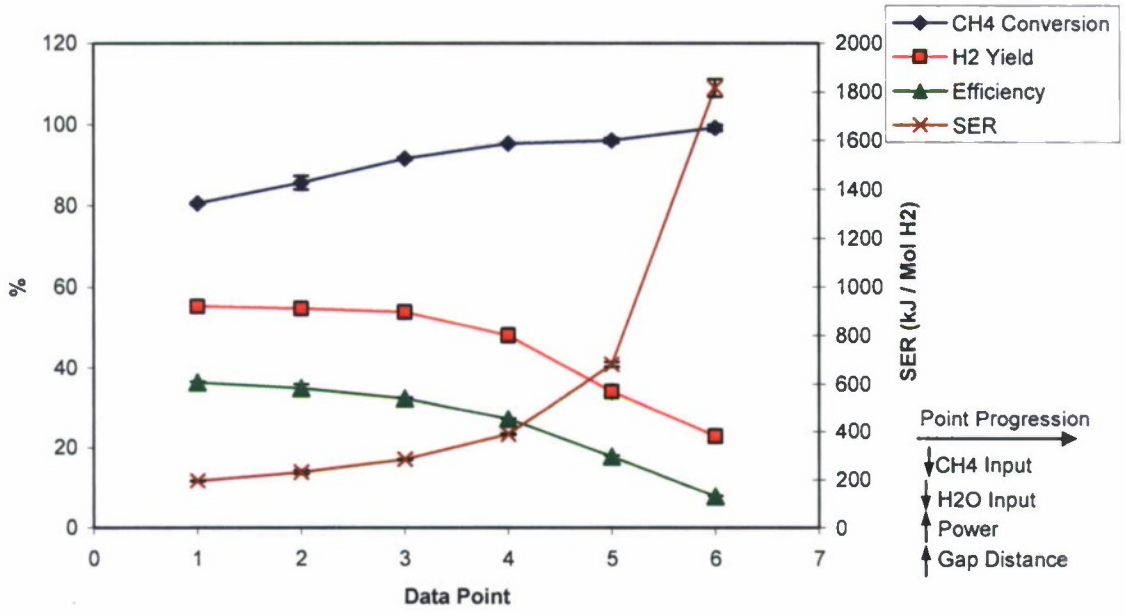

Figure 4.15. Results of the first path of steepest ascent experiments using methane conversion as the performance metric. Data points correspond to description in Table 4.15.

4.4.2.3 Path of Steepest Ascent, Selectivity Metric

A second path of steepest ascent was calculated using selectivity as the performance metric. This path of steepest ascent is shown in Table 4.16. According to the results from the first factorial design, power had no significant effect on selectivity. Thus, the runs were made at a constant power input, first at 200 W and then at 250 W, because the arc could not be sustained past step 2 at 200 W. At 250 W, the system failed after step 4 due to arc failure as seen in Figure 4.16.

Table 4.16. Values of independent variables along the path of steepest ascent using selectivity as the performance metric at a constant power of 250 W.

Step #	Steam (ml / min)	CH4 Input (LPM)	Gap (mm)	Power (W)
0 (base)	0.8	0.8	30	250
1	0.7	0.94	31.65	250
2	0.6	1.08	33.3	250
3	0.5	1.22	34.95	250
4	0.4	1.36	36.6	250

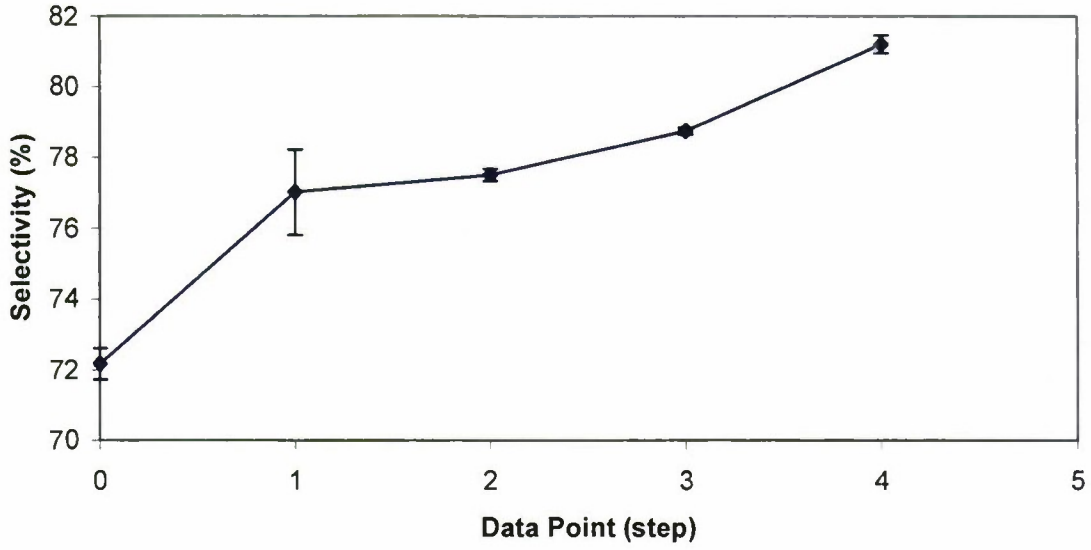

Figure 4.16. Selectivity results along the path of steepest ascent using selectivity as the performance metric. See Table 4.16 for independent variable values.

4.4.2.4 Second Factorial test

The path of steepest ascent based on selectivity described in the previous section was used to develop a second factorial experiment. The center point for the second factorial test was based on point 4 shown in Figure 4.16. This test was run as a full factorial, 2^4 design with two levels for each of the independent variables as summarized in Table 4.17. A minimum of four data points were collected at each test condition following the methodology from the first factorial test.

Table 4.17. Summary of values of independent variables at the center point and step sizes for second factorial test.

Variables	center point	step size	units
Gap Distance	36.5	2	mm
Steam Input	0.4	0.2	g / min
Methane Input	1.35	0.1	lpm
Power Input	250	10	W

Second Factorial Test Results

These center point test conditions were near the physical limits of system operation and several combinations of the independent variables identified in the design did not produce stable operating results due to soot formation or arc extinction as seen in Table 4.18. Sets of operating conditions near the limits of operation resulted in the highest values of the performance indicators. Because several sets of operating conditions did not produce stable results, a complete analysis of the factor space and interaction effects could not be performed. The main effects and interaction effects that could be calculated are reported in Table 4.19.

Because data were not available for some of the test conditions, the calculations for the second and higher order effects could not be calculated with as thorough an approach as for the first factorial test. In order to calculate effects, the differences between the high and low levels at a given condition must be known. The effect comes from the average of these differences; first order effects had a maximum of 8 averages in a 2^4 factorial experiment. For second order effects, two sets of averages are needed, one for each of the two factors at their respective high and low levels. These two sets were then subtracted from each other and divided by two to find the second order effect. Third order effects followed the same pattern, with four sets of two differences. Fourth order simply had eight differences averaged. Thus, if data points are missing for a given condition it cannot be included in the calculations; accordingly, its corresponding high or low value cannot be utilized as its counterpart is missing. Thus, most second order effects could be calculated utilizing only one of the differences instead of the average for the set. Most of the third order effects could not be calculated due to missing data for given conditions. The fourth order effects as sets were not being averaged together, simply omitted the missing conditions, which leads to a limited certainty of the value of the fourth order effects shown.

Because data were not available for some of the test conditions, the averages for the effects from high to low values could not be computed. This led to some effects being calculated based on one high to low effect instead of the average of multiple effects. As the interactions increased, the ability to compute any effects dropped drastically, because instead of taking the average of some high to low levels, one high to low level was necessary but unavailable. The fourth order interaction was computed by setting all values that could not be computed to zero. Thus, the certainty of the ABCD effect is severely limited.

Table 4.18. Design for second factorial tests and results for performance metrics.

Design Run	Order	A Power	B Methane	C Steam	D Gap	Methane Conversion	H2 Yield %	Efficiency %	SER kJ/ Mol H2	Selectivity %
1	4	-1	-1	-1	-1	77.0	61.4	41.7	141.4	79.7
2	5	1	-1	-1	-1	74.6	59.5	40.0	155.9	79.7
3	16	-1	1	-1	-1	62.6	47.5	33.9	154.6	75.9
4	11	1	1	-1	-1	64.2	49.1	34.5	161.6	76.5
5	13	-1	-1	1	-1	76.7	62.3	42.1	140.5	81.2
6	3	1	-1	1	-1	79.8	66.5	43.5	144.1	83.3
7	9	-1	1	1	-1	69.2	56.1	38.7	136.4	81.1
8	10	1	1	1	-1	73.1	59.9	40.5	137.9	82.0
9	1	-1	-1	-1	1	76.2	60.4	41.0	143.8	79.3
10	12	1	-1	-1	1	76.3	63.0	41.7	149.8	82.6
11	6	-1	1	-1	1	75.7	38.3	34.7	0.0	50.6
12	8	1	1	-1	1	69.9	54.9	38.0	146.5	78.6
13	7	-1	-1	1	1	76.4	62.8	42.3	139.4	82.3
14	14	1	-1	1	1	79.9	65.8	43.3	144.5	82.4
15	2	-1	1	1	1	DNR	DNR	DNR	DNR	DNR
16	15	1	1	1	1	72.2	59.9	40.5	138.3	82.9

Failure Due To Soot Production	Failure Due To Arc Extinction	DNR : Did Not Run	Best Performance for Metric

As can be seen in Table 4.19, the main effects for the four independent variables using selectivity as the performance indicator were less than the previous factorial test, showing that an optimum was approached. Only power input and steam input may still have effects on the selectivity of

the system; however, the power supply can only provide 270 W at full output. Following a path of steepest ascent is thus not possible in regards to power input. Further decreasing steam input is also not possible after this point because soot would be produced. Thus as it stands, the best selectivity that can be achieved is 83.3 ± 0.85% at flow rates of 2 slpm N_2, 0.56 slpm O_2, 1.25 slpm CH_4, 0.6 ml steam min^{-1}, a gap distance of 34.5 mm and a power input of 260 W. At this point a hydrogen-to-carbon monoxide ratio of 2.14 was produced.

Table 4.19. Summary of results of the second factorial design showing main and higher order effects. % data incomplete is taken from the average value missing the most data.

effect (% data incomplete)	Methane Conversion	Hydrogen Yield	SER	Efficiency	Indarto Selectivity
A (power) (37.5)	1.65	2.34	6.13	0.63	1.29
B (methane) (62.5)	-7.28	-6.25	-5.52	-3.06	-0.36
C (steam) (50)	2.13	3.28	-5.54	1.71	2.01
D (gap) (37.5)	-0.04	0.49	-0.81	0.20	0.71
AB (75)	1.43	0.95	-2.90	0.75	-0.22
AC (50)	2.31	1.66	-3.44	0.98	-0.29
AD (75)	0.13	0.38	-0.50	0.16	0.36
BC (100)	NA	NA	NA	NA	NA
BD (75)	-0.29	0.19	-0.54	0.20	0.60
CD (50)	-0.28	-0.67	0.75	-0.26	-0.58
ABC (100)	NA	NA	NA	NA	NA
ABD (100)	NA	NA	NA	NA	NA
ACD (50)	0.23	-1.25	2.55	-0.66	-1.92
BCD (100)	NA	NA	NA	NA	NA
ABCD* (100)	-0.05	0.48	-3.00	0.28	0.66

*Modified fourth order effect, see text for explanation

4.5 Papers and Presentations Resulting from Efforts

William Piavis, a student working toward an MS degree in mechanical engineering at the University of Hawaii is nearing completion of his thesis based on this work. Papers and presentations will be forthcoming.

5. Methane Hydrates

Methane hydrates in ocean sediments constitute an enormous energy reservoir that is estimated to exceed the energy content of all known coal, oil, and conventional natural gas resources. Located on continental margins throughout the world, methane hydrates offer unique opportunities as an onsite source of fuel for various marine applications and are believed to play a major role in seafloor stability and global climate.

National R&D programs on methane hydrates were initiated in Japan and India in the mid-1990s with the goal of commercial gas production within a 20-year time horizon. The U.S. established its own program in May 2000. The Methane Hydrate Research and Development Act of 2000 (Public Law 106-193) included seven technical areas of focus: (1) identification, exploration, assessment, and development of methane hydrate as a source of energy; (2) technology development for efficient and environmentally sound recovery of methane from hydrates; (3) transport and storage of methane produced from methane hydrates; (4) education and training related to methane hydrate resource R&D; (5) assessment and mitigation of environmental impacts of natural and purposeful hydrate degassing; (6) development of technologies to reduce the risks of drilling through methane hydrates; and (7) support of exploratory drilling projects. The objectives of the Methane Hydrates Task of the Hawaii Energy & Environmental Technologies (HEET) initiative, which was initiated in 2001, reflect most of the priorities of P.L. 106-193, but emphasize those areas of particular relevance to the Office of Naval Research (ONR) and which are consistent to the overall goals of HEET. Specifically, the development of hydrates and related sources of seafloor methane as logistical fuels for Naval applications and related marine environmental issues, have been the principal areas of interest; exploratory drilling projects and seafloor stability/safety have received limited attention. Work also has been initiated to explore engineering applications of hydrates such as desalination and hydrogen storage. Task objectives were devised to fully leverage hydrate R&D expertise and infrastructure that had been developed at HNEI during previous research programs on CO_2 ocean sequestration and deep oil spills.

During the present reporting period (09/07-03/10), the goals of the HEET Methane Hydrates Task were:

- Pursue development of methods to recover methane gas from hydrates.
- Explore the use of seafloor methane sources for subsea power generation.
- Investigate the microbial processes in sediment that generate and modulate methane levels.
- Investigate the fate of methane released into the water column from the seafloor.
- Investigate engineering applications of hydrate.
- In cooperation with NRL and ONR Global (previously ONR-IFO), promote international collaborative research on methane hydrates.

Specific technical objectives that were pursued to attain the above goals included:

- Conduct laboratory experiments using the Raman calorimeter on hydrate destabilization using chemical inhibitors.
- Develop a model of hydrate destabilization by chemical inhibitors.
- Pursue the technical development of subsea power generation systems using seafloor methane.

- Characterize the microbial assemblage that modulates methane leakage into the water column, in samples of deep ocean sediment overlying hydrates.
- Participate in collaborative field studies of offshore hydrate biogeochemistry with NRL.
- Initiate exploratory laboratory experiments of engineering applications of hydrates such as gas or water purification.
- Organize workshops to promote international collaboration on methane hydrate R&D.

5.1 Scope of Work and Approach

Pursuant to the goals and technical objectives identified in the preceding section, work on the Methane Hydrates Task during the present reporting period focused on four primary areas which are described below.

5.1.1 Hydrate Thermochemistry and Kinetics

The major priority of this subtask was to elucidate the fundamental mechanism of methane hydrate destabilization for the purpose of producing fuel gas (and, to a lesser extent, to clear hydrate blockages that can form in natural gas conduits). This was undertaken by a combination of laboratory experiments and modeling. Two facilities developed previously as part of the HEET initiative were available to conduct experiments: the hydrate synthesis and destabilization system and a Raman calorimeter. The present tests focused on the utilization of liquid chemical reagents to dissociate hydrate.

A second priority was to pursue technical development of systems to generate electrical power on the seafloor (for underwater instrumentation, monitoring, recharging of AUVs, etc.) using methane gas seeps or hydrates. This activity is a continuation of a one-year conceptual design study conducted for DARPA.

5.1.2 Environmental Impacts of Methane Release from Seafloor Hydrates

This subtask is a continuation of activities pursued in previous years to: (1) assess the consequences of inadvertent or purposeful releases of methane from seafloor hydrates via the development of a model of methane transport through the ocean water column to the atmosphere; and (2) elucidate the mechanisms by which sediment microbes control free methane gas levels in, and methane leakage from, the seafloor sediment and arctic permafrost.

During the present phase, we initiated development of a full 3-D numerical model of methane in the ocean and attempted to identify the microbial assemblage in the upper layer of sediment collected during a 2006 oceanographic research cruise on the Hikurangi Margin offshore of the North Island of New Zealand.

HNEI also participated in a research cruise with NRL in the Beaufort Sea off the North Slope of Alaska in September 2009. Additional porewater and sediment samples were collected during this expedition and are being cultured to investigate methane consumption by resident methanotrophs.

5.1.3 Hydrate Engineering Applications

The major priority of this subtask was to initiate exploratory studies of the use of gas hydrates for various engineering applications relevant to DOD interests. Candidate applications include water purification, gas separation, and fuel gas storage. To the extent possible, this subtask would leverage facilities and protocols developed in previous phases of the HEET initiative.

5.1.4 International Collaborative R&D

To promote international R&D cooperation on methane hydrates, HNEI has sponsored and helped to organize a series of workshops on methane hydrates that was started under the HEET initiative in 2001. During the current phase, the 6th International Fiery Ice Workshop was held in Bergen, Norway in May 2008 and planning was underway for the 7th Workshop scheduled for May 2010 in Wellington, New Zealand.

5.2 Technical Accomplishments

The principal technical accomplishments of the HEET Methane Hydrates Task for each of the components identified above are described in the following sections.

5.2.1 Methane Hydrate Destabilization

During the present reporting period, the primary accomplishments of this subtask were: (1) completed modeling analyses of two sets of hydrate destabilization experiments described in previous HEET reports and published these results in the technical literature; and (2) performed an experimental study of the heat capacity of water at elevated pressures. The hydrate destabilization work constituted the M.S. thesis research of a Mechanical Engineering student at UH who was awarded his degree in August 2008. The investigation of the heat capacity of water at elevated pressure was pursued to provide fundamental data that can be applied to fuel cell, methane reforming, and cooling components of subsea power systems which operate under deep ocean conditions.

5.2.1.1 Reagent Destabilization of Methane Hydrates

Three methods have been proposed to destabilize and extract fuel gas from hydrates: heating, depressurization, and chemical reagents. Chemical reagents, notably alcohols and other antifreeze compounds, also have been employed for decades to avoid hydrate blockages in natural gas pipelines and, as a result, are often referred to as thermodynamic inhibitors. While there is a substantial amount of information in the literature regarding hydrate decomposition using thermodynamic inhibitors, most studies have been limited to determining the pressure-temperature stability curve of hydrates in the presence of these inhibitors. The mechanism by which they decompose hydrates remains elusive. Knowledge about the fundamental mechanism could help identify more environmentally-benign and cost-effective alternatives (for, say, methane recovery from hydrates in seafloor sediment or permafrost where the injection of large quantities of methanol or ethylene glycol is not acceptable). Toward this end, we have been pursuing complementary experimental and modeling studies of reagent destabilization of hydrates. These studies and their results have been described in previous HEET reports.

5.2.1.1.1 Determination of Reagent Effectiveness from Raman Calorimetry Experiments

The effectiveness of three common alcohols and one diol to decompose hydrate was investigated and related to the structure of these compounds. A Calvet-Tien calorimeter was modified to allow liquid reagents to be injected into the sample cell within the calorimeter at a steady and selectable flow rate and nearly constant pressure and temperature. A fiberoptic link was developed to perform Raman spectroscopy measurements of the contents of the calorimeter sample cell, which provided clear evidence of the existence of methane hydrate in the cell. The primary conclusions of these experiments include:

- At -5 °C and 6.89 MPa, experimental results indicated that, on a per mole basis, ethylene glycol disassociates the most hydrate, followed in order by methanol, ethanol, and then 2-propanol.
- Based on the these results, it was hypothesized that an inhibitor decomposes hydrates by binding up the released water molecules in the quasi-liquid layer and preventing it from re-crystallizing. The number of hydroxyl groups and the size of the alkyl group are the primary factors that influence an inhibitor's ability to bind to the free water molecules at the hydrate surface. The hydroxyl group allows the inhibitor to bind to water molecules. Through steric effects, the alkyl group influences the hydrogen bonding capability of the inhibitor, as well as the strength of the hydrogen bonds formed between the inhibitor and water molecules.

5.2.1.1.2 Theory

A novel method based on the non-ergodic theory of mobile order thermodynamics (MOT) was proposed to estimate the activity of water in binary mixtures with ethylene glycol and several common alcohols. Details of the method and results of the analyses were discussed extensively in the previous HEET report. The primary conclusions of this component our study of hydrate destabilization include:

- Calculations were shown to be in good agreement with those obtained with the widely used UNIQAC equation, thereby establishing the soundness of the alternative MOT framework for hydrogen-bonded liquids.
- Consistent with the behavior observed in the dissociation experiments we conducted, results of this analysis suggest that alcohol molecules with a smaller alkyl group or a greater number of hydroxyl groups lower the activity of water more effectively. Primary alcohol isomers (e.g., 1-propanol) seem to affect the activity of water slightly less than secondary alcohol isomers (e.g., 2-propanol).
- In the case of diols like diethylene and triethylene glycol that have more complex molecular structures, it was shown that the present MOT formalism requires further development to properly describe hydrogen-bonding behavior.
- Since hydrate stability is determined by an equilibrium condition of equal chemical potentials for water in the hydrate and liquid phases, this analysis is relevant to better understand how alcohols inhibit the formation of gas hydrates and, in general, supports and offers an explanation of the results of our experiments.

A manuscript on this work entitled "A Determination of the Activity of Water-alcohol Mixtures Using Mobile Order Thermodynamics," was submitted for review and subsequently published in

the journal *Chemical Engineering Science* during the present reporting period (Nihous *et al.*, 2009).

5.2.1.1.3 Heat and Mass Transfer Considerations During Hydrate Destabilization.

We previously conducted experiments of methane hydrate destabilization by chemical reagents using our hydrate synthesis facility. Whereas the recent tests performed in the Raman Calorimetry device provide information of equilibrium phenomena, these earlier experiments offered insight into the kinetics of dissociation.

The results of the kinetics experiments and related analyses were reported in an article entitled "An Analysis of Gas Hydrate Dissociation in the Presence of Thermodynamic Inhibitors," that was published (online; the print version appeared in 2010) in the journal *Chemical Engineering Science* during the present reporting period (Nihous *et al.*, 2010). A summary of this investigation is provided below.

The existence of a fundamental intrinsic rate of hydrate decomposition has been postulated. This speed limit of sorts imposed by molecular constraints was measured and expressed in a two-parameter equation (Kim *et al.*, 1987; Clarke and Bishnoi, 2000; Clarke and Bishnoi, 2001; Clarke and Bishnoi, 2004). In most practical cases, however, heat and mass transfer tend to limit the extent of hydrate decomposition.

The rapid depressurization and resulting dissociation of hydrate samples to ambient pressures of one to a few atmospheres has been well studied in the laboratory (e.g., Circone *et al.*, 2000a; Komai *et al.*, 2004). On the other hand, very low pressures (e.g., 200 Pa) have been used to examine the effect of heat, provided as radiation, on hydrate dissociation kinetics (Ullerich *et al.*, 1987). High pressures of a few tens of atmospheres, however, are more representative of *in situ* conditions that would prevail for marine hydrates.

A suite of experiments was performed to provide data on liquid reagent-induced decomposition of methane hydrates at constant, high-pressure conditions similar to those that would prevail during gas production in deep sea environments. A unique experimental facility was employed in which the liberated methane gas exhausts freely into a reservoir at the same pressure as the hydrate sample to minimize artifacts of any pressure letdown devices (e.g., throttling valves or regulators). A one-dimensional time-domain analytical model was developed to simulate the experimental procedure. It allows the inclusion of intrinsic hydrate dissociation kinetics in a basic heat and mass transfer framework.

Experimental apparatus

Figure 5-1 presents a schematic diagram of the experimental apparatus. Pure methane hydrate is synthesized and dissociated within a vertical, stainless steel high pressure cell lined with Teflon® (2.86 cm internal diameter; 50.4 cm height). The cell is enclosed in a computer controlled freezer that allows selection and adjustment of temperatures. A coaxial injector at the top of the cell delivers liquid reagents through a tube, and gas is infused (during synthesis) or flows out of the cell (during destabilization) through the annulus between the tube and cylinder. A multipoint thermocouple probe through the bottom penetration measures temperature inside the cell.

Pure methane gas (99.99%) is infused in the cell to set the pressure at the start of each experiment. Pressure in the cell is monitored continuously with a pressure transducer (≤±1.3 psi/9000 Pa accuracy). Liquid reagents are stored in a bladder accumulator reservoir that maintains an essentially constant supply pressure. Flow rate is controlled with a metering valve and is monitored with a Coriolis flow meter better than ±0.5% (of measurement) accurate. The temperature of the injected liquid is adjusted in a heat exchanger comprising a long coil of tubing immersed in a constant temperature bath.

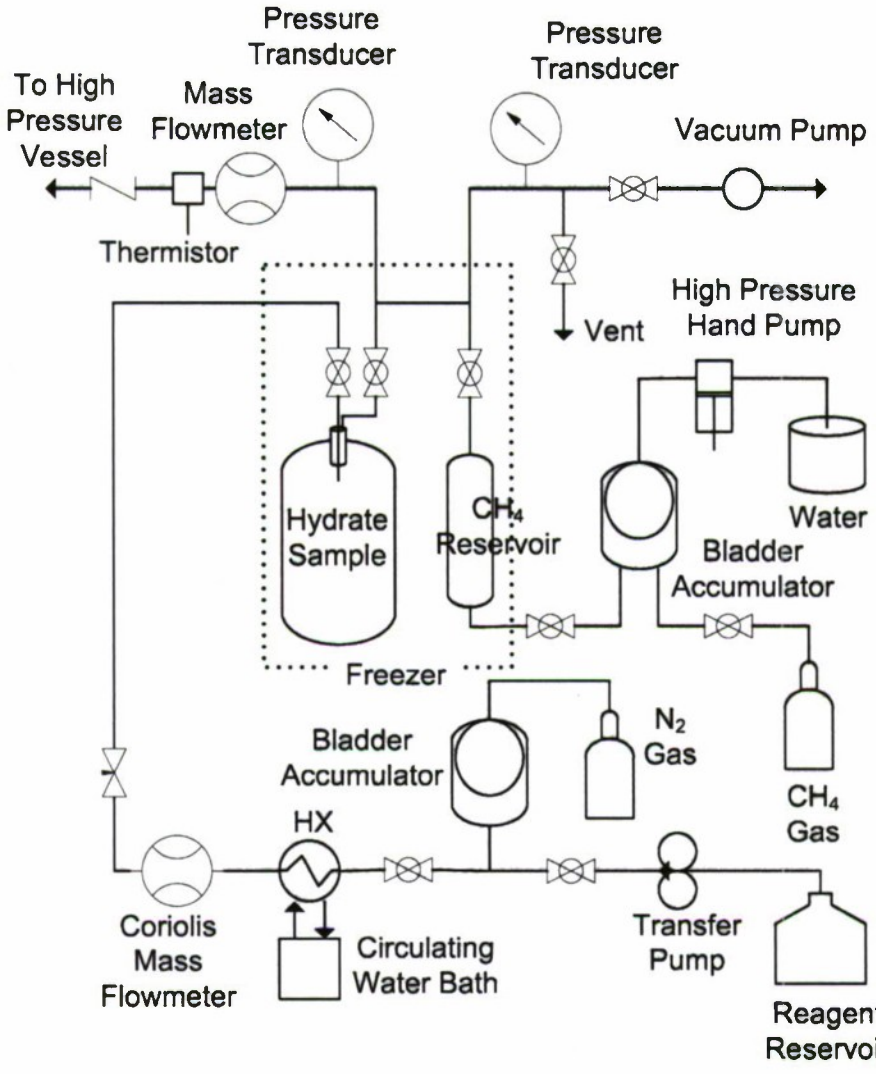

Figure 5.1. Schematic diagram of hydrate synthesis and destabilization system.

Figure 5.2 presents a schematic diagram of the system used to monitor the flow of gas evolved from a destabilizing hydrate core. This gas flows freely into a large pressure vessel containing a custom-built flow meter based on the principle of the Torricelli tube. Circone *et al.* (2000b) employed a similar instrument to conduct studies of hydrate destabilization by pressure reduction where evolved gas was measured at ambient pressure. In our case, the gas flow measurement

system is housed in a pressure vessel maintained at the same pressure as the decomposing hydrate sample to minimize potential restrictions arising from inline backpressure regulators or relief valves. The internal diameter of this vessel is 146 cm, and its length is 105 cm. The vessel is rated for continuous operation at 10.3 MPa which establishes the upper pressure limit of the experiments. It is equipped with multiple penetrations along its axis and end flanges, which are fitted with windows and instruments used for material addition and extraction.

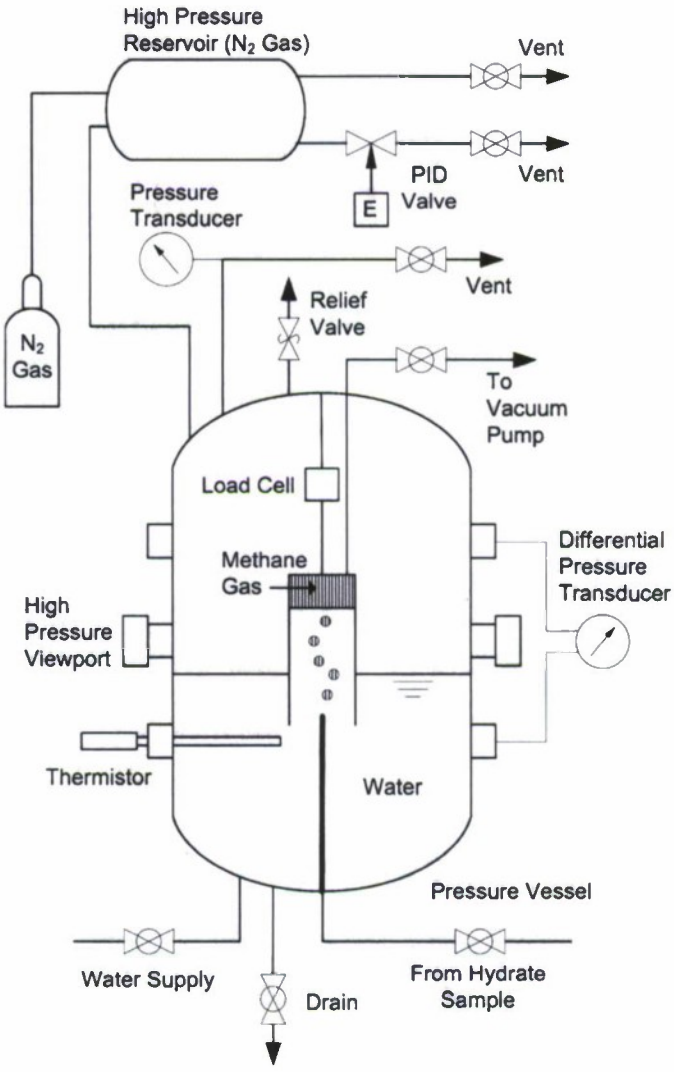

Figure 5.2. Schematic diagram of pressurized evolved-gas collection reservoir and Torricelli-tube flow meter.

Pressure in the vessel is set by charging the space above the water used for the Torricelli tube with nitrogen or argon. When pressure is the same as in the hydrate cell system, the plug valve in the connecting gas line is opened. As evolved gas flows, it displaces water in the inverted cup, the level of which is initially drawn up above that of the surrounding water with a vacuum pump. The suspended load cell (*Transducer Techniques* model *MDB*-10) connected to the cup measures the corresponding change in the weight of the water column, which can be related to

the volume of evolved gas. The displaced water also causes the water level in the vessel to rise and this provides another estimate of the volume of evolved gas by means of the differential pressure transducer shown in Figure 2. A process controller is used to vent the inert gas from the vessel through an electronic valve to maintain a constant pressure as the water level rises. A third redundant measurement of the methane release rate is provided by an in-line thermal mass flow meter (shown in Figure 1). This instrument causes a negligible excess back-pressure in the hydrate cell and it is insensitive to the potential effects of the dissolution of methane gas into water in the pressure vessel, which could affect the Torricelli tube and water level measurements. The amount of dissolved methane was estimated by collecting and analyzing a pressurized water sample through one of the side ports after each experiment.

Experimental procedure

Methane hydrate is synthesized from granular ice and pressurized methane gas using the method of Stern *et al.* (1996). After synthesis, the samples are maintained within the hydrate stability zone under a pure methane atmosphere until destabilization experiments are started. At that time, the methane gas pressure is adjusted to the desired test pressure and the temperature is also set to a selected value.

After setting the hydrate pressure and temperature, the pressure vessel serving as the evolved gas reservoir and housing the Torricelli tube flow meter is charged with inert gas until its pressure equals the pressure in the hydrate cell. A plug valve connecting the two chambers is then opened to allow evolved gas to move freely between them. Destabilization is initiated with the injection of a liquid solution (e.g., methanol and water) of known composition and temperature at a constant rate for a prescribed time. A methane gas space initially is left open above the hydrate core so that injection of the liquid does not pressurize the system. The volume of methane displaced by the injection of the inhibitor solution is accounted for in the data reduction.

One-dimensional time-domain model of hydrate sample dissociation

The modeled configuration is illustrated in Figure 5.3. Side walls are assumed to be adiabatic and the sample is radially symmetric. It is reasonable, then, to consider the problem as spatially one-dimensional (in the vertical coordinate z). A cylindrical methane hydrate sample of molar composition $CH_4 \bullet H_2O$ is assumed to be isolated except for its upper surface A. At time $t = 0$, the injection of an inhibitor solution triggers hydrate dissociation on the surface A. Both injection and the release of water initially bound in the hydrate will generate a bulk liquid phase overlying the shrinking hydrate sample.

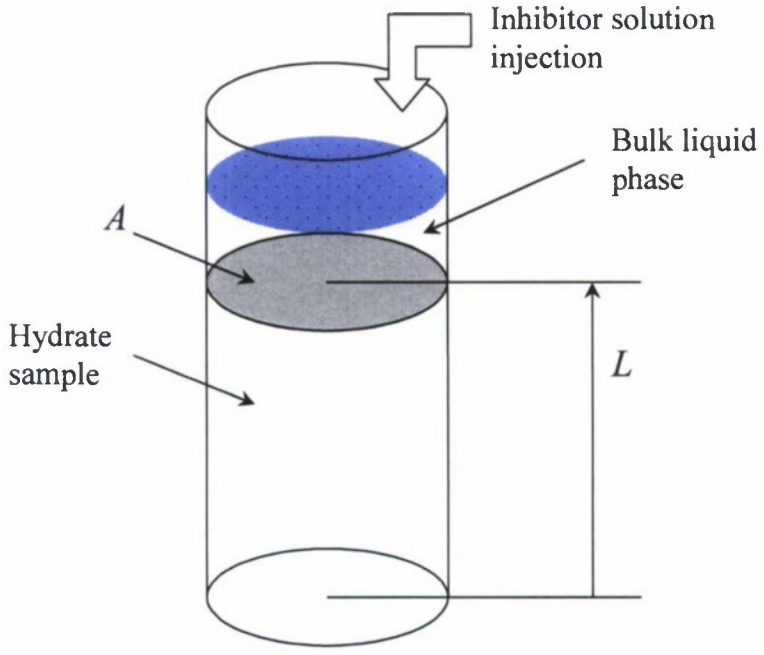

Figure 5.3. Model of dissociating hydrate sample.

Within the hydrate sample of thermal diffusivity $\alpha = k/(\rho c_p)$, where ρ and c_p are the molar density and specific heat, respectively, heat conduction is governed by the following partial differential equation:

$$\frac{\partial T}{\partial t} = \alpha \frac{\partial^2 T}{\partial z^2} \tag{1}$$

The boundary conditions are $\partial T/\partial t(0, t) = 0$ and $T(L, t) = T_s$. The temperature T_s and the vertical coordinate L of the decomposing hydrate surface are both unknown *a priori*.

The bulk liquid phase is considered to be well mixed at temperature θ, and heat transfer at the decomposing hydrate surface is represented with a simple convective term $H(\theta - T_s)$. Calling λ the molar enthalpy of methane-hydrate dissociation, a heat balance at the decomposition front yields:

$$-\lambda\rho\frac{dL}{dt} = -k\frac{\partial T}{\partial z}(L) + H(\theta - T_s) \tag{2}$$

A methanol-water solution at temperature T_{inj} with a methanol mass fraction s_0 is injected at a prescribed mass rate q_{inj}. At any time, the enthalpy of the bulk liquid phase then is

$$\{[c_{pl}s_0 + c_{pw}(1 - s_0)]\int_0^t q_{inj}\,dt + c_{pw}nM_w\rho A(L_0 - L)\}\theta$$

Its time derivative must be equal to the enthalpy change per unit time given by the expression below:

$$- c_{pw} n M_w \rho A T_s \frac{dL}{dt} + [c_{pi} s_0 + c_{pw}(1 - s_0)] q_{inj} T_{inj}$$

This procedure (considering the temperature dependence of the specific heats as negligible) leads to the following equation:

$$\frac{d\theta}{dt} = \frac{[c_{pi} s_0 + c_{pw}(1 - s_0)] q_{inj} (T_{inj} - \theta) - c_{pw} n M_w \rho A (T_s - \theta) \frac{dL}{dt}}{[c_{pi} s_0 + c_{pw}(1 - s_0)] \int_0^t q_{inj} dt + c_{pw} n M_w \rho A (L_0 - L)} \tag{3}$$

An equation to determine T_s is still needed. The easiest approach is to postulate that the decomposing surface always is at equilibrium, or $T_s = T_{eq}$. If three-phase equilibrium conditions are represented by a function $p_{eq}(T; s)$, then T_s is the solution of the implicit equation $p_{eq}(T_s; s) = p$, where p is the ambient pressure. At any time, the mass fraction of inhibitor (e.g., methanol) s is available from an elementary mass balance:

$$s = \frac{s_0 \int_0^t q_{inj} dt}{\int_0^t q_{inj} dt + n M_w \rho A (L_0 - L)} \tag{4}$$

Alternatively, Kim *et al.* (1987) proposed an intrinsic hydrate dissociation mechanism taking place in a desorption layer at the hydrate surface. Here, the decomposing surface must be *away* from equilibrium to provide a 'driving force' (e.g., a fugacity difference). Using a two-parameter kinetic constant $K_d = K_0 \exp\{-E/(RT_s)\}$, the molar dissociation rate in well-stirred isothermal experiments, where dissociation was induced by depressurization, was expressed as[1]:

$$\frac{dN}{dt} = - K_d A \{ f[p_{eq}(T_s; s), T_s] - f(p, T_s) \} \tag{5}$$

Clarke and Bishnoi (2001) recently improved the measurement procedure of Kim *et al.* (1987) with revised values of the basic constant K_0 (36000 mol/m^2-Pa-s) and molar activation energy E (81000 J/mol). Mathematically, the decomposing hydrate surface would be at equilibrium if K_d were infinite.

Jamaluddin *et al.* (1989) suggested that the same formalism was applicable when hydrates are dissociated at constant pressure. The definition of the driving fugacity difference, shown as δf in Figure 5.4, leads to some ambiguity, however, since there is no obvious physical meaning for $p_{eq}(T_s)$ in this case. This approach was nevertheless tested here, even though its general applicability (when hydrates are not dissociated by depressurization) has never been verified to our knowledge.

[1] The parametric dependence of equilibrium pressure on inhibitor mass fraction s is shown here for the sake of generality although no inhibitor was used (s = 1.0) by Kim *et al.* (1987) or Clarke and Bishnoi (2001).

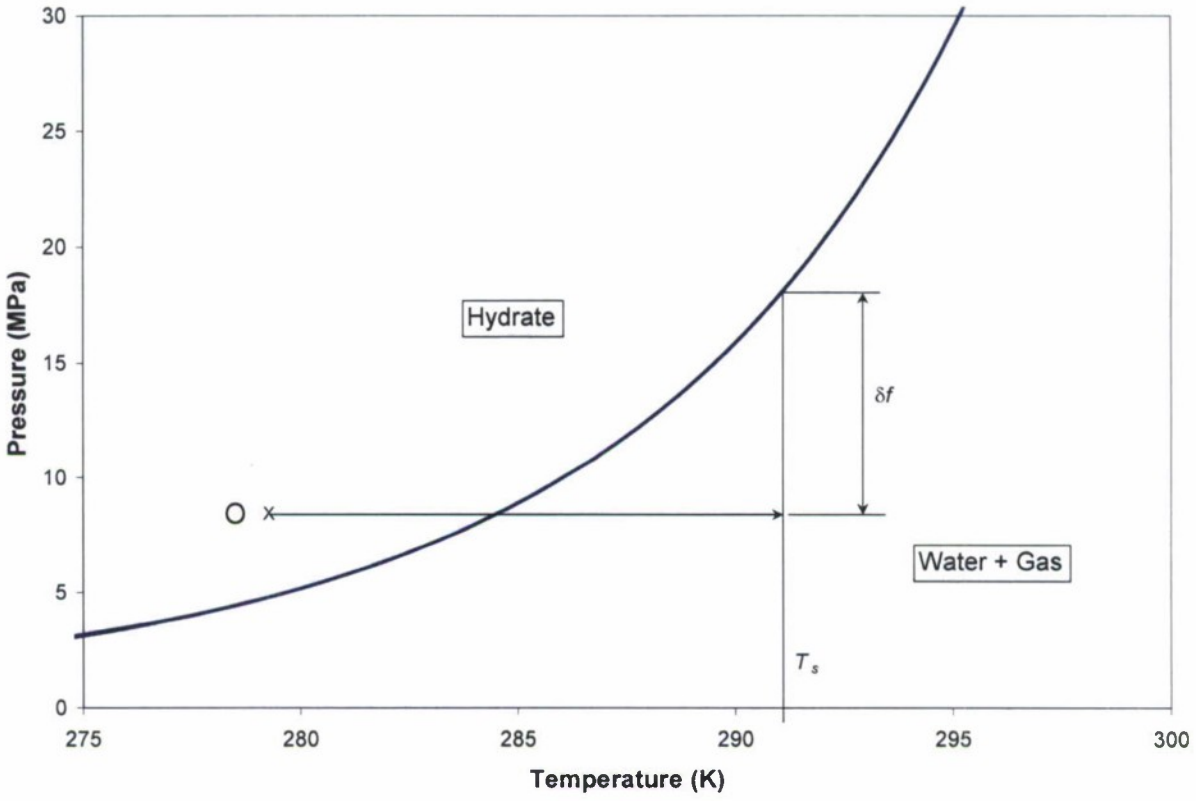

Figure 5.4. Definition of the driving fugacity difference δf in the intrinsic hydrate dissociation kinetics.

Assuming that the hydrate decomposition area is the same as the sample geometric upper surface area, the obvious relationship $dN/dt = \rho A(dL/dt)$ holds. A combination of this identity with Equations (2) and (5) yields an implicit equation in T_s:

$$-k\frac{\partial T}{\partial z}(L) + H(\theta - T_s) - \lambda K_0 \exp\left(-\frac{E}{RT_s}\right)\{f[p_{eq}(T_s;s),T_s] - f(p,T_s)\} = 0 \tag{6}$$

The overall solution procedure is adapted from Jamaluddin *et al.* (1989) who considered hydrate decomposition from a constant supply of radiant heat. It involves a discretization of Equation (1) using pseudo-coordinates z_i proportional to L within the hydrate sample. This yields a number of (time) first-order ordinary differential equations (ODEs). Replacing z with the pseudo-coordinates, however, gives rise to advective terms of the form $\frac{dz_i}{dt}\frac{\partial}{\partial z_i}$ in the right-hand-sides of the ODEs. This was not accounted for in Jamaluddin *et al.* (1989). Additional ODEs for L and θ are available from Equations (2) and (3). At each time step, s is given by Equation (4) and T_s determined either by invoking thermodynamic equilibrium or by solving Equation (6). The complete system of ODEs can be solved with a standard fourth-order Runge-Kutta scheme.

Initial conditions, sample geometry and injection characteristics must be provided. Other parameters are typical estimates from the literature. In preliminary calculations, the heat transfer coefficient H was selected as a constant.

The value measured by the Coriolis flow meter is proportional to $\frac{dN_{gas}}{dt} = -\frac{dN}{dt}$ while the cumulative values derived from both water level and load cell are proportional to $N_{gas} = \rho A(L_0 - L)$.

Data reduction protocol

Experimental parameters are shown in Table 5.1. The density of the injected methanol-water solution, ρ_{inj}, is from Mikhail and Kimel (1961). One of the features of the experimental apparatus is the redundancy provided for the measurement of the amount of methane released during hydrate dissociation. This is done directly by a flow meter while time-integrated values are accessible from water level and load cell measurements. One issue with the injection of a liquid solution as ($q_{inj} \neq 0$) is that a volume of gas is displaced from the headspace overlying the hydrate sample. This occurs *per se*, whether concurrent hydrate dissociation takes place or not. Such an extraneous contribution must be evaluated precisely and subtracted from the data records. Also, the range of direct measurements from the selected Coriolis flow meter could not exceed about 1.1 standard liter per minute (slpm). Therefore, information from this instrument was not available at times of higher gas release which roughly coincided with methanol injection.

Table 5.1. Selected record parameters.

Record # (date)	MEOH (% volume)	s_0	ρ_{inj} (kg/m^3)	$p_{chamber}$ - p_{atm} (psig)	p_{core} - p_{atm} (psig)	T_0 (°C)	T_{inj} (°C)
051108	0	0	1000	733	715	4	4
051028	25	0.208	963	734	730	4	4
051031	25	0.208	963	735	730	4	4
050930	50	0.440	924	732	800	4	4
051109	50	0.440	924	734	715	4	6
051003	75	0.702	867	732	800	4	10
051012	100	1	786	736	730	4	10

Calibration is greatly facilitated by the existence of data collected on November 8, 2005 (Record # 051108) when distilled water was injected and no detectable hydrate dissociation took place. The response of the load cell and level indicator can entirely be ascribed to the gas displacement effect from liquid injection. Neglecting small temperature differences between the container holding the hydrate core sample and the chamber where load cell and water level indicator are located, the volume flow rate anomaly υ corresponding to liquid injection simply is:

$$\upsilon = \frac{q_{inj} p_{core}}{\rho_{inj} p_{chamber}} \tag{7}$$

Calling LV the water level time history, the following equality holds for Record # 051108:

$$LV(t)-LV(0)=\{LV(\infty)-LV(0)\}\frac{\int_0^t q_{inj}\,dt}{\int_0^\infty q_{inj}\,dt} \tag{8}$$

A similar equation is valid for the load time history LC of Record # 051108.

Figure 5.5 shows excellent agreement between measured values of $LV(t)$ - $LV(0)$ and Equation (8). A residual background signal of about 0.06 g/s had to be removed from the injection data. This offset was observed for all records.

By virtue of Equations (7) and (8), the following water level correction term δLV should be subtracted from the water level time history of any record:

$$\delta LV(t)=[\frac{\{LV(\infty)-LV(0)\}\rho_{inj}\,p_{chamber}}{p_{core}\int_0^\infty q_{inj}\,dt}]_{051108}\frac{p_{core}}{\rho_{inj}\,p_{chamber}}\int_0^t q_{inj}\,dt \tag{9}$$

A similar formula is applicable to load cell data. In Equations (8) and (9), pressures are assumed steady enough to be averaged out of the time integrals. Figures 5.6a and 5.6b display the corrected water level and load cell time series obtained by subtracting δLV and δLC, respectively, from the raw data for Record # 051003.

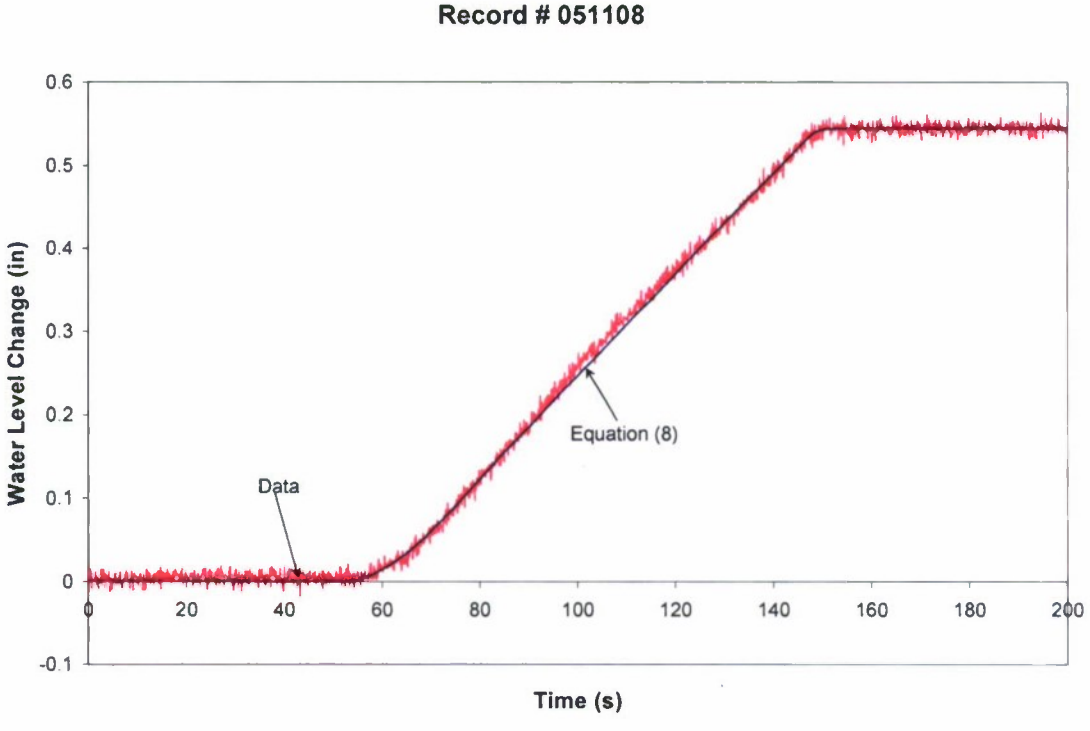

Figure 5.5. Calibration of the gas displacement resulting from liquid injection.

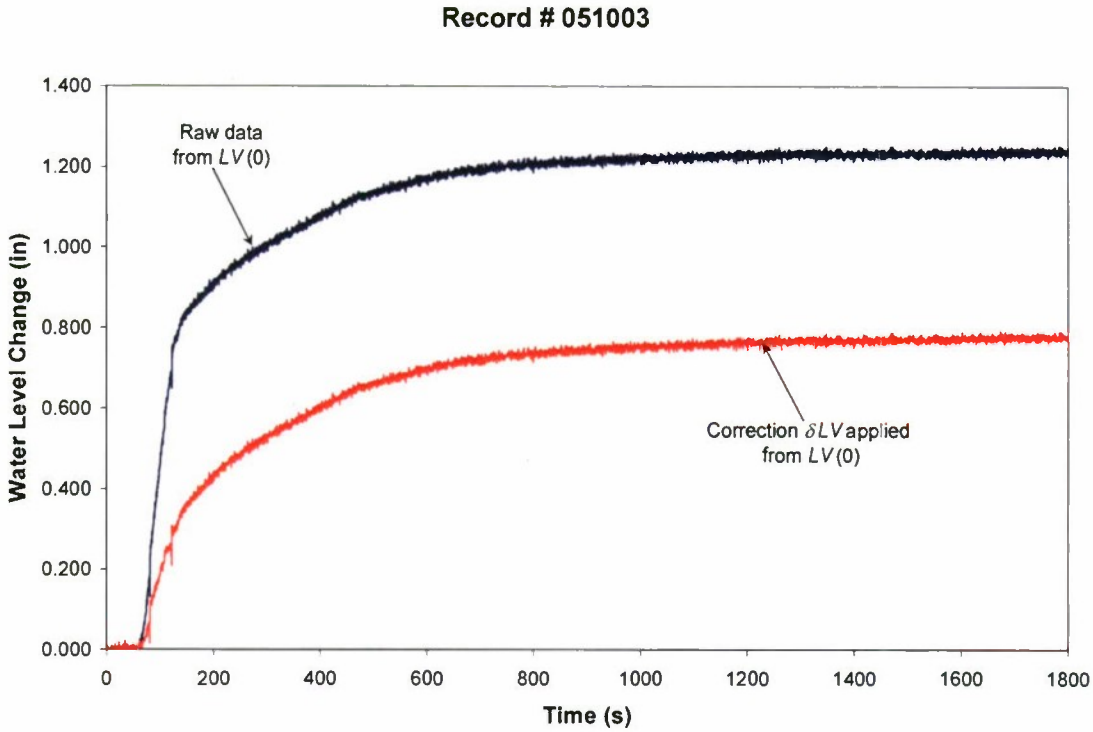

Figure 5.6a. Example of water level data corrected for the gas displacement resulting from liquid injection.

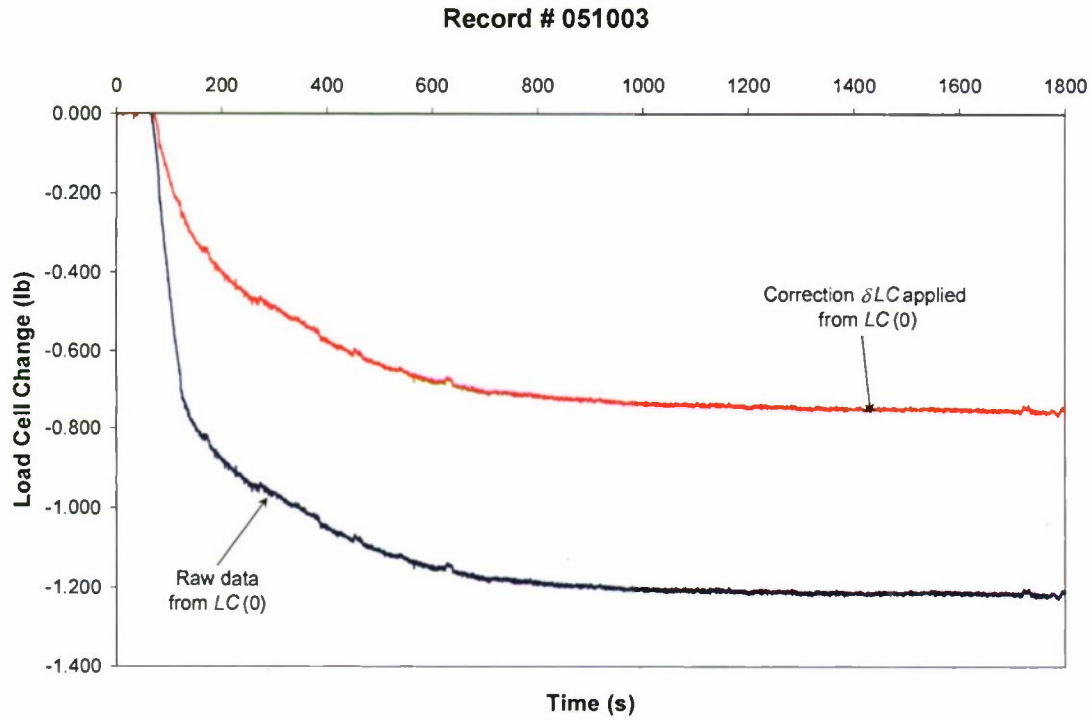

Figure 5.6b. Example of load cell data corrected for the gas displacement resulting from liquid injection.

Calculations

A computer code was written based on the model described above. Some of the input parameters (e.g., s_0, T_0 and T_{inj}) are given in Table 1. Although L_0 could be estimated in each case, small values of a few centimeters resulted in numerical instabilities as the spatial grid shrank too much with time; while improvements of the numerical scheme are possible, L_0 was set to 0.5 m instead. With little loss of generality, the methane hydrate sample was assumed to have full guest-molecule occupancy ($n = 5.75$).

The three-phase equilibrium pressure $p_{eq}(T; s)$ depends on the methanol mass fraction s in the liquid. This dependency was parametrized by including a temperature offset δT in the formula of Handa (1990) for $p_{eq}(T; 0)$:

$$\begin{cases} p_{eq} = p_{atm} \exp\{-1205.907 + \dfrac{44097}{T + \delta T} + 186.7594 \log(T + \delta T)\} \\ \delta T = 5\left(\dfrac{s}{0.1}\right)^{1.2} \end{cases} \tag{10}$$

Figure 5.7 shows a reasonable fit between Equation (10) and available data (compiled from Sloan, 1998, *p. 404, Ch. 6*).

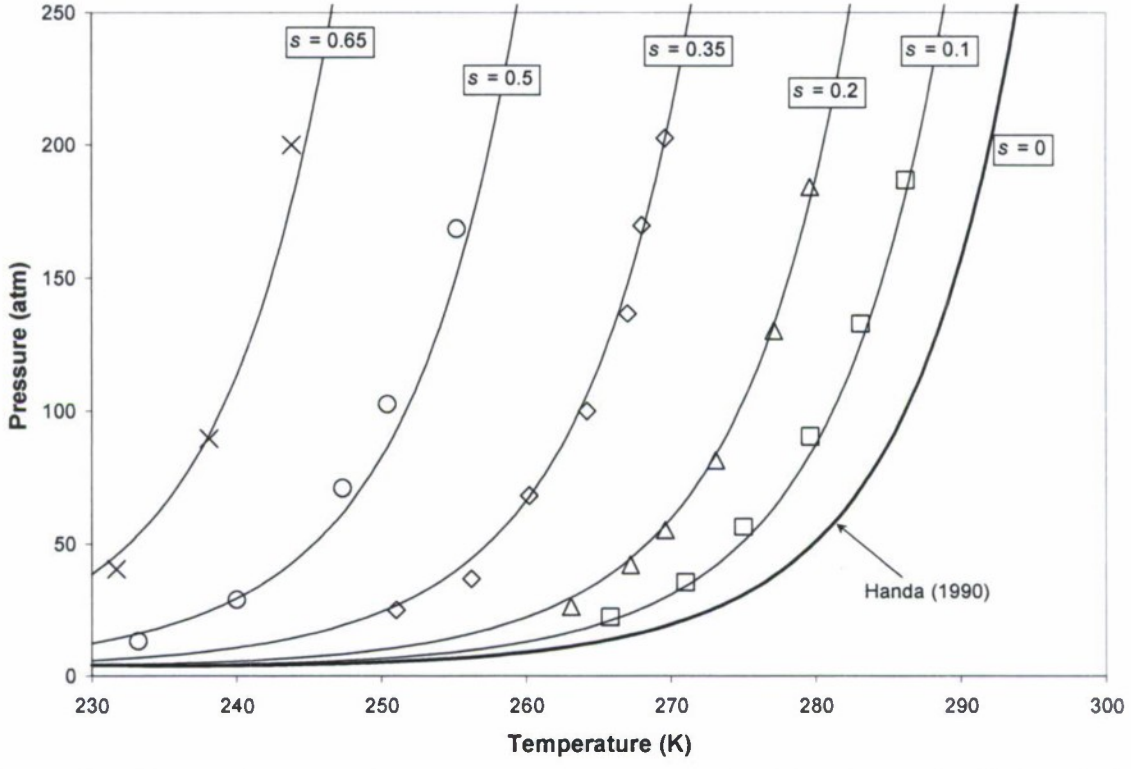

Figure 5.7. Three-phase equilibrium pressure p_{eq} as s varies: Equation (10) (thin lines); data (symbols).

The methanol solution injection function q_{inj} was simplified into a finite-width step, as illustrated in Figure 5.8. This reflects the selected experimental protocol accurately while eliminating noise from the data; also, time integrals of q_{inj} become straightforward. A value of 1.7 g/s was adopted and the injection time was prorated in inverse proportion to the initial methanol volume fraction, from 188 s with Record # 051028 (25% MEOH).

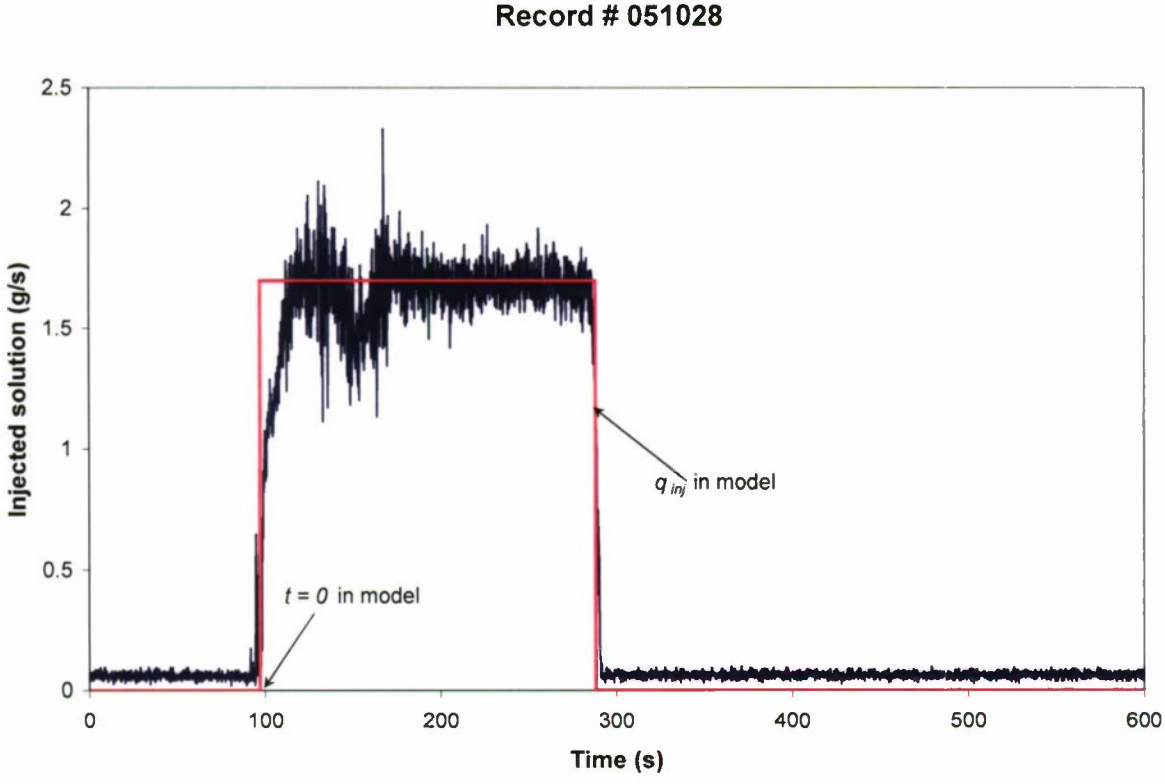

Figure 5.8. Sample representation of q_{inj} in computer model.

Results (constant H)

The two methods described previously to determine the hydrate surface temperature T_s were labeled 'Equilibrium' and 'Clarke Bishnoi,' respectively. Three experimental tests corresponding to different methanol concentrations of the inhibitor solution were selected for preliminary calculations: Records # 051028, 050930 and 051003. The turbulent convective heat transfer coefficient H was assumed constant, with values of 1000 or 3000 W/m^2-K. Figures 5.9 through 5.11 show calculated results of gas flow rate and load cell change for the three Records under consideration. Gas flow rate data in Figures 5.9a, 5.10a, and 5.11a are only relevant below about 1.1 slpm, the maximum reading from the Coriolis flow meter. Fortunately, physical phenomena taking place during higher gas release, especially when the liquid inhibitor solution is injected, may be examined via the load cell and water level data.

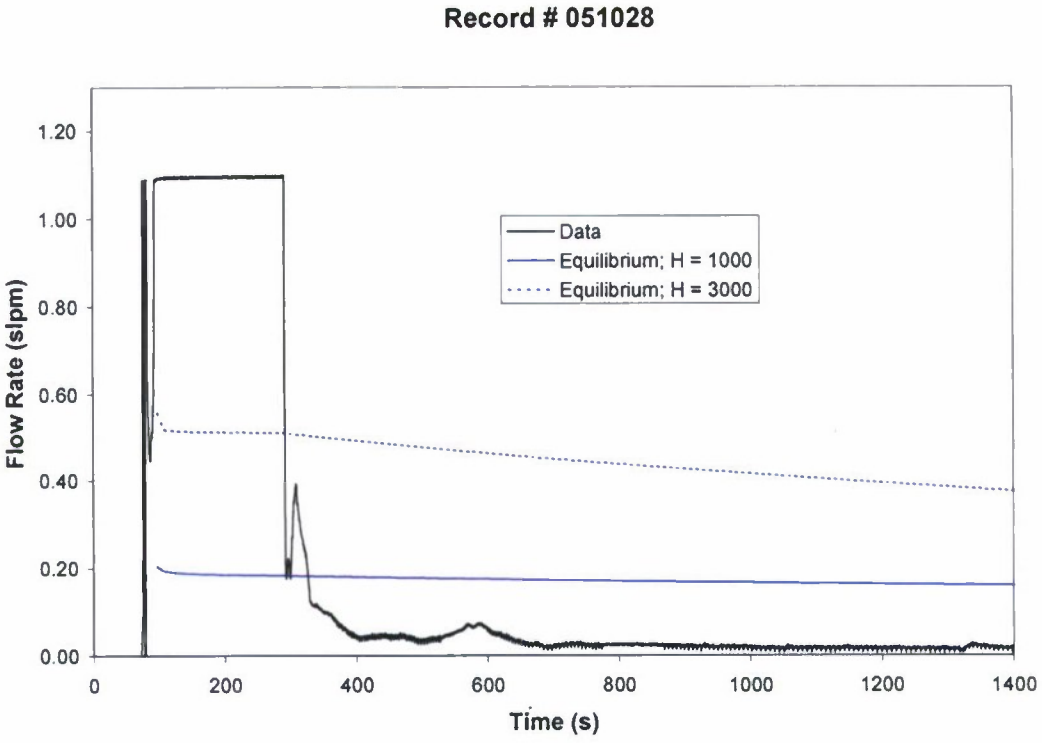

Figure 5.9a. Coriolis flow meter data and preliminary calculations for Record # 051028.

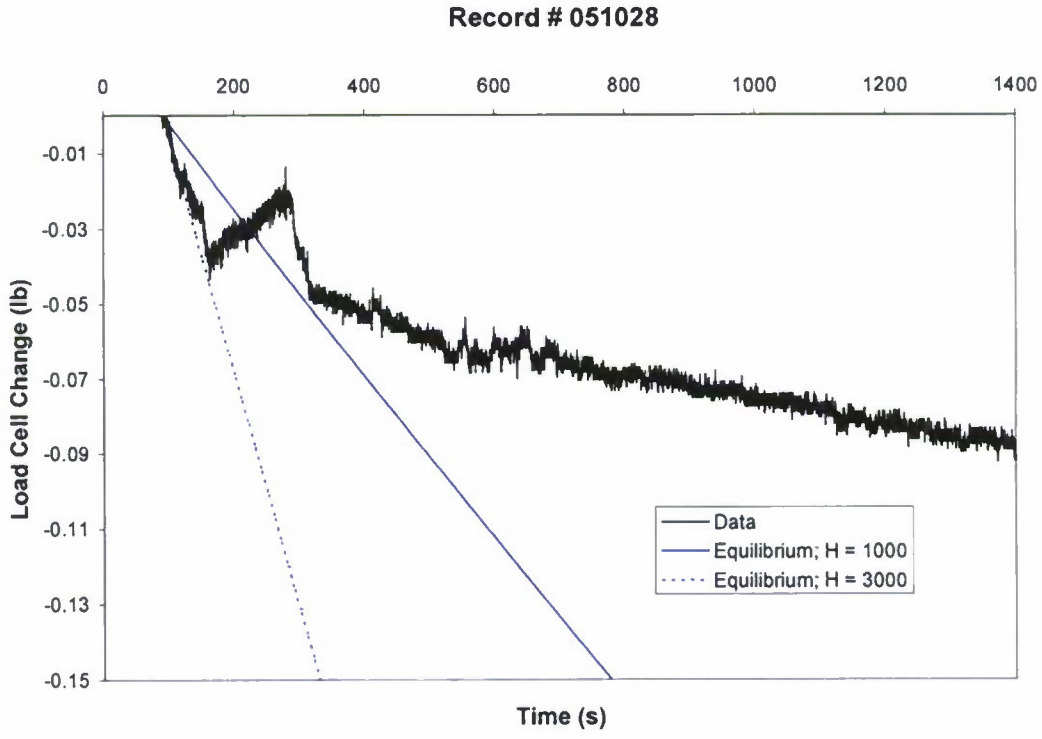

Figure 5.9b. Load cell data and preliminary calculations for Record # 051028.

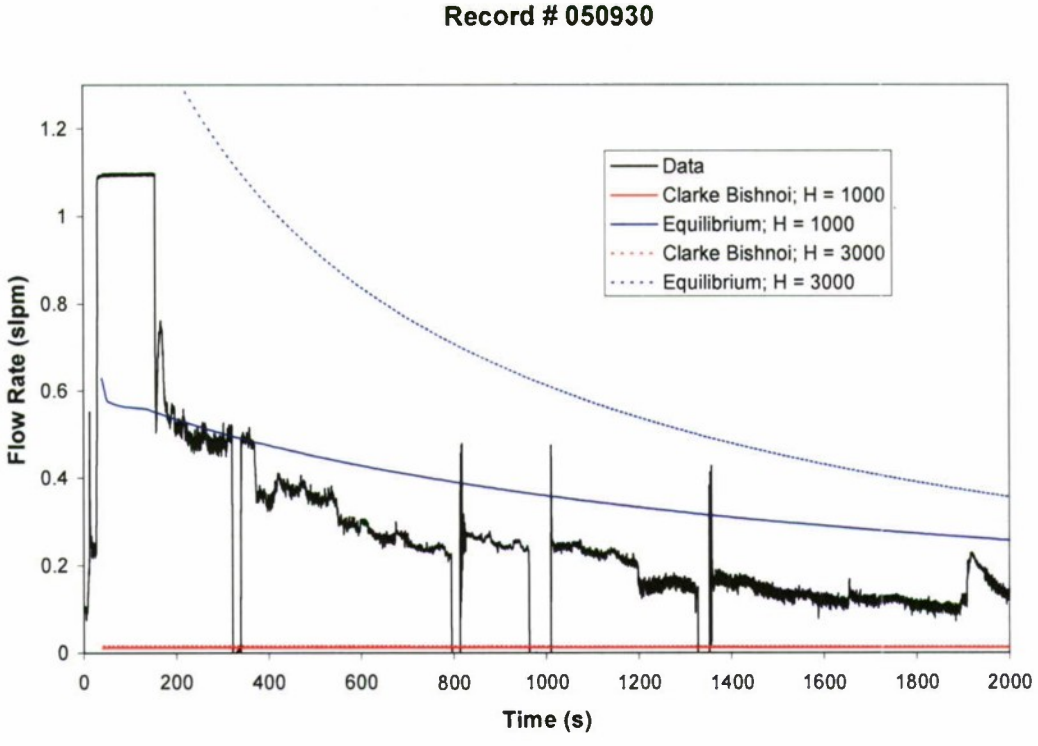

Figure 5.10a. Coriolis flow meter data and preliminary calculations for Record # 050930. Coriolis meter signal dropouts in the time record are due to small, short-term pressure adjustments made manually to the evolved-gas collection reservoir.

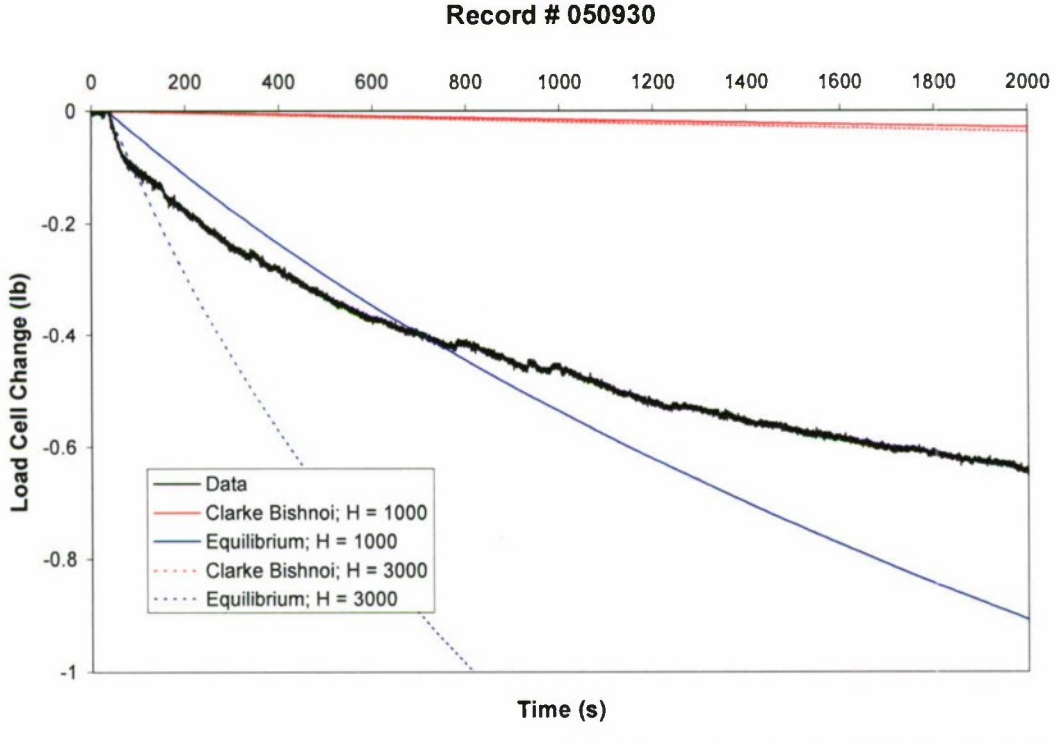

Figure 5.10b. Load cell data and preliminary calculations for Record # 050930.

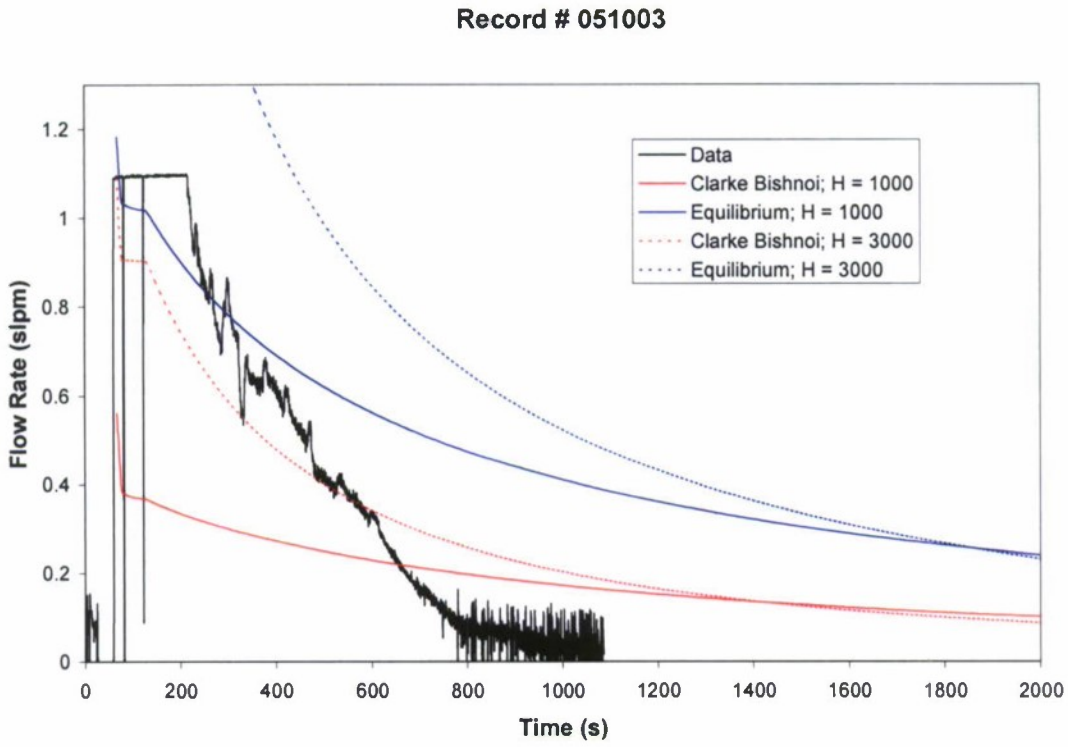

Figure 5.11a. Coriolis flow meter data and preliminary calculations for Record # 051003.

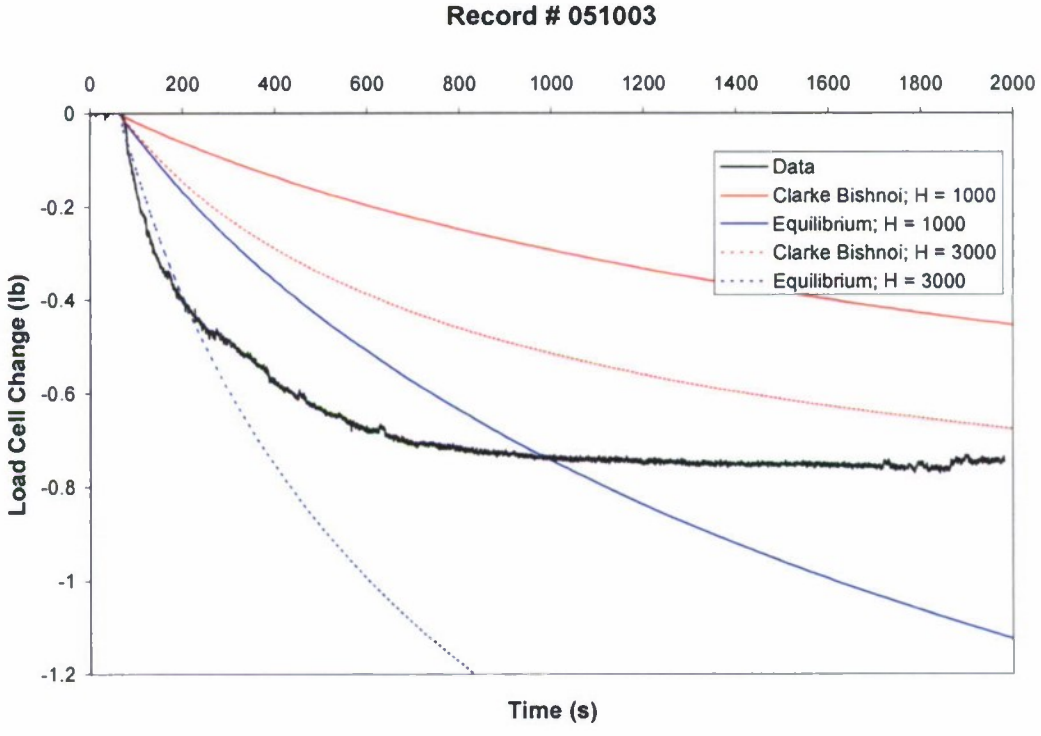

Figure 5.11b. Load cell data and preliminary calculations for Record # 051003.

For Record # 051028 (injection of 25% MEOH solution by volume), the intrinsic dissociation kinetics of Clarke and Bishnoi (2001) yield such small hydrate dissociation rates that the corresponding calculations do not appear in Figures 5.9a and 5.9b. Results in Figure 5.9b with a dissociation surface at equilibrium suggest that much faster kinetics may hold at least for a minute or two.

These observations essentially are corroborated with Record # 050930 (injection of 50% MEOH solution by volume). Here again, equilibrium kinetics seems relatively more successful in representing the data. While a higher heat transfer coefficient H of 3000 W/m^2-K still does well immediately following injection, a more moderate value of about 1000 W/m^2-K provides reasonable predictions over 10 to 20 minutes.

Record # 051003 (injection of 75% MEOH solution by volume) finally shows substantial hydrate dissociation even with the 'Clarke-Bishnoi' kinetics. 'Equilibrium; H = 3000' results still do quite well matching the data at small times of a couple of minutes.

As conceived, the one-dimensional model using Equation (5) has three fundamental parameters (K_0, E and H), while only H must be set when equilibrium kinetics is used. There likely are different ways to fit these model parameters to match the data, but a given choice should hold fairly well for all data records, especially in the case of *intrinsic* processes. While established on well-written publications, the Clarke-Bishnoi hydrate dissociation formalism already has proved difficult to use with hydrate dissociation mechanisms other than depressurization without substantial *ad hoc* modifications of the kinetic constants (Moridis *et al.*, 2005; Nihous and Masutani, 2006). This is believed to reflect a fundamental ambiguity in using the fugacity driving force δf (cf. Figure 5.4) as a metric ('distance' from equilibrium) for all hydrate dissociation mechanisms. In the case of experiments at constant pressure, for example, a more natural choice for such a metric would be (T_s - T_{eq}). A preliminary exploration of this concept was attempted in the present model, and the new kinetic formalism did not appear to fare any worse than the Clarke-Bishnoi equation. Such an approach, however, only shifts the problem from one thermodynamic variable to another, since one ultimately may have to consider cases of hydrate dissociation under *simultaneous* depressurization and heating.

Results with variable H

Since the 'Equilibrium' approach is simpler and appeared to predict experimental measurements relatively better and more consistently, it was adopted before letting the heat transfer H vary with time. Intuitively, the more gas is released per unit dissociation area, the more turbulence occurs in the liquid phase contacting the hydrate surface. This is anticipated to affect thermal transport through the multiphase fluid field. The rate of gas release per unit area is proportional to the dissociation front velocity dL/dt. This motivated the choice of simple functional forms $H = C\,(\mathrm{d}L/\mathrm{d}t)^m$ to be tested in the numerical model, where C is a constant and m a positive exponent. The evolution Equation (2) for dL/dt becomes implicit and must be solved at each time step within the Runge-Kutta scheme.

Figures 5.12 through 5.17 show selected load-cell and water-level data records versus numerical results. In particular, Figures 5.12 through 5.14 can be compared to Figures 5.9b, 5.10b and 5.11b.

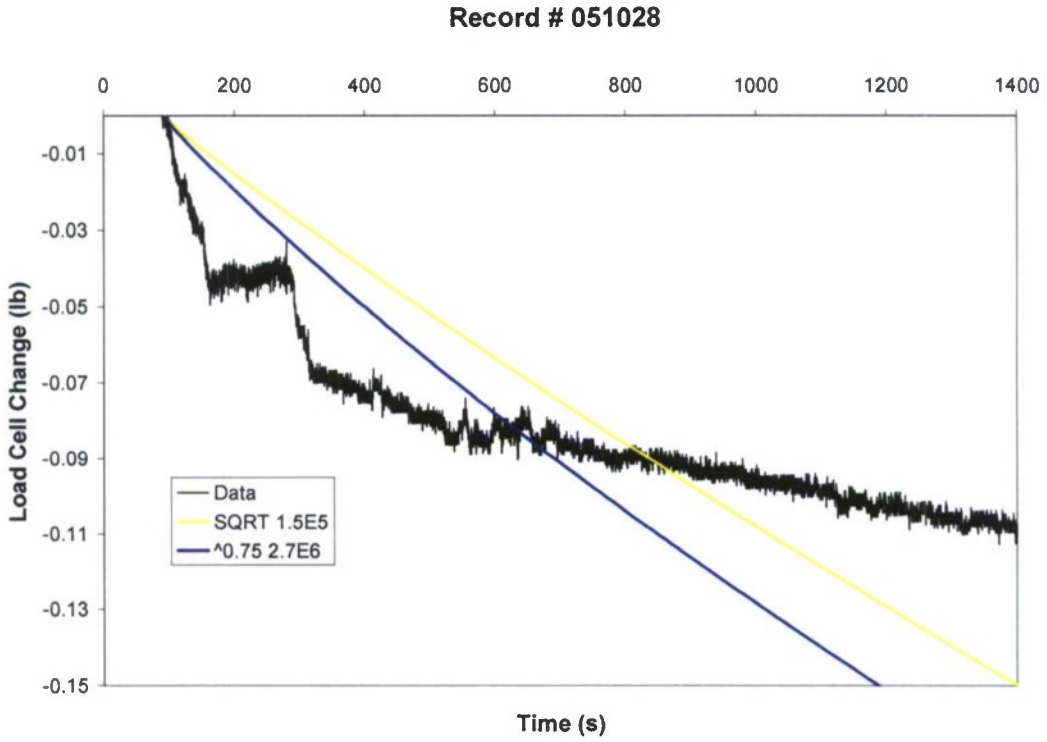

Figure 5.12. Load cell data and variable heat transfer coefficient calculations: Record # 051028.

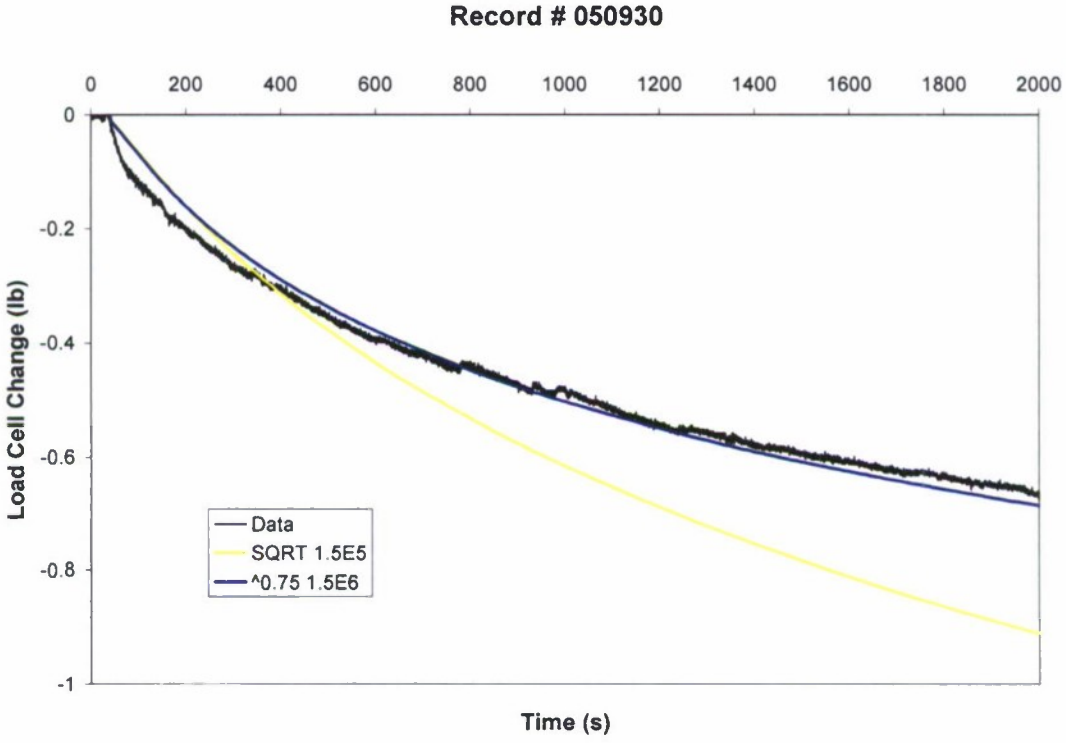

Figure 5.13. Load cell data and variable heat transfer coefficient calculations: Record # 050930.

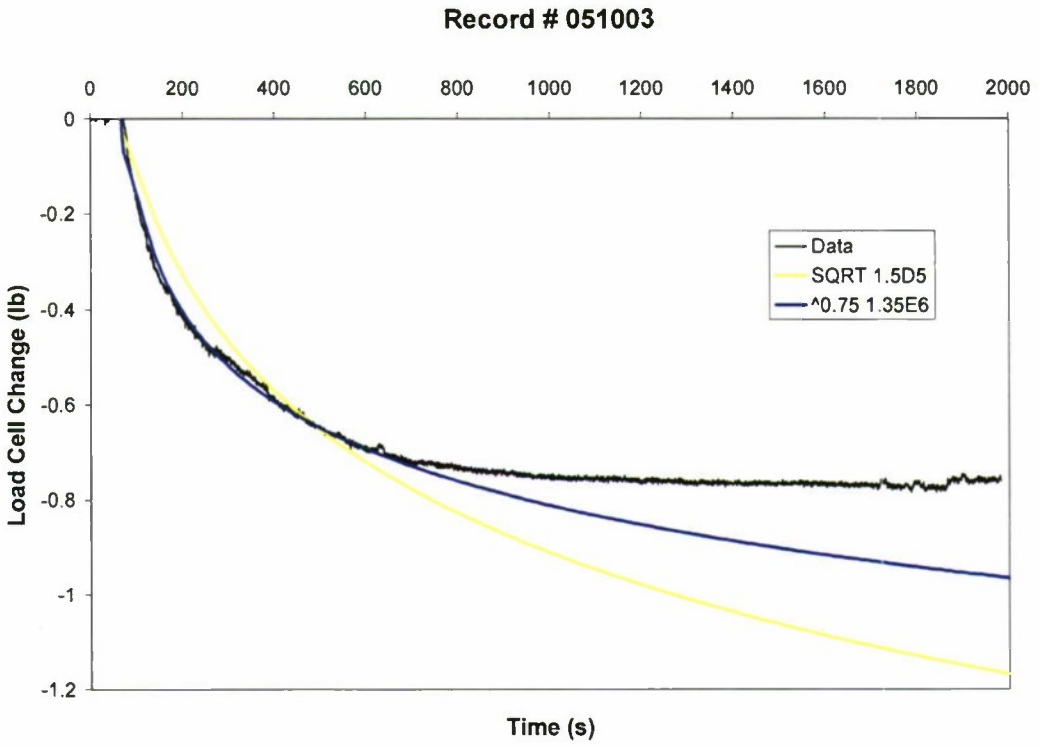

Figure 5.14. Load cell data and variable heat transfer coefficient calculations: Record # 051003.

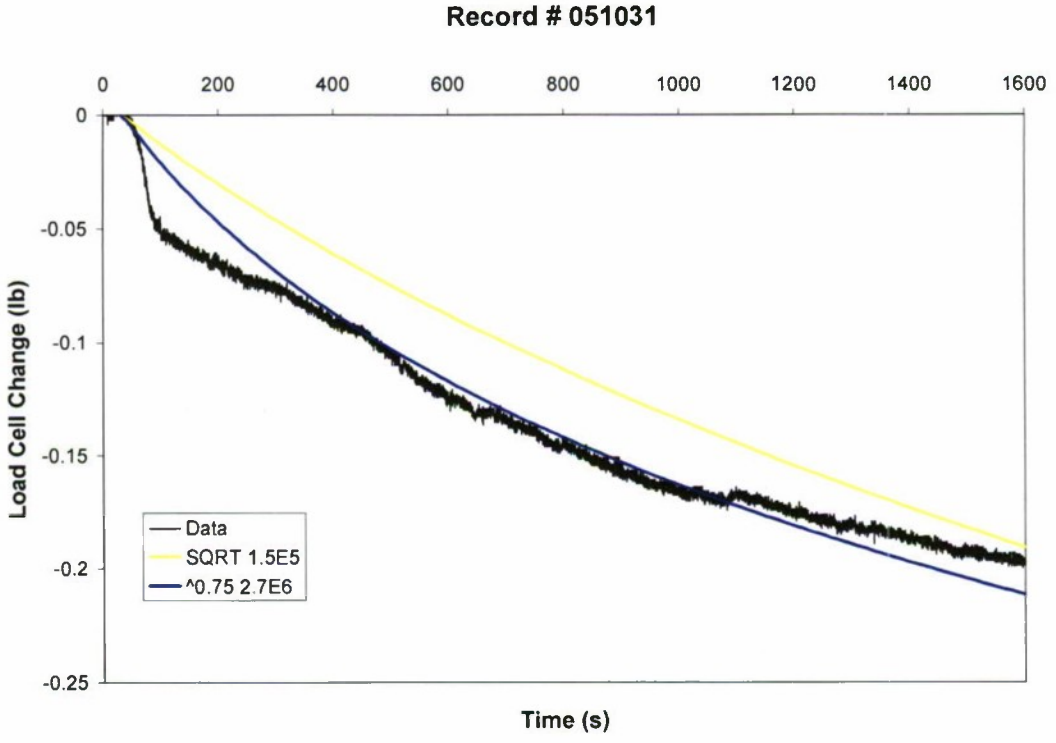

Figure 5.15. Load cell data and variable heat transfer coefficient calculations: Record # 051031.

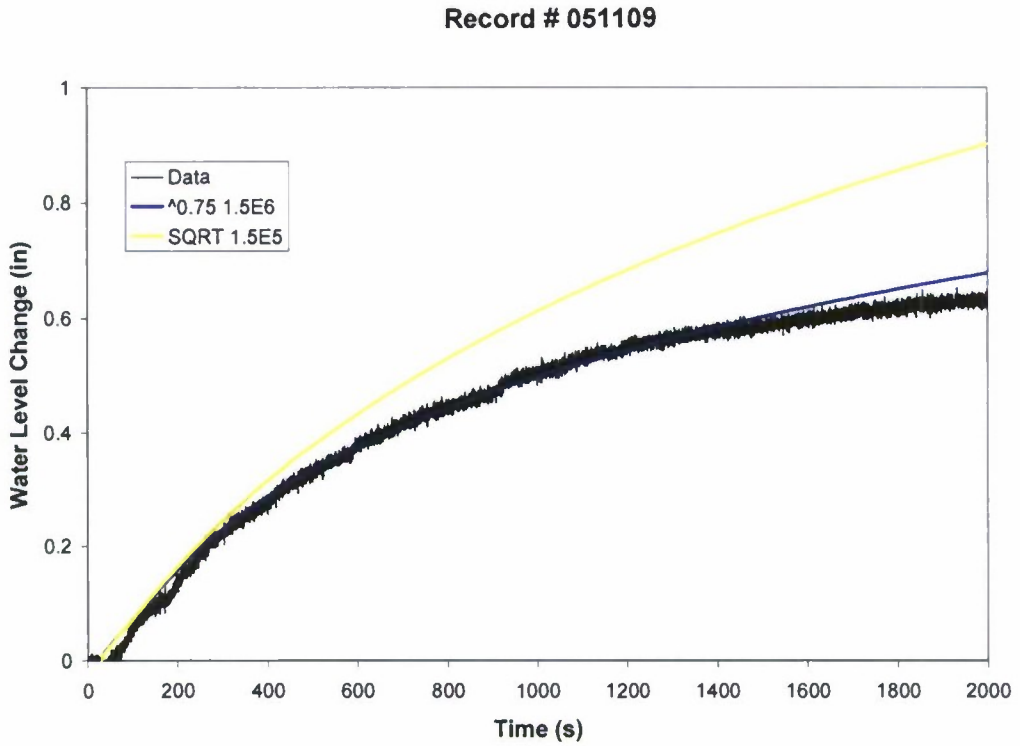

Figure 5.16. Water level data and variable heat transfer coefficient calculations: Record #051109.

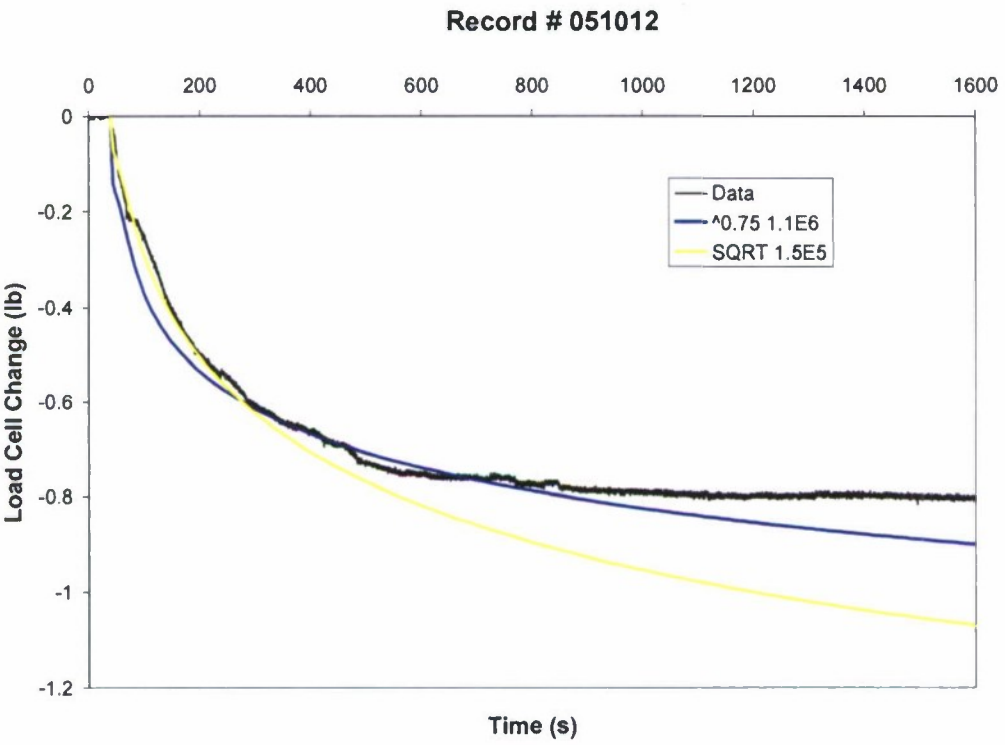

Figure 5.17. Load cell data and variable heat transfer coefficient calculations: Record # 051012.

One set of calculations, labeled 'SQRT 1.5E5', corresponds to $m = 0.5$ and C equal to 150,000. The other set was obtained with $m = 0.75$ and values of C increasing from 1.1×10^6 to 2.7×10^6 as the methanol concentration of the injected solution decreases[1]. Overall, a reasonable match between data and calculations was obtained. With the methanol-rich cases of Records # 051003 and 051012, it should be noted that after about 10 minutes, the *real* hydrate sample a few centimeters long is likely to have been consumed, while the numerical sample ($L_0 = 0.5$ m) would continue to dissociate. A single value of C when $m = 0.5$ may be attractive for the sake of formal simplicity, but there is no reason *a priori* to rule against a value of C being different with different methanol concentrations since the physical properties of methanol-water solutions significantly change with composition. In this case, the choice $m = 0.75$ provides some very good fit with the data.

A dimensional analysis of typical convective heat transfer problems results in a relationship between Nusselt, Prandlt and Reynolds numbers. Many empirical relationships, sometimes based on boundary-layer theory, express the Nusselt number as the product of fractional powers of the Reynolds and Prandtl numbers, up to a multiplicative constant (e.g., Kreith and Bohn, 2001). Data on the density, viscosity and thermal conductivity of liquid methanol-water solution was collected from the literature (Mikhail and Kimmel, 1961; Isdale *et al.*, 1985; Li, 1976) and a linear dependence of specific heat on composition was assumed. Interpreting dL/dt as the velocity in a Reynolds number, we tried to relate the expression selected for H in the numerical algorithm to an equivalent empirical relationship between non-dimensional numbers. Although all physical properties of methanol-water solutions monotonically increase as the methanol contents drops, with the exception of viscosity, no satisfactory correlation was found that could explain the variation of C when $m = 0.75$.

Conclusions

The kinetic behavior of methane hydrate samples as they dissociate in the presence of a thermodynamic inhibitor (methanol) was investigated experimentally. A liquid phase resulting from the initial injection of the inhibitor solution and evolved water from hydrate dissociation was allowed to stay in contact with the samples. Dissociation kinetics were estimated by measuring the rate of release of gas (methane). A one-dimensional time-domain representation of the thermal processes involved was developed. This allowed a simulation of the experimental procedure while testing several hydrate dissociation kinetic and heat transfer models at the decomposing hydrate interface.

While keeping the convective (liquid side) heat transfer coefficient constant, preliminary calculations were performed. The dissociating hydrate surface either was assumed to be at equilibrium, or its temperature was determined by including an existing intrinsic dissociation kinetic model. Results suggested that the simpler equilibrium assumption was better able to represent experimental data. The apparent difficulty with the intrinsic dissociation formalism may indicate a more general lack of its applicability to situations when hydrates are not decomposed by depressurization, since the definition of a driving fugacity difference then becomes ambiguous.

Finally, variations of the convective heat transfer coefficient as a function of the dissociating front velocity were allowed in the numerical model. This was pursued as a means to examine the intuitive argument that the level of turbulence at the interface should increase with the rate of gas

[1] Units for C vary with m and correspond to H and dL/dt expressed in SI units.

release, affecting thermal transport in the complex bubbly flow. Results indicated that a simple square root relationship (exponent 0.5) and a single multiplicative factor—similar in concept to typical empirical correlations—provided a reasonably good match with all data sets. A slightly higher exponent (0.75) with multiplicative factors adjusted for specific experimental conditions (composition of the injected methanol-water solution) yielded even better fits between calculations and data. Many physical parameters of methanol-water solutions, such as thermal conductivity, specific heat and density, increase as methanol content decreases. The same trend in the adjusted multiplicative factors was observed, but it could not be precisely interpreted at this time.

While more experimental and theoretical work undoubtedly could shed additional light on the issue, the present set of experiments and the corresponding analysis tend to indicate that hydrate dissociation is controlled by heat and mass transfer at the interface. Existing models of intrinsic dissociation kinetics may ultimately be refined to more precisely quantify the state of disequilibrium of the interface, but it remains to be determined whether overall predictive capabilities would improve as a result, since such kinetic phenomena may be faster than earlier postulated. In the meantime, complex heat transfer characteristics in the multiphase dissociating hydrate region seem worthy of more scrutiny.

Nomenclature

A decomposition area (m^2)
C constant in the expression of H as a function of dL/dt (variable units)
c_p specific heat of hydrate (J/mol-K)
c_{pi} specific heat of methanol (J/kg-K)
c_{pw} specific heat of water (J/kg-K)
E molar activation energy for hydrate dissociation (J/mol)
f methane fugacity (Pa)
H turbulent convective heat transfer coefficient (W/m^2-K)
k hydrate heat conductivity (W/m-K)
K_0 hydrate dissociation constant (mol/m^2-Pa-s)
K_d hydrate dissociation constant (mol/m^2-Pa-s)
L hydrate sample length (m)
L_0 initial hydrate sample length (m)
LC load cell reading (N)
LV water level (m)
m exponent in the expression of H as a function of dL/dt
M_w molar mass of water (kg/mol)
n hydrate number
N mole of hydrate (composition $CH_4.nH_2O$)
N_{gas} mole of methane (from dissociation)
p pressure (Pa)
p_{atm} atmospheric pressure (Pa)
$p_{chamber}$ pressure in load cell container (Pa)
p_{core} pressure in hydrate sample container (Pa)
p_{eq} three-phase methane hydrate equilibrium pressure (Pa)
q_{inj} mass injection rate for methanol solution (kg/s)
R gas constant (J/mol-K)
s methanol mass fraction

s_0 initial methanol mass fraction
t time (s)
T hydrate temperature (K)
T_0 initial hydrate temperature (K)
T_{eq} three-phase methane hydrate equilibrium temperature (K)
T_{ref} reference temperature (K)
T_{inj} temperature of injected methanol solution (K)
T_s hydrate decomposition temperature (K)
V_{ref} reference ideal-gas molar volume (m^3)
z vertical coordinate (m)
z_i pseudo-vertical coordinate depending on L (m)

Greek

α hydrate thermal diffusivity (m^2/s)
δf driving fugacity difference in intrinsic decomposition rate (Pa)
δLC load cell correction from liquid injection effect (N)
δLV water level correction from liquid injection effect (m)
λ hydrate heat of dissociation (J/mol)
ρ hydrate density (mol/m^3)
ρ_{inj} density of injected methanol solution (mol/m^3)
θ bulk liquid temperature (K)
υ flow rate anomaly during liquid injection (m^3/s)

5.2.1.2 Subsea Power Generation: Heat Capacity of Water at Elevated Pressure

The deep ocean is a region of great tactical, commercial, and scientific significance. A principal hurdle to deep subsea operations is the availability of energy. For example, there are thousands of instruments deployed on the ocean floor for monitoring, surveillance, and navigation that are powered by battery packs with finite lifetimes and capacities. After these batteries are exhausted, typically in less than a year, the device must either be recovered or abandoned. Deep submersibles also run on batteries or are tethered to the surface by a power umbilical. Autonomous Underwater Vehicles (AUVs) that are driven by fuel cells using onboard stores of hydrogen and oxygen are under development, but they have limited range and will need to surface periodically for refueling. Seafloor power cables have also been employed to bring electricity from shore to the ocean depths, but they cannot be deployed at all locales to all depths and, like umbilicals, are vulnerable to natural and human hazards.

The widespread abundance of accessible methane on the seafloor, in the form of free gas seeps or hydrate deposits, offers the possibility for development as an *in situ* energy resource. Toward this end, HNEI received a grant from DARPA (Grant No. HR0011-05-1-0039) in 2005 to conduct a one-year study to evaluate the technical feasibility of generating electrical power in the deep ocean from seafloor methane and to initiate the design of a first prototype system for field deployment. That investigation concluded that it would be possible to produce net power of the order of 100 W employing existing technologies. The lifetime of such a system was unclear; however, values of 1 – 5 years appear to be reasonable, and probably could be extended through additional R&D, careful design, and component redundancy.

The recommended configuration would thermochemically reform methane fuel gas from seeps or hydrates to H_2, which would be converted to electricity in a fuel cell. Although the long-reaching goal is for self-sufficient systems, i.e., devices that run entirely on ambient fuel and oxidizer resources, it was concluded that some stored oxidizer brought from the surface will be required, since the current level of technology to extract dissolved O_2 from sea water is not adequate to provide the concentrations needed to reform methane. On the other hand, dissolved oxygen (DO) extraction does appear to be a viable option to supply the fuel cell cathode.

The DARPA study concluded that the necessary next step was to test and characterize major components (i.e., reformer; fuel cell; membrane contactor), first on the benchtop, then in pressure chambers at simulated underwater conditions, and finally offshore. During the assessment of candidate devices prior to initiating this testing, questions arose regarding the thermal properties of water and aqueous solutions at the elevated pressures which prevail in the deep ocean. The ability to predict accurately these properties is important to determine the performance of aqueous alkaline fuel cells and other devices that will likely be employed in the subsea power system.

In 1995, the International Association for the Properties of Water and Steam (IAPWS) adopted a new formulation called "The IAPWS Formulation 1995 for the Thermodynamic Properties of Ordinary Water Substance for General and Scientific Use." In that work, nearly all the data for the isobaric heat capacity (C_p) for water are based on measurements of Sirota's group in the former Soviet Union conducted during the period from 1956 to 1970 (Wagner & Pruss, 2002; Sirota and Maltsev, 1959). Since then, only two further C_p data sets have been published that were used for fitting the IAPWS-95 formulation. These are the measurements of Angell *et al.* (1982), who investigated subcooled liquid water at ambient pressure, and the high-pressure C_p data measured by Czarnota (1984). Recently, Archer and Carter (2000) published C_p measurements for subcooled liquid water, which cover almost the same region as the data of Angell and coworkers (1982).

When we attempted to confirm experimentally the predictions of the IAPWS 1995 model for conditions relevant to our subsea power generation application, we observed significant discrepancies. It seemed reasonable, therefore, to seek corroborations of the experimental reliability of the calorimetric data obtained many years ago, especially for high-temperature and high-pressure measurements in liquid phase (i.e., calorimetric experiments potentially affected by large systematic errors).

Experiments to Determine the Heat Capacity of High Pressure Water

Experiments were conducted to measure the specific isobaric heat capacity of pure water at elevated pressure (4.0 MPa) over a temperatures range of 298.15 K to 465.65 K for comparison with the IAPWS 1995 model predictions and with reference data reported by Wagner and Pruss (2002). The experiments were performed using our Calvet-Tian differential scanning calorimeter (Setaram, Model BT2.15), Figure 5.18. Water used in the study was deionized (resistivity $\geq$ 18 MΩ cm) and then degassed using helium. The helium-saturated water was then subjected to a vacuum to extract the helium and stored in a sealed glass container under a N_2 atmosphere. The pH value of the water was 7.0. Approximately 2.0 mL of the purified water was transferred into the calorimeter sample cell in a N_2-filled glove box to prevent absorption of CO_2 from the atmosphere. The sample cell was then placed in the calorimeter and connected to

the gas lines shown in Figure 5.18. The gas lines and buffer reservoirs were vacuum evacuated and purged with N_2 gas, and then pressurized to 4.0 MPa with N_2.

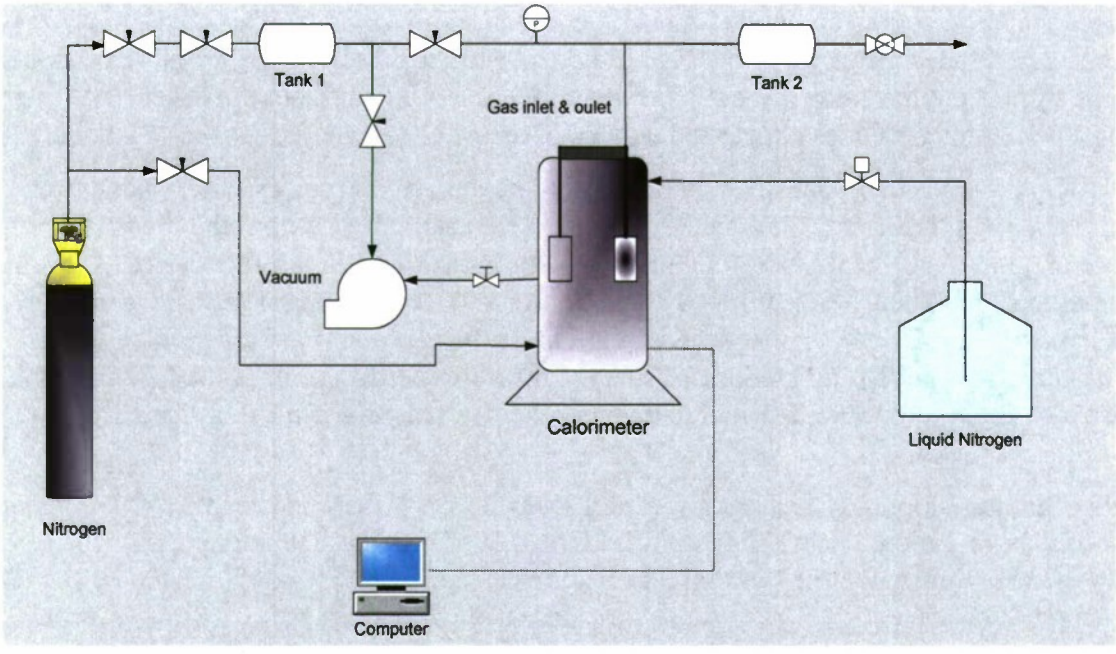

Figure 5.18. Calorimeter system employed to conduct heat capacity experiments.

Two different heating programs were employed to change the sample temperature. One program increased temperature continuously at a constant rate while the other increased sample temperature in steps. Figure 5.19 and Table 5.2 show the temperature histories employed to determine heat capacity.

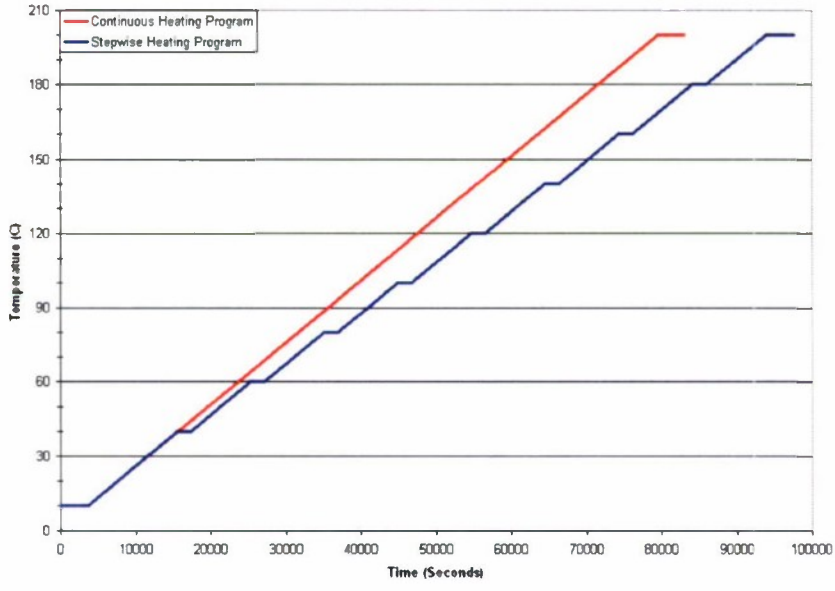

Figure 5.19. Heating programs used in the experiments.

Table 5.2. Continuous and stepwise heating programs.

Stage	Start Time (Seconds)	End Time (Seconds)	Initial Temperature (K)	Final Temperature (K)	Rate of Temperature Change (K/min)
			Continuous Heating Program		
1	0	3600	283.15	283.15	0
2	3600	79600	283.15	473.15	0.15
3	79600	83200	473.15	473.15	0
			Stepwise Heating Program		
1	0	3600	283.15	283.15	0
2	3600	15600	283.15	313.15	0.15
3	15600	17400	313.15	313.15	0
4	17400	25400	313.15	333.15	0.15
5	25400	27200	333.15	333.15	0
6	27200	35200	333.15	353.15	0.15
7	35200	37000	353.15	353.15	0
8	37000	45000	353.15	373.15	0.15
9	45000	46800	373.15	373.15	0
10	46800	54800	373.15	393.15	0.15
11	54800	56600	393.15	393.15	0
12	56600	64600	393.15	413.15	0.15
13	64600	66400	413.15	413.15	0
14	66400	74400	413.15	433.15	0.15
15	74400	76200	433.15	433.15	0
16	76200	84200	433.15	453.15	0.15
17	84200	86000	453.15	453.15	0
18	86000	94000	453.15	473.15	0.15
19	94000	97600	473.15	473.15	0

The advantage of the stepwise heating program over the continuous heating program is that the sample is allowed time to reach thermal equilibrium during the periods between temperature increases. The disadvantage, however, is that more time is needed to complete an experiment. Representative calorimetry data are shown in Figures 5.20 and 5.21 for continuous heating and stepwise heating, respectively.

Only a portion of the thermal energy measured with the calorimeter is absorbed by the water sample. The rest is used to heat the stainless steel sample cell and the nitrogen gas overlying the water. To account for this, continuous heating and stepwise heating tests were performed using a sample cell that did not contain water. Figure 5.22 compares thermograms obtained during continuous heating with and without water in the cell.

In addition to subtracting the energy required to heat the sample cell and N_2 gas, an additional correction was applied to the data to account for the change in the partial vapor pressure of water at elevated temperatures. Tables 5.3 and 5.4 present heat capacities determined from the continuous heating and the stepwise heating experiments. Mean and standard deviations are included for the triplicate tests that were performed. The tables also compare the present results with those of Wagner and Pruss (2002). Significant differences exist that appear to be exacerbated as temperature increases.

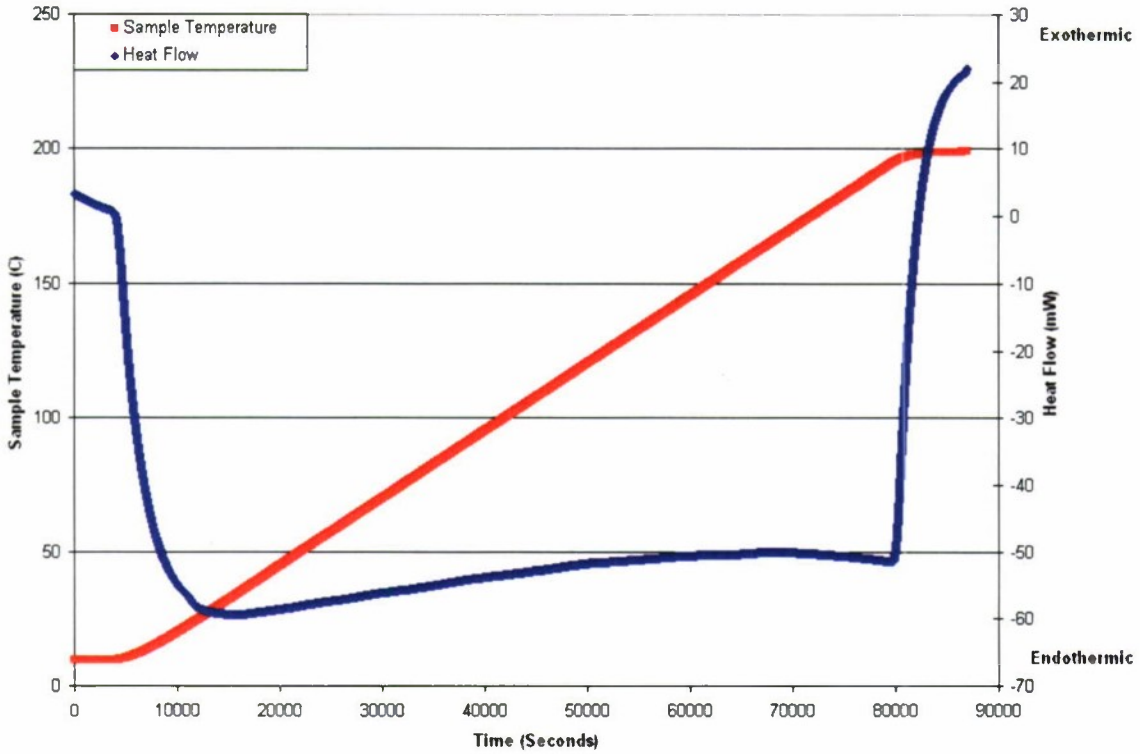

Figure 5.20. Calorimeter thermogram for continuous heating of water under N_2 at 4.0 MPa.

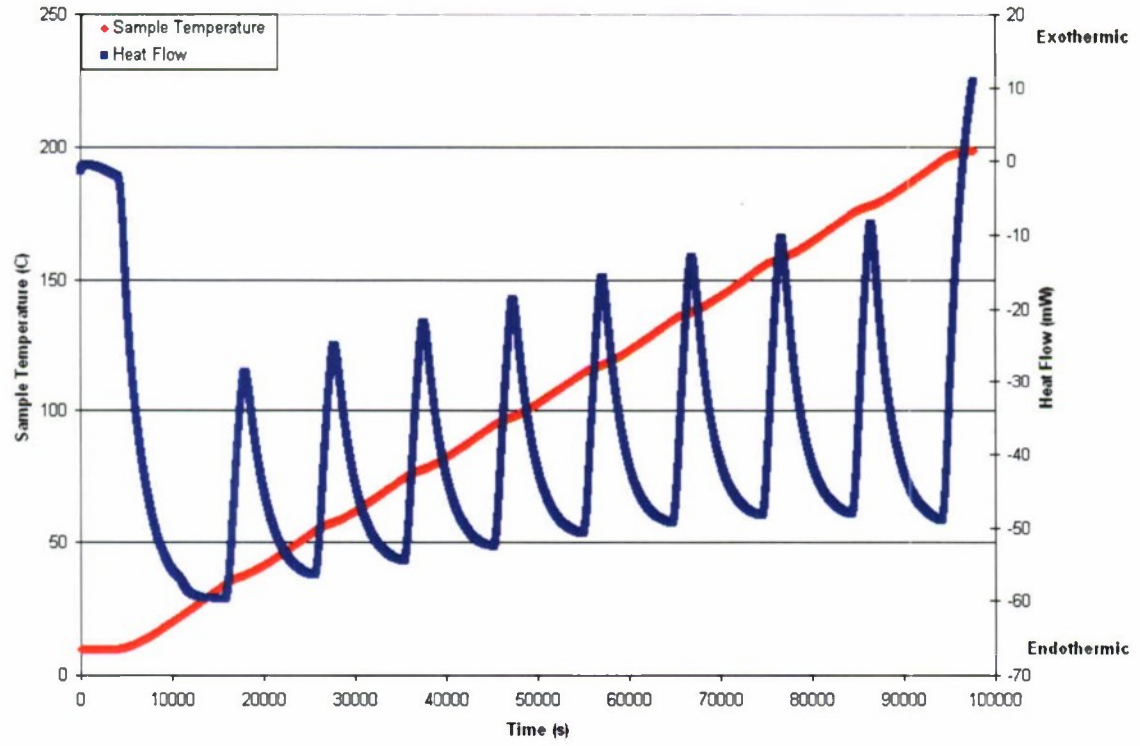

Figure 5.21. Calorimeter thermogram for stepwise heating of water under N_2 at 4.0 MPa.

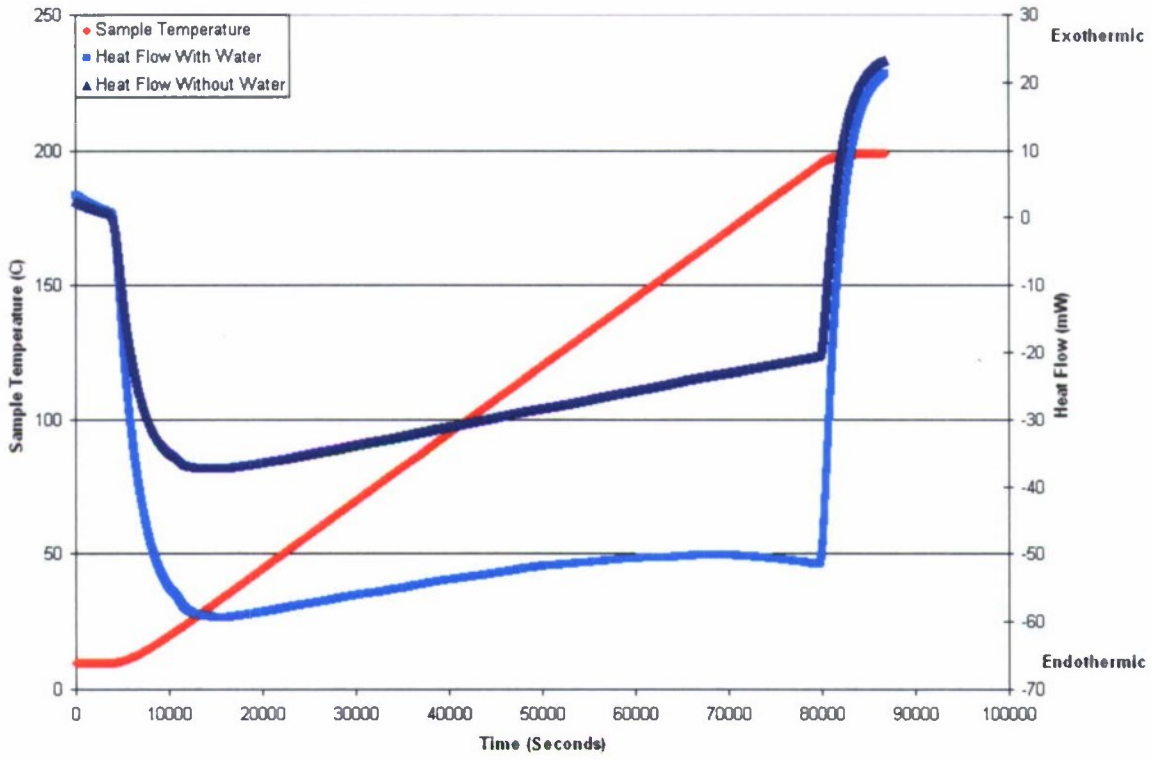

Figure 22. Comparison of calorimeter thermograms for continuous heating of sample cell containing N_2 at 4.0 MPa with (light blue) and without (dark blue) water.

Table 5.3. Heat capacity of pure water at 4.0 MPa determined by continuous heating experiments.

Temperature (K)	Average C_p^* (J g^{-1} K^{-1})	Standard deviation of triplicate experiments (%)	C_p values reported by Wagner and Pruss (J g^{-1} K^{-1})	Difference (%)
298.15	4.3121	0.1339	4.1704	3.40
326.65	4.3603	0.0449	4.1737	4.48
345.65	4.3245	0.1198	4.1832	3.36
366.65	4.3506	0.1015	4.1999	3.61
385.65	4.3604	0.0201	4.2226	3.26
406.65	4.3740	0.0175	4.2583	2.72
425.65	4.4839	0.0413	4.3024	4.22
446.65	4.7124	0.0512	4.3674	7.90
465.65	5.1114	0.0266	4.4443	14.99

Table 5.4. Heat capacity of pure water at 4.0 MPa determined by stepwise heating experiments.

Temperature (K)	Average C_p^* (J g^{-1} K^{-1})	Standard deviation of triplicate experiments (%)	C_p values reported by Wagner and Pruss (J g^{-1} K^{-1})	Difference (%)
298.15	4.3021	0.2205	4.1704	3.16
303.15	4.3861	0.0026	4.1695	5.20
308.15	4.4283	0.1076	4.1694	6.21
313.15	4.4426	0.0156	4.1700	6.54
318.15	4.4437	0.0064	4.1710	6.54
323.15	4.4363	0.0141	4.1725	6.32
328.15	4.4304	0.0117	4.1742	6.14
333.15	4.4237	0.0030	4.1764	5.92
338.15	4.4139	0.0065	4.1788	5.63
343.15	4.4159	0.0125	4.1816	5.60
348.15	4.4122	0.0240	4.1847	5.44
353.15	4.4004	0.0230	4.1882	5.07
358.15	4.3991	0.0132	4.1922	4.94
363.15	4.4046	0.0267	4.1965	4.96
368.15	4.3972	0.0104	4.2014	4.66
373.15	4.3991	0.0397	4.2067	4.57
378.15	4.4219	0.0105	4.2126	4.97
383.15	4.4364	0.0384	4.2190	5.15
388.15	4.4400	0.0148	4.2261	5.06
393.15	4.4388	0.0550	4.2337	4.84
398.15	4.4435	0.0202	4.2421	4.75
403.15	4.4565	0.0736	4.2514	4.82
408.15	4.4733	0.0816	4.2612	4.98
413.15	4.4952	0.0696	4.2719	5.23
418.15	4.5187	0.0667	4.2833	5.50
423.15	4.5470	0.0910	4.2958	5.85
428.15	4.5906	0.0861	4.3090	6.54
433.15	4.6418	0.0791	4.3234	7.36
438.15	4.6972	0.0976	4.3386	8.26
443.15	4.7587	0.1070	4.3552	9.27
448.15	4.8389	0.1183	4.3726	10.66
453.15	4.9334	0.1235	4.3917	12.34
458.15	5.0287	0.0944	4.4118	13.98
463.15	5.1096	0.0958	4.4336	15.25

Additional experiments and analyses are ongoing. A manuscript on this investigation has been prepared that will be submitted for publication in 2010.

5.2.2 Environmental Impacts of Methane Release from Seafloor Hydrates

The long-term goal of this subtask is to develop a robust three-dimensional numerical model of methane in the ocean. Methane is a potent greenhouse gas with a significantly higher Global Warming Potential than CO_2, but much lower levels of emissions into the atmosphere. Whereas the oceans currently are a net sink for atmospheric CO_2, they represent a net source of CH_4. Moreover, the historical record contains evidence of massive methane outgassing from marine and permafrost hydrate reservoirs that may have greatly exacerbated earlier episodes of global warming.

The target model will need to consider the production, oxidation, and transport of CH_4 and will require an understanding of processes that affect the exchange of methane between the atmosphere, ocean, and seafloor sediment. During the present reporting period, work continued on the development of components of the 3D model and experimental investigations of the role of microbes in methane production and consumption.

5.2.2.1 Modeling

Carbon Isotope Fractionation by Aerobic CH_4-oxidizing Bacteria

Temperature dependence

Although the preferential uptake of $^{12}CH_4$ over $^{13}CH_4$ during methane oxidation mediated by aerobic bacteria has become an important investigative tool, the reliability of isotope analyses in the evaluation of methane reservoirs and fluxes is commensurate with our knowledge of isotope fractionation *per se*, e.g., how it may depend on environmental factors such as temperature.

In a review of isotope fractionation during bacterially mediated methanogenesis and methanotrophy, Whiticar (1999) wrote that "there is no evidence indicating that temperature affects the carbon or hydrogen isotopes related to methane oxidation, although some effect, albeit small, could be anticipated." Yet, the experimental data of Coleman *et al.* (1981) suggest that carbon (and hydrogen) isotope fractionation by methane-oxidizing bacteria in aqueous media increases with increasing temperature. The experimenters were puzzled by their finding and called it an inverse temperature effect. Even though occasional instances of a similar trend have been reported since in soil studies, (Bergamaschi *et al.*, 1998; Snover and Quay, 2000), a decrease of α with temperature generally has been established, e.g., from laboratory measurements on bacterial lipids (Jahnke *et al.*, 1999). A drop in carbon isotope fractionation at higher temperatures also was confirmed for aerobic methane oxidation in soils and landfill cover materials, with a suggested trend of -0.0004 $^{\circ}C^{-1}$ (Chanton *et al.*, 2008).

Several field studies in cold marine environments, however, lend credibility to the possibility of an inverse temperature effect for methane oxidation mediated by bacteria in aqueous media. A reported value of α equal to 1.0077 at 2 °C (Cowen *et al.*, 2002) was interpreted by the authors as the cold end of a wide temperature range for similar enough bacteria that would encompass the experimental conditions of Coleman *et al.* (1981). They proposed a linear relationship between α and temperature in the range between 2 °C and 26 °C based on three data points: theirs at 2 °C, and Coleman *et al.*'s at 11.5 °C and 26 °C. This approach appears questionable because of a minimal supporting data set and a temperature range that likely spans different populations of methane-oxidizing bacteria. Yet, work by Grant and Whiticar (2002) provides some supporting evidence for it. Working in the vicinity of methane-rich plumes along Hydrate Ridge, off the Oregon coast, they determined α to range from 1.002 to 1.013 for water samples collected in

several Conductivity-Temperature-Depth (CTD) hydrocast profiles taken between a water depth of about 900 m and the surface. Historical monthly average temperature data from the World Ocean Atlas 2005 (Locarnini *et al.*, 2006) suggest a temperature range of 4 °C to 12 °C for a location (44.5°N, 125.5°W) and month (May) closest to experimental conditions.

Some of the issues raised in the preceding paragraphs were considered by paying close attention to the definition of kinetic ratios. In particular, it is suggested that some of the elementary processes that contribute to the measured quantity α could exhibit competing behaviors as temperature changes.

Fractionation factor due to the first oxidation step

The fractionation factor α_{MMO} due to the oxidation of methane into methanol by aerobic bacteria is assumed to be constant for a given temperature. This hypothesis seems consistent with experimental data (Coleman *et al.*, 1981; Cowen *et al.*, 2002) provided that the possible effects of extrinsic phenomena have been eliminated or accounted for. This point is explained as follows: by definition, the kinetic rates of extrinsic physical processes do not explicitly depend on bacterial concentration (e.g., turbulent ocean mixing, methane bubble dissolution, mass transfer across liquid-gas interface, etc.); in contrast, intrinsic processes such as methane oxidation by methanotrophs, or bacterial biomass buildup are keyed to bacterial concentration, with the related rates typically being proportional to it.

In experimental setups such as those of Coleman *et al.* (1981) and Templeton *et al.* (2006), the fractionation factor conveniently is determined from gas-phase measurements (except for biomass), even though the bacterial medium is a liquid. With low bacterial populations, intrinsic rates are limiting and the method is unbiased. If the bacterial concentration increases so much, in the course of an experiment, that intrinsic and extrinsic rates may kinetically be of the same order, then large apparent fractionation shifts can be observed (Templeton *et al.*, 2006). In such cases, there is substantial ambiguity in interpreting the data without a detailed quantitative analysis of the overall system (Nihous, 2008), even though complexities inherent to many environments often make quantification difficult or impractical. In particular, proposed relationships between fractionation factor and cell density or oxidation rate (Templeton *et al.*, 2006; Chanton *et al.*, 2008) warrant caution, as they may be more representative of specific experimental setups than of fundamental oxidation phenomena.

Nihous (2008) rigorously analyzed the experiments of Templeton *et al.* (2006) and of Coleman *et al.* (1981) with a detailed mathematical formulation of the evolution equations. It was shown that the apparent dependence of the measured fractionation factor on cell density at higher bacterial concentrations could be the result of a relatively slow mass transfer across the gas-liquid interface. In the case of Coleman *et al.* (1981), two different cultures (A and B) were first incubated at different temperatures (warm and cold). The fact that plots of isotopic separation as a function of fraction of residual methane were straight lines indicates that intrinsic phenomena were limiting. When the authors decided to subsequently incubate the cold culture (B) at the warm temperature, isotopic fractionation initially was the same as for culture A until a change of slope occurred. The authors attributed this change to the possible development of an alternative oxidation pathway; the modeling of Nihous (2008) suggested instead that with a high initial bacterial concentration in the re-start mode, the assumption of limiting intrinsic rates broke down after a short incubation time, as shown by an inflection of the initial straight line. Interestingly,

experimental results for hydrogen isotopes obtained with deuterated methane did not show much difference between both cultures at the warm temperature.

We consider here a situation where Rayleigh distillation holds so that measurements of the isotopic composition of the dissolved substrate (CH_4 and $^{13}CH_4$) are sufficient to evaluate isotopic fractionation. As illustrated in Figure 5.23, however, the resulting isotopic fractionation factor α represents the expression of several fundamental intrinsic mechanisms as methane is adsorbed to and desorbed from the bacterial cell walls before the conversion into methanol catalyzed by methane monooxygenase (MMO) enzymes occurs. Each of the steps may *a priori* proceed at a specific rate with a specific isotope fractionation. A simplified representation of the overall oxidation pathway is shown in Figure 5.24 when the assimilatory branch follows the ribulose monophosphate (RuMP) cycle. Additional details can be found in Jahnke *et al.* (1999).

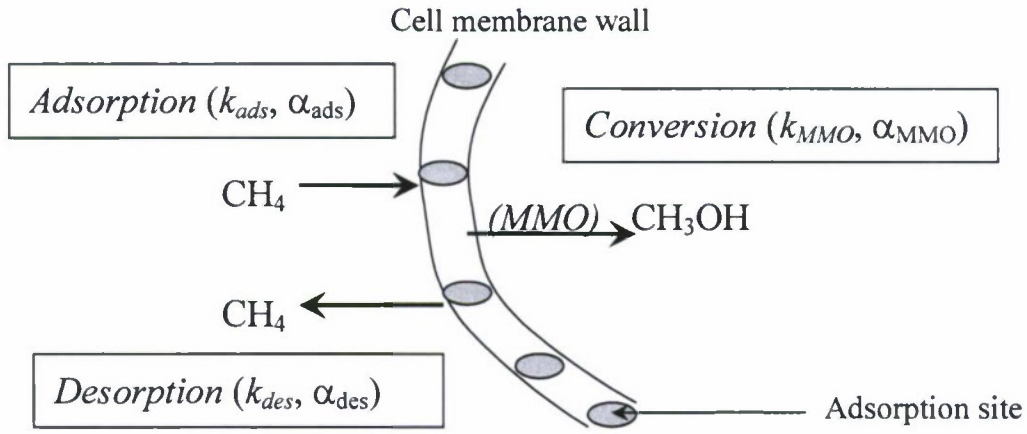

Figure 5.23. Elementary processes in first methane oxidation step (conversion into methanol).

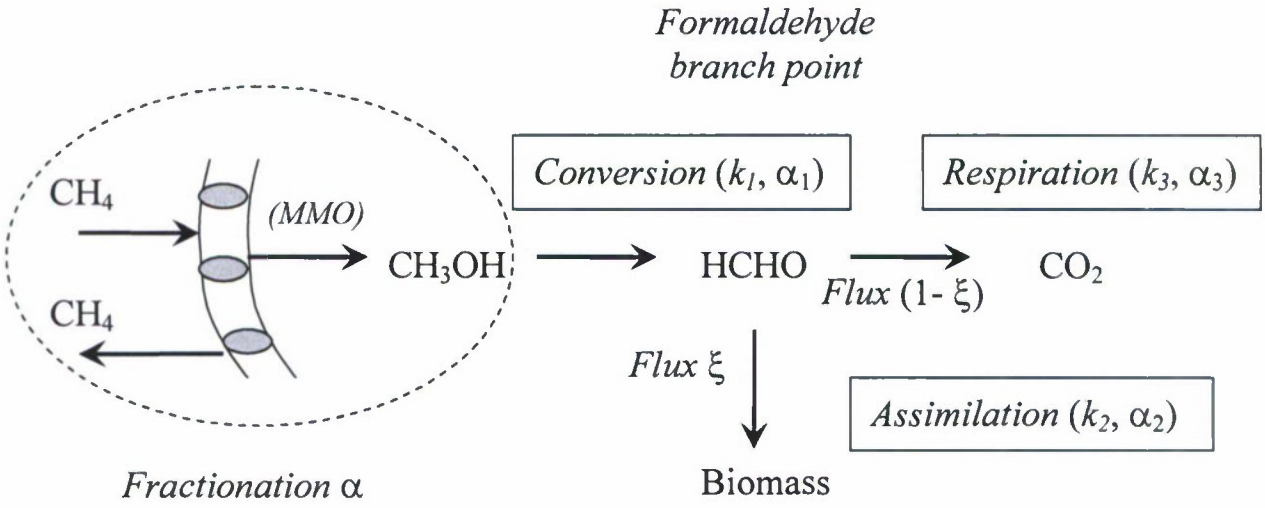

Figure 5.24. Simplified representation of overall methane oxidation (RuMP pathway).

The abundance of ^{13}C-species is low and isotopic kinetic ratios are close to one. Therefore, no distinction is made between overall and ^{12}C values of concentrations and kinetic rates in the discussion that follows.

Evolution equations for s, x, and ^{13}x, the concentrations of biomass-bound carbon, methane, and ^{13}C-methane in solution, respectively, are:

$$ds/dt = \xi\, k_{MMO}\, \lambda\, s \tag{11}$$

$$dx/dt = k_{des}\, \lambda s - k_{ads}\,(1 - \lambda)\, s\, x \tag{12}$$

$$d^{13}x/dt = (k_{des}/\alpha_{des})\, {}^{13}\lambda s - (k_{ads}/\alpha_{ads})\,(1 - \lambda)\, s\, {}^{13}x \tag{13}$$

where ξ is the biomass carbon assimilation ratio (yield), λ the fractional occupancy of methane adsorption sites on the bacterial cell walls and $^{13}\lambda$ the fractional occupancy of methane adsorption sites by ^{13}C-methane. Equation (11) implies that the concentrations of the intermediate products methanol and formaldehyde are at steady-state; this assumption is supported by experimental evidence that biomass and CO_2 are the only significant carbon sinks during the growth of CH_4-oxidizing bacteria (Templeton *et al.*, 2006). Two more equations are needed since both λ and $^{13}\lambda$ must be known. We define X as the mole number of occupied adsorption sites per liter, which may be specified as $\{n/(\omega\mathcal{N})\}\lambda s$; n is the number of adsorption sites per cell, ω the molar carbon content per cell and $\mathcal{N}$ the Avogadro number. An evolution equation for X then is:

$$dX/dt = -(k_{des} + k_{MMO})\, \lambda s + k_{ads}\,(1 - \lambda)\, s\, x \tag{14}$$

If it is assumed that the fractional occupancy λ varies slowly enough to be considered stationary ($d\lambda/dt = 0$), then Equation (14) can be written as a second-degree polynomial in λ using Equation (11). The term leftover on the left-hand-side of Equation(14) which is proportional to ds/dt is negligible, however, since the mole number of adsorption sites per biomass-bound mole of carbon, $n/(\omega\mathcal{N})$, can be shown to be very small. The order of magnitude of ω was recently estimated to be 1 femtomole per methanotroph (10^{-15} mol-C/cell) (Nihous and Masutani, 2007). At 50% carbon content by weight (Sundh *et al.*, 2005), the dry cell weight is about 24×10^{-12} mg. In turn, cytoplasmic volume estimates of about 1.6 μL/(mg-dry-cell) given in Table 1 of Khmelenina *et al.* (1999) suggest that if methanotrophs are quasi-spherical, their diameters will be of the order of 0.4 μm. The number of particulate MMO (pMMO) enzymes bound within the cell membrane wall can be assumed to be a proxy for n. This equivalence should hold to at least an order of magnitude. Incidentally, it does not imply that the actual conversion of methane into methanol must be catalyzed by pMMO and the proposed model should also be applicable to bacteria expressing soluble MMO (sMMO) activity at high copper concentrations. For a common methanotroph, Yu *et al.* (2003) established that pMMO accounts for 20% to 80% of the proteins in the bacterial cell wall depending on copper concentration. A structural investigation recently showed pMMO to be a trimer of gross dimension 100 Å (Lieberman and Rosenweig, 2005). Therefore, we surmise that $n \approx 0.2\ \pi(0.4 \times 10^{-6})^2/(10^{-8})^2 \approx 1000$ for copper-depleted conditions representative of most natural environments. This value could be about four times as

high but within an order-of-magnitude. It follows that $n/(\omega\mathcal{N})$ is of order 10^{-6}. Setting the left-hand side of Equation (14) to zero, the Langmuir isotherm of the present adsorption problem is:

$$\lambda = \frac{x}{\frac{k_{MMO} + k_{des}}{k_{ads}} + x} \tag{15}$$

A Michaelis-Menten formalism is recovered for methane consumption by substituting Equation (15) into Equation (12), with the half-saturation constant $K_m = (k_{des} + k_{MMO})/ k_{ads}$. An order-of-magnitude estimate of K_m is 1 μM (Dunfield *et al.*, 1999). An evolution equation similar to Equation (14) can be written for ^{13}X, the mole number of adsorption sites occupied by $^{13}CH_4$ per liter:

$$d^{13}X/dt = -(k_{des}/\alpha_{des} + k_{MMO}/\alpha_{MMO})\, {}^{13}\lambda s + (k_{ads}/\alpha_{ads})(1 - \lambda)\, s\, {}^{13}x \tag{16}$$

Setting the left-hand-side to zero as before, and using Equation (15), we obtain the stationary site coverage $^{13}\lambda$:

$${}^{13}\lambda = \frac{\frac{k_{des} + k_{MMO}}{\alpha_{ads}}}{\frac{k_{des}}{\alpha_{des}} + \frac{k_{MMO}}{\alpha_{MMO}}} \frac{{}^{13}x}{K_m + x} \tag{17}$$

The overall isotope fractionation factor α for Rayleigh distillation is the ratio of $dLog(x)/dt$ over $dLog(^{13}x)/dt$ (Mahieu *et al.*, 2006). After substituting Equations (15) and (17) into Equations (12) and (13), α can be obtained after some elementary algebra:

$$\alpha = \alpha_{ads} \frac{\frac{\alpha_{MMO}}{\alpha_{des}} + \frac{k_{MMO}}{k_{des}}}{1 + \frac{k_{MMO}}{k_{des}}} \tag{18}$$

In the above derivation, note that Equation (11) was merely used to simplify Equation (14). Equation (18) is formally identical to *Equation (7)* in O'Leary and Osmond (1980) obtained for the fractionation occurring in the assimilation of CO_2 by certain plants. This similarity essentially reflects a steady-state assumption made at an intermediate point in the sequence of elementary reactions (fractional occupancy of methane adsorption sites or CO_2 concentration inside the plant's intercellular air space). Other examples of similar situations can be found in the literature (Hunkeler and Aravena, 2000; Nijenhuis *et al.*, 2005). In the theoretical limit of fast conversion to methanol ($k_{MMO} >> k_{des}$), $\alpha \approx \alpha_{ads}$ would simply express isotopic discrimination from methane adsorption to the cell wall. If instead, conversion to methanol were slow ($k_{MMO} << k_{des}$), then $\alpha \approx \alpha_{ads}\alpha_{MMO}/\alpha_{des}$ would be the ratio of the product of the forward-process fractionation values over the backward process (desorption) fractionation value.

Inferences

An important aspect of Equation (18) is the presence of a ratio of elementary reaction rates (desorption and MMO-mediated oxidation). As a result, the behavior of α_{MMO} may be masked

by k_{MMO}/k_{des} in the measurement of α. It is therefore possible for α and α_{MMO} to have different temperature dependences. With α_{MMO} a decreasing function of temperature, α could exhibit an opposite trend if, for example, k_{des} increased a lot faster than k_{MMO} with temperature. The behavior of k_{des} likely depends on the growth medium so that data obtained for different environments could display contradictory tendencies. The apparent temperature inversion shown by α in aqueous media warrants further examination.

The desorption reaction rate can be assumed to vary with temperature via an Arrhenius-like term, i.e., $k_{des} = \nu\exp(-E_{des}/RT)$, where R is the gas constant, T the absolute temperature ($T_0 + \theta$), ν an attempt frequency independent of temperature, and E_{des} is the activation energy for desorption. By expressing Equation (18) at two distinct temperatures θ_1 and θ_2, an expression for E_{des} independent of ν can be obtained:

$$E_{des} = \frac{R(T_0+\theta_1)(T_0+\theta_2)}{(\theta_1-\theta_2)} Log[\frac{k_{MMO}(\theta_1)}{k_{MMO}(\theta_2)} \frac{\alpha(\theta_1)-\alpha_{ads}}{\alpha(\theta_2)-\alpha_{ads}} \frac{\frac{\alpha_{MMO}(\theta_2)\alpha_{ads}}{\alpha_{des}} - \alpha(\theta_2)}{\frac{\alpha_{MMO}(\theta_1)\alpha_{ads}}{\alpha_{des}} - \alpha(\theta_1)}] \qquad (19)$$

If it is assumed that any isotopic fractionation associated with methane adsorption and desorption is negligible ($\alpha_{ads} = \alpha_{des} \approx 1$), then Equation (18) can be applied to verify that $\alpha_{MMO} > \alpha$ as long as $\alpha > 1$. Coleman *et al.* (1981) measured $\alpha(\theta_1) = 1.025$ and $\alpha(\theta_2) = 1.013$ at $\theta_1 = 26$ °C and $\theta_2 = 11.5$ °C. Relative rates of substrate depletion in their bacterial cultures were reported to be 50% in 15 days at $\theta_1 = 26$ °C and 50% in 6 months at $\theta_1 = 11.5$ °C. A simple manipulation of Equations (11), (12), (14) (with $dX/dt \approx 0$), and (15) (in the limit of high methane concentrations, $x >> K_m$) suggests that ($\xi\ k_{MMO}\ t$) is constant for a given relative rate of substrate depletion. Assuming that the biomass carbon assimilation ratio is insensitive to temperature, we can write $k_{MMO}(\theta_1)/k_{MMO}(\theta_2) \approx 180/15 = 12$ This approach was validated in quantitative modeling of the experiments of Coleman *et al.* (1981). Cowen *et al.* (2002) later proposed a linear expression $\alpha = 1.0056 + 0.0007\theta$ that would be valid in the range $2\ °C \leq \theta \leq 26\ °C$; it is based on three data points including a value from their own field measurements and the results of Coleman *et al.* (1981). It is further postulated that the temperature dependence established for α in landfill cover materials (Chanton *et al.*, 2008) is also applicable to α_{MMO}. This would apply as long as the desorption rate far exceeds the methane oxidation rate at all temperatures in soil incubation experiments. Considering a moderately masked value of α_{MMO} at 26 °C, such as 1.030, the expression $\alpha_{MMO}(\theta) = 1.030 + 4 \times 10^{-4} (26 - \theta)$ is obtained. Using the above relationships in Equation (19), for $\theta_1 = 26$ °C and $\theta_2 = 11.5$ °C, leads to an estimated value $E_{des} = 211$ kJ/mol.

Given the many simplifications and assumptions adopted so far, it may be inferred that $E_{des} \approx$ 200 kJ/mol. Desorption activation energies of 63.7 kJ/mol and 78.6 kJ/mol have been reported for silicon fluoride molecules during the chemical etching of silicon in a fluorine atmosphere (Knizikevičius, 2002; 2005). A measured value of 94.6 kJ/mol for the desorption of bacteriophage SPP1 from the cell wall of *Bacillus subtilis* provides another reference (Baptista *et al.*, 2008). Hence, the estimated value of E_{des} may seem a little high but certainly is possible. It should be noted that if both isotopic fractionation ratios α and α_{MMO} had been found to be insensitive to temperature, then Equation (19) would yield $E_{des} = 121$ kJ/mol for the two

temperatures under consideration and $k_{MMO}(\theta_1)/k_{MMO}(\theta_2) \approx 12$. This situation would closely correspond to the results shown for Culture B in Coleman *et al.* (1981) if the value of $\alpha(\theta_1)$ measured at high substrate depletion is retained.

To provide a different perspective on the issue, Equation (19) may be recast as:

$$\eta(\theta_2)=\frac{k_{MMO}(\theta_2)}{k_{MMO}(\theta_1)}=\exp[-\frac{E_{des}}{R}(\frac{1}{T_2}-\frac{1}{T_1})]\frac{\alpha(\theta_1)-1}{\alpha(\theta_2)-1}\frac{\alpha_{MMO}(\theta_2)-\alpha(\theta_2)}{\alpha_{MMO}(\theta_1)-\alpha(\theta_1)} \quad (20)$$

As long as the biomass carbon assimilation ratio (yield) ξ is stable with temperature, η expresses the maximal specific bacterial growth rate normalized to its value at reference temperature θ_1. With $\theta_1 = 26$ °C, $E_{des} = 211$ kJ/mol and the linear relationships proposed earlier for α and α_{MMO}, the curve $\eta(\theta)$ corresponding to Equation (10) is shown in Figure 5.25. The question arises whether methanotroph species realistically could exhibit similar (normalized) maximal specific growth rates as temperature varies. Substantial psychrotolerance has been documented in mesophilic methanotroph cultures (Jahnke *et al.*, 1999; Kevbrina *et al.*, 2001), but there is no evidence that it would extend to temperatures as cold as 2 °C.

A convenient representation of non-dimensional maximal specific bacterial growth rate is the three-parameter Rosso model (Kevbrina *et al.*, 2001) where $\eta(\theta)$ is determined simply by picking minimum, optimum and maximum temperatures for growth (dimensionalization would require a fourth parameter, the optimal growth rate equal to the greatest maximal specific rate). As shown in Figure 5.25 (+ symbols), Rosso parameters that allow a decent match with the linear fractionation curve in the range 26 °C > θ > 11.5 °C could be found, with minimum, optimum and maximum temperatures for growth equal to 6.6 °C, 27.5 °C and 31.5 °C, respectively; the constraint $\eta(11.5\ °C) = 1/12$ was enforced to conform with experimental observations. A bacterial population represented by these parameters seems fairly typical of psychrotolerant mesophilic methanotrophs (e.g., *Methylomonas methanica*), but it would not grow at 2 °C. For illustrative purposes, a Rosso curve that intersects the linear fractionation curve at both 2 °C and 11.5 °C was drawn (among many possible choices) for hypothetical psychrophilic bacteria. Since parametric models alone do not constitute evidence, the above discussion does not rule out the possible validity of an expression like $\alpha = 1.0056 + 0.0007\ \theta$ in the temperature range 2 °C $\leq \theta \leq$ 26 °C (Cowen *et al.*, 2002). This relationship, however, may be fortuitous inasmuch as it might describe the behavior of different types of methanotrophs from too few data points.

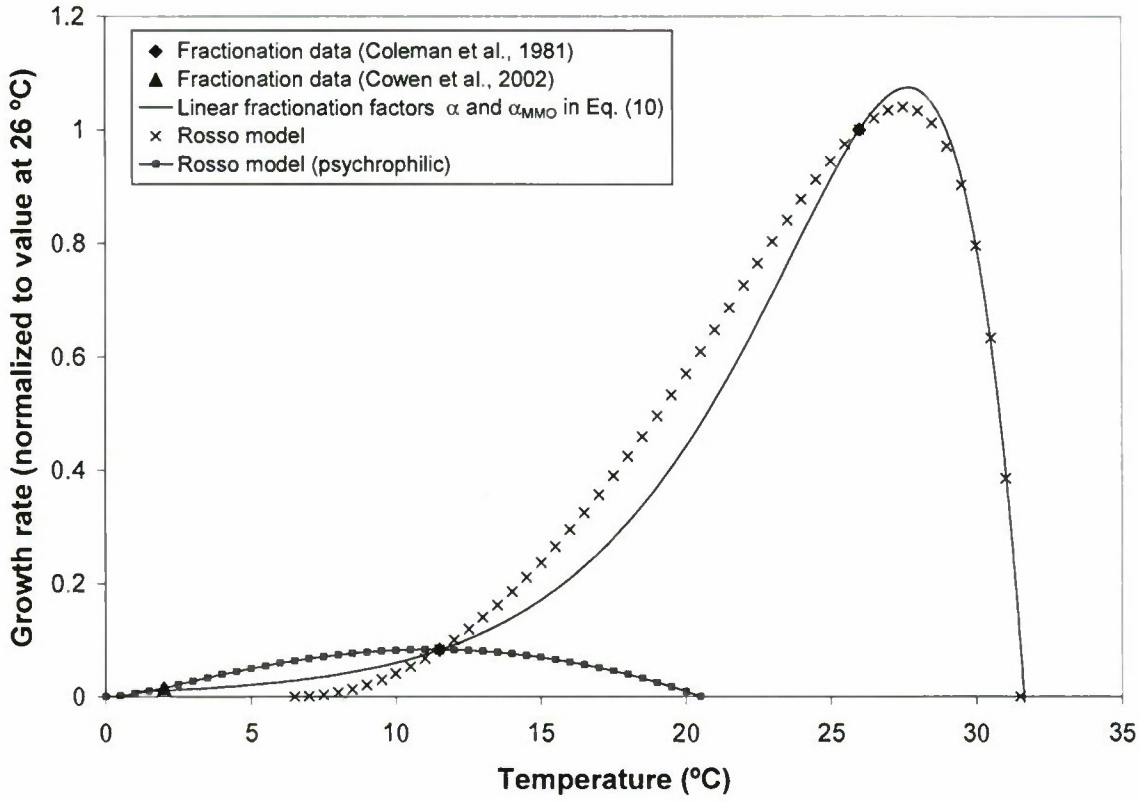

Figure 5.25. Possible maximal methanotroph specific growth rate (normalized to 26 °C value).

Modeling of the fate of methane released from the seafloor

The 3D codes under development to determine the transport and evolution of methane in the ocean require robust computing capabilities. During the present reporting period, equipment was specified, and procurement of this equipment was initiated (with UH internal funds). The components include a Dell PowerEdge R710 head node connected to a cluster of eight Dell PowerEdge R410 computing nodes, each based on powerful dual processors. The low-latency network connection is effected with state-of-the-art Infiniband technology. This setup lends itself to difficult hydrodynamic calculations, e.g., in cases where the vertical fluid momentum equation cannot be simplified to a hydrostatic approximation. It is anticipated that ocean general circulation models such as MITGCM or ROMS easily can be run on this new platform.

5.2.2.2 Hydrate Microbiology

Studies have been ongoing as part of this Task to investigate methane cycling in both sediments and the water column. To date, the sediment work has focused on understanding biological formation and the anaerobic oxidation of methane. Anaerobic oxidation of methane (AOM) occurs through an undefined process and is potentially the largest sink for methane in sediments. Biological AOM is thought to be mediated by a consortium of micro-organisms composed of sulfate-reducing bacteria and methanogenic *Archaea*. Geochemical data suggests that the majority of methane produced in sediments is oxidized anaerobically within a narrow depth range called the sulfate methane interface (SMI). The sediment depth of the SMI is influenced

by the rates of methane flux. Stronger methane flux results in shallower SMIs, and the possibility of methane releases into the water column.

In terrestrial environments, biological methane oxidation typically occurs as an obligate aerobic process mediated by methanotrophic bacteria. This suggests that a methane sink could also exist at the sediment-water interface in the ocean where there is dissolved oxygen. In consideration of this, we have recently expanded our research scope to investigate aerobic as well as anaerobic methane oxidation at this interface, as well as the associated prokaryotic methanotrophic populations.

Molecular analyses of the microbial community that utilize 16S rRNA and pmoA phylogenies have been performed in different environments that include the Kuroshima Knoll (Inagaki *et al.*, 2004), Gulf of Mexico (Yan *et al.*, 2006), Haakon-Mosby mud volcano (Niemann *et al.*, 2006), and the East Pacific rise and Mid Atlantic vent fields (Nercessian *et al.*, 2005). While this approach can be employed to evaluate the potential for bacterial aerobic methane oxidation in marine sediments, it generally does not provide estimates of the methane oxidation rates.

In mid-September 2009, we participated in a 12-day oceanographic research cruise on the U.S. Coast Guard Cutter Polar Sea in the Beaufort Sea off the North Slope of Alaska. This cruise was organized by the Naval Research Laboratory. There were 34 international participants, including scientists from university and government research agencies from the U.S., Netherlands, Belgium, Germany and Canada.

The Arctic Ocean expedition provided a unique opportunity to study the microbial communities and aerobic C1 metabolisms in shallow and cold water environments in methane-rich areas. Comparative analysis of collected samples utilizing data that includes concentrations of C1-metabolizing prokaryotes and sediment and water chemistries could yield important information about the methane sink at the sediment-water interface.

Preliminary Beaufort Sea Sample Analysis Results

Six multicore samples were collected during the Beaufort Sea cruise. These samples are better suited for the analysis of methanotrophic bacteria than the piston cores collected in previous expeditions since there is less disturbance of the upper sediment layer. The multicores were not tested onboard for geochemical SMI to correlate with the biological data. Although it originally was planned to employ the multicorer at mounds with high methane fluxes, unfortunately no samples were obtained from active seeps.

As discussed in previous HEET reports, DNA extractions performed at our laboratory at UH from sediment pore water collected in past expeditions yielded samples containing high concentrations of humic acids. These samples were visually tinted after extraction and were difficult to purify, resulting in less-than-optimal molecular analyses. During the Beaufort Sea cruise, DNA was extracted onboard from the cores immediately after collection, instead of after shipping the pore water to our laboratory in Hawaii. This approach maximizes the recovery of DNA from low cell populations, reducing potential bias that could result from storage and transport. DNA extraction was performed, using a commercially available kit, from a homogenate of the uppermost 1 cm of sediment from the core. It was observed that these DNA samples were clear, exhibiting no visual tinting. Triplicate 10 g frozen extracts were brought back to our laboratory for analysis at the end of the cruise.

It was believed that measurable rates of methane oxidation by methanotrophic bacteria might be determined from samples collected from high methane flux areas. In comparison to the rates typically observed in investigations of AOM (0.7 fmol CH_4/cell/24hrs), aerobic oxidation rates can be considerably larger in methane-rich environments (Nauhaus *et al.* 2005, Ruo *et al.* 2008). During the cruise, 1 g core samples were weighed and placed into sterilized Hungate tubes containing a seawater-based enrichment media and 1 gram of silica to increase the porosity of the often clay-like sediments (Holmes *et al.*, 1995; Whittenbury *et al.*, 1970). An artificial atmosphere containing 10% methane in air was infused into the tubes after innoculation. Methane concentrations were measured using a head space method (Kiene and Capone, 1985) with a gas chromatograph equipped with an FID detector. The extent of methane consumption in the experiments, however, was insufficient to determine oxidation rates, probably due to low cell density since we were unable to collect cores from areas stimulated by high methane gas fluxes. To address this problem, enrichments were maintained and sent back to our laboratory where they currently are incubating. If cell density can be increased, then the oxidation rate experiments will be repeated in the future.

16S rRNA diversity studies were initiated using primers sets that broadly identify bacteria (Lane *et al.*, 1991) and type I methanotrophs (Chen *et al.*, 2007; Wise *et al.*, 1999). Analysis of the *pmoA* gene for the functional enzyme methane monooxygenase are also being investigated. The *pmoA* gene sequences have been shown to produce phylogenies that are congruent with the 16S rRNA of the same organisms (Holmes *et al.*, 1999; Kolb *et al.*, 2003). For methanotrophic organisms, the largest data set of partial sequences available in GenBank are of the functional enzyme methane monooxygenase, for the *pmoA* gene sequence.

Collected DNA samples have been PCR amplified using bacterial primers and type I specific methanotroph 16S rRNA probes. All of the samples amplified very well using the bacterial primers. The specific methanotroph probes clearly amplified 5 of the 6 samples. Further optimization, followed by cloning and sequencing as shown in Figure 5.26, will be performed to assess the specificity of the amplification.

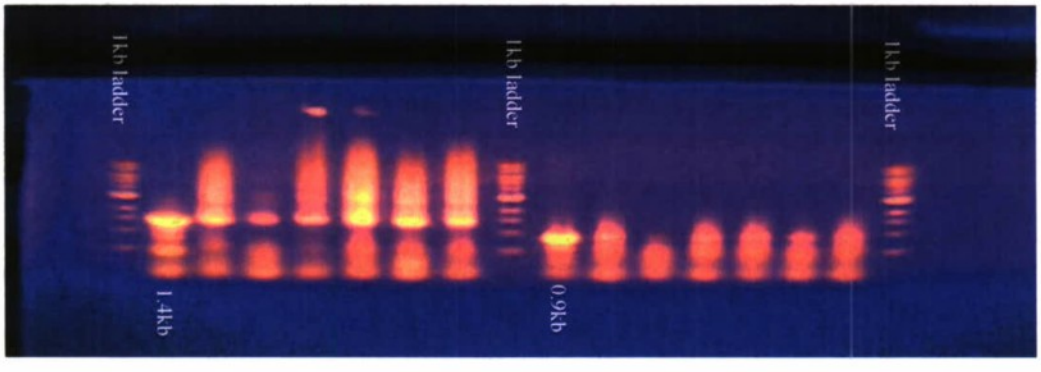

Figure 5.26. Lanes 1, 9, and 17: 1kb DNA ladder; Lanes 2 (1.4kb) and 10: control samples using *Methylococcus capsulatus* DNA; Lanes 3-8: collected sediment samples amplified using 16SrRNA primers; Lanes 11-16: samples amplified using methanotroph specific primers.

5.2.3 Hydrate Engineering Applications

Although we have been exploring the potential of hydrates for water purification and gas separation, an obvious application is fuel gas storage. Commercial development of hydrate as a means to transport and supply methane has been under development in Japan for several years and a trial distribution program of hydrate pellets currently is underway. At a larger scale, Mitsubishi Heavy Industries has conducted design studies of tanker ships to transport hydrate instead of Liquified Natural Gas (LNG). Although LNG has a higher methane density than methane hydrate, it requires storage at much lower temperatures.

Given the progress made in Japan on this topic, it did not appear worthwhile to pursue parallel development in our HEET Task. Recently, however, advances have been reported in synthesizing hydrogen (H_2) hydrate that suggest that it may be feasible to store and transport this molecule as a hydrate guest. Since H_2 is the fuel of choice for many fuel cell systems under investigation as part of the HEET Initiative, an investigation of hydrate H_2 storage appeared to warrant consideration, and work on this topic was therefore initiated during the present reporting period.

THF/H_2 Hydrate Synthesis Experiments

Objectives

The extremely high pressures and low temperatures required to synthesize and maintain pure hydrogen hydrate make it impractical as a medium to store and transport fuel (Lee *et al.*, 2005). Vos *et al.* (1993) used X-ray and Raman spectroscopy to study hydrogen/water mixtures at pressures between 0.75 GPa and 3.1 GPa and temperatures between 17 °C and 177 °C. Mao *et al.* (2002) applied Raman, infrared, X-ray, and neutron techniques to identify the presence of sII hydrate at 200 MPa and 7 °C, as well as under vacuum (~10 kPa) at a temperatures of -195 °C. They reported two hydrogen molecules in the small hydrate cages and four hydrogen molecules in the large cage. Dyadin *et al.* (1999) used differential thermal analysis to look at hydrogen hydrate formation over a temperature range of approximately -10 °C to 40 °C and pressures up to 1000 MPa. Tanaka *et. al.* (2004) developed pure hydrogen hydrates at 200 MPa and -23 °C.

Recently, hydrate promoters such as tetrahydrofuran (THF) have been explored as a means to facilitate H_2 hydrate formation. THF has been added to the water to occupy the large hydrate cages and to stabilize the crystal at more desirable pressure and temperature conditions. Using THF, Fluorusse *et al.* (2004) were able to store H_2 in hydrate at 5 MPa and 6.6 °C. They employed X-ray powder diffraction to verify the sII hydrate structure, Raman spectroscopy to confirm the existence of THF/H_2 hydrate, and Raman and NMR spectroscopy to detect H_2 molecules within the hydrate crystal. They noted that adding a promoter such as THF decreased the amount of H_2 that could be stored within the hydrate.

Pure H_2 hydrate contains about 5.0 wt% H_2, whereas THF/H_2 hydrate typically contains approximately 2.0 wt% H_2 (Yedlapalli *et al.*, 2010). In an effort to increase the amount of H_2 stored in THF/H_2 hydrate, Lee *et al.* (2005) varied the concentration of THF added to the formation water. They showed that, as expected, the wt% of H_2 in the hydrate decreased with increasing THF concentration.

The application of hydrate promoters to form stable hydrates that can be employed to store and transport H_2 fuel at reasonable temperatures and pressures appears feasible and experiments directed toward this goal were initiated. The first step was to synthesize THF/H_2 hydrate with

our Raman calorimeter. Once an appropriate protocol is identified and any required modifications to the facility are completed, then we will proceed to attempt to fully characterize this hydrate and to explore other less hazardous promoters (THF has a tendency to form highly explosive peroxides when in contact with air for prolonged periods) that could improve the stability of the H_2 hydrate and/or increase H_2 storage capacity.

THF/H_2 Formation Experiments

The THF/H_2 hydrate formation experiments were conducted with the Raman calorimeter facility that has been described in detail in previous HEET reports. A schematic diagram of the facility is shown in Figure 5.27.

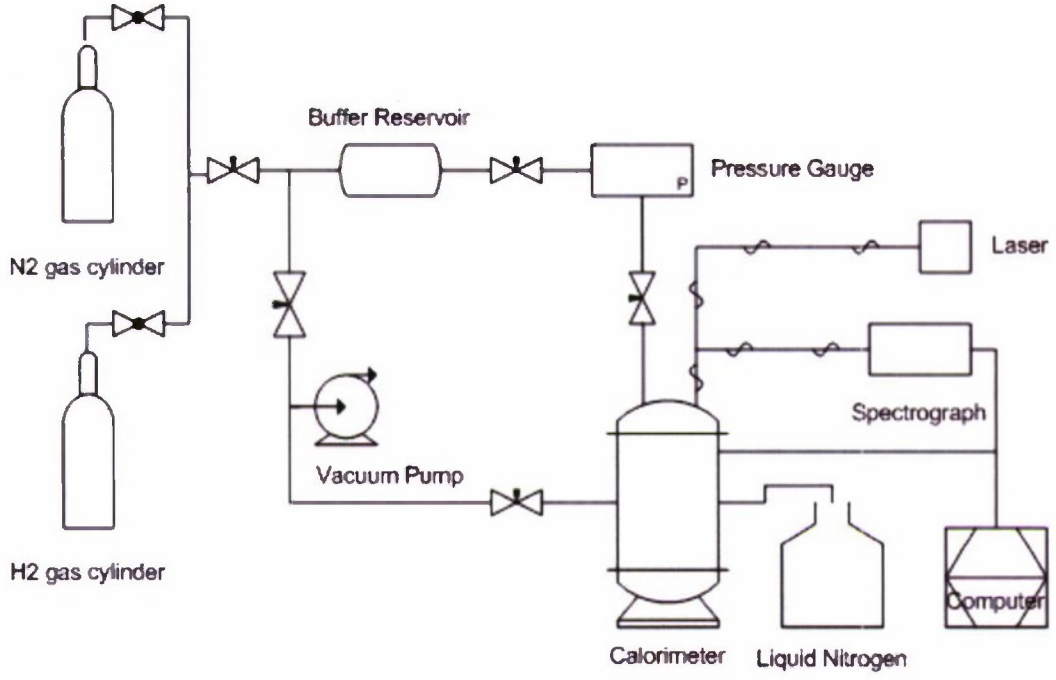

Figure 5.27. The Raman calorimeter experimental facility.

The method used to produce THF/H_2 hydrate was similar to that employed by Lee *et al.* (2005) and Strobel *et al.* (2009), where the THF hydrate is formed first and then pressurized with H_2 gas. In our experiments, the temperature of the calorimeter was initially set to -20 °C. As the calorimeter was cooling, 16 g of distilled, deionized water was mixed with 8 g of THF. The THF/water mixture was placed in a freezer at -25 °C to form THF hydrate. The THF hydrate was crushed and approximately 6 mL of it was loaded into a calorimeter mixing cell. When the temperature of the calorimeter reached -20 °C, the mixing cell was inserted into the calorimeter well and the gas lines were connected. The cell was then vacuum evacuated twice and purged with Grade 4.0 N_2 gas. After a second purge, the cell was vacuum evacuated and filled with Grade 4.0 H_2 gas to 6.90 MPa. Raman spectra were taken to confirm the presence of both THF hydrate and H_2 gas within the cell. The temperature of the sample was then increased to -5 °C and held for approximately 12 hours. Raman spectra were again taken to confirm formation of

the THF/H_2 hydrate. The temperature of the calorimeter finally was increased from -5 °C to 50 °C at a rate of 0.15 °C/min to obtain a thermogram of the decomposition of the hydrate.

THF/H_2 Results

Figure 5.28 shows an example of the calorimeter data collected during a THF/H_2 formation run. The chart comprises a record (blue) of energy rejected or absorbed by the sample and the temperature-time history. Some important features of the data that are identified in Figure 5.28 are:

1. Laser turned on and Raman spectra taken (Exothermic)
2. Ice melting (Endothermic)
3. Hydrate melting (Endothermic)

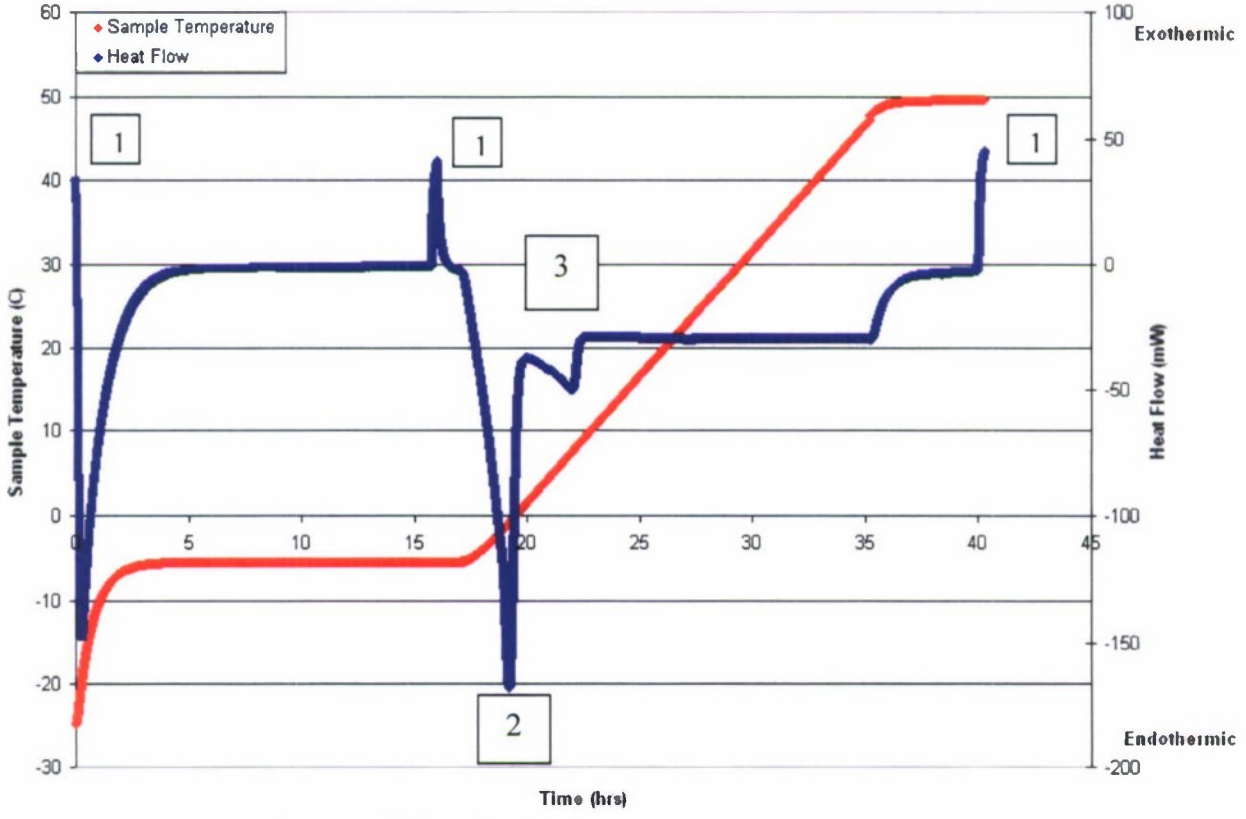

Figure 5.28.Calorimeter record of the THF/H_2 experiment.

Figures 5.29 and 5.30 present Raman spectra of hydrogen gas and THF hydrate, respectively, at 6.90 MPa and -5 °C.

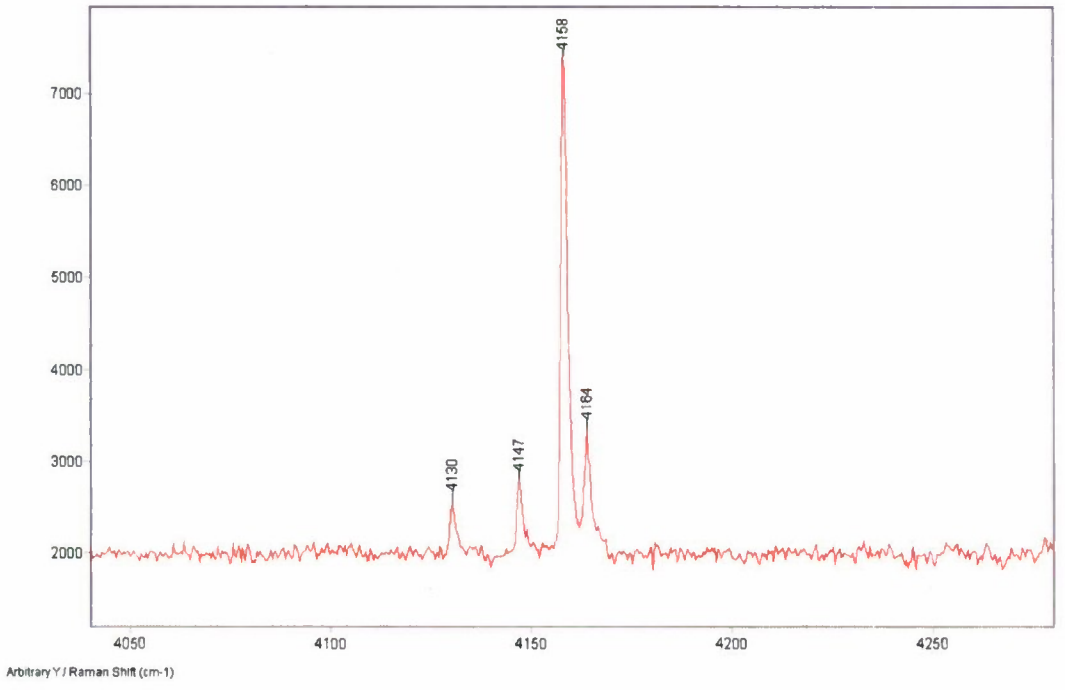

Figure 5.29. Raman spectrum of the H-H stretching vibrational mode in the gas phase; Hashimoto *et al.* (2006) measured H-H vibration peaks at 4128, 4146, 4158, and 4165 cm^{-1}.

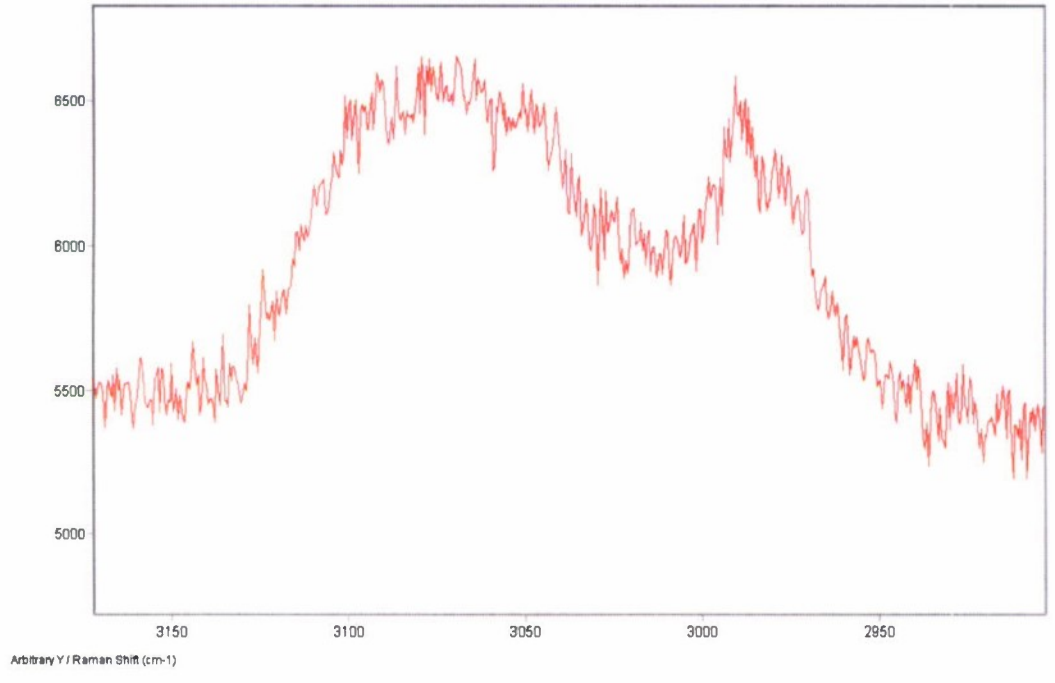

Figure 5.30. Raman spectrum of the C-H vibrational mode of THF hydrate; Tulk *et al.* (1998) reported a similar Raman spectrum for the THF hydrate.

Figure 5.28 clearly indicates that there are two endothermic heat flow signals, which suggest at least two separate phase changes. The first endothermic phase change is probably ice melting since it occurs at approximately 0 °C. The second endothermic phase change could be either THF hydrate and/or THF/H_2 hydrate decomposition. The dissociation temperature of THF hydrate at 6.90 MPa is approximately 4 °C (Gough and Davidson, 1971) and the dissociation temperature of THF/ H_2 hydrate at 6.90 MPa is approximately 6.5 °C (Hashimoto *et al.*, 2006). With the heating protocol employed to date and the potential for the persistence of superheated hydrate phases, it has not been possible yet to determine the origin of the second endothermic signature in the thermogram.

The Raman spectrum shown in Figure 5.30 provides clear evidence of the presence of THF hydrate in the sample cell. Unfortunately, we have not been able to detect the Raman signature of THF/H_2 hydrate. When the sample was removed from the calorimeter at -5 °C, however, it was observed to outgas, suggesting that H_2 was stored within the hydrate. Whether this was due to inclusions of H_2 gas in the THF hydrate or incorporation of H_2 in the crystal (i.e., formation of THF/H_2 hydrate) remains to be determined.

Future Work

Although we followed the same protocol as Strobel *et al.* (2009), we were not able to detect the formation of THF/H_2 hydrate with Raman spectroscopy. To eliminate the possibility of overlap of the dissociation heat flow signals of THF hydrate and THF/H_2 hydrate in our thermograms, the experiments currently are being repeated using a slower temperature ramp of 0.01 °C/min. Hopefully, this approach will provide evidence of the formation of the THF/H_2 hydrate.

Once we have confirmed our THF/H_2 hydrate synthesis protocol, we will then attempt to fully characterize its stability regime. We also will explore ways to enhance H_2 storage capacity and try to identify other benign hydrate promoters that can be used effectively for this application.

5.2.4 International Collaborative R&D

The 6th international workshop on methane hydrate R&D was held in Bergen, Norway on 13-15 May 2008. This series of meetings was initiated as part of HEET and HNEI has served on the organizing committee and as a sponsor for all of the past workshops. The 6th Workshop was attended by 55 scientists, engineers, and other stakeholder from 12 countries. The workshop report is available from the Defense Technical Information Center website:

http://www.dtic.mil/cgi-bin/GetTRDoc?AD=ADA505438&Location=U2&doc=GetTRDoc.pdf

Immediately following completion of the Bergen workshop, planning commenced for the 7th workshop that will be held in Wellington, New Zealand in May 2010. GNS Science, a research organization owned by the Government of New Zealand, is taking the lead for this workshop and HNEI will once again serve on the organizing committee and provide sponsorship. A workshop report should be available during the next phase of the HEET initiative.

5.3 Publications Resulting from Efforts

During the present reporting period, R&D conducted as part of the HEET Methane Hydrates Task has produced the following publications.

Nihous, G.C., C.K. Kinoshita and S.M. Masutani (2009) A determination of the activity of water in water-alcohol mixtures using Mobile Order Thermodynamics, *Chem. Eng. Sci.*, **64**(11), pp. 2767-2771.

Nihous, G.C., K. Kuroda, J.R. Lobos-González , R.J. Kurasaki and S.M. Masutani (2010) An analysis of gas hydrate dissociation in the presence of thermodynamic inhibitors, *Chem. Eng. Sci.*, **65**(5), pp. 1748-1761.

Nihous, G.C. Notes on the temperature dependence of carbon isotope fractionation by aerobic CH_4 oxydizing bacteria, *Isotopes in Environmental and Health Studies*, in press, 2010.

5.4 References

Angell, C.A., Sichina, W.J.; and Oguni, M. (1982) Heat capacity of water at extremes of supercooling and superheating, *J. Phys. Chem.*, **86**, 998–1002.

Archer, D.G. and Carter, R.W. (2000) Thermodynamic properties of the NaCl + H2O System 4. heat capacities of H_2O and NaCl(aq) in cold-stable and supercooled states, *J. Phys. Chem. B.*, **104**, 8563–8584.

Baptista, C., Santos, M.A. and Saõ-José, C. (2008) Phage SPP1 reversible adsorption to Bacillus subtilis cell wall teichoic acids accelerates virus recognition of membrane receptor YueB, *J. Bacteriol.*, **190**(14), 4989-4996.

Bergamaschi, P., Lubina, C., Konigstedt, R., Fisher, H., Veltkamp, A.C. and Zwaagstra, O. (1998) Stable isotope signatures (δ13C, δD) of methane from Euroandfil L sites, *J. Geophys. Res.*, **103**, D7:8251–8265.

Bussman, I., Pester, M., Brune, A. and Schink, B. (2004) Preferential cultivation of type II methanotrophic bacteria from littoral sediments (Lake Constance), *FEMS Microbiol. and Ecol.*, **47**, 179-189.

Chanton, J.P., Powelson, D.K., Abichou, T., Fields, D. and Green, R. (2008) Effect of temperature and oxidation rate on carbon-isotope fractionation during methane oxidation by landfill cover materials, *Environ. Sci. Technol.*, **42**, 7818-7823.

Chen, Y., Dumont, M.G., Cebron, A. and Murrell, J.C. (2007) Identification of active methanotrophs in a landfill cover soil through detection of expression of 16S rRNA and functional genes, *Environ. Microbiol.*, **9**(11), 2855-2869.

Circone, S., Stern, L.A., Kirby, S.H., Pinkston, J.C., and Durham, W.B. (2000a) Methane hydrate dissociation rates at 0.1 MPa and temperatures above 272 K, *Annals of the New York Academy of Sciences*, **912**, 544-555.

Circone, S., Kirby, S.H., Pinkston, J.C., and Stern, L.A. (2000b) Measurement of gas yield and flow rates using a custom flowmeter, *Rev. Sci. Instr.*, **72**(6), 2709-2716.

Clarke, M. and Bishnoi, P.R. (2000) Determination of the intrinsic rate of ethane gas hydrate decomposition, *Chem. Eng. Sci.*, **55**, 4869-4883.

Clarke, M. and Bishnoi, P.R. (2001) Determination of the activation energy and intrinsic rate constant of methane gas hydrate decomposition, *Canadian J. Chem. Eng.*, **79**, 143-147.

Clarke, M. and Bishnoi, P.R. (2004) Determination of the intrinsic rate constant and activation energy of CO_2 gas hydrate decomposition using in-situ particle size analysis, *Chem. Eng. Sci.*, **59**, 2983-2993.

Coleman, D., Risatti, J.B. and Schoell, M. (1981) Fractionation of carbon and hydrogen isotopes by methane-oxidizing bacteria, *Geochim. Cosmochim. Acta*, **45**, 1033-1037.

Cowen J.P., Wen X. and Popp B.N. (2002) Methane in aging hydrothermal plumes, *Geochim. Cosmochim. Acta*, **66**, 3563-3571.

Czarnota, I. (1984) Heat capacity of water at high pressure, *High Temp.-High Press.*, **16**, 295-302.

Dyadin, Y.A., Larionov, E.G., Aladko, E.Y., Manakov, A.Y., Zhurko, F.V. and Mikina, T.V. (1999) Clathrate formation in water-noble gas (hydrogen) systems at high pressures, *Journal of Structural Chemistry*, **40**, 790-795.

Dunfield, P.F., Liesack, W., Henckel, T., Knowles, R. and Conrad, R. (1999) High-affinity methane oxidation by a soil enrichment culture containing a Type II methanotroph, *Appl. Environ. Microbiol.*, **65**, 1009-1014.

Florusse, L.J., Peters, C.J., Schoonman, J., Hester, K.C., Koh, C.A., Dec, S.F., Marsh, K.N. and Sloan, E.D. (2004) Stable low-pressure hydrogen clusters stored in a binary clathrate hydrate, *Science*, **306**, 469-471.

Gough, S.R. and Davidson, D.W. (1971) Composition of tetrahydrofuran hydrate and the effect of pressure on the decomposition, *Canadian Journal of Chemistry*, **49**, 2691-2699.

Grant, N.J. and Whiticar, M.J. (2002) Stable carbon isotopic evidence for methane oxidation in plumes above Hydrate Ridge, Cascadia Oregon Margin, *Global Biogeochem. Cycles*, **16**, 1124-1136.

Handa, Y.P. (1990) Effect of hydrostatic pressure and salinity on the stability of gas hydrates, *J. Phys. Chem.*, **94**, 2652-2657.

Hashimoto, S., Murayama, S., Sugahara, T., Sato, H., and Ohgaki, K. (2006) Thermodynamic and Raman spectroscopic studies on H_2+tetrahydrofuran+water and H_2+tetra-n-butyl ammonium bromide+water mixtures containing gas hydrates, *Chem. Eng. Sci.*, **61**, 7884-7888.

Holmes A.J., Roslev P., McDonald R., Iversen N., Henriksen, K. and Murrell, J.C. (1999) Characterization of methanotrophic bacterial populations in soils showing atmospheric methane uptake, *Appl. Environ. Microbiol*, **65**, 3312-3318.

Huang, D.-S. and Chan, S.I. (2003) Production of high-quality particulate methane monooxygenase in high yields from Methylococcus capsulatus (Bath) with a hollow-fiber membrane bioreactor, *J. Bacteriol.*, **185**, 5915-5924.

Hunkeler, D. and Aravena, R. (2000) Evidence of substantial carbon isotope fractionation among substrate, inorganic carbon, and biomass during aerobic mineralization of 1, 2-dichloroethane by Xanthobacter autotrophicus, *Appl. Environ. Microbiol.*, **66**(11), 4870-4876.

Inagaki F., Tsunogai U., Suzuki M., Kosaka A., Machiyama H., Takai K., Nunoura T., Nealson K.H., Horikoshi K. (2004) Characterization of C1-metabolizing prokaryotic communities in

methane seep habitats at the Kuroshima Knoll, southern Ryukyu Arc, by analyzing *pmoA, mmoX, mxaF, mcrA,* and 16rRNA Genes, *Appl. Environ. Microbiol.*, **70**. 7445–7455.

Isdale, J.D., Easteal, A.J., and Woolf, L.A. (1985) Shear viscosity of methanol and methanol-water mixtures under pressure, *International Journal of Thermophysics*, **6**(5), 439-450.

Jahnke, L.L., Summons, R.E., Hope, J.M. and Des Marais, D.J. (1999) Carbon isotopic fractionation in lipids from methanotrophic bacteria II: The effects of physiology and environmental parameters on the biosynthesis and isotopic signatures of biomarkers, *Geochim. Cosmochim. Acta*, **63**, 79-93.

Jamaluddin, A.K.M., Kalogerakis, N., and Bishnoi, P.R. (1989) Modelling of decomposition of a synthetic core of methane gas hydrate by coupling intrinsic kinetics with heat transfer rates, *Canadian Journal of Chemical Engineering*, **67**, 948-954.

Kevbrina, M.V., Okhapkina, A.A., Akhlynin, D.S., Kravchenko, I.K., Nozhevnikova, A.N. and Gal'chenko, V.F. (2001) Growth of mesophilic methanotrophs at low temperatures, *Microbiology*, **70**, 384-391.

Khmelenina, V.N., Kalyuzhanya, M.G., Sakharovsky, V.G., Suzina, N.E., Trotsenko, Y.A. and Gottschalk, G. (1999) Osmoadaptation in halophilic and alkaliphilic methanotrophs, *Arch. Microbiol.*, **172**, 321-329.

Kiene R.P. and Capone, R. (1985) Degassing of pore water methane during sediment incubations, *Appl. Environ. Microbiol.*, **49**: 143-147.

Kim, H.C., Bishnoi, P.R., Heidemann, R.A., and Rizvi, S.S.H. (1987) Kinetics of methane hydrate decomposition, *Chem. Eng. Sci.*, **42**(7), 1645-1653.

Knizikevičius, R. (2002) Evaluation of desorption activation energy of SiF4 molecules, *Vacuum*, **68**, 29-30.

Knizikevičius, R. (2005) Evaluation of desorption activation energy of SiF2 molecules, *Chem. Phys. Lett.*, **410**, 177-178.

Kolb, S., Kneif, C., Stubner, S. and Conrad. R. (2003) Quantitative detection of methanotrophs in soil by novel pmo! Targeted real time PCR assays, *Appl. Environ. Microbiol.*, **69**, 2423-2429.

Komai, T., Kang, S.P., Yoon, J.H., Yamamoto, Y., and Kawamura, T. (2004) In situ Raman spectroscopy investigation of the dissociation of methane hydrate at temperatures just below the ice point, *Journal of Physical Chemistry B*, **108**(23), 8062-8068.

Kreith, F. and Bohn, M.S. (2001) Principles of Heat Transfer, 6th edition, Brooks/Cole, 700 pp. and appendices.

Lane, D. J. (1991) 16S/23S rRNA sequencing, in *Nucleic Acid Techniques in Bacterial Systematics*, pp. 115–175. Edited by E. Stackebrandt & M. Goodfellow. London: Wiley.

Li, C.C. (1976) Thermal conductivity of liquid mixtures, *AIChe J.*, **22**(5), 927-930.

Lee, H., Lee, J-W., Kim, D.Y., Park, J., Seo, Y-T., Zeng, H., Moudrakovski, I.L., Ratcliffe, C.I., and Ripmeester, J.A. (2005) Tuning clathrate hydrates for hydrogen storage, *Nature*, **434**(7034), 743-746.

Lieberman, R. L. and Rosensweig, A.C. (2005) Crystal structure of a membrane-bound metalloenzyme that catalyses the biological oxidation of methane, *Nature*, **434**, 177-182.

Locarnini, R.A., Mishonov, A.V., Antonov, J.I., Boyer, T.P. and Garcia, H.E. (2006) World Ocean Atlas 2005, Volume 1: Temperature. NOAA Atlas NESDIS 61, S. Levitus, ed., U.S. Government Printing Office, Washington, D.C. 182 pp.

Mahieu, K., De Visscher, A., Vanrolleghem, P.A. and Cleemput, O.V. (2006) Carbon and hydrogen isotope fractionation by microbial methane oxidation: Improved determination, *Waste Managem.*, **26**, 389-398.

Mao, W.L., Mao, H., Goncharov, A.F., Struzhkin, W.W., Guo, Q., Hu, J., Shu, J., Hemley, R.J., Somayazulu, M. and Zhao, Y. (2002) Hydrogen clusters in clathrate hydrate, *Science*, **297**, 2247-2249.

Mikhail, S.Z. and Kimel, W.R. (1961) Densities and viscosities of methanol-water mixtures, *J. Chem. Eng. Data*, **6**(4), 533-537.

Moridis, G.J., Seol, Y. and Kneafsey, T. (2005) Studies of reaction kinetics of methane hydrate dissociation in porous media, Lawrence Berkeley Laboratory Report LBNL-57298 (also in the Proceedings of the 5th International Conference on Gas Hydrates, Trondheim, Norway, June 13-16, 2005).

Nauhaus, K., Treude, T., Boetius, A. and Kruger, M. (2005) Environmental regulation of the anaerobic oxidation of methane: a comparison of ANME-1 and ANME II communities, *Appl. Environ. Microbiol.*, **7**, 98-106.

Nercessian O., Bienvenu N., Moreira D., Prieur D., Jeanthon C. (2005) Diversity of functional genes of methanogenes, methanotrophs and sulfate reducers in deep-sea hydrothermal vents, *Environ. Microbiol.*, **7**(1), 118–132.

Niemann H., Lösekann T., de Beer D., Elvert M., T., Knittel K., Amann R., Sauter E.J., Schlüter M., Klages M., Foucher J.P., Boetius A. (2006) Novel microbial communities of the Haakon Mosby mud volcano and their role as a methane sink, *Nature,* **443**, 854-858.

Nihous G.C. (2008) A quantitative interpretation of recent experimental results on stable carbon isotope fractionation by aerobic CH4-oxidizing bacteria, *Geochim Cosmochim. Acta*, **72**, 4469-4475.

Nihous, G.C. and Masutani, S.M. (2006) Notes on the dissolution rate of gas hydrates in undersaturated water, *Chem. Eng. Sci.*, **61**(23), 7827-7830.

Nihous G.C. and Masutani S.M. (2007) Notes on the modeling of methane in aging hydrothermal vents, *J. Mar. Res.*, **65**(6), 789-812.

Nihous, G.C., Kinoshita, C.K. and S.M. Masutani (2009) A determination of the activity of water in water–alcohol mixtures using mobile order thermodynamics, *Chem. Eng. Sci.*, **64**(11), 2767-2771.

Nihous, G.C., Kuroda, K., Lobos-González, J.R., Kurasaki, R.J. and Masutani, S.M. (2010) An analysis of gas hydrate dissociation in the presence of thermodynamic inhibitors, *Chem. Eng. Sci.*, **65**(5), 1748-1761.

Nijenhuis, I., Andert, J., Beck, K., Kästner, M., Diekert, J. and Richnow, H.-H. (2005) Stable isotope fractionation of tetrachloroethene during reductive dechlorination by Sulfurospirillum multivorans and Desulfitobacterium sp. Strain PCE-S and abiotic reactions with cyanocobalamin, *Appl. Environ. Microbiol.*, **71**(7), 3413-3419.

O'Leary, M. and Osmond, C B. (1980) Diffusional contribution to carbon isotope fractionation during dark CO_2 fixation in CAM plants, *Plant Physiol.*, **66**, 931-934.

Ruo, H., Ruan, A., Jiang, C. and Shen, D.S. (2008) Responses of oxidation rate and microbial communities to methane in simulated landfill conver soil microcosms, *Biosource. Technol.*, **99**, 7192-7199.

Sirota, A.M. and Mal'tsev, B.K. (1959) Experimental investigation of the heat capacity of water at 1–500° C and to pressures of 500 kbar/cm^2, *Teploenergetika*, **6**, 7.

Sloan, E.D. (1998) Clathrate Hydrates of Natural Gases (2nd ed.), Marcel Dekker, New York, 730 pp.

Snover, A.K. and Quay, P.D. (2000) Hydrogen and carbon kinetic isotope effects during soil uptake of atmospheric methane, *Global Biogeochem. Cycles*, **14** (1), 25–39.

Strobel, T.A., Sloan, E.D. and Koh, C.A. (2009) Raman spectroscopic studies of hydrogen clathrate hydrates, *J. Chemical Physics*, **130**, 014506.

Sundh, I., Bastviken, D. and Tranvik, L.J. (2005) Abundance, activity, and community structure of pelagic methane-oxidizing bacteria in temperate lakes, *Appl. Environ. Microbiol.*, **71**, 6746-6752.

Tanaka, H., Nakatsuka, T. and Koga, K. (2004) On the thermodynamic stability of clathrate hydrates IV: double occupancy of cages, *J. Chemical Physics A,* **121**(11), 5488-5493.

Templeton, A.S., Chu, K.-H., Alvarez-Cohen, L. and Conrad, M.E. (2006) Variable carbon isotope fractionation expressed by aerobic CH_4-oxidizing bacteria, *Geochim Cosmochim. Acta*, **70**, 1739-1752.

Tulk, C.A., Klug, D.D. and Ripmeester, J.A. (1998) Raman spectroscopic studies of THF clathrate hydrate, *J. Physical Chemistry A.*, **102**, 8734-8739.

Ullerich, J.W., Selim, M.S., and Sloan, E.D. (1987) Theory and measurement of hydrate dissociation. AIChE Journal, 33(5), 747-752.

Vos, W.L., Finger, L.W., Hemley, R.J., and Mao, H-K. (1993) Novel H_2-H_2O clathrates at high pressures, *Physical Review Letters*, **71**(19), 3150-3153.

Wagner, W. and Pruss, A. (2002) The IAPWS formulation 1995 for the thermodynamic properties of ordinary water substance for general and scientific use, *J. Phys. Chem. Ref. Data,* **31**, 387–535.

Whiticar, M. J. (1999) Carbon and hydrogen isotope systematics of bacterial formation and oxidation of methane, *Chem. Geol.*, **161**, 291-314.

Whittenbury, R., Phillips, K.C. and Wilkinson, J.F. (1970) Enrichment, isolation and some properties of methane utilizing bacteria, *J. Gen Microbiol.*, **61**, 205-218.

Wise, M.G., McAuthur, J.V. and Shimkets, L.J. (1999) Methanotroph diversity in landfill soil: isolation of novel type I and type II methanotrophs whose presence was suggested by culture independent 16S ribosomal DNA analysis, *App. Environ. Microbiol.*, **65**(11), 4887-4897.

Yan T., Ye Q., Zhou J., Zhang C.L. (2004) Diversity of functional genes for methanotrophs in sediments associated with gas hydrates and hydrocarbon seeps in the Gulf of Mexico. *FEMS Micro. Ecol.* 57: 251-259

Yedlapalli, P., Lee, S. and Lee, J.W. (2010) Stable occupancy of hydrogen molecules in H_2 clathrate hydrates and H_2+THF clathrate hydrates determined by *ab initio* calculations, *Journal of Thermodynamics,* Article ID 651819.

Yu, S.S.-F., Chen, K.H.-C., Tseng, M.Y.-H., Wang, Y.-S., Tseng, C.-F., Chen, Y.-J., Huang, D.-S. and Chan, S. I. (2003) Production of high-quality particulate methane monooxygenase in high yields from Methylococcus capsulatus (Bath) with a hollow-fiber membrane bioreactor, *J. Bacteriol.*, **185**, 5915-5924.